Université de Montréal

Stochastic Simulation to Improve Land-Cover Estimates Derived from Coarse Spatial Resolution Satellite Imagery

(La simulation stochastique pour améliorer les estimations de la couverture des sols à partir d'images satellitales à résolution spatiale grossière)

par

Conrad M. Bielski

Département de géographie

Faculté des arts et des sciences

Thèse présentée à la Faculté des études supérieures

en vue de l'obtention du grade de

Philosophiae Doctor (Ph.D.)

en géographie

novembre, 2001

© Conrad M. Bielski

Université de Montréal

Faculté des études supérieures

Cette thèse intitulée:

Stochastic Simulation to Improve Land-Cover Estimates Derived from Coarse Spatial Resolution Satellite Imagery

(La simulation stochastique pour améliorer les estimations de la couverture des sols à partir d' images satellitales à résolution spatiale grossière)

présentée par:

Conrad M. Bielski

a été évaluée par un jury composé des personnes suivantes:

Dr. André Roy Géographie, Université de Montréal	président-rapporteur
Dr. François Cavayas Géographie, Université de Montréal	directeur de recherche
Dr. Marc D'Iorio Centre canadien de télédétection	co-directeur de recherche
Dr. Langis Gagnon Centre de recherche informatique de Montréal	membre du jury
Dr. Pierre Goovaerts Civil and Environmental Engineering, University of Michigan	examinateur externe
Dr. Jean Meunier Informatique et recherche opérationnelle, Université de Montréal	représentent du doyen de la FES

ABSTRACT

Stochastic Simulation to Improve Land-Cover Estimates Derived from Coarse Spatial Resolution Satellite Imagery

by Conrad M. Bielski

Keywords: stochastic imaging, remote sensing, land-cover and scale change

Today's land-cover monitoring studies at regional to global scales using optical satellite based remote sensing is confined to the use of coarse spatial resolution imagery. Due to the coarse spatial resolution, land-cover identification is poor and estimation is error prone. Some land-cover investigations apply a scaling-up approach where fine spatial resolution imagery is aggregated until the wanted mapping scale is attained. Here, the opposite approach (scaling-down) is investigated through the use of geostatistical stochastic imaging techniques. The objective of this thesis is to examine the possibility of generating finer spatial resolution multi-spectral like images based on available multi-spectral coarse spatial resolution imagery to extract land-cover information. Other ideas addressed were: a) whether stochastic imaging can indeed generate multi-spectral like finer spatial resolution imagery based on coarse spatial resolution imagery, b) the possibility of introducing SAR imagery to improve the spatial location of the generated image features and, c) the applicability of an automatic spectral segmentation algorithm to the generated imagery. The sequential gaussian simulation algorithm was used to generate the finer spatial resolution multi-spectral like images. This algorithm was applied using the local varying mean and co-simulation options and always conditioned to the coarse spatial

resolution imagery. From aboard the SPOT-4 satellite, the VEGETATION (VGT) instrument provided the coarse spatial resolution imagery while the HRVIR instrument provided the fine spatial resolution imagery for validation. Algorithm parameters were taken directly and derived from the VGT imagery. RADARSAT ScanSAR wide imagery was also used in the stochastic imaging process. Four test sites in the vicinity of the Island of Montreal were chosen each measuring 15 km x 15 km. The tests resulted in the generation of multi-spectral images with red, NIR and SWIR bands. Three different sets of input parameters were used to generate the finer spatial resolution images. The first set was based on the VGT image statistics, the second was based on derived finer spatial resolution statistics and the last set was based on the second set of parameters with the inclusion of SAR imagery. The K-means algorithm was chosen to segment the generated finer spatial resolution images. Overall, this experiment served to: a) demonstrate that coarse spatial resolution imagery can be applied to generation of finer spatial resolution imagery with stochastic imaging techniques. However, before spectral reproducibility can be achieved, the sensing system and scale relationships must be better understood, b) illustrate the appropriateness of the co-simulation technique but also show that the input parameters (variogram and distribution) have a significant impact on the resulting scale of the generated finer spatial resolution images, c) demonstrate that the use of SAR imagery is beneficial to the process of generating finer spatial resolution imagery because it helps fix the ground scene characteristics, but the relationship to the optical imagery (an important input parameter for co-simulation) varies depending on the scene and must be further investigated, d) show that spectral

segmentation of synthetic imagery is possible but validation remains difficult using the standard approach.

RÉSUMÉ

La simulation stochastique pour améliorer les estimations de la couverture des sols à partir d'images satellitales à résolution spatiale grossière

par Conrad M. Bielski

mots clés: simulation stochastique, télédétection, couverture des sols, changement d'échelle

À l'heure actuelle, le suivi de la couverture du sol par télédétection à des échelles allant du régional au planétaire est confiné à des capteurs à résolution spatiale grossière. Une telle résolution cause l'agrégation des objets, ce qui mène à des estimations erronées quant à l'étendue et aux types de classes extraites des images. Ce problème est beaucoup plus aigu lorsque le territoire présente une grande hétérogénéité. C'est pourquoi plusieurs préfèrent classifier des images à résolution fine et par la suite agréger les classes pour obtenir une cartographie à des échelles moins détaillées. Cette technique est cependant coûteuse et ne répond pas aux exigences d'un suivi régulier pour les échelles allant du régional au planétaire. Dans cette thèse nous examinons le problème inverse, c'est-à-dire de générer des images à résolution spatiale fine en se servant des images à résolution spatiale grossière.

Plus particulièrement, l'objectif principal de cette recherche était d'évaluer la capacité des techniques géostatistiques de simulation stochastique afin de générer des images multispectrales à une résolution spatiale fine. Ces images permettraient ainsi

d'obtenir des données sur la couverture du sol mieux adaptées aux besoins du suivi du territoire qu'en se servant des images originales à résolution grossière. Les objectifs spécifiques de cette étude étaient les suivants : a) étudier le potentiel des différentes techniques de simulation stochastique pour générer des images à résolution fine ayant des caractéristiques spectrales similaires aux images acquises par des capteurs à cette résolution fine, b) étudier la possibilité d'intégrer des images non-optiques dans le processus de simulation afin d'introduire des informations complémentaires qui pourraient améliorer la caractérisation du territoire, et c) évaluer le potentiel de classification automatique des images générées.

Pour ce faire, des images provenant du satellite SPOT-4 ont été utilisées. Les images du capteur VEGETATION (VGT) étaient les images de base à résolution grossière (1 km). Les images du capteur HRVIR à résolution fine (20 m) ont servi comme données de validation pour les images générées à l'aide des algorithmes de simulation stochastique. L'imagerie non-optique SAR du satellite RADARSAT-1 (mode ScanSAR, résolution nominale de 100 m) complétait la série de données. Quatre sous-régions de 15 x 15 km dans la région métropolitaine de Montréal ont été choisies afin de couvrir différents types paysages (urbain, péri-urbain et rural).

Pour chaque sous-région des images multispectrales (rouge, PIR, IROC) ont été générées en utilisant l'algorithme SGSIM (Sequential Gaussian SIMulation) et les techniques LVM (local varying mean) et co-simulation. L'expérimentation comprenait trois phases; chaque phase amenait des informations suplementaires a la

simuation stochastique. Dans la première phase, les intrants (variogramme et distribution) provenaient directement des images VGT. Dans la seconde phase, ces intrants étaient fixés pour représenter les caractéristiques des images à résolution fine. Puisque ces intrants n'étaient pas conformes aux statistiques des images HRVIR, ces dernières ont finalement servies à la simulation de la phase II. Dans la troisième phase les images RADARSAT ont été introduites avec les intrants de la phase II. Dans les deux premières phases les deux techniques (LVM et co-simulation) ont été appliquées, tandis que dans la troisième phase seule la co-simulation a été employée. Pour la co-simulation avec les données RADARSAT, la corrélation avec les données optiques n'était assez forte pour influencer la génération d'images. C'est pourquoi nous avons fixé une corrélation arbitraire de 0.75 mais en conservant le signe de la relation radar-optique.

La segmentation des images générées dans chaque phase ainsi que des images de base a été réalisée à l'aide de l'algorithme *K-means* puisque notre objectif était d'évaluer les similarités des espaces spectraux de chacune des images. Les groupes spectraux (clusters) établis par l'algorithme ont été comparés. Les images classifiées ont aussi été analysées en fonction des données disponibles sur les occupations du sol afin d'analyser la correspondance entre classes spectrales et classes d'occupation du sol.

Les principaux résultats des trois phases d'expérimentation sont les suivants : L'utilisation des intrants provenant uniquement de VGT (phase I) permettent la

génération des images à une résolution spatiale plus fine, cependant leurs caractéristiques sont passablement similaires aux images originales VGT ; L'utilisation des intrants provenant de HRVIR (phase II) permet de générer des images avec un contenu spectral plus varié mais difficile à faire correspondre aux images HRVIR ; L'ajout de l'image RADAR dans le processus de simulation (phase III) permet d'obtenir des patrons spatiaux qui correspondent mieux à ceux de HRVIR.

Les résultats de l'application de l'algorithme K-means démontrent qu'il est possible d'obtenir des regroupments distincts. Cependant leur nombre variait selon la sous-région et les images analysées (8-16 regroupments). L'examen comparatif des regroupments dans l'espace spectral ainsi que des proportions de pixels par regroupment a montré qu'il est difficile d'établir des liens clairs entre les regroupments des images générées et ceux obtenus par HRVIR. Les regroupments obtenus dans la phase I étaient similaires à ceux de l'image VGT. Par contre, les regroupments étaient différents dans la phase II et III, sauf ceux obtenus avec la technique LVM. La validation avec les données sur les occupations du sol n'était concluante. En effet, même dans le cas de HRVIR, à l'exception de la classe eau, il n'y avait pas un regroupments dominant par type d'occupation du sol. Les images générées dans la phase II et III avec la co-simulation présentaient le plus d'intérêt. En effet, deux ou trois regroupments dominants correspondaient à une classe d'occupation du sol, de la même manière que les images HRVIR.

Les conclusions de cette recherche sont: a) l'algorithme SGSIM permet de générer des images à une résolution spatiale plus fine à partir des images à résolution grossière ; cette recherche ouvre donc une nouvelle voie pour étudier les mécanismes de changement d'échelle dans le cas des images de télédétection ; b) les images à résolution fines générées dans cette recherche présentent des différences de distribution spectrale par rapport aux images "réelles." Prise seule, la différence entre les résolutions spatiales de VGT et HRVIR ne peut pas expliquer ces différences dans les distributions spectrales. Les conditions d'expérimentation étant bien choisies au départ (acquisition des images en parallèle, zones centrales des images, mêmes bandes spectrales) nous ont permis de minimiser les incertitudes dues aux conditions d'acquisition. Ceci nous amène à conclure que les différences sont plutôt attribuables aux systèmes de captage eux-mêmes (différences dans le système optique, résolution radiométrique différente, sensibilités spectrales différentes des détecteurs, etc.). Il y a donc matière à étude comparative plus poussée dans le domaine de captage des données avant que l'on puisse s'assurer que les différences observées ne sont pas des artefacts de l'algorithme de simulation; c) L'algorithme SGSIM est facilement adaptable à des conditions d'application pratique. Cependant, le choix des intrants dans cet algorithme est important parce que les images générées sont très sensibles aux conditions initiales, particulièrement le variogramme et la forme de la distribution des valeurs ; le problème mentionné plus haut sur la difficulté d'obtenir un variogramme ponctuel pour des sous-régions à partir du variogramme de VGT mérite d'être étudié plus à fond car pour que la méthode proposée ici soit pratique nous devons nous affranchir des données à résolution spatiale fine ; d) L'utilisation

des images SAR s'est avérée importante pour donner un aspect spatial plus réaliste aux images générées. La solution adoptée ici pour leur intégration est nouvelle et appropriée. En étudiant les relations optique-radar à partir d'autres images il est possible de mieux étalonner la valeur du coefficient de corrélation nécessaire à l'application de la technique de co-simulation ; e) la validation des résultats est difficile compte tenu de l'incompatibilité entre classes spectrales (peu importe l'image utilisée) et les catégories générales d'occupation du sol telles qu'employées à la cartographie standard à échelle régionale (urbain, agricole, forestier, etc.).

Table of Contents

List of Tables

List of Figures

Glossary

AVHRR – Advanced Visible High Resolution Radiometer

BOREAS – BOReal Ecosystem-Atmosphere Study

CDF – cumulative distribution function

CCDF – conditional cumulative distribution function

CORINE – Co-Ordination of Information on the Environment

EM – Electromagnetic (refers to the Electromagnetic spectrum)

DN – Digital Number

IFOV – Instantaneous Field of View

VGT – VEGETATION sensor onboard the SPOT 4 satellite

HRVIR – High Resolution Visible Infrared sensor onboard the SPOT 4 satellite

Land-cover – the composition and characteristics of land surface elements

NIR – Near Infrared

NOAA – National Oceanic and Atmospheric Administration

OK – Ordinary Kriging

PSF – Point Spread Function

RF – Random Function

RV – Random Variable

Scaling-up (or bottom up) – Aggregation process where the original spatial data are reduced to a smaller number of data units.

Scaling-down (or top down) – the reverse of scaling-up, i.e. increasing the number of data units based on a limited data set.

SAR – Synthetic Aperture Radar

SD – Standard Deviation

SWIR – Short Wave Infrared

SGSIM – Sequential Gaussian Simulation

TREES – TRopical Ecosystem Environment observation by Satellite

To my wonderful family: Anita, Dorian, Roman & George

Acknowledgements

Dr. François Cavayas is my director, employer and friend. I wish to thank him for the support that he gave me throughout these last four years. His encouragement and friendship allowed me to finish without losing my mind. A special thanks to Dr. Marc D'Iorio of the Canada Centre for Remote Sensing for co-directing and asking those special questions that everyone else seemed to forget.

This thesis would not be possible without data, which was made possible by a grant from the EODS (Earth Observation Data Sets) program, Canada Centre for Remote Sensing. Additional support was received from the FCAR Bourses de recherche en milieu pratique (Fonds FCAR-MRST) of the government of Québec which allowed me to work with Dr. Langis Gagnon at the CRIM (Centre de Recherche en Informatique de Montréal).

A special thank you to all those who in my final year (the year that I wrote this thesis) gave me a roof over my head. I will never forget the graciousness that you showed me and you are always welcome to visit (Natasha, Pierre, Bronek, Genevieve, Gabriel, and François).

Dzienkuje Mama za dach nad glowa i pomoc ze wszystkim.

Chapter 1 – Introduction

Scientists and policy-makers rely upon satellite based remotely sensed data to extract pertinent information relating to the state of the environment. At the global scale, categorising geographic space into broad land-cover classes (e.g. forest, urban, etc.) and monitoring their changes over time are important because land-cover distribution and change are inputs to many studies including desertification, greenhouse effects, etc. Projects such as TREES (TREES 1999) or NASA's Landsat Pathfinder Humid Tropical Deforestation Project (UMD 1998) use estimates of the total tropical forest cover across the globe to help measure changes caused by natural and anthropogenic disturbances over time. Land-cover can also be used as a surrogate for specific parameters (e.g. plant biomass or canopy conductance) that cannot be measured directly over large regions (Cihlar *et al*. 1997) as in the case of the BOREAS project that deals with ecosystem-atmosphere interactions (BOREAS; Sellers *et al*. 1995). Future monitoring will support governments for environmental action. The Kyoto protocol (UNFCCC 2001) calls for better forest management and countries are rewarded or penalised depending on the state of their forests. Such monitoring demands accuracy in order to make sure that protocol compliance be rewarded and non-compliance be penalised. Uncertainties in such situations (Townshend *et al*. 1992) provide political loopholes and no means of upholding the law because verification is erroneous.

Acquiring data on the state of and changes in land-cover at the global scale however, is not an easy task. The most suitable satellite imagery provides large area

coverage while maintaining an adequate spatial resolution for land-cover characterization. The extent of the recorded image determines the total ground scene area that can be sensed and must be large enough to supply a "snapshot" in time of the land-cover state of the whole Earth. A large extent also allows for a finer temporal resolution providing important monitoring information that can be used to separate seasonal trends in land-cover change from disturbances and modifications. In a practical sense, optical data benefits from such a fine temporal resolution because cloud cover and atmospheric effects, in general, are reduced.

However, such an ideal remote sensor does not exist because there is always a trade-off between extent of coverage and fineness of the spatial resolution. Over the last 20 years, experimentation with the NOAA AVHRR series of satellite based sensors (about 2000 km of spatial coverage at 1 km spatial resolution and daily coverage) has shown the difficulty of applying coarse spatial resolution optical imagery specifically to the extraction of thematic content and estimating its proportions (Justice *et al*. 1989, Townshend *et al*. 1991, Townshend *et al*. 1992, Townshend *et al*. 1994, Mayaux and Lambin 1995; 1997). The fact that recorded observations and derived conclusions are scale dependent is well known (Gosz 1986, Addicott *et al*. 1987). The certainty in identifying ground scene composition and characteristics increases as the scale of observation (i.e. resolution and extent of image data) provides the necessary details at the scale of inference (i.e. resolution and extent of extracted information). Thus, a general practice applied today to obtain an exact characterisation of broad land-cover categories is to classify fine spatial resolution satellite data and scale-up. The scaling-up procedure involves aggregating

the land-cover classes based on cartographic generalisation criteria e.g. at what map scale will side roads still be shown. The European CORINE land-cover program is based on the principle of cartographic generalisation and in Canada this principle will also be utilised to meet the Kyoto protocol requirements. However, such an approach is very time consuming and does not meet the fine temporal revisit criterion.

In order to extract the same broad land-cover categories from satellite based optical coarse spatial resolution imagery the opposite procedure would need to be applied: scaling-down. Scaling-down is more problematic because less information is available at the start. Technological advances provide better optical coarse spatial resolution imagery and favourable experimental conditions to examine the feasibility of such a scaling-down procedure. In fact the VGT and the HRVIR sensors on board the SPOT-4 satellite provides respectively large extent/coarse spatial resolution imagery and small extent/fine spatial resolution imagery that can be recorded in parallel (VEGETATION 1999). Thus it is possible to generate data sets of the same area of interest at both fine and coarse spatial resolutions under the same external conditions (time of the day, atmospheric and solar illumination conditions). In addition, the availability of SAR satellite images with relatively large area coverage (500 km x 500 km) and medium spatial resolution (<100 m), such as the ScanSAR wide mode of RADARSAT-1, could be introduced as an independent source of information into this scaling-down procedure. A scaling-down procedure could be realised and the quality of the scaled-down imagery in terms of land-cover characterization constitute the core of this thesis. Geostatistical stochastic imaging

techniques are the privileged tool for such a procedure for the reasons explained in the next section.

1.1 Available Techniques

The existing techniques that aim to improve the information extraction potential from coarse spatial resolution images introduce "exogenous image data". These techniques can be separated into two general categories (table 1.I). Image enhancement tries to provide a visually more appealing product while error correction attempts to correct land-cover estimates.

Table 1.I – Various approaches to improve image quality and derived information.

Goal	Method	References
Image Enhancement	Fusion	Carper *et al*. 1990; Chavez *et al*. 1991; Pohl and Van Genderen 1998; Ranchin and Wald 2000; Liu 2000; Del Carmen Valdes and Inamura 2001
Error Correction	Regression	Kong and Vidal-Madjar 1988; Foody 1994; Oleson *et al*. 1995; Mayaux and Lambin 1995; Fazakas and Nilsson 1996; Maselli *et al*. 1998
	Modelling	Iverson *et al*. 1989; Zhu and Evans 1992; Cross *et al*. 1991; Kerdiles and Grondona 1995; Ouaidrari *et al*. 1996; Atkinson *et al*. 1997

Image enhancement (table 1.I – first row) is primarily achieved through fusion techniques. Fusion techniques use fine spectral/coarse spatial resolution imagery that is combined with coarse spectral/fine spatial-resolution imagery to obtain an image with the finest spectral/spatial resolution combination.

Error correction procedures are often based on either regression or modelling. When regression is used (table 1.I – middle row), relationships between samples of fine spatial resolution parameters and the matching coarse spatial resolution parameters are computed. These relationships are then extrapolated over regions where only the coarse spatial resolution parameter is present to estimate the fine spatial resolution parameters.

Modelling can encompass a large number of techniques. One of the more used techniques is mixture modelling (table 1.I – last row). Mixture modelling is based on the assumption that the measured spectral response from a particular image pixel is related to the mixture or patterns of cover types in that location.

The afore mentioned techniques, however, do not provide all the necessary solutions to improve image data quality gathered over large regions. Image fusion necessarily requires a fine spatial/coarse spectral resolution image as well as a coarse spatial/fine spectral resolution image that both cover the same region. Monitoring large regions using this technique is therefore unfeasible because fine spatial resolution imagery is usually not available. The regression and modelling techniques require fine spatial resolution image samples for calibration. The larger the area under investigation, the more sample sites are required. Furthermore, the complexity of the ground scene is a determining factor in the required number of sample and validation sites and thus the number of required fine spatial resolution samples increases as spatial heterogeneity increases.

Previous studies showed that coarse spatial resolution optical imagery (NOAA AVHRR) had quantifiable spatial variability based on the variogram (e.g. Gohin 1989, Bielski 1997). This information together with image statistics could be the input for various geostatistical methods (i.e. kriging or stochastic imaging) to generate finer spatial resolution imagery.

Geostatistical methods, which were originally developed for the mining industry in the 1950's, were later introduced into the remote sensing context in the late 1980's by Woodcock *et al*. (1988a, 1988b). Many remote sensing studies and applications have since used geostatistics and some typical studies are presented in table 1.II. However, no attempt has been documented until now to generate a finer spatial resolution image using geostatistical techniques. More importantly, no attempt has been made to examine whether such a scaling-down procedure can generate an image whose spectral characteristics approach those of a fine spatial resolution image that is considered optimal for land-cover classification at the regional scale.

Table 1.II – A listing of geostatistical applications in the remote sensing context.

Curran and Dungan 1988	Used the semi-variogram to isolate sensor noise and remove intra-pixel variability
Gohin 1989	Used the variogram and co-variogram to compare sea surface temperatures taken in situ and from satellites to evaluate the importance of spatial structures in the data and instrument error.
Webster *et al*. 1989	Variogram was used to design sampling schemes for estimating the mean to meet some specified tolerance expressed in terms of standard error.
Atkinson *et al*. 1990	Selection of sufficient image data for compressed storage.
Cohen *et al*. 1990	Computed semivariograms on images of a variety of Douglas-fir stands and found relationships between patterns in stand structure, canopy layering and percent cover.
Bhatti *et al*. 1991	Interpolated ground measurements of soil properties and crop yield over large areas combined with Landsat TM data using kriging and co-kriging.
Atkinson *et al*. 1992	Applied co-kriging using ground based radiometry.
D'Agostina and Zelenka 1992	Applied the co-kriging technique to two available information sources to reduce the estimation error.
Dungan *et al*. 1994	Provided examples of kriging and stochastic imaging to map vegetation quantities using ground and image data.
Lacaze et al. 1994	Compared variogram of different Mediterranean environments based on images from a variety of sources (air and satellite based).
Rossi *et al*. 1994	Interpolated land-cover classes found under the clouds with kriging.
Atkinson and Curran 1995	Evaluation of the relation of size of support with the precision of estimating the mean of several properties using kriging.
St-Onge and Cavayas 1995	Used the directional variogram from high spatial resolution images to estimate height and stocking of forest stands.
Eklundh 1995	Noise estimation in AVHRR data using the nugget variance.
Lark 1996	Computed semi-variance in a local window for lags of different length and direction to discriminate land-cover classes.
Van der Meer 1996	Development of indicator kriging based classification technique for hyperspectral data.
Curran and Atkinson 1998	Presented overview of geostatistics in remote sensing with examples.
Dungan 1998	Compared regression, co-kriging and stochastic imaging techniques to generate maps based on sampled imagery.
Wulder *et al*. 1998	Used variogram model parameters to compute the semivariance moment texture as a surrogate of forest structure to related LAI and vegetation indices.
Atkinson and Emery 1999	Explored the spatial structure of different bands using the variogram.

Initial attempts by the author to generate finer spatial resolution images were done using the kriging interpolator with unsatisfactory results (Bielski and Cavayas 1998, Bielski 1999). Kriging proved to be inadequate because the interpolation algorithm generated smoothed images whose overall statistics did not reproduce the anticipated results at the finer spatial resolution. These difficulties could in principle be overcome with the application of the geostatistical stochastic imaging technique (Dungan 1998, Goovaerts 2000) because the simulated data is not smoothed.

1.2 Objectives and Hypotheses

An attempt is made in this thesis to establish a practical procedure to generate finer spatial resolution imagery based on coarse spatial resolution optical imagery and stochastic imaging. This generated imagery could then provide a better land-cover characterization than the original imagery could. The generated finer spatial resolution imagery would provide a finer unit of measurement (finer spatial resolution) and more spectral variability to discern different land-cover types.

The specific objectives of the study are as follows:

- analyse the ways that experimental variograms and other statistical parameters extracted from the sole coarse spatial resolution imagery could be used as a support for generating finer spatial resolution imagery;
- analyse the possibility of using information provided by non optical sensors (SAR imagery);
- validate the various generated images in terms of location and possible class labels.

The working hypotheses based on previous personal work are:

- that the coarse spatial resolution imagery preserves enough information to generate new data with similar spectral characteristics compared to a finer spatial resolution imagery;
- that geostatistical theory as well as the stochastic imaging techniques can be used to change the spatial scale of remotely sensed imagery;
- that SAR imagery can provide spatial location information to enhance the generated optical images;
- that an automatic segmentation algorithm is applicable to synthetic multi-spectral imagery in order to obtain meaningful land-cover classes.

A tool able to zoom-in (or out) on available coarse spatial resolution imagery based on geostatistical knowledge could provide the data necessary to fill in the gaps between unavailable finer resolution sensor data. This approach presented here concentrates on the structure of the data itself and generates image data in the same spectral bands as those found in the original coarse spatial resolution imagery. The procedure itself is based on generating data with similar characteristics as that of finer spatial resolution imagery and information extraction therefore becomes a secondary step. Information extraction as a secondary step facilitates the creation or loss of information rather than modelling how land-cover objects appear or disappear depending on the scale of observation. A reliable segmentation or supervised classification method thus remains an integral part of the information extraction procedure.

1.3 Originality and Contribution of the Thesis

The novel idea behind the approach presented in this thesis is to apply a stochastic imaging technique to generate imagery at a finer spatial resolution. The stochastic imaging algorithm explored for this purpose was the sequential gaussian simulation algorithm. In addition, both the locally varying mean (LVM) and co-simulation techniques were tested. Theoretically such an approach could be applied without recourse to any spatial data set. However, the goal is to generate a finer spatial resolution data set based solely on available coarse spatial resolution imagery whose characteristics are similar to a fine spatial resolution image that could be acquired in reality. Furthermore, the emphasis is placed on modelling the change in the overall statistics of the images rather than modelling the manner in which land-cover classes change over different spatial scales. Consequently, applying traditional segmentation techniques and classification strategies to generated finer spatial resolution optical imagery is a new tactic.

Testing the viability of zooming-in to coarse spatial resolution data by means of geostatistical stochastic imaging is important because of the possibility of increasing certainty about derived information. This particular approach could increase certainty through the availability of finer spatial resolution data. Use of finer spatial resolution data means that the scale of observation is closer to that required by the user (scale of inference) and should therefore reduce error. The usefulness of the resulting generated finer spatial resolution image data however, is entirely dependent

on whether the theory behind the stochastic imaging algorithms is sound. Success in this work would allow researchers to generate finer spatial resolution imagery for global studies based on coarse spatial resolution data. As such, historical AVHRR imagery can also be re-examined to improve land-cover assessment.

Another novelty of this thesis is the inclusion of SAR imagery into the scaling-down process. SAR data differs from optical data in that the sensor is active as well as the fact that it records wavelengths in the cm range. The benefit of the SAR data to generating finer spatial resolution imagery is that it can provide spatial location information that is lacking in the original coarse spatial resolution data.

As mentioned earlier, satellite based remote sensing image data are available in a multitude of configurations because no single sensor can provide the user with all the information associated with a specific ground scene. It is expected that the results of this research will give increased confidence in using coarse spatial resolution images for deriving and estimating land-cover at the regional scale of observation.

1.4 Structure of the Thesis

The thesis is subdivided into nine chapters. Chapter 2 discusses the role of resolution and extent in deriving information from remotely sensed data. The remotely sensed data chosen for this investigation were image data that recorded in either the optical or microwave region of the EM spectrum. This choice rests on the fact that these are presently the two most common sensor configurations for satellite

remote sensing platforms. A discussion of the spatial, spectral, radiometric and temporal scales related to these types of sensors is also presented. The scale of observation is based on the sensor characteristics while the scale of inference pertains to the scale at which conclusions are made (Csillag *et al*. 2000). The final goal of any remote sensing campaign is to extract pertinent information from the image data. The relationship between the scale of observation and the scale of inference determines the certainty with which one can draw conclusions but this relationship is usually unknown.

Remotely sensed imagery is a regionalised variable and chapter 3 provides a practical explanation of the geostatistical tools applied including the experimental variogram, the model variogram, regularisation and stochastic imaging. Specifically, the sequential gaussian simulation algorithm was chosen for this research because of its ease of implementation, speed and suitability for the available data. Both LVM and co-simulation implementations were tested.

The methodology as well as the data are presented in chapter 4. Chapters 5 to 7 describe the three phases of the experiment. Each phase was designed to introduce more information into stochastic imaging process. Phase I generates finer spatial resolution imagery based on coarse spatial resolution statistics and data. Phase II generates finer spatial resolution imagery based on derived fine spatial resolution statistics and coarse spatial resolution data. The final phase uses the same information as phase II to which it incorporates SAR imagery to better localise spectral objects. In chapter 8, each of the generated images is then segmented in order to analyse their

usefulness in deriving and estimating land-cover at the regional scale of observation. Finally, the resulting spectral segments are validated with Canadian Land Inventory (CLI) data. Chapter 9 presents a summary discussion of the work as well as the conclusions.

Chapter 2 – The Remotely Sensed Image

The remotely sensed image itself is a recording of spectral measurements arranged in space. These data are ultimately used to derive land-cover information about a recorded ground scene. The data itself and the scale of observation directly determine the information content and is based on the spatial, spectral, radiometric and temporal characteristics. In digital form, the data are easily manipulated and algorithms help enhance and automate the information extraction process. The following sections discuss the remotely sensed image characteristics and the difficulties in extracting the desired information, especially from coarse spatial resolution images.

2.1 Remotely Sensed Image Characteristics

An important characteristic of remotely sensed image data quality is resolution (or the overall fineness of detail characterising the image) and extent. The resolution is the smallest unit from which a meaningful measurement can be recorded. Qualitatively it is described as either fine or coarse. The extent refers to the limits of the resolution characteristic in question with small and large describing its qualities. The two are inseparable and context dependent.

2.1.1 Spatial resolution

The most obvious characteristic of any remotely sensed image is spatial resolution. Optical sensors record reflected energy in the visible and reflective IR

regions of the EM spectrum (0.4 – 2.5 μm). The spatial resolution of these sensors can be defined by

- the geometrical properties of the imaging system,
- the ability to distinguish between point targets,
- the ability to measure the spectral properties of small targets and,
- the ability to measure the periodicity of repetitive targets (separability) (Mather 1987),
- dwell time in new sensors.

The IFOV of a sensor is the ground scene area contributing to a single measurement as defined by the sensor's aperture (geometric properties) (figure 2.1). The IFOV is the area on the ground that is viewed by the instrument from a given altitude at any given instant in time. The equation

$$D = H * b$$

computes the spatial resolution (diameter D) of an image knowing the height of the sensor (H) and the IFOV in radians (b). The resulting image data is affected by the IFOV because for a given flying height, the IFOV is positively related to the sampled ground extent but negatively related to the spatial resolution (Curran 1985).

The point spread function (PSF) of a sensor, or the distribution of intensity from a single point source, influences the spatial resolution through the sensor's ability to distinguish between point targets. The presence of relatively bright or dark objects within the IFOV of the sensor will increase or decrease the amplitude of the

PSF so as to make the observed radiance either higher or lower than that of the surrounding areas. Therefore, objects that are smaller than the IFOV spatial resolution of the sensor can still be detected (e.g. small rivers in the NIR band).

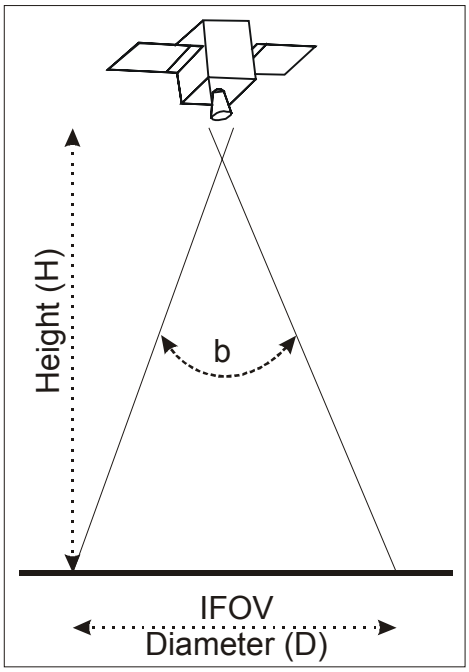

Figure 2.1 – Spatial resolution based on the geometric properties of the imaging system where D is the diameter of the ground sampling element in metres, H is the height of the sensor and b is the IFOV in radians.

The Effective Resolution Element (ERE) is a measure of spatial resolution based on the size of an area for which a single radiance value can be assigned with reasonable assurance that the response is within 5 % of the value representing the actual relative radiance. The Effective Instantaneous Field of View (EIFOV) is based on the spatial frequency of distinguishable objects. This measure is usually based on

theoretical targets and therefore is likely to exceed the performance of an instrument in actual applications (Mather 1987).

Optical sensors depend on reflected sunlight (passive system) while a radar sensor sends and receives energy pulses (active system) in the millimetre to metre range. The spatial resolution of a radar system is based on the ability of its antenna to identify two closely spaced targets as separate points, i.e. the points will appear on the image as two distinct dots. For example, if a particular radar system is able to distinguish two closely spaced objects as separate; a lower resolution system may only distinguish one object. Radar spatial resolution is measured in both the azimuth (i.e. flight) and range (i.e. side looking) directions and is controlled by the radar system and antenna characteristics. The signal pulse length (figure 2.2) and the beam width (figure 2.3) thus control the radar systems spatial resolution. The signal pulse length dictates the spatial resolution in the direction of energy propagation where shorter pulses will result in a finer spatial resolution in the range direction. The width of the beam dictates the resolution in the azimuth direction. The beam width is directly proportional to the radar wavelength and is inversely proportional to the length of the transmitting antenna. This means that spatial resolution deteriorates as the distance increases from the antenna with respect to the target. Therefore a long radar antenna is required to achieve finer spatial resolution in the flight direction. Since satellites are very far from their targets, in theory this would require the system to carry an enormous antenna.

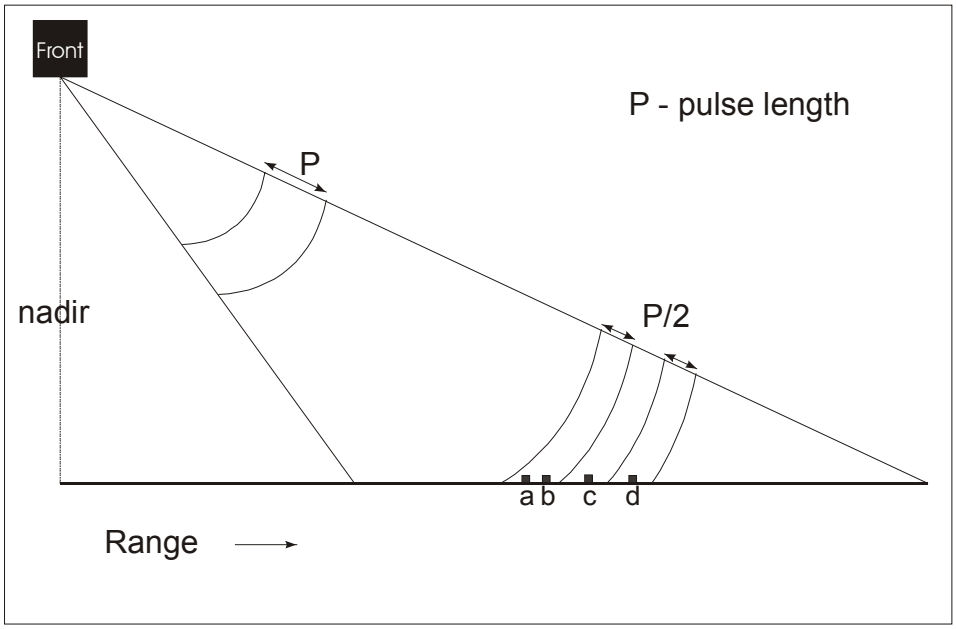

Figure 2.2 – Spatial resolution in the range direction for a radar system.

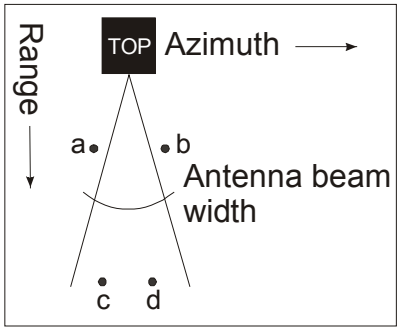

Figure 2.3 – Spatial resolution in the azimuth direction for a radar system.

In order to circumvent the need for a very long antenna, the Synthetic Aperture Radar (SAR) was developed. SAR uses a short antenna that can simulate a much larger antenna through modified data recording and signal processing techniques. Signal processing techniques also allow azimuth resolution to be independent of range resolution (CCRS 2001).

Figure 2.4 presents a diagram of the geometry of a radar system. The diagram indicates that the range resolution is divided into two different types of spatial resolutions, slant (e) and ground (a) resolutions.

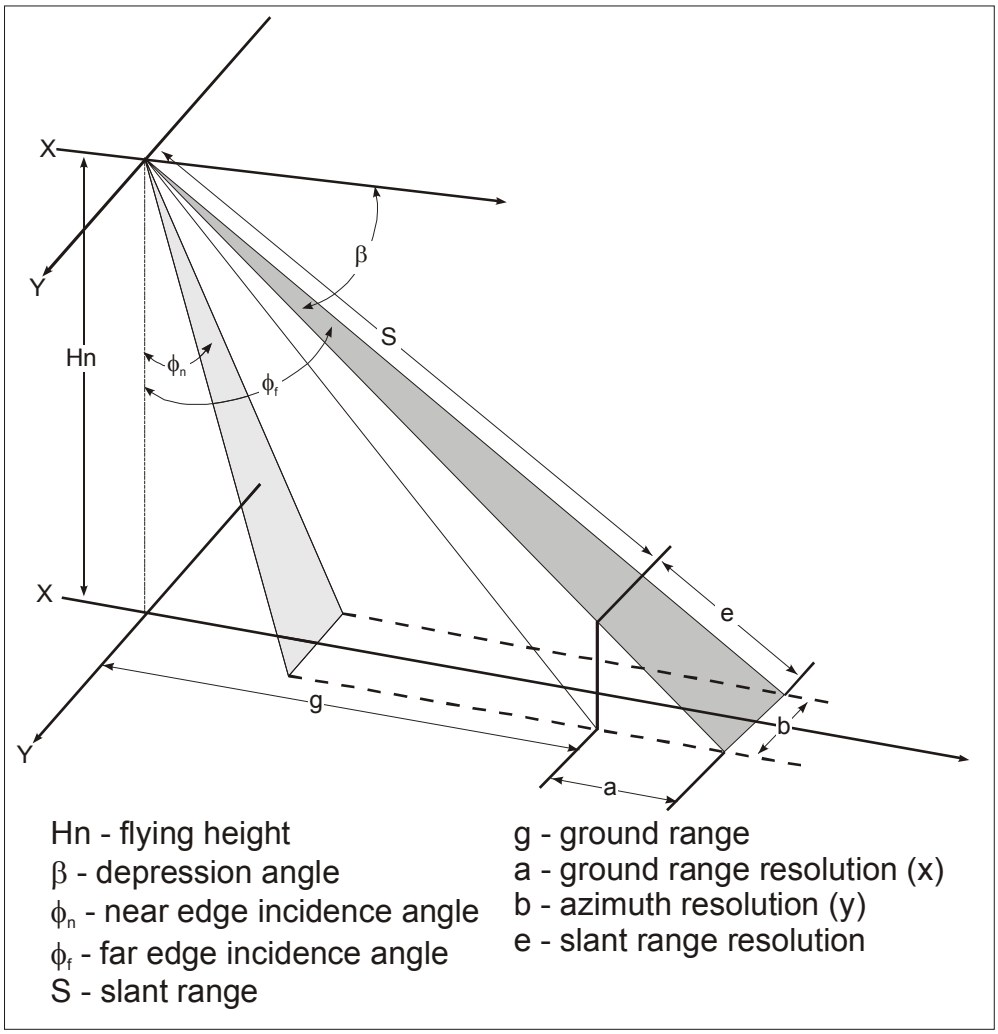

Figure 2.4 – The geometry of a radar system.

The range resolution is determined by the frequency bandwidth of the transmitted pulse and thus by the duration (width) of the range-focused pulse. Large bandwidths yield small focused pulse widths. The range resolution of imaging radars depends on signal pulse length and therefore the actual distance resolved is that

distance between the leading and the trailing edge of the pulse. These pulses can be shown in the form of signal wave fronts propagating from the sensor (figure 2.4 (e)). When these wave front arcs are projected to intersect a flat earth surface, the resolution distance in ground range is always larger (coarser) than the slant range resolution (figure 2.4 (a)). The resolution in the azimuth direction is theoretically one-half of the radar antenna.

The SAR system collects signal history that is not in image format. The raw data is impossible to interpret visually and therefore must be digitally processed in a procedure called compression. Compression converts the history in the range and azimuth directions to a two-dimensional grid format whose basic subdivision is the slant range and zero Doppler resolution cell. This cell relates to the smallest ground area for which a reflection intensity value was calculated during processing (single look). A single look is prone to excessive speckle and therefore the signals are usually processed using several looks. This degrades the spatial resolution of the generated image but attenuates the speckle.

Another type of spatial resolution pertains to the manner in which digital imagery is viewed. Digital imagery is most often displayed on a computer screen where the pixel, or picture element, is the smallest element able to display data. This pixel has nothing to do with the physical attributes recorded by the sensor and therefore, the on-screen spatial resolution of an image can be changed effortlessly. The term ‘pixel’ also pertains to the area on the ground represented by the data values (Colwell 1983) in the remote sensing context.

In geostatistics, the term support is used instead of spatial resolution. Support describes the size, geometry and orientation of the space on which an observation is defined. Support is normally equivalent to spatial resolution, however, in practice the geometry of the support may be complex because of the PSF of the sensor, and the true size of support is likely to be greater than the spatial resolution. The true support varies across the image due to the scan angle of the sensor (Atkinson and Curran 1995).

2.1.2 Spectral resolution

The spectral resolution of a digital image is the smallest wavelength interval of the EM spectrum that can be recorded by the sensor commonly referred to as the spectral band or channel. The spectral resolution can vary even within the same sensor configuration (figure 2.5).

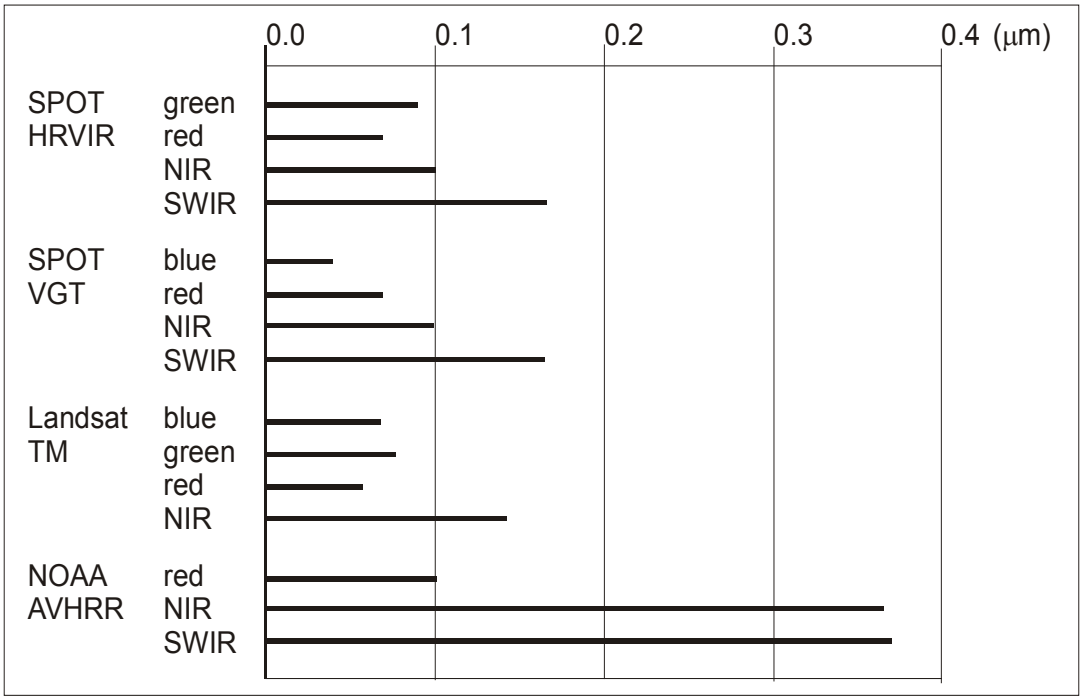

Figure 2.5 – Spectral resolution of four different satellite based sensors.

2.1.3 Radiometric resolution

Strictly speaking, the radiometric resolution is the bit, i.e. the binary manner in which data are encoded. However, since technology today is all based on the bit, the more traditional remote sensing definition of the radiometric resolution is the smallest detectable difference in the incoming EM signal. Figure 2.6 shows the difficulty that a coarse spectral resolution sensor will have to detect small changes in the incoming EM energy. This notion is strongly connected to radiometric extent (number of bits) and influenced by the spatial and spectral resolution. The precision of the technology and the sensitivity of the material (in the case of optical sensors) are very much a limiting factor of radiometric resolution.

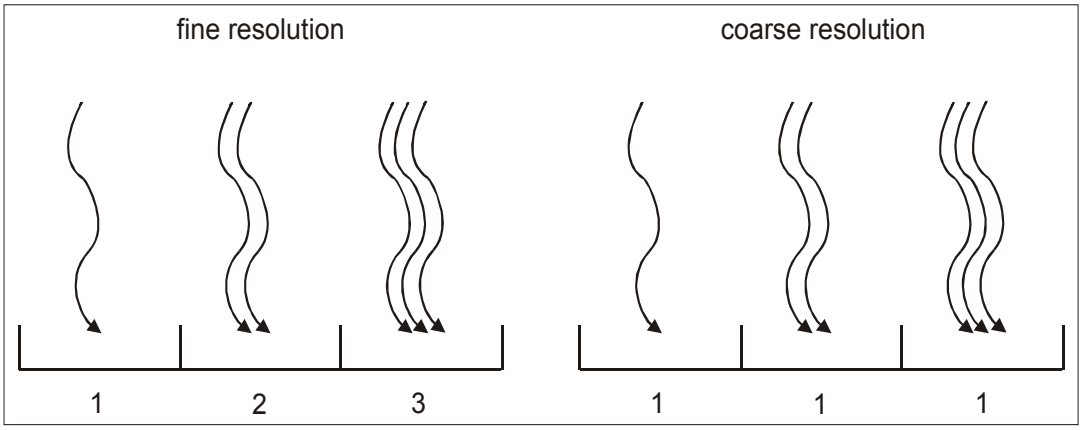

Figure 2.6 – The incoming energy (represented by the arrows) is easily quantified with the sensors on the left (fine radiometric resolution) but not those on the right (coarse radiometric resolution).

2.1.4 Temporal resolution

The temporal resolution is the smallest time step between two successive recordings of the same ground scene (figure 2.7).

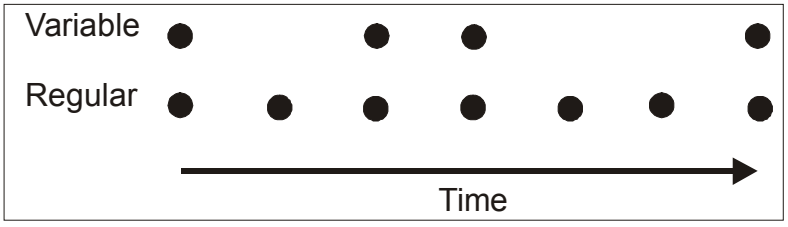

Figure 2.7 – Temporal resolution of two sets of images.

To describe the temporal resolution it is necessary to specify the variability in temporal resolution within a given data set. Therefore the minimum and maximum time between image acquisitions of the same region must be known. A variable

temporal resolution will have different minimum and maximum time steps between image acquisitions while a regular temporal resolution will have equal minimum and maximum time steps.

2.2 Image Extent

Resolution cannot exist without extent. Therefore the extent is associated with all notions of resolution in the remote sensing context.

2.2.1 Spatial extent

The spatial extent is the total area observed or under study. The ground scene is the extent (or area) on the ground that is recorded. The sensors spatial extent is the total area that is captured in an image. However, a data set can be made up of several images connected together thereby increasing the total extent originally captured by the sensor itself.

2.2.2 Spectral extent

The total width of the EM spectrum that can be sensed by a sensor is the spectral extent. Satellite based sensors provide different spectral extents (table 2.I). In multi-spectral data, the spectral extent is not necessarily contiguous.

Table 2.I – The spectral extent of several satellite based sensors.

Sensor system	Range Min. (μm)	Range Max. (μm)
SPOT HRVIR	0.5	1.75
SPOT VGT	0.43	1.75
Landsat TM	0.45	12.5
NOAA AVHRR	0.58	12.5

2.2.3 Radiometric extent

The radiometric extent is the maximum range of values that can be used to store a measured variable. Similarly, it is the number of discrete levels into which a signal may be divided (figure 2.8) where the signal is considered as a spectral band. For example, 8 bit data is able to store up to 256 different values while 9 bit data can store up to 512 different values. The decision for the radiometric extent is based on the dynamic range or the sensor signal-to-noise ratio (Richards and Jia 1999).

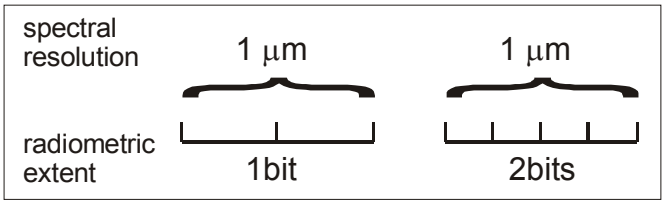

Figure 2.8 – Radiometric extent shown in conjunction with spectral resolution and radiometric resolution.

2.2.4 Temporal extent

Turner *et al*. (1989) have defined the temporal extent as the duration of time under consideration.

2.3 Remotely Sensed Image Scale

Scale is best known as the mathematical relationship between the size of objects as represented on maps, airphotos or other remotely sensed data and the actual size of the objects themselves (Colwell 1983). This type of scale is referred to as the cartographic or map scale. Cartographic scale can be absolute; the actual distance, direction, shape, and geometry or relative; a transformation of absolute scale to a scale that describes the relative distance, direction, or geometry based on some functional relationship (Turner *et al*. 1989).

Remotely sensed image scale refers to the spatial, spectral, radiometric and temporal relationship between resolution and extent. The image scale changes depending on the sensor because of differences in either sensor resolution or extent characteristics. These scale changes fundamentally affect the recorded data complicating direct comparison between different sensors. Also, changing the meaning of scale from resolution to extent can have important qualitative and quantitative effects on how measurements change across scales (Turner *et al*. 1989).

The scale of observation in the remote sensing context pertains to the resolution and extent of what is being measured, i.e. the ground scene and is solely dependent on the imaging sensor. The scale of observation therefore, is inherently linked to the spatial, spectral, radiometric and temporal characteristics of the sensor and only exists in the data itself (not in the scene). For example, the scale of

observation can be regarded as the relationship between resolution and extent as captured by the sensing device and consequently the actual scene never changes scale (figure 2.9). It is our inability to record all aspects of resolution and extent that produces scale.

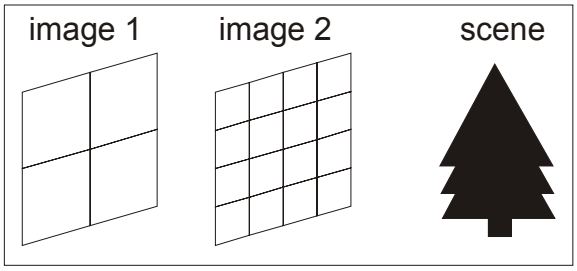

Figure 2.9 – The spatial resolution and/or extent can change depending on the sensor configuration. The scene itself however remains the same.

Just as important is the scale of inference, i.e. the scale at which conclusions are made or information is presented. The scale of inference is not necessarily equal to the scale of observation, however, the difference between the scale of observation and that of inference should be accurately expressed, especially where different data sources are related to different scales of observation[1] (Csillag *et al*. 2000). In many cases, as shown in figure 2.10, the scale of observation is different than the scale of inference and the manner in which the scale of inference was produced is not known.

[1] The scale of observation or inference cannot be described by a single adjective because it is a two dimensional concept and language is one-dimensional. Thus, image scale should not be used as a descriptor but rather as a method of introducing the characteristic in question. For example, the spatial scale can have coarse resolution and small extent and not coarse spatial scale.

Differences in image scale also complicate observations of events or objects by modifying the data itself. As the data are modified through scale, events or objects can appear or disappear because events and objects all have an optimal resolution and extent. The difficulty is to relate phenomena or objects at different scales. Therefore, the ideal image scale is not scene dependent but rather object dependent.

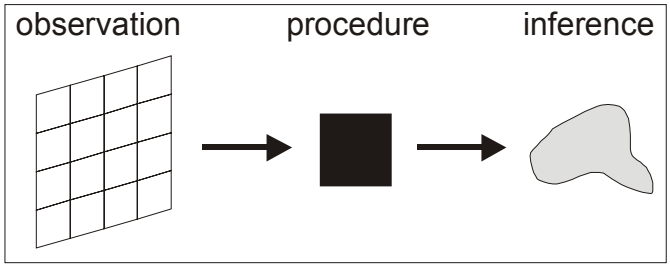

Figure 2.10 – The life cycle of image data that has been recorded at a specific scale of observation. The final product will have a scale of inference that is not necessarily that of the original data.

2.4 Information Extraction from Imagery

The extraction of information from remotely sensed imagery depends on the object or phenomenon under study and the stages of analysis can range from simple to complex. The most simple corresponds to detectability, the ability to discover or notice the existence or presence of an object or phenomenon and the most complex is interpretability, the ability to explain or understand in a particular way.

Detection in remote sensing is the determination of the presence or absence of an object. This object is non-specific and non-identified. The interpretation is a

simple dichotomy such as yes/no, true/false, or 1/0. The stimuli for detection are variations in tone, texture, pattern, configuration and other image characteristics (Colwell 1983). The ability to detect phenomena or objects under surveillance involves all image scale characteristics and is the initial step in gathering information.

The spatial resolution of an image plays an important role in detecting objects. Figure 2.11 (left graph) graphically portrays the chances of detecting an object based on the size of the object and the spatial resolution of the imagery assuming a linear relationship between spatial resolution and object size. The diagonal (from bottom left to top right) of this diagram represents the region where detection is most uncertain while the upper left and lower right regions provide the greatest certainty of detection or non-detection respectively. Detection based on extent requires that the imagery encompasses the object or phenomenon under study. Chances of detection can also improve when the encompassing area is much larger than the object or phenomenon of interest (figure 2.11, right graph).

Object detection in the radiometric scale depends on the ability to discern changes between measurements. This is also intimately related to spectral scale detection which is based on the reflectance of an object (optical system) in the same wavelengths as that of the sensor itself and the ability to differentiate the signal from other objects. For example, too small a radiometric extent for a large spectral band would make it difficult to differentiate between objects with a similar spectral signature because small variations in the intensity for the given band would not be differentiated.

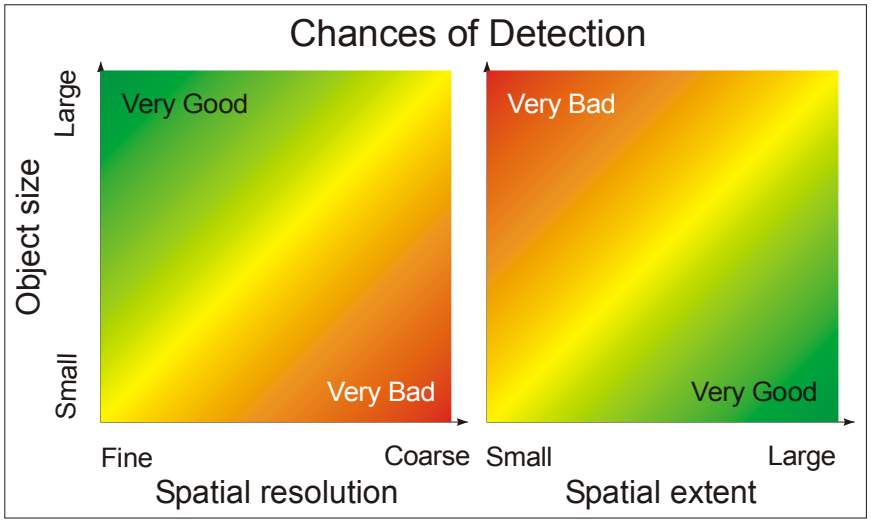

Figure 2.11 – The chances of object detection based on the spatial scale.

Object or phenomenon detection also depends on the temporal scale. Too short a temporal resolution may only generate a lot of unnecessary data while too coarse of a temporal resolution may not be enough to capture the event being monitored. The same is true for temporal extent, where a remote sensing campaign might stop acquiring data just before the beginning or the end of a phenomenon.

Detectability in remotely sensed images can be a result of chance or planned around the object/phenomenon under study. Moreover, for a given spatial resolution, the radiometric resolution can improve detection of scene objects.

Distinguishing separate identities as being such in an image is called separability and is the next step after detection. Separability helps identify scene elements. In order to separate objects the spatial and spectral resolutions must be fine

enough to distinguish an object from the rest of the scene. Object separability in the spectral scale is also dependent on the radiometric scale of the recording sensor. Finally, the temporal scale can help distinguish between objects in time due to changes over time both natural and anthropogenic.

Interpretation is the final and most difficult phase and requires the greatest amount of information and knowledge. Psychological analysis regards image interpretation as if it occurred in a time sequence. The sequence begins with the detection and identification of objects, followed by measurement of the objects and finally the communication of perception and significance of the objects (Colwell 1983). Automating interpretability using computers is difficult because the communication of perception and significance requires knowledge but such knowledge is difficult to program. Interpretability determines information beyond identification.

Interpretability can also be the ability by which probabilistic statements can be made about objects, phenomena and relationships found in the imagery. The more knowledge one has about the scene, the greater the probability that the interpretations will be correct (Colwell 1983).

All sensor characteristic scales have a role in the extraction of information. Therefore, one must consider the role of each sensor characteristic scale (spatial, spectral (Buttner and Csillag 1989), radiometric and temporal) when making observations. Satellite based monitoring also provides a wide range of observation

scales generating important data for information extraction but also creating difficulties in relating the different images. The scales at which data are collected and analysed directly influence the level and kinds of information that may be obtained. Information derived from data collected at a particular scale is dependent on that scale (Colwell 1983).

Scale is based on the resolution and extent established by the sensor characteristics. The sensor itself is sub-optimal for some or all of the phenomena or objects of a ground scene because they are not identical across the ground scene. This implies loss of information.

2.5 Aggregation and Scale Changes

Aggregating spatial data is a current technique in the environmental sciences, including remote sensing. During an aggregation process, the original spatial data are reduced to a smaller number of data units (points, lines, polygons, pixels) for the same spatial extent (Ling and Butler 1999). This idea has come to be known as scaling-up (or bottom-up approach (Turner *et al*. 1989)) and is applied to test or reveal spatial patterns and their effects that are present or emergent at coarser spatial resolutions (Zhang and Montgomery 1994, Turner *et al*. 1989) or to reduce model complexity (Rastetter *et al*. 1992).

Aggregation can be based on the original data recorded (such as the DN of an image) (Justice *et al*. 1989) or based on already interpreted or classified data (such as

land-cover maps (Turner *et al*. 1989b, Benson and MacKenzie 1995)). The aggregation method is also important (Ling and Butler 1999). When aggregating involves averaging, the effect is to reduce the variance of the data and to make their distribution more symmetric. The standard deviation, the coefficient of variation and the difference between the mean and median all decrease as the resolution becomes coarser. Though the support of the data has an effect on the spread and the symmetry of the distribution, it does not affect the mean (Isaaks and Srivastava 1989). Aggregation can also create spatial associations between variables that were not originally associated together at the individual (finest) level. This affects in a fundamental manner the characteristics of the data, and the results of subsequent analysis (Openshaw, 1981).

The spatial resolution changes when aggregation is performed from fine to coarse thereby producing a change of scale. Scale problems have been acknowledged in a variety of studies (e.g. Allen and Starr 1982, O'Neil *et al*. 1986, Meentemeyer and Box 1987, Rosswall *et al*. 1988), and the importance of spatial heterogeneity has also been recognised (e.g. Risser *et al*. 1984, Forman and Godron 1986, Turner 1987, 1989). However, 'scaling rules' have not been developed, and scaling limits have been difficult to identify (Turner *et al*. 1989). As one tries to scale-up, qualitative shifts can occur where the dominant processes that structure the patterns change as scale changes (Benson and MacKenzie 1995).

Studies have also described the important effects that can be observed on the proportion of landscape occupied by a particular land-cover type when aggregation is

made (Henderson-Sellers *et al*. 1985, Turner *et al*. 1989a, Moody and Woodcock 1994, 1995). The earth sciences deal with processes that occur at a variety of temporal and spatial scales. The requirements proposed by Turner *et al*. (1989a) in order to make predictions at more than one level of resolution are:

- the identification of the processes of interest and parameters that affect this process at different scales,
- the development of rules to translate information across scales and,
- the ability to test these predictions at the relevant spatial and temporal scales.

If information were available about the relationship between spatial covariance of data with coarse spatial resolution and that of data with fine spatial resolution, either through theoretical (Zhang *et al*. 1990) or experimental (Woodcock *et al*. 1988, Rubin and Gomez-Hernandez 1990) means, it could be used to scale-up knowledge from local to regional scales (Dungan *et al*. 1994).

As the remote sensing study area increases (particularly for landscape studies), the natural tendency is to decrease the resolution thereby losing the details and concentrating on the general themes. This natural tendency is due to our inability to absorb the significant amount of data associated with fine spatial resolution over a large study area. With database technology constantly improving, management of such large amounts of data becomes possible and directly interpretable.

Some common observations of aggregation can also be made based on already classified fine spatial resolution data. Classes consisting of large, homogeneous

patches tend to grow larger with aggregation. Classes characterised by highly clumped distributions, but small or intermediate sized patches, first grow, and then decrease in size as the spatial resolution is progressively degraded beyond the typical patch size for that class. Classes composed of small, fragmented units rapidly disappear as more clumped cover types, through the aggregation procedure, dominate them. Naturally, most classes do not fall neatly into any of these categories (Moody and Woodcock 1994). Therefore it is difficult to model the behaviour of aggregating cover types.

The effect of aggregation on global statistics when averaging over an image is greatest for data sets that are spatially uncorrelated, i.e. heterogeneous in nature. In such cases, the standard deviation decreases and the distribution rapidly becomes more symmetric. As the values become more homogeneous, this effect decreases and the reduction in spread and symmetrization occur less rapidly because they depend on the spatial arrangement of the data values (Isaaks and Srivastava 1989). Isaaks and Srivastava (1989) also show that the effect of aggregation on the symmetry of the distribution is related to the connectedness of extreme values and not adequately described by the semivariogram (i.e. the connectedness of extreme values). Therefore, the expected degree of symmetrization is based on available qualitative information about the spatial arrangement of the data and one's own judgement.

The reverse estimation, however, from coarse spatial resolution to fine spatial resolution (or scaling-down) may be more problematic unless an empirical relation has been established between the coarse and fine spatial resolutions. This is because

features at a fine spatial resolution may not be recoverable from coarse spatial resolution information (Benson and Mackenzie 1995). More importantly, even with an empirical relationship, one could not get around the problem of spatial location of the estimated fine spatial resolution images.

Benson and MacKenzie (1995) support the view that scaling issues must be addressed when using satellite imagery to derive landscape parameters since most landscape parameters are sensitive to changes in grain. Multi-scale studies based on imagery showed that the relationship between spatial patterns and ecological processes in tallgrass prairie ecosystems is not restricted to a particular scale of observation (Nellis and Briggs 1989). Turner *et al*. (1989b) studied the effect of scale change not only by changing the resolution but also the extent. They showed the difficulty of modelling such changes. Lacaze *et al*. (1994) demonstrated the possibility of multi-scale analysis using the experimental variogram and showed the usefulness of this tool for scale related research.

John Wiens in 1989 challenged researchers to make scaling issues a primary focus of research efforts. Since that time we have learned that the successful application of research findings depends critically on both identifying the appropriate scale of observation for the application and the ability to extrapolate findings across scales (Gustafson 1998) to an appropriate scale of inference. It is an accepted fact that the characterisation of landscape structure is scale of observation dependent (Nellis and Briggs 1989). However, identifying the appropriate scale of observation is not readily evident and one should be aware of this fact and document it accordingly.

2.6 The Error, Accuracy and Precision Relationship

Error is intimately related to accuracy and precision. Accuracy is the conformity to fact, the exactness, and the degree to which a measurement is known to approximate a given value. Precision is made so as to vary minimally from a set standard, clearly expressed or delineated and it corresponds to a statistical measure of repeatability, usually expressed as a variance or standard deviation of repeated measurements (figure 2.12). The variance is the basic measure for precision, and a fundamental parameter in probability and statistics.

DeFries and Belward (2000) recognise that accurate land-cover information is an essential requirement for science and policy applications. Precision however is not well established in the remote sensing sciences due to the lack of repeated measurements for any given landscape. Ideally, one expects an information product that is both accurate and precise.

Accuracy is a relative term. In cartography it can refer to the closeness with which data on the map are located with respect to defined geographical positions, to the detail with which elevations are indicated, or to the degree to which a mapped distribution portrays the 'real' distribution. The concept can only be dealt with in terms of 'accuracy for what purpose' but does not in any way change the fact that the accuracy of source data must always be a matter of primary concern. Errors can easily be propagated and exaggerated through the compilation process when accuracy is

poor. Unfortunately, the quality of the source data is not always readily evident (Robinson *et al*. 1984) and therefore accuracy assessment tends to be strongly constrained by the resources available. Journel (1996) goes even further to say that there is no exact data. There are only specific representations of reality deemed more relevant than others are and that relevance is goal dependent.

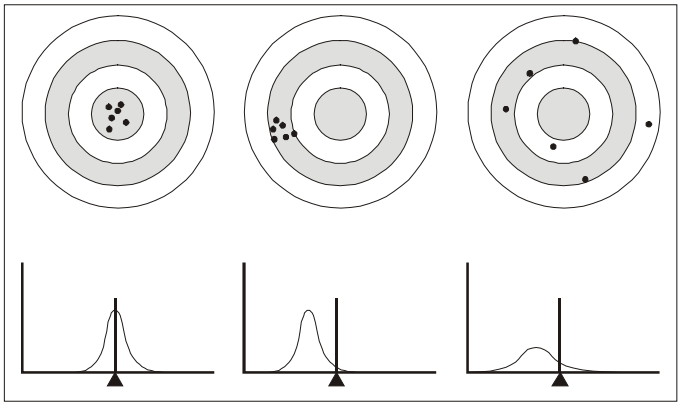

Figure 2.12 – The importance of accuracy and precision. The left graphs present a target and distribution, which is both accurate and precise. The middle graph represents poor accuracy but good precision and the right hand graph shows both poor accuracy and precision.

Aggregation produces unfamiliar data (i.e. everyday objects are not easily distinguished) at certain scales of observation. This unfamiliarity drives us to look for things that are familiar thus introducing errors (or inaccuracies). At a specific scale of observation there is no error. The error is produced by the desire or need to 'see' the information that we are accustomed to or require. Scaling-up produces qualitative unknowns that are then considered as errors. Degrading an image using an averaging filter produces quantitative results but the generated image is intuitively error prone

because of the lack of understanding of the process of scaling. Strictly speaking there is no error if the averaging computations were done correctly. Error is introduced when we try to extract information about objects and/or phenomena that are not compatible with the available scale of observation. In such a case, the scale of inference is not the same as the scale of observation and thus error is introduced. Error is minimised, however, when the scale of observation coincides with the phenomenon being observed (or the scale of inference).

Aggregation of fine spatial resolution land-cover maps to coarser spatial resolutions means that estimates of the proportions of land-cover types vary as a function of spatial resolution. The magnitude of the errors appears to be a function of the spatial resolution of the map, the original size of the land-cover classes, the variability among fine-scale components, and the spatial pattern of the classes (Rastetter *et al*. 1992, Moody and Woodcock 1994). As such, aggregation plays a part in the magnitude of the errors.

Mapping at very broad spatial extents on the basis of high spatial resolution data has clear advantages for accuracy because complex land-cover patterns are finely resolved, and map outputs can be more properly validated than coarse resolution maps. This is the path taken by NASA's Landsat Pathfinder Tropical Deforestation Project (UMD 1998). However, this high spatial resolution approach requires the processing of very large volumes of data that are not necessarily recorded in any particular temporal order due to acquisition difficulties. Moreover, the classification of cover types at a fine resolution requires a good knowledge of the ecology and of

the land-cover patterns of the area under investigation - something that is difficult to achieve when monitoring very large extents (Mayaux and Lambin 1995).

Woodcock and Strahler (1987) present relationships between spatial resolution and mean local variance of image data at different scales. The spatial resolution at which local variance reaches a maximum is considered to match closely the characteristic scale of scene variation. This study and others (Markham and Townshend 1981, Cushine 1987) have discussed the relevance of resolution-dependent effects on the accuracy of multi-spectral image classification. Specifically, spatial resolution determines the relative variability between and within land-cover classes, influencing spectral separability. Marceau *et al*. (1994a, 1994b) have used the resolution dependence of classification accuracy to assess optimum spatial resolutions for feature extraction.

Sample support size is of fundamental importance for various measurement and estimation problems. For example, sensor geometry, comparisons of alternative measurement devices, and plot size determination, all require examination of the variability of results as influenced by dimensions of the sample (Zhang *et al*. 1990). The best way to handle the support effect is to use sampled data that have the same support as the area we intend to estimate; unfortunately, this is rarely possible. Without such data, we must make some correction based on assumptions concerning the changes in the distribution of values as their support increases. This correction is usually rather imprecise and heavily dependent on assumptions. Nevertheless, it is

certainly better to make a coarse correction (and to carefully document the assumptions) than to ignore the problem (Zhang *et al*. 1990).

The loss of accuracy introduced by aggregation must be balanced against a loss in precision through the accumulation of errors associated with the estimation of a large number of parameters in complex, non-aggregated models (O'Neil, 1973). Precision for the most part does not necessarily play an important role in land-cover estimates because most often there is only one map produced and compared to 'known' land-cover estimates. However, when a large number of possible scenarios are available, precision may be a confidence indicator. The possible scenarios can be generated using stochastic imaging techniques. Moreover, with no 'base map' to compare to, precision could also be a surrogate to accuracy by providing an insight into the most likely value. Here, a most likely value could be the mean or median of the distribution of values. Accuracy, however, can only be evaluated if the true value is known. With a distribution of values, the relative precision resulting from generating several realisations of images is readily assessed by measuring the spread of the output distribution which in geostatistics is often referred to as uncertainty space (Goovaerts 1997).

Both accuracy and precision are very important for land-cover estimation and mapping. Poor accuracy and/or precision will affect extracted information and conclusions. Both are important for continental to global land-cover mapping but the problem still remains as to how to measure the accuracy or precision of such data when there is no standard. A variety of efforts are currently underway to map land-

cover at continental up to global extents using a variety of remotely sensed data sources. Rigorous assessment of the accuracy of these maps continues to be difficult.

Several researchers have already presented their conclusions on this subject. Kong and Vidal-Madjar (1988) have reported that before we can use fine and coarse spatial resolution imagery together, it is necessary to understand how the statistical properties of the landscape are modified when the dimension of the sub-scene is varied. Moody and Woodcock (1994) have suggested that in order to better understand the scaling issues and implications of accuracy in land-cover data, it is of interest to investigate the relationships between land-cover map error, scale of observation and scene spatial structure.

Large errors arise as land-cover data are sampled at progressively coarser resolutions and have significant implications for coarse spatial resolution modelling and monitoring activities. An understanding of the role of spatial characteristics in governing the loss of information with decreasing resolution may improve our ability to preserve this information across scales or to quantify the errors expected in coarse spatial resolution surface representations. Both Turner (1989) and Moody and Woodcock (1995) provided results that indicated significant relationships between the spatial characteristics of cover types and scale-dependent proportion errors.

2.6.1 Error correction and validation

The solution of the problem of making reliable maps has to be accompanied by the recognition that "accurate" and "erroneous" are not disjunct sets, but can rather be viewed as a continuum (Csillag and Kertesz 1989). Several methods have also been proposed to help correct information that is based on a scale of observation with coarse spatial resolution to one with a finer spatial resolution. Model inversion is based on the idea that it is theoretically possible to predict the loss of information in the scaling process with the spatial resolution degradation if the degree of adjacency - or contiguity - of land cover types is known (Turner *et al*. 1989). Another study concluded that relationships do exist between the fine scale spatial arrangement of land-cover and the proportional errors found at a coarse spatial resolution (Moody and Woodcock 1995). However, the difficulty lies in knowing the degree of the spatial arrangement at both fine and coarse spatial resolutions. In reality, only the spatial arrangement at a coarse spatial resolution is known for the entire extent when dealing with coarse spatial resolution image data over large extents.

Other techniques try to correct land-cover information errors based on a relationship between samples of coarse and fine spatial resolution imagery. This relationship can then be extrapolated over a large region where fine spatial resolution data is not available. A major challenge in applying this type of method is the difficulty to establish a correspondence between data sampled using two different sensor configurations especially in the case of ground scenes that are heterogeneous in nature (Kong and Vidal-Madjar 1988).

In order to quantify error, known reference information must be available for comparison. Moody and Woodcock (1995) say that this type of validation requires methods for aggregating reference maps from fine to coarse scales, as well as knowledge of the types and magnitudes of errors that this scaling will introduce into the reference data. Any effective aggregation of fine-scale knowledge to anticipate coarse-scale response requires some data or information from the coarser scale (Rastetter *et al*. 1992). As a consequence a scaling model (modelling changes from the scale of observation to the scale of inference) cannot be verified without data at both the initial scale and final scale of observation.

Lunetta *et al*. (1991) have indicated areas where errors can be found and thereby influencing the final accuracy of the remotely sensed derived information product. Errors generated by atmospheric conditions and natural variability of the landscape cannot be controlled. Other difficulties can be controlled such as errors due to data collection, (e.g. geometric or radiometric error) where geometric inaccuracies lead to misregistration (Kleinn *et al*. 1996). Location accuracy of corrected remote sensor data are very susceptible and cannot be better than the ground control upon which the rectification coefficients are based. Another area of accuracy assumption is in data processing. Such error can be generated during data conversion or improper choice of algorithms. Furthermore, a large variety of data and information sources are available in the earth sciences. These data originate from various measurement devices that have different precision and that are taken over different volumes or time intervals.

Remote sensing is, however, an efficient means of mapping land-cover or other characteristics of local sites. Summary statistics from these thematic maps estimate the proportion or area of the geographic space in each cover category. Areal estimates are often needed for strategic planning, land management, and resource assessments (Czaplewski *et al*. 1992). Due to aggregation effects, coarse spatial resolution remotely sensed data does not provide the exactitude needed. More importantly, there is no data set to which land-cover estimates can be compared. These data sets are not available because data cannot be gathered with a finer spatial resolution as quickly as those with a much coarser spatial resolution. Thus, a workaround practise that is widely used is to find relationships using small areas where fine spatial resolution data is available and extrapolating those relationships to the entire extent where similar landscape properties are observed (Mayaux and Lambin 1995, 1997). Accuracy in such instances is computed on sample areas where both fine and coarse spatial resolution data are available.

Oleson *et al*. (1995) studied the potential for using AVHRR data to retrieve fine temporal resolution reflectance estimates at the Landsat TM spatial resolution. Their approach compared land-cover classes to raw DN. Their work gave mixed results but instead of correcting the coarse spatial resolution data they tried to generate their own fine spatial resolution image data set based on coarse spatial resolution image data.

In most practical applications, the support of the samples is not the same as the support of the estimates we are trying to calculate. Errors associated with the remote sensing and GIS data acquisition, processing, analysis, conversion, and final product presentation can have significant impact on the confidence of decisions made using the data. Performing spatial data analysis operations with data of unknown accuracy, or with incompatible error types, will produce a product with low confidence limits and restricted use in the decision making process (Lunetta *et al*. 1991). The contradiction between the requirements of constant accuracy and constant resolution will necessitate significant contributions from different branches of science for modelling co-regionalized and/or elaborating classification strategies that can lead from rasters to vectors, or from vectors to rasters. It is also understood that whenever a choice is made concerning data representation, it implies that a particular model is used to estimate accuracy (Csillag and Kertesz 1989).

Different classification procedures provide different areal estimates in some cases, and possible ways to resolve these differences must be studied (Cihlar *et al*. 1997). If more accurate information is needed then data at a finer spatial resolution is required resulting in a change in scale (Csillag and Kertesz 1989). Land-cover is a key environmental information and the objective is to present data in a format from which accurate land cover information can be extracted (Cihlar 2000). The scale determines the accuracy and accuracy determines error. The greater the error, the lower the precision. As digital cartography and geographic information systems mature, more need is seen for the development of measures of accuracy, error or uncertainty for spatial data (Goodchild 1988).

Models and measurements of phenomena that occur over large regions, such as the effects of acid precipitation, global carbon and nitrogen cycles, increased desertification and climate change, are scale dependent. Consequently, the level of resolution and the heterogeneity at all relevant scales must be considered when defining the research goals and sampling design for studies conducted across spatial/temporal scales (Cullinan and Thomas 1992).

2.7 Discussion

The above discussion sheds some light on the possible results of the experiment presented in this thesis. Generating coarse spatial resolution imagery based on fine spatial resolution imagery will produce an image that appears similar to a coarse spatial resolution image that was acquired over the same region. Of course the degree of similarity will depend on the scene itself as well as the different parameters discussed previously. The reverse is not true in that generating a finer spatial resolution image based on coarse spatial resolution imagery will not look like a fine spatial resolution acquired over the same region. Down-scaling produces finer spatial resolution images that do not have object location information. For example, road networks or intricate objects that are at the spatial limit at the finer spatial resolution will not be reconstructed based solely on coarse spatial resolution information.

Other differences can be observed when comparing a real and generated image. For example, it is not guaranteed that a degraded image will have the same distribution as that of an image acquired directly by the sensor itself because the aggregation methods are different (i.e. mathematical vs. sensor system).

Chapter 3 – Geostatistics

Geostatistical tools such as the variogram and stochastic imaging could provide the means to generate finer spatial resolution imagery based on coarse spatial resolution imagery. This chapter discusses the regionalized variable, the variogram and its modelling, and the stochastic imaging technique using the sequential gaussian simulation algorithm. The presentation is based on three primary sources: Goovaerts (1997), Deutsch and Journel (1998), and Journel and Huijbregts (1989), unless otherwise noted.

3.1 Background

Spatial statistics provides advanced methods for analysing image data and is able to cope with observational interdependencies (Griffith 1993) i.e. the variability between samples. Simply stated, geostatistics is "the study of phenomena that fluctuate in space" (Olea 1991) and is principally the application of the regionalized variable theory. The regionalized variable theory and the methods it embodies are applicable throughout the earth sciences for investigating the spatial variation of, and for estimating, continuous random variables (Oliver 1987). Observations of remotely sensed imagery tend to show that pixels that are near to each other are more alike than those further apart and the degree of dissimilarity depends on both the environment and nature of the recorded scene. Such observations can be quantified using geostatistics, which offers a collection of deterministic and statistical tools aimed at understanding and modelling spatial variability (Curran and Atkinson 1998).

The fundamental assumption of classical inferential statistical analysis is the independence of observations. However, because the spatial structures we find in nature are commonly patches or gradients, this assumption is usually violated at specific (and usually unknown) scales of sampling. Therefore, it is imperative to know something about the degree and scale of spatial dependence in the system being studied. Geostatistics provide methods to both describe spatial structure and to make statistical inferences that are robust in the presence of spatially dependent relationships (Gustafson 1998).

3.2 Remotely Sensed Imagery and Geostatistics

Remotely sensed image data can be viewed as a regionalized variable, meaning that it is a variable whose position in space is known (x, y). The data are regionalized variables because the recorded EM radiation has a location in space associated with it (figure 3.1 – top). Each image pixel is also considered a random variable (RV). The RV is the set of possible outcomes of a single pixel within the data set (figure 3.1 – middle). This set of possible outcomes models the local uncertainty about the variable at its location and is information dependent because the distribution changes as more data about the RV become available. The set of all the available RVs defined over an image of interest is the Random Function (RF) (figure 3.1 – bottom) whereby the set of unknown values is regarded as a set of spatially dependent RVs. This allows us to account for structures in the spatial variation of the attribute. The RF is usually defined strictly to a single band (attribute b1), hence

another RF would be defined to model the spatial variability of any other band (attribute b2). The set of realizations of the RF models the uncertainty about the spatial distribution of the EM radiation (i.e. the attribute) recorded over the entire image (study area).

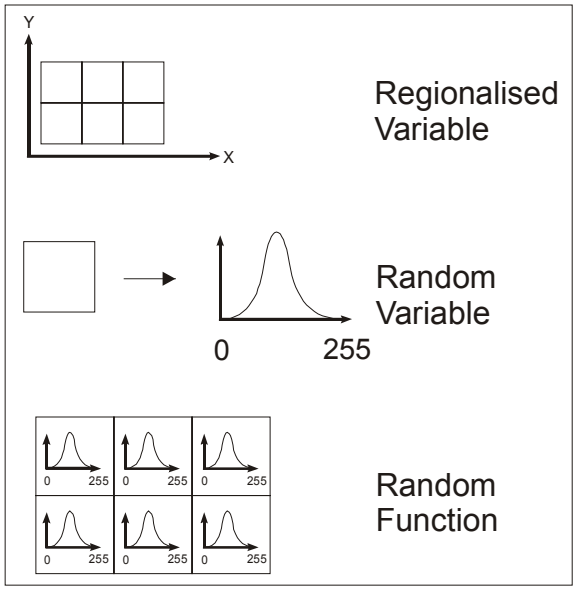

Figure 3.1 – A graphical representation of the regionalized variable (top graph), the Random Variable (RV) (middle graph) and the Random Function (RF) (bottom graph). Each square represents a recorded value within an image.

In the geostatistical literature, z represents the actual value (be it unsampled/unknown or the outcome) and Z represents the RV (the possible distribution of values for z). Since these values are location dependent, (u) denotes the location in space and/or time. The basic paradigm of the probabilistic approach, underpinning geostatistics, is to characterise or model the unknown z(u) (unsampled variable at location u) as a RV Z(u) (the distribution of possible outcomes of the

unsampled variable at location u), the probability distribution of which models the uncertainty about z. The difficulty of assessing the uncertainty about the pixel value at location u thus reduces to that of modelling the probability distribution of the RV Z(u). Uncertainty is maximal when no information is available and the probability of occurrence for all outcomes is the same. For example, the probability of occurrence would be the same for each pixel within the range of values between 0 and 255 for an 8-bit image. In order to increase certainty, more information about the behaviour of the pixel must be known. This information is derived from nearby pixels that condition the probability distribution of the RV Z(u) thereby reducing the uncertainty at the pixel location. By accounting for the dependence between RVs at different locations the RF model allows such updating.

The continuous RV Z(u) is fully characterized by its cumulative distribution function (cdf) which gives the probability that the variable Z at location u is no greater than any given threshold z. Each pixel $z(u_\alpha)$ therefore, is viewed as a particular realization of the random variable $Z(u_\alpha)$. Provided measurements are precise, there is no uncertainty about the recorded pixel value $z(u_\alpha)$. Thus, the probability for the random variable Z at u_α to be no greater than a threshold z is one for any threshold greater than or equal to the datum $z(u_\alpha)$ and zero for other thresholds $z < z(u_\alpha)$.

In geostatistics, most of the information related to an unsampled value z(u) comes from sample values at neighbouring locations u', whether defined on the same

attribute z or on some related attribute y. Therefore it is important to model the degree of correlation or dependence between any number of RV's Z(u), $Z(u_\alpha)$, α=1, ..., n and more generally Z(u), $Z(u_\alpha)$, α=1, ..., n, $Y(u'_\beta)$, β=1,..,n'. The concept of a RF allows such modelling and updating of prior cdfs into posterior conditional cumulative distribution functions (ccdf). As mentioned, a RF is defined as a set of usually dependent RVs Z(u), one for each location u in the study area A (Goovaerts 1997).

Just as a RV Z(u) is characterised by its cdf, a RF Z(u) is characterized by the set of all its K-variate cdfs for any number K and any choice of the K locations u_k, k = 1, ..., K:

$$F(u_1, ..., u_k; z_1, ..., z_k) = \text{Prob}\{Z(u_1) < z_1, ..., Z(u_k) < z_k\} \quad (1)$$

The univariate cdf of the RV Z(u) is used to model uncertainty about the value z(u) and similarly the multivariate cdf is used to model joint uncertainty about the K values $z(u_1)$, ..., $z(u_k)$ (Goovaerts 1997).

3.3 Inference and Stationarity

Repetitive sampling is required to infer any statistic. For example, a single value cannot provide the necessary information to deduce the possible outcomes (or distribution) of a variable. Generally remote sensing only provides a single measure for any one pixel within an image. Therefore, the RV model is impossible to generate from a single remotely sensed image. The paradigm underlying most inference processes is to trade the unavailable replication at location u for another replication

available somewhere else in space. For example, the cdf may be inferred from the cumulative histogram of the z-samples collected at pixel locations other than the pixel of interest, within the same area. This trade of replication or sample spaces corresponds to the hypothesis (or rather a decision) of stationarity.

The RF of a specified area of an image (or the entire image) is said to be stationary if its multivariate (multi-pixel) cdf is invariant under any translation of the K-coordinate vectors u_k, that is $F(u_1,...,u_k;z_1,...,z_k) = F(u_1+1,...u_k+1; z_1,...,z_k)$, for the entire translation vector 1 (figure 3.2). Invariance of the multivariate cdf entails invariance of any lower order cdf, including the univariate and bivariate cdfs, and invariance of all their moments (e.g. mean, variance and covariance). The decision of stationarity allows inference. For example, the unique stationary cdf $F(z) = F(u;z)$, for all u in the set of A, can be inferred from the cumulative sample histogram of the z-data values available at various locations within the area A. Stationarity can also be considered as an assumption about a given area that all samples came from the same probability distribution.

A proper decision concerning the stationarity of the data is critical for the representativeness and reliability of the geostatistical tools used. Consequently, pooling data across different landscapes could mask important differences; on the other hand, splitting the image data into too many smaller images may lead to unreliable statistics based on too few data and an overall confusion. The rule in statistical inference is to pool the largest amount of relevant information to formulate predictive statements (Goovaerts 1997). Furthermore, stationarity is a property of the

model; thus the decision of stationarity may change if the scale of the study changes or if more data become available. If the goal of the study is global, then local details can be averaged out; conversely, the more data available, the more statistically significant differentiations become possible.

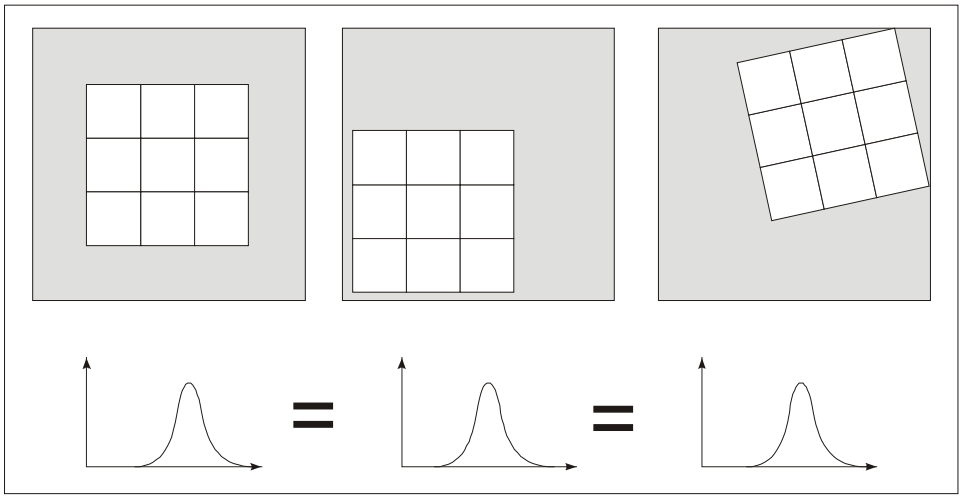

Figure 3.2 – Any translation of the data (represented by the grid) within the area deemed stationary would result in the same distribution.

3.4 The Variogram

When dealing with variability between two attributes, one of the first statistical measures that come to mind is the covariance. The general covariance statistic can be extended to a spatial context to measure similarity between data that are not at the same location. The covariance between data that are separated by a specific distance is computed as:

$$C(\mathbf{h}) = \frac{1}{N(\mathbf{h})} \sum_{\alpha=1}^{N(\mathbf{h})} z(\mathbf{u}_\alpha) \bullet z(\mathbf{u}_\alpha + \mathbf{h}) - m_{-\mathbf{h}} \bullet m_{+\mathbf{h}}$$

with: (2)

$$m_{-\mathbf{h}} = \frac{1}{N(\mathbf{h})} \sum_{\alpha=1}^{N(\mathbf{h})} z(\mathbf{u}_\alpha), m_{+\mathbf{h}} = \frac{1}{N(\mathbf{h})} \sum_{\alpha=1}^{N(\mathbf{h})} z(\mathbf{u}_\alpha + \mathbf{h}) \quad (3)$$

where N(**h**) is the number of data pairs within the class of distance and direction, $m_{-\mathrm{h}}$ and $m_{+\mathrm{h}}$ are the means of the corresponding tail and head values. The covariance can be computed for different classes of distance (e.g. h1, h2, etc.) and the ordered set of covariance (C(h1), C(h2), etc.) is called the experimental autocovariance function. This statistic measures the average similarity between pixels within a class of distance.

The central tool in geostatistics (and an alternative to the covariance) is the variogram. It is a measure of spatial dissimilarity in a regionalized variable and can quantify the scale and pattern of spatial variability (Oliver 1987, Curran and Atkinson 1998). The variogram, $2\gamma(h)$, is defined as the variance of the increment [Z(u)-Z(u+h)]. Thus for a stationary RF, $2\gamma(h) = \mathrm{Var}[Z(u+h) - Z(u)]$.

In a more applied context, the variogram is computed as half the average squared difference between pairs of pixels separated by a distance h or

$$\gamma(\mathbf{h}) = \frac{1}{2N(\mathbf{h})} \sum_{\alpha=1}^{N(\mathbf{h})} [z(\mathbf{u}_\alpha) - z(\mathbf{u}_\alpha + \mathbf{h})]^2 \quad (4)$$

where $[z(u_\alpha) - z(u_\alpha + h)]$ is the difference in the variable z between two pixels separated by a distance h. The vector (**u**) are the co-ordinates for z at the location α. For example, if we consider a line of pixels extracted from an image where z is the DN (figure 3.3), the variogram is estimated by the average squared difference between all pairs a distance h apart (the lag distance). In figure 3.3, the lag intervals shown are 1, 2, 3, and 4 pixels apart. These lags are based on the available data and the separation distance between pixels. The variogram is a useful measure of dissimilarity between pixels (Jupp *et al.* 1988) where a larger variance indicates less similarity between the pixels. An idealised variogram could be similar to that shown in figure 3.4. The sill is the plateau that the variogram reaches at the range (the distance at which the sill is reached). The variogram also reflects the variance components acting at different scales, enabling the extent of the zone of influence of a phenomenon to be characterized and therefore, providing useful information about the nature of the phenomenon (Bellehumeur and Legendre 1998).

The computed variogram based on the image data, otherwise known as the experimental variogram, is actually not continuous and only provides experimental values for a finite number of lags. If one is to use the experimental variogram in geostatistical techniques such as kriging or stochastic imaging, it is necessary to fit a mathematical model to the computed experimental variogram. A continuous function must be fitted to the experimental variogram values so as to deduce variogram or

covariance values for any possible lag h required by interpolation algorithms, and also to smooth out sample fluctuations. The model fitted is defined by its type and model coefficients.

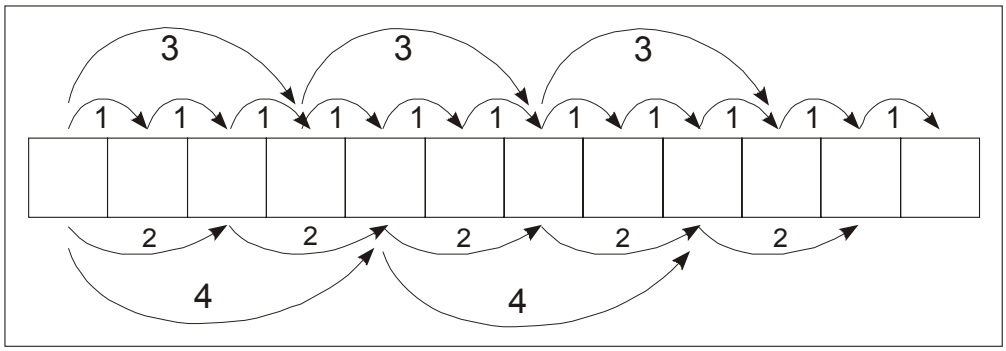

Figure 3.3 – Pairs of pixels representing the distance classes that would be used to compute the variogram along a line of pixels.

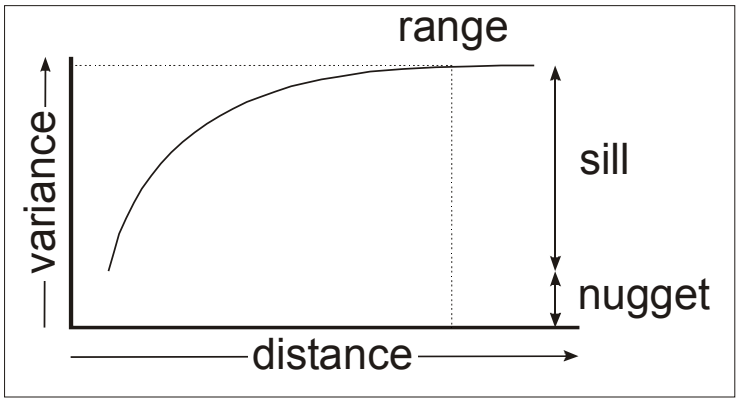

Figure 3.4 – An idealised variogram. The variogram is a graph showing the dissimilarity in pairs of values separated by a specific distance (or lag).

Permissible models must also pass the positive definite condition. The positive definite condition requires the covariance model C(h) to be non-negative and

to not fluctuate. However, in order for the covariance model to be positive definite would require the variance of any finite linear combination of RVs over a set area (deemed stationary) to also be non-negative. There are only a few families of simple functions that meet these criteria. The spherical and exponential schemes are the most often encountered members. If more complex models are needed they can be formed by combining two or more simple models (McBratney and Webster 1986).

In order to avoid having to test a posteriori the permissibility of a variogram model a common practice consists of using only linear combinations of basic models that are known to be permissible (Christakos 1984). Five basic models are widely used in the earth sciences however only two are presented here because previous work has shown that these are the most applicable in the remote sensing context: the spherical and exponential models. The spherical model with range a is equal to:

$$g(h) = Sph\left(\frac{h}{a}\right) = \begin{cases} 1.5\bullet\frac{h}{a} - 0.5\bullet\left(\frac{h}{a}\right)^3 & If \quad h \le a \\ 1 & otherwise \end{cases} \tag{5}$$

and the exponential model with practical range a is equal to:

$$g(h) = 1 - Exp\left(\frac{-3h}{a}\right) \tag{6}$$

The permissible models can also be classified according to their behaviour at infinity and at the origin. Both the spherical and exponential models are bounded, meaning that they actually reach a sill at the range. At the origin both spherical and

exponential models have a linear behaviour. Note that for a same practical range, the exponential model starts to increase faster than the spherical model.

3.4.1 Variogram regularisation

Geometrically, regularisation is simply increasing the size of support over which a spatial process is averaged. In the context of remote sensing it means increasing the size of the pixels and coarsening the spatial resolution. Regularisation is a key to understanding the relations between spatial dependence and size of support (Atkinson and Curran 1995). The difficulty lies in the fact that remotely sensed image data are always regularised and thus a 'point' model variogram is never available. Thus, statistics and functions, including the variogram, that are derived from a regularised variable are themselves regularised (Clark, 1977).

3.5 Informed Guessing or Local Estimation

Sampling a particular area generally provides only measurements at specific locations. The unsampled locations however, are just as important and knowing the distance from the closest sampled locations to the unsampled location is important if one were to guess the attribute value for the unsampled location. To develop an estimator using the same notion, it would be reasonable to use a weighted average of the sample values, with the 'closer' samples having more weight. This estimator would be of the form: $Z^*=w_1z_1 + w_2z_2 + \ldots + w_nz_n$ where the weightings (w) sum to 1. If this condition is met and there is no trend (locally) then Z* is an unbiased

estimator. This means that over a number of estimations the average error will be zero. This type of estimator is called a linear estimator because it is a linear combination of the sampled values (Clark 1977).

Building on this idea, kriging is the generic name adopted by geostatisticians for a family of generalised least-squares regression algorithms in recognition of the pioneering work of Danie Krige (1951). All kriging estimators are variants of the basic linear regression estimator Z*(u) defined as:

(7)

$$Z^*(\mathbf{u}) - m(\mathbf{u}) = \sum_{\alpha=1}^{n(\mathbf{u})} \lambda_\alpha(\mathbf{u})\left[Z(\mathbf{u}_\alpha) - m(\mathbf{u}_\alpha)\right]$$

where $\lambda_\alpha(u)$ is the weight assigned to datum $z(u_\alpha)$ interpreted as a realisation of the RV $Z(u_\alpha)$. The quantities $m(u)$ and $m(u_\alpha)$ are the expected values of the RVs Z(u) and $Z(u_\alpha)$. Note that the number of data involved in the estimation as well as their weights may change from one location to another. In practice, only the $n(u)$ data closest to the location u being estimated are retained, i.e. the data within a given neighbourhood or window $W(u)$ centred on u (Goovaerts 1997).

The interpretation of the unknown value z(u) and data values $z(u_\alpha)$ as realisations of RVs Z(u) and $Z(u_\alpha)$ allows one to define the estimation error as a RV Z*(u) - Z(u). All flavours of kriging share the same objective of minimising the estimation or error variance $\sigma^2_E(u)$ under the constraint of unbiasedness of the estimator; i.e.

$$\sigma^2_E(u) = \mathrm{Var}\{Z^*(u) - Z(u)\} \quad (8)$$

is minimised under the constraint that:

$$E\{Z^*(u)-Z(u)\} = 0 \quad (9)$$

The kriging estimator varies depending on the model adopted for the RF Z(u) itself. The RF Z(u) is usually decomposed into a residual component R(u) and a trend component m(u): $Z(u) = R(u) + m(u)$. The residual component is modelled as a stationary RF with zero mean and covariance $C_r(h)$:

$$E\{R(u)\} = 0 \quad (10)$$

$$\mathrm{Cov}\{R(u), R(u+h)\} = E\{R(u)*R(u+h)\} = C_r(h) \quad (11)$$

The expected value of the RV Z at location u is thus the value of the trend component at that location: $E\{Z(u)\} = m(u)$. Once a RF model has been chosen, the next step consists of inferring its parameters from the available information. The inference process aims at estimating the parameters of the RF model from the sample information available over the study area. Inference of the two first moments (mean and covariance) of the multivariate RF Z(u) which are required by the interpolation algorithms (kriging).

The kriging weighting system accounts for a) the proximity of data to the location u being estimated and b) data redundancy. Instead of the Euclidean distance $|u_\alpha - u|$ common to all variables, the distance considered in kriging is the variogram

distance $\gamma(u_\alpha - u)$ as modelled from the data and specific to the variable under study. Note that the kriging weights depend only on the shape (relative nugget effect, anisotropy, correlation range) of the semivariogram and not on its global sill or any factor multiplying the variogram or covariance model.

Beyond providing a least-squares estimate of the attribute z, kriging also provides the attached error variance, e.g. for ordinary kriging:

$$\sigma^2{}_{OK}(\mathbf{u}) = C(0) - \sum_{\alpha=1}^{n(\mathbf{u})} \lambda_\alpha^{OK}(\mathbf{u}) C(\mathbf{u}_\alpha - \mathbf{u}) - \mu_{OK}(\mathbf{u}) \tag{12}$$

That error variance is:

- covariance model-dependent, which is an excellent feature because the estimation precision should depend on the complexity of the spatial variability of z as modelled by the covariance,
- data configuration-dependent. The terms $C(u_\alpha - u)$ account for the relative geometry of data locations u_α and their distances to the location u being estimated,
- independent of data values. For a given covariance model, two identical data configurations would yield the same kriging variance no matter what the data were.

Kriging is an interpolator. However, remote sensing measures EM radiation for entire scenes and the resulting image data cover the entire region of interest. Interpolation is not required unless there is missing data due to atmospheric effects

(Rossi *et al*. 1994) or other technical difficulties, which is not the case here. As it has been previously mentioned however, the scale of observation of the data itself is often not ideal. The strengths of geostatistics are the possibilities to both estimate the spatial structure at a different support (spatial resolution) and to interpolate.

If the goal were to change the spatial scale, then one would need to fill in the holes when fixing the image data onto a finer grid, i.e. finer spatial resolution. This would require knowing the spatial structure at the finer spatial resolution and also a means of assigning values to all the finer grid nodes. In a sense one would be interpolating onto the new grid and kriging would be the perfect choice because the spatial structure at the finer spatial resolution could be inferred with the variogram. However, kriged estimates produce variances that are less than those based on the original data. This smoothing effect should not occur when moving from a coarse to a fine spatial resolution, but rather the variance should increase. A smoothed map as provided by kriging is appropriate for showing global trends (Deutsch and Journel 1998). Since image data is ultimately used to extract other types of information, a generated finer spatial resolution image should have more spatial variability than that of the original. Furthermore, the sample variogram is altered such that the pattern of spatial variation is different from that of the original data. Consequently, kriged maps could never exist in reality (that is, they could never be observed through measurement) (Curran and Atkinson 1998). Previous work has shown finer spatial resolution kriged images to produce unrealistic results (Bielski and Cavayas 1998, Bielski 1999) because spatially the images were smoothed instead of becoming more variable as is expected when down-scaling occurs.

3.6 Local Uncertainty

The presentation so far has shown how kriging computes a 'best' estimate and attaches an error term to it. Another possibility is to first assess the uncertainty about the unknown, then from that assessment deduce an estimate optimal in some appropriate sense (Srivastava 1987, Journel 1989 – lesson 4). This approach is based on what is known, i.e. the available sampled data. Modelling the uncertainty about z(u) with the RV Z(u) can be achieved by computing the distribution function $F(u;z|(n)) = \text{Prob}\{Z(u) < z|(n)\}$ which is made conditional to the available data (n). This probability distribution is a model of the uncertainty about z(u) because probability intervals can be derived: $\text{Prob}\{Z(u) \in (a,b]|(n)\} = F(u;b|(n)) - F(u;a|(n))$.

Note that these probability intervals are independent of any particular estimate z*(u) of the unknown value z(u). Indeed, uncertainty depends on the information available (n) and not on a particular optimality criterion retained to define an estimate (Goovaerts 1997).

For example, an 8-bit image provides a minimum of information: the constraint interval $[z_{min}, z_{max}]$ being 0 and 255 respectively. This information is the basis of our uncertainty model and is not location specific. Therefore any unknown pixel within the image is assumed to have equal probability of a DN between 0 and 255. In such a case, all RVs have the same cdf:

$$F(u;z) = \begin{cases} 0 \text{ if } z < 0, \\ z/255 \text{ if in the set of } (0,255], \text{ for all } z \\ 1 \text{ if } z > 255 \end{cases} \quad (13)$$

For any one specific image deemed stationary, the uncertainty model can be updated and modelled from its cdf and could result in a different cdf by reducing the range of possible values, for example to a range of 10 to 235. However, even with this update, the uncertainty model is still not location specific because it takes into account the entire recorded scene (that was deemed stationary). The range of DN is still large and as a result the RV is the same again for all locations. In order to concentrate the uncertainty model further, the spatial dependence between pixels should be exploited by making it conditional to local DN values rather than global DN values. This latest update, the conditional cdf (ccdf) (conditional to the spatially dependent neighbouring pixels) is based on the (n) neighbouring pixels. The equation

$$F(u;z|(n)) = \text{Prob}\ \{Z(u) \leq z|(n)\} \quad (14)$$

represents this idea and " |n " expresses conditioning to the local information $n(u)$ neighbouring data $z(u_\alpha)$ and thus is location dependent.

The neighbouring data $z(u_\alpha)$, however, are made up of only a few samples. Not nearly enough to generate a continuous ccdf as is required. The easiest manner to derive the ccdfs from the available local data is based on the multiGaussian model because its properties render the inference of the parameters of the ccdf straightforward. Under the multiGaussian model, the mean and variance of the ccdf at location u are identical to the simple kriging estimate $y^*_{SK}(u)$ and simple kriging

variance $\sigma^2_{SK}(u)$ obtained from the n(u) data $y(u_\alpha)$ (Journel and Huijbregts 1989). One also has the choice of adopting other kriging algorithms (such as ordinary kriging) depending on the nature of the data under study.

The normal score transform is one technique used for generating the ccdf based on the few data available. A normal score transformation sees the original z-data transformed into y-values with a standard normal histogram. This transformation can be made graphically by correspondence between the cumulative one-point distributions of the original and standard normal variables where the p-quantiles z_p and y_p of the two distributions are equal. This can be achieved in three steps.

1. The n original data $z(u_\alpha)$ are ranked in ascending order: $[z(u_\alpha')](1) \leq \ldots \leq [z(u\alpha)](k) \leq \ldots \leq [z(u_\alpha'')](n)$ where k is equal to the rank of the datum $z(u_\alpha)$ among all n data.
2. The sample cumulative frequency of the datum $z(u_\alpha)$ with rank k is then computed as $p^*_k = k/n - 0.5/n$ if all data $z(u_\alpha)$ receive the same weight 1/n; that is, if the sample histogram is deemed representative of the study area.
3. The normal score transform of the z-datum with rank k is matched to the p^*_k-quantile of the standard normal cdf.

Using these three steps it is possible to build models of uncertainty for any location within a study area of interest. Knowledge of the ccdf model at location u allows a straightforward assessment of the uncertainty about the unknown z(u) prior and independently of the choice of a particular estimate for that unknown (Goovaerts

1997). Instead of just picking a single value out of the model of uncertainty, it is possible to draw a series of L simulated values $z^{(l)}(u)$, $l = 1, \ldots, L$. Each value $z^{(l)}(u)$ represents a possible outcome of the RV Z(u) modelling the uncertainty at location u. The L simulated values $z^{(l)}(u)$ are distributed according to the ccdf because the random numbers are uniformly distributed in [0,1]. This is called the 'Monte Carlo' simulation of the value at location u.

This property of the ccdf reproduction allows one to approximate any moment or quantile of the conditional distribution by the corresponding moment or quantile of the histogram of many realizations $z^{(l)}(u)$. Monte-Carlo simulation can thus approximate the conditional variance and mean (E-type estimate) of the distribution and provides an alternative to the approximations for computing the conditional variance or E-type estimate. Note that determination of the quantile value still requires interpolation and extrapolation from calculated ccdf values.

3.7 Stochastic Imaging

A kriged image is 'best' in the least-squares sense in that the local error variance Var{Z*(u)-Z(u)} is minimum. The image of such best local estimates, however, may not be best as a whole. As mentioned, interpolation algorithms tend to smooth out local details of the spatial variation of the attribute (Curran and Atkinson 1998, Bielski and Cavayas 1998). Typically small values are overestimated while large values are underestimated. Such conditional bias is a serious shortcoming when the aim is to detect patterns of extreme attribute values such as regions of the same

object or phenomenon. Another drawback of estimation is that the smoothing is not uniform. Rather it depends on the local data configuration: smoothing is minimal close to the data locations. A map of kriging estimates appears more variable in densely sampled areas than in sparsely sampled areas. Thus the kriged map may display artefact structures. Smooth interpolated maps should not be used for applications sensitive to the presence of extreme values and their patterns of continuity.

Stochastic imaging aims to generate a map or a realization of z-values, say $\{z^{(l)}(u)$, u in the set of A$\}$ with *l* denoting the *l*th realization, which reproduces statistics deemed most consequential for the problem in hand, i.e. reproducing model statistics. Typical requirements for such simulated map are:

1. Data values are honoured at their locations: $z^{(l)}(u) = z(u_\alpha)$, for all $u = u_\alpha$, $\alpha=1,...,n$. The realization is then said to be conditional.
2. The histogram of simulated values reproduces closely the declustered sample histogram.
3. The covariance model C(h) is reproduced

More complex features such as spatial correlation with a secondary attribute or multiple-point statistics may also be reproduced (Goovaerts 1997).

Stochastic imaging reproduces the sample histogram and the variogram model much better than kriging, yet it is not exact nor should it be because it is but a possible outcome. Reasons for departure between model and realization statistics are

the type of algorithm, the density of conditioning data, the variogram parameters, and the size of the simulation grid (Goovaerts 1997). As a result, stochastic imaging can generate multiple realizations that all match reasonably well the same sample statistics and exactly the conditioning data. The set of alternative realizations $\{z^{(l)}(u)$, u in the set of A$\}$, l=1, ..., L, provides a visual and quantitative measure (actually a model) of spatial uncertainty. Spatial features such as specific strings of large values (such as rivers in a remotely sensed image) are deemed certain if seen on most of the L simulated images. Conversely, a feature is deemed uncertain if seen only on a few simulated images.

Using the spatial uncertainty model by generating alternative realisations of the spatial distribution of an attribute is rarely a goal per se. Rather, these realisations serve as input to complex transfer functions that consider all locations simultaneously rather than one at a time. The processing of each input realisation yields a unique value for each response. For example, this could be a unique number or estimate of land-cover types. Image segmentation utilises all locations simultaneously as well, however unlike transfer functions, the result is not a single response value but rather groupings of similar spectral associations and the area taken up by each group. The distribution (histogram) of the L response values corresponding to the L input realizations provides a measure of response uncertainty resulting from our imperfect knowledge of the distribution in space of z. That measure can then be also used in risk analysis and decision-making.

3.7.1 Stochastic imaging theory

A set of simulated maps $\{z^{(l)}(u'_j), j=1,...N\}$, $l=1, ... L$, can be generated by sampling the N-variate or N-point ccdf modelling the joint uncertainty at the N locations u'_j:

$$F(u'_1, ...u'_N;z_1,...z_N|(n)) = \text{Prob}\{Z(u'_1) \leq z_1, ..., Z(u'_N) \leq z_N|(n)\} \quad (15)$$

Inference of the conditional cdf requires knowledge or stringent hypotheses about the spatial law of the RF Z(u). The multivariate gaussian RF model is one model whose spatial law is fully determined by the sole z-covariance function. This model underlies several simulation algorithms. I chose to use the sequential gaussian simulation algorithm. The sequential gaussian simulation algorithm models and samples a one-point ccdf at each of the N nodes visited along a random sequence instead of modelling the N-point ccdf, i.e. the ccdf modelling the joint uncertainty at the N locations u'_j . To ensure reproduction of the z-covariance model each one-point ccdf is made conditional not only to the original n data but also to all values simulated at previously visited locations.

The sequential simulation paradigm is based on Bayes' axiom that states that any two-point ccdf can be expressed as a product of one-point ccdfs:

$$F(u'_1,u'_2;z_1, z_2|(n)) = F(u'_2; z_2 | (n+1)) \cdot F(u'_1;z_1 | (n)) \quad (16)$$

where " | $(n+1)$ " denotes conditioning to the n data values $z(u_\alpha)$ and the realization $Z(u'_1) = z^{(l)}(u'_1)$. What this actually means is that it is possible to generate more than one realization in sequence thus not having to model the N-point ccdf. The sequence

is that the value $z^{(l)}$ is first drawn from the ccdf $F(u'_1;z_1 \mid (n))$, then the ccdf at location u'_2 is conditioned to the realisation $z^{(l)}(u'_1)$ in addition to the original data (n), its sampling yields the correlated value $z^{(l)}(u'_2)$. The idea is to trade the sampling, hence modelling of the two-point ccdf, for the sequential sampling of two-point ccdfs that are easier to infer.

This notion can be further generalised to more than two locations. By recursive application of Bayes' axiom, the N-point conditional cdf can be written as the product of N one-point conditional cdfs. This decomposition allows one to generate a realization of the random vector $\{Z(u'_j), j=1,...N\}$ in N successive steps:

Step 1. Model the cdf at the first location u'_1 conditional to the n original data $z(u_\alpha)$: $F(u'_1;z|(n)) = \text{Prob}\{Z(u'_1 \leq z|(n)\}$.

Step 2. Draw from that ccdf a realization $z^{(l)}(u'_1)$ which becomes a conditioning datum for all subsequent drawings.

…

Step N-3. At the i-th node u'_i visited, model the ccdf of $Z(u'_i)$ given the n original data and all (i-1) values $z^{(l)}(u'_j)$ simulated at the previously visited locations u'_j, j=1,...i-1:

$$F(u'_i;z|(n+i-1)) = \text{Prob}\{Z(u'_i) \leq z|(n+i-1)\}.$$

Step N-2. Draw from that ccdf a realization $z^{(l)}(u'_i)$ which becomes a conditioning datum for all subsequent drawings.

Step N. Repeat the two previous steps until all N nodes are visited and each has been given a simulated value.

The resulting set of simulated values $\{z^{(l)}(u'_j),\ j=1,...N\}$ represents one realisation of the RF $\{Z(u),u$ in the set of $A\}$ over the N nodes u'_j. Any number L of such realisations, $\{z^{(l)}(u'_j),\ j=1,...N\}$, $l=1,...L$ can be obtained by repeating L times the entire sequential process with possibly different paths to visit the N nodes.

The sequential simulation algorithm requires the determination of a ccdf at each location being simulated, which is achieved using the multiGaussian formalism presented above i.e. the RF model is gaussian and thus is named sequential gaussian simulation. The sequential gaussian simulation algorithm honours data at their locations. At any datum location u_α, the simulated value is drawn from a zero-variance, unit-step conditional cdf with mean equal to the z-datum $z(u_\alpha)$ itself. This basically means that the conditioning value is unchanged during stochastic imaging.

The sequential principle can also be extended to the simulation of several continuous attributes. This study needs to generate data that is related to previously simulated images to jointly simulate the spectral bands. One way to achieve this is by defining a hierarchy of variables. Instead of trying to simulate all the bands simultaneously, several researchers propose to simulate other bands (or variables) in turn as long as it is done conditionally to the previously simulated values. (Gomez-Hernandez and Journel 1993, Almeida and Journel 1994). The predefined hierarchy allows the implementation of the co-located co-kriging approximation. This hierarchy of spectral channels is based on the correlation between spectral bands. The higher a channel correlation, the more important the channel. However, in order to choose the

first band to be simulated, the total variance was considered. It was deemed that a higher variance provided more information content and thus was the first band to be simulated.

3.7.2 Practical stochastic imaging

In the context of this work, the actual simulation would proceed as follows (figure 3.5). The parameters that are required in order to run this simulation are the modelled variogram, the minimum and maximum values of the simulation output, and the original data for conditioning the simulation. In addition to these parameters the grid onto which the simulated values will be attached must also be given.

1. The remotely sensed image data are transformed to a standard normal cdf using the normal scores transform.
2. The sequential gaussian simulation is performed on the transformed data. The sequential gaussian simulation proceeds as follows:
    a. A random path is defined visiting each node on the finer spatial resolution grid only once.
    b. At each node, a RV is generated conditional to the local data. This is achieved by determining the parameters (mean and variance) of the gaussian ccdf using OK and the normal score variogram model. The conditioning data consists of transformed original image data and previously simulated data found at nearby nodes.
    c. A value is drawn from the gaussian ccdf randomly and added to the current node being visited.

d. Then proceed to the next node along the random path and repeat steps b and c.
e. Continue advancing to other nodes (locations) until all nodes have been visited at least once.

3. The resulting generated image must be back-transformed. Since the simulation was performed in normal scores space, the resulting output must be converted back to match the range and distribution of the original DN values.

Variations do exist in the above methodology based on the input parameters and data. For instance, when stochastic imaging is applied to generate three different channels that are based on the same recorded scene, the first channel to be simulated is only conditioned by the original imagery. All subsequent channels are conditioned to the previously simulated channel based on the given correlation between channels as well as the original imagery.

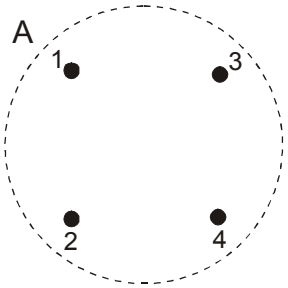

- Let $\{Z(u'_j), j = 1, ..., N\}$ be a set of RV defined at N locations u'_j within the study area A; These locations need not be gridded. The objective is to generate several joint realisations of these N Rvs:

$$\{Z^{(l)}(u'_j), j=5,6\}, l=1,$$

conditional to the data set $\{z(u_\alpha), \alpha=1,2,3,4\}$.

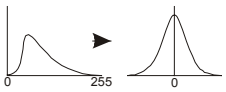

- Transform the original data to normal scores.

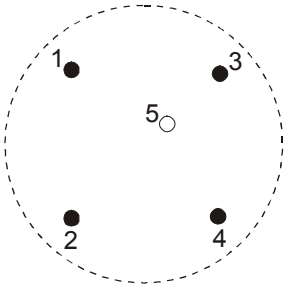

- Randomly choose a location within area A.

- At the chosen location, determine the parameters (mean and variance) of the Gaussian ccdf $G(u';y|(n))$ using SK. The conditioning information (n) consists of the measured values 1 through 4.

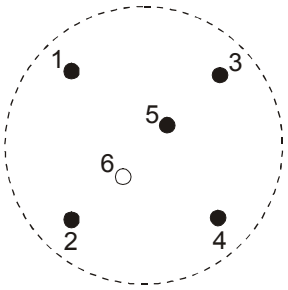

- Draw a simulated value $y^{(l)}(u')$ from that ccdf, and add it to the data set.

- Randomly choose another location within area A.

- At the chosen location, determine the parameters of the Gaussian ccdf $G(u';y|(n))$ using SK. The conditioning information (n) consists of the measured values 1 through 4 and the simulated value 5.

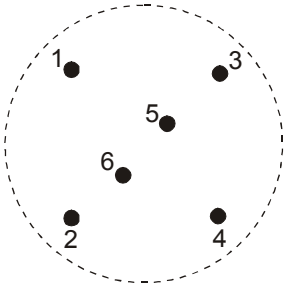

- Draw a simulated value $y^{(l)}(u')$ from that ccdf, and add it to the data set.

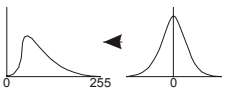

Finally, back-transform the simulated normal scores into simulated values for the original variable.

Figure 3.5 – The sequential gaussian simulation algorithm represented graphically.

3.7.3 Simple kriging with locally varying mean (LVM)

The LVM option in the SGSIM algorithm refers to simple kriging (SK) with varying local means. Normally the SK algorithm uses the mean value of the area under consideration deemed stationary. In such a case the mean is not location dependent. When there is access to secondary information, the known stationary mean of the primary data may be replaced by known varying means $m^*_{SK}(\mathbf{u})$:

$$Z^*_{SKlm}(\mathbf{u}) - m^*_{SK}(\mathbf{u}) = \sum_{\alpha=1}^{n(\mathbf{u})} \lambda^{SK}_{\alpha}(\mathbf{u})\left[Z(\mathbf{u}_\alpha) - m^*_{SK}(\mathbf{u}_\alpha)\right] \tag{17}$$

where '*lm*' stands for 'local mean'. Local mean refers to the trend component that is modeled as a function of the location **u**. When a continuous secondary attribute is available, then the primary local mean can be a function (linear or not) of the secondary attribute value at u. Here the secondary attribute is taken to be the coarse spatial resolution VGT imagery itself. In doing so, there is a perfect linear relationship between the primary and secondary attributes.

The kriging weights $\lambda^{SK}_{\alpha}(\mathbf{u})$ are obtained by solving a SK system:

$$\sum_{\beta=1}^{n(\mathbf{u})} \lambda^{SK}_{\beta}(\mathbf{u}) C_R(\mathbf{u}_\alpha - \mathbf{u}_\beta) = C_R(\mathbf{u}_\alpha - \mathbf{u}), \alpha = 1,\ldots,n(\mathbf{u}) \tag{18}$$

where $C_R(h)$ is the covariance function of the residual RF $R(u) = Z(u) – m(u)$ and not that of Z(u) itself. Therefore, in practice one needs the variogram of residuals. This is obtained by subtracting the trend from the primary attribute and computing the variogram on the residuals. The residual values are then estimated using SK and the closest available residual data $r(u_\alpha)$. The final estimate of the primary data is obtained by adding the trend estimate to the SK estimate of the residual r^*_{SK} (taken from Goovaerts 1998).

3.7.4 Co-simulation

The second option that was used in conjunction with the SGSIM algorithm to generate finer spatial resolution images was the co-simulation option. The co-simulation option was used to generate the different channels of the finer spatial resolution images as well as help better localise simulated images (in the case of using the SAR imagery). In the first case, generating the different channels based solely on the conditioning data would not assure spectral objects to be something that could be found on the ground. Therefore a certain relationship had to be maintained. In the second case, the relationship between the SAR data and the optical data was used to constrain the simulation of the optical data to real world locations. In both cases the joint spatial variability of the attributes needed to be reproduced.

To reproduce the joint spatial variability in general, it is necessary to model not only the variograms of the primary and secondary data, but also the cross-variograms between the primary and secondary data (as in co-kriging). Almeida and

Journel (1994) propose an approach that does not require the inference and modeling of the matrix of covariances and cross-covariances. The proposed simulation algorithm is in essence a joint sequential Gaussian simulation capitalizing on the collocation idea to reduce the co-kriging system and a Markov model to reduce the burden of inference. The Markov model hypothesis does not fully determine the coregionalization of the primary and secondary data sets, i.e. it does not yield a specific model; however, whenever a single secondary datum is retained, as in collocated cokriging, the covariance of the secondary data is not called for. As such, secondary data is necessary at all locations where the primary variable is to be estimated.

For this approach to work, a hierarchy of variables requires to be defined because the algorithm accounts for spatial correlation between primary variables by retaining, for the simulation of any particular primary variable, the collocated value of all previously simulated primary variables of a different type. This predefined hierarchy allows the implementation of the co-located co-kriging approximation. This hierarchy should be based on the autocovariance and cross-covariances that are most critical to reproduce. In the phase I and II experiments, the first channel to be simulated was the one with the greatest variability. This channel was simulated to generate an image with values at all the nodes. The second channel was co-simulated based on the strongest correlation with the first simulated channel. The final channel was co-simulated based on the strongest correlation between the other generated channels.

After defining the hierarchy of variables the algorithm proceeds as follows (from Goovaerts 1997):

1. Transform all the channels Z_i into their normal scores Y_i.
2. Define a random path visiting only once each node to be simulated (just as in sequential simulation paradigm).
3. At each node u′:

- Use SK to determine the parameters of the Gaussian ccdf of the first variable $Y_1(u')$. The conditioning information consists of neighbouring normal score data $y_1(u_{\alpha 1})$ and previously simulated values $y_1^{(l)}(u')$ from that ccdf, and add it to the conditioning data set.
- Use co-located simple co-kriging to determine the parameters of the Gaussian ccdf of the second variable $Y_2(u')$. In addition to neighbouring normal score data $y_2(u_{\alpha 2})$ and previously simulated values $y_2^{(l)}(u'_j)$, the previously simulated co-located value $y_1^{(l)}(u')$ is retained as datum. Then, draw a simulated value $y_2^{(l)}(u')$ from that ccdf, and add it to the conditioning data set.

.

.

.

- Use co-located simple co-kriging to determine the parameters of the Gaussian ccdf of the last variable $Y_{Nv}(u')$. The conditioning information consists of the neighbouring normal score data $y_{Nv}(u_{\alpha i})$ and previously simulated values $y^{(l)}{}_{Nv}(u'_j)$ of that variable, plus all previously simulated co-located values $y_1^{(l)}(u')$, …, $y^{(l)}{}_{Nv}$-

$_1(u')$. Then, draw a simulated value $y^{(l)}_{Nv}(u')$ from that ccdf, and add it to the conditioning data set.

4. Loop until all N nodes are simulated.
5. Back-transform the N_v realizations into simulated values for the original variable.

Therefore a model of co-regionalisation is not required when using this algorithm (taken from Almeida and Journel 1994).

Chapter 4 – Methodology and Data

The goal of this work is to generate fine spatial resolution optical-like imagery based on coarse spatial resolution optical imagery and the stochastic imaging paradigm and to validate the generated imagery to real fine spatial resolution imagery. The diagram (figure 4.1) presents the basic framework of the proposed methodology organised into three phases based on the distinct sources of information applied.

The design of this experiment is based on three phases where each phase made use of the sequential gaussian simulation algorithm to generate finer spatial resolution imagery. The three phases differed from each other in the type of information that was input into the simulation algorithm. In the first phase the input information was based solely on the coarse spatial resolution VGT imagery. This information included the imagery itself as well as the distribution and the spatial parameters such as the variogram. In phase II the coarse spatial resolution imagery itself was still applied however the input parameters were based on the wanted finer spatial resolution HRVIR imagery. The final phase utilised the same input parameters as those in phase II with the addition of RADARSAT SAR imagery. This strategy was chosen in order to see whether the resulting generated finer spatial resolution images were improved with the more complex input parameters.

The final analysis involved the segmentation and validation of the generated finer spatial resolution images. Segmentation was performed automatically with the

K-means algorithm and validation of the results was attempted in different ways including the use of land-cover maps.

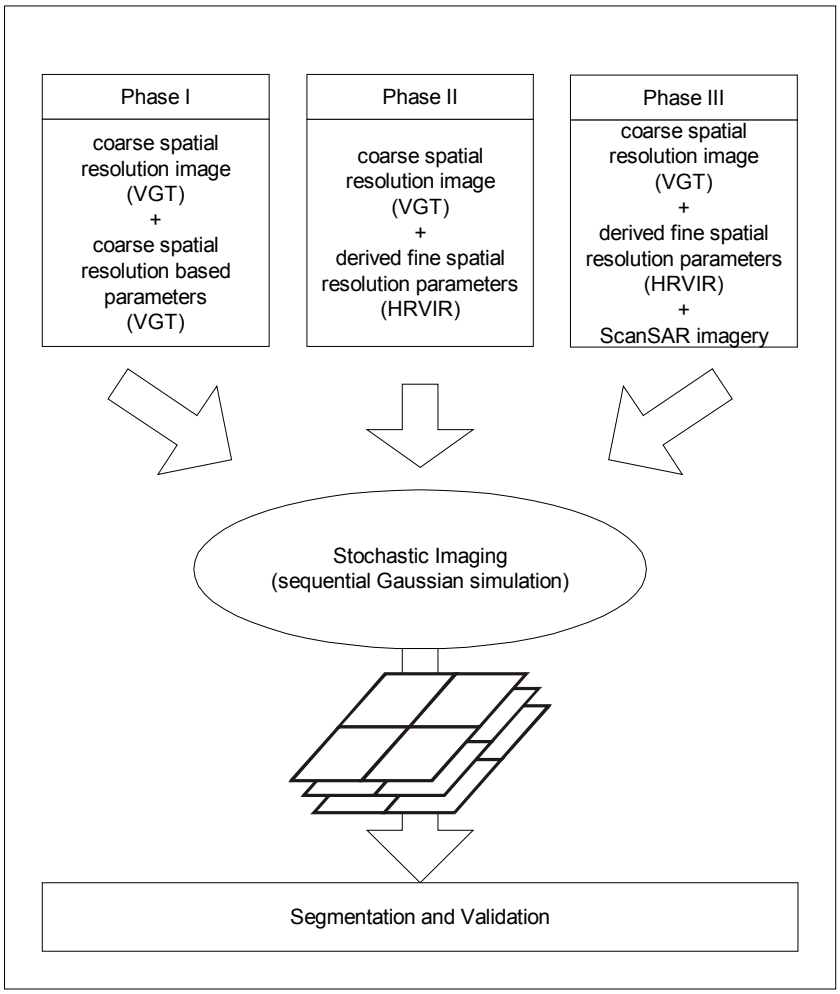

Figure 4.1 – A diagram of the proposed methodology. The three phases are related to the different types of information used to generate the finer spatial resolution imagery.

4.1 Image Data

A myriad of optical satellite remote sensing imagery is currently available. However, the goal here is to zero in on the spatial aspect of the imagery itself, concentrating only on the image spatial scale, i.e. spatial resolution and/or spatial extent. Therefore, the ideal set of imagery (coarse and fine spatial resolution) for both testing and validating the approach would have the same spectral and radiometric scales, be acquired at the same time to avoid atmospheric differences and have a similar viewing geometry. Currently, the only platform that satisfies most of these requirements is SPOT 4. The SPOT 4 system is unique because the two main sensors onboard, HRVIR and VGT share a similar spectral scale for three channels, i.e. three identical bands (table 4.I). Furthermore, both types of imagery can be taken simultaneously providing an ideal situation for comparing data at two different scales of observation because the atmospheric conditions are similar and the viewing geometry is almost the same. The primary difference between the two sensor configurations is spatial resolution and extent (table 4.I). The difference in spatial resolution is two orders of magnitude and the area covered is even greater. These characteristics allow one to study the image spatial scale without introducing unwanted variability from other image scales, such as spectral or temporal; differences normally associated with comparing two different sensors. Note however, that the radiometric scales are different (10 bits for VGT vs. 8 bits for HRVIR). Unfortunately, the radiometric extent could not be equal because of the limits of present sensor technologies.

Table 4.I – HRVIR and VGT sensor characteristics onboard the SPOT 4 satellite.

SPOT 4 Sensor	HRVIR	VGT
Blue band (μm)	N/A	0.43 - 0.47
Green band (μm)	0.50 - 0.59	N/A
Red band (μm)	0.61-0.68	0.61-0.68
NIR band (μm)	0.79-0.89	0.78-0.89
SWIR band (μm)	1.58-1.75	1.58-1.75
Radiometric resolution	8 bit	10 bit
Pixel resolution (m)	20 x 20	1000 x 1000
Swath width (km)	60 (at nadir)	2200

One of the original goals of the SPOT 4 system was to combine the benefits of the VGT sensor's revisit capability and the HRVIR sensor's high spatial resolution for detailed modelling and multi-scale sampling. The HRVIR and VGT sensors use the same geometric reference system in order to facilitate the study of multi-scale observations (VEGETATION 1999).

For this study, the coarse spatial resolution imagery was recorded on May 24, 1998 by the VGT instrument. This image covers a large portion of western Quebec, eastern Ontario (Canada) and northern New York and Vermont states (USA) (figure 4.2 inset). Four study sites were chosen in the region of Montréal, Québec, and are delineated in figure 4.2. Each study site is made up of a total area of 15 x 15 VGT pixels which is approximately equivalent to 15 km x 15 km. Study area A is located on the Island of Montreal in a highly urbanised region that includes the downtown core and several different residential areas. Study area B is located on the southern shore of the St. Lawrence River in a highly agricultural area with rural settlements. Due to the acquisition date in late May, some of the fields appear to be quite bare. Study area C comprises of a mixed forest/agriculture region with some rural

settlement and finally study area D is on the urban/rural divide on the northern edge of the region of Montreal where forest, agriculture and suburban regions can be identified. The VGT study areas are examples of the type of data that is provided by coarse spatial resolution optical imagery in northern cold temperate zones.

The imagery in the figures from this point on will always be shown as a false colour composite unless otherwise noted. The channel combinations are blue = channel 2 (red), green = channel 3 (NIR) and red = channel 4 (SWIR).

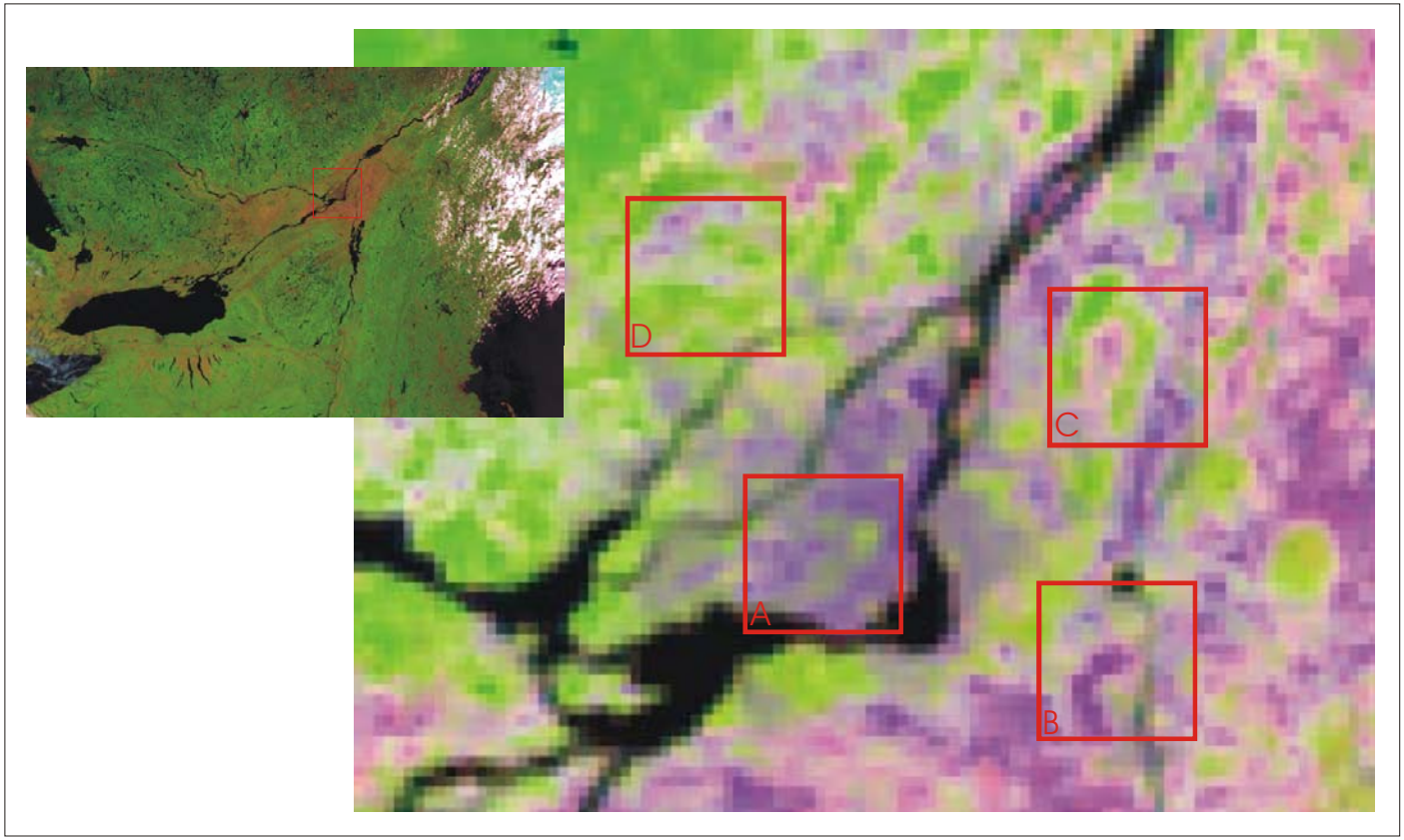

Figure 4.2 – SPOT 4 VGT imagery. Upper left inset presents the areal extent that can be sensed by the VGT sensor (about 2200 km). The central image presents a magnification of the island of Montreal and surrounding areas that is approximately equal to the extent covered by a single SPOT 4 HRVIR image. The red squares each encompass a study area 15 x 15 km denoted as study areas A through D.

Although a single VGT scene can cover a much larger area, the small sub-samples were chosen within a confined region for several reasons. One of the most important technical reasons is the availability of fine spatial resolution validation data, i.e. SPOT 4 HRVIR. HRVIR imagery only covers a swath 60 km wide, far less than that provided by a single VGT image. Therefore, validation sites needed to be found within the extent of the available HRVIR imagery. Secondly, the availability of space to store the data. A single VGT sub-sample, including 3 bands, needs just over 1 K of memory. However, simulating many realisations at a much finer spatial resolution does require large amounts of storage space that were not available to me. Finally, the study sites were chosen within different land-cover regions (e.g. urban landscape, agricultural landscape, etc.). Choosing specific land-cover regions also satisfied my decision of stationarity (see chapter 3).

A simultaneously recorded HRVIR image of the region of Montreal provided the fine spatial resolution imagery for the four study sites (figure 4.3). The four HRVIR sub-samples also cover the same extent as their VGT sub-sample counterparts (A through D).

In order to compare the coarse and fine spatial resolution images of the four study sites directly, the images were corrected geometrically (image to image) using control points without spatially degrading the resolution of the HRVIR image. Their geometric accuracy is in reality difficult to assess because of the great smoothing effect generated by the VGT IFOV compared to the ‘point’ samples that are captured

by the HRVIR instrument. The HRVIR imagery was the base image for the geometric correction. A degraded HRVIR image was also not used to correct geometrically because it was felt that it would introduce unnecessary inaccuracies because the degradation focal point is not known. A visual inspection indicates that the study sites at both spatial resolutions correspond adequately. The spatial detail provided by the HRVIR images are those desirable for local to regional level studies because everyday objects can be fairly easily delineated.

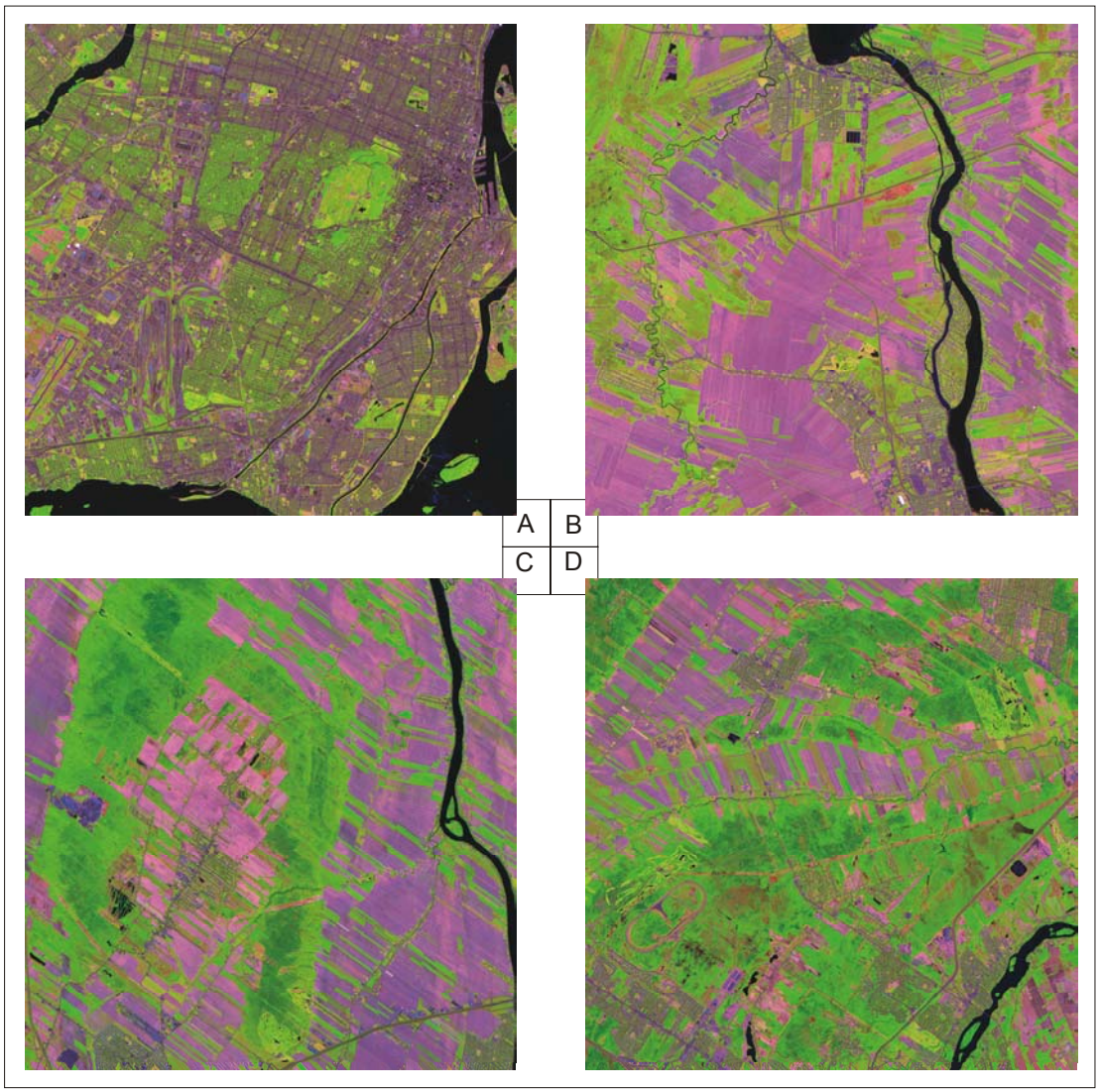

Figure 4.3 – SPOT 4 HRVIR imagery of the four study sites denoted A through D.

As was noted above, the radiometric scale of the HRVIR and VGT images is not the same. Initial tests on the data using the raw DN showed inconsistencies between the expected values that were observed at the two different spatial resolutions. These inconsistencies were discovered when summary statistics were compared (e.g. mean and median) and the computed variogram for both HRVIR and VGT images. The most obvious inconsistency being the expected mean values for

both types of images were very different. In order to minimise the effect of the differences found in the radiometric dimension of the two types of imagery, it was decided that reflectance be used as the compatible measure because both images would be expressed in the same units. The converted reflectance data of both the HRVIR and VGT images was within the desired accuracy found in the literature (Henry and Meygret 1999).

Both the VGT and HRVIR images were acquired simultaneously and the chosen study sites were near the centre of the VGT imagery. It was considered that the atmospheric effects on both types of images were similar and therefore the DN were only converted to top of the atmosphere (TOA) reflectance. Transformation of the VGT and HRVIR DN image to a reflectance image was achieved using correction equations provided by SPOT (SPOT 2000, VITO 2000). Applying the equation:

$$\text{TOA reflectance VGT} = a * DN + b \qquad (19)$$

where a = 0.0005 and b = 0.0 for all bands. A similar correction was applied to the HRVIR image data. At first the TOA radiance was computed based on the absolute calibration gains provided (table 4.II) in the HRVIR image header file:

$$\text{TOA radiance } (L) = DN/a + b \qquad (20)$$

where a is the absolute calibration gain (ACG) value and b is the calibration offset usually set to zero. The next step was to convert this into TOA reflectance. Computing TOA reflectance values requires knowledge of the sun's whereabouts at the time of recording. Thus:

$$\text{TOA reflectance (HRVIR)} = \pi L/E \cos z \qquad (21)$$

where L is the TOA radiance (from above), E is the solar spectral constant and z is the suns zenith angle (table 4.II).

Table 4.II – Calibration coefficients used to transform the SPOT 4 HRVIR imagery to TOA reflectance values.

HRVIR channel	ACG	Solar Constant (Wm^{-2} μ m^{-1})	Sun Zenith Angle
Channel 2	1.29086	1586	28°10′
Channel 3	1.08	1054	28°10′
Channel 4	5.93	240	28°10′′

One of the desired objectives was to produce finer spatial resolution synthetic images whose spatial locations were true to the underlying scene. This required additional spatial information at a spatial resolution comparable to the final product. The secondary spatial information was provided by RADARSAT-1 ScanSAR wide mode imagery because it can record scenes over large extents and at a spatial resolution that is much finer than that of the VGT sensor. Furthermore, fine spatial resolution optical imagery cannot be used in this case because the technology is not far enough advanced for large area monitoring due to platform characteristics such as a low revisit rate, and other technical difficulties such as atmospheric interference. The possibilities of mixing optical and SAR imagery with stochastic imaging techniques are explored. Table 4.III presents the characteristics of the ScanSAR wide mode imagery that was chosen for this research and acquired by RADARSAT-1. The large coverage of a single ScanSAR wide mode image is comparable to that of a VGT scene in extent. As a result, both sensors (i.e. VGT and RADARSAT-1) within a reasonable amount of time could cover the same extent. The spatial resolution of

imagery acquired in ScanSAR wide beam mode is also much finer than that of the VGT imagery.

Table 4.III – RADARSAT ScanSAR wide beam mode image characteristics.

Beam Mode	Nominal Area	Nominal Resolution	Pass Mode	Radiometric Resolution
ScanSAR wide	500 km x 500 km	100 m	Ascending	8 bits

SAR imagery can be acquired during the day or night with rain or clouds. These qualities alone make it a very useful alternative to sensors that record in the visible spectrum. However, the difficulty associated with segmenting/classifying land-cover and subsequently estimating land-cover using SAR data is quite important. Measurements taken in the visible spectrum are much more convenient for such work especially when vegetation is involved. It is postulated that the spatial information provided by a RADARSAT SAR sensor can complement and/or enhance the generated fine spatial resolution imagery.

Optical and SAR based imagery are different. A SAR image portrays information that is qualitatively different from that of an optical image because microwave and optical frequencies are sensitive to different target surface characteristics. Optical frequencies interact with materials at a molecular level and respond to the surface chemistry of target materials whereas radar frequencies interact with materials at a macroscopic structural level and respond to the bulk electrical properties of target materials at resolutions near the radar wavelength. What appears on the SAR image is dependent on such variables as geometric shape, surface roughness and moisture content of the target object, as well as the sensor target

geometry and the transmission direction (look direction) and the polarization state of the radar sensor. To understand radar output one needs to understand the radar configuration, the energy associated with radar remote sensing, the way in which that energy interacts with objects at the Earth's surface, and the manner in which this interaction is represented as an image. Even though the manner in which the imagery is produced is completely different than that of the optical imagery, the spatial details associated with such an image can be compared to that of optical images. Objects may not look the same on the different images but they are in the same spot. For example, a river will be dark in both a SAR image and a red band image but a silo would be bright on the SAR image but not necessarily on the red image because it depends on the colour and surrounding objects.

The RADARSAT-1 satellite acquired the SAR data on May 19, 1998. The entire scene is presented in figure 4.4 (inset) while the study sites are presented in the main figure. Geometric registration was based on the HRVIR imagery. Raw DN values were also converted to backscatter values because prior experience showed poor correlation between any of the optical channels (NACOG 2000). The data was converted to radar backscatter values using the PCI (2000) SARSIGMA routine.

The date of acquisition of the ScanSAR wide imagery differs from that of the optical images by five days (earlier). Thus, the differences between the two images in terms of land-cover changes between acquisition dates were considered minimal.

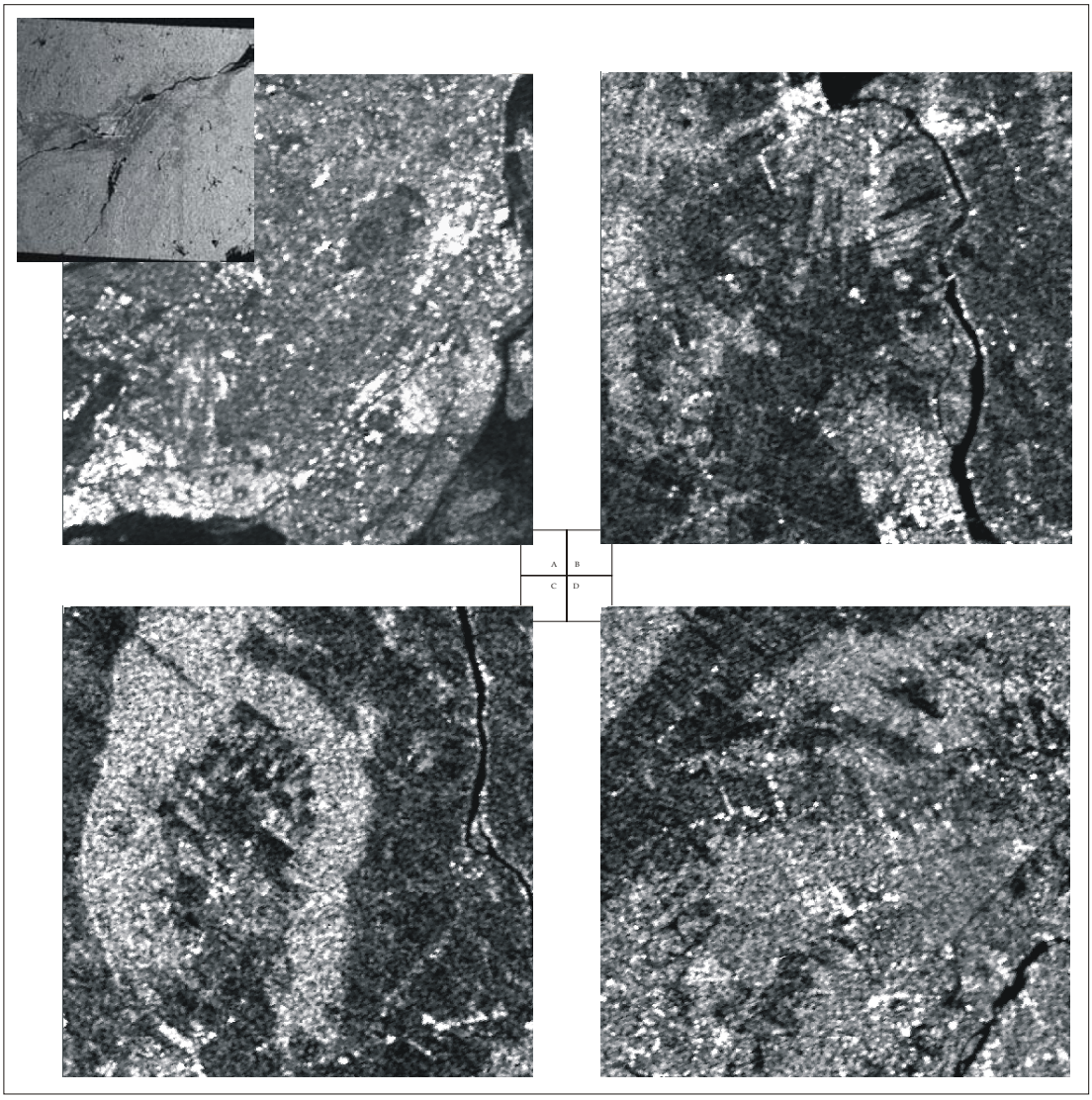

Figure 4.4 – RADARSAT-1 ScanSAR wide beam mode imagery. Upper left inset presents the full RADARSAT-1 image in ScanSAR wide beam mode. The image was recorded while ascending and produced using the w1, w2, s5 and s6 beam modes. Each of the images (A through D) covers the same area as that of the HRVIR and VGT image subsets.

The RADARSAT-1 ScanSAR wide imagery covers a large swath by switching the beam position in the range direction. Special processing is required to combine data from individual beam positions into a single scene (Raney *et al*. 1991).

4.2 Generating Finer Spatial Resolution Imagery

The novel approach proposed here was to use stochastic imaging to generate synthetic fine spatial resolution optical-like imagery based on available coarse spatial resolution imagery. Specifically, the sequential gaussian simulation (SGSIM) algorithm (Deutsch and Journel 1998) was chosen because the image data are continuous (between 0% and 100% for reflectance) and the output imagery also needed to be continuous.

Goovaerts (1997) shows that ordinary kriging yields, on average, better predictions than the simulation algorithm in that the mean absolute prediction error is smaller for kriging estimates than for simulated values. This behaviour is expected because there is no smoothing effect with stochastic imaging. However, kriging does underestimate high and low values (conditional bias) which lead to underestimating global attributes (Goovaerts 1997). This behaviour was also observed in previous work (Bielski and Cavayas 1998, Bielski 1999) especially in terms of the requirements for a scale change.

As shown in the diagram at the beginning of the chapter (figure 4.1), the SGSIM algorithm was fed three different input parameters that are associated with each phase of the experiment. These sets of parameters differ in their spatial variability and histogram characteristics and conditioning data. The primary source of these parameters is the coarse spatial resolution VGT imagery. Furthermore, the

SGSIM algorithm was used to generate imagery using the co-simulation and LVM options.

For each study site, a single realisation is generated as well as a set of 50 realisations (only in the co-simulation case). Since the goal is to provide optical-like imagery, this process is repeated for each available channel (red, NIR and SWIR channels). These three particular channels were chosen because the SPOT 4 HRVIR and VGT sensors share these three common channels, even though they each have at least one other channel available (table 4.I).

The difficulty in visualising 50 different realisations for analysis also required a method of generalising the output images. This was accomplished by computing four statistics and generating statistical maps for interpretation. The four statistics used were the E-type estimate and the 10^{th}, 50^{th} and 90^{th} percentiles. These statistics were computed for the same pixel location across all 50 realisations per spectral band creating a statistical image where the pixel value equalled the statistic for that location.

The applied stochastic imaging algorithm necessarily required a grid onto which generated values were assigned. All realisations were generated onto a grid with 750 nodes in the x and y directions. The 750 nodes in both directions were equivalent to the number of HRVIR pixels found within an area 15 x 15 km. The minimum node location was 0.6 and the distance between nodes was 0.02. These values are based on the 1000 m coarse spatial resolution VGT data set. Dividing the

actual spatial resolution (in m) of the HRVIR data by 1000 will give the node size. The minimum node location was chosen as 0.6 (rather than 0.5) in order to place the VGT data off centre (figure 4.5).

4.2.1 Phase I parameters

The SGSIM algorithm requires several parameters including the minimum, maximum, and normalised variogram model at the very least (for an unconditional simulation). In phase I, the parameters were directly taken from the VGT imagery. Therefore, an experimental variogram was computed for each study site for all spectral channels of the VGT imagery. The same imagery was used to compute the histogram and all univariate image statistics providing the necessary minimum and maximum values as well as the distribution. The variogram model parameters were derived from the computed experimental variogram and automatically fitted to each channel.

The VGT imagery can be considered as the entire population for a recorded scene. Specifically, one has measured the entire extent within the area of interest. Therefore, at the scale of observation provided by the VGT sensor (and provided no atmospheric interference as in our case) all the data for the region was known. With this in mind two different conditioning scenarios were applied to generate the realisations. The first scenario used the LVM option of the SGSIM algorithm. The LVM or locally varying mean option requires a value to be assigned to every node of the simulation grid. This value represents a local average that was equal to the original VGT data and varies spatially. All simulated values were conditioned to this

data. Therefore, the same reflectance VGT value was assigned to every node where the same value would cover a region 50 x 50 nodes (figure 4.5 – left side). This area corresponds in size to the spatial resolution of a single VGT pixel. The second scenario also used the VGT image data for conditioning the realisations however only one node within a 50 x 50 node area was assigned a value (figure 4.5 – right side). This second scenario considered the single VGT value as a random variable at the 20 m spatial resolution. The goal of this approach was to minimise the conditioning influence of the VGT data on the finer spatial resolution realisations. Such a data configuration provided some conditioning information but less spatial structure than that provided by the LVM scenario.

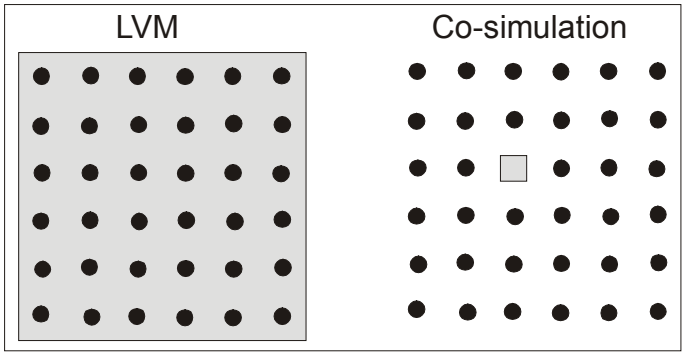

Figure 4.5 – The LVM and co-simulation node configurations. The LVM case has a background value for all the nodes that are within a single VGT pixel while the co-simulation case places the VGT pixel value as a central node within a single VGT pixel extent.

4.2.2 Phase II parameters

The phase II parameters were a modification of phase I parameters. The modifications were based on the idea that parameters approximated to the wanted fine spatial resolution would generate an image with similar global statistics. One of the most important required parameters, the variogram, can be derived from the coarse spatial resolution image data by determining the model for the punctual variogram (Clark 1977, Atkinson and Curran 1995, Collins and Woodcock 1996). For validation purposes, the punctual variogram was considered to be equal to that based on the HRVIR imagery. The hypothesis behind using the punctual variogram as opposed to the regularised variogram was that punctual variogram would introduce greater spatial variability into the generated finer spatial resolution imagery which was an expectation when down-scaling occurs.

The realisations based on phase II parameters also used both the LVM and co-simulation SGSIM options and were also conditioned to the VGT imagery. The parameters that were adjusted to try and match those of the HRVIR scale of observation were the minimum, maximum and model variogram. However, the distribution was still based on the VGT imagery.

4.2.3 Phase III parameters

The addition of RADARSAT-1 imagery to integrate location information into the simulation process distinguished the phase III parameters. The phase III base parameters were equivalent to those of phase II, i.e. minimum, maximum, variogram

model, etc. The realisations were again conditioned by the coarse spatial resolution VGT imagery.

In this final attempt only co-simulation was used with the SAR data because no available SGSIM algorithms were able to simultaneously run both co-simulation (to integrate the SAR data) and LVM. The SAR data was co-simulated with the visible channel of each study site with the strongest correlation to generate the finer spatial resolution imagery.

4.3 Image Segmentation and Validation

Ultimately, one must extract information from the generated fine spatial resolution optical-like images. Defries and Belward (2000) call for improved analysis techniques that could help the global monitoring effort. Segmenting the generated finer spatial resolution imagery is a first step in the information extraction process.

Image segmentation is carried out to determine, based on spectral characteristics, the kinds of objects that can be separated. Spectral objects are entities in channel space (i.e. red, NIR and SWIR) that can be automatically delineated. The segmentation algorithm was run on all available data including the SPOT 4 HRVIR, VGT and generated image data. Automatically segmenting the imagery permitted analysis of the results in an objective manner because it was based strictly on the spectral separability rather than user input.

The K-means algorithm was chosen to perform the segmentation. A simple image segmentation algorithm was chosen because it was easy to implement in the three-dimensional feature space and it required little user intervention. The only user supplied information was the maximum number of desired clusters. For each of the study sites, the K-means algorithm was run twice: once with a maximum of 16 clusters and a second time with 10 clusters. Such a small number of clusters was chosen based on prior hands-on experience and the fact that within the coarse spatial resolution images the number of discernible land-cover objects was quite small.

The Narenda-Goldberg (Narenda and Goldberg 1977) algorithm based on multi-dimensional histograms of the spectral data was also considered as a possible automatic segmentation algorithm. However, preliminary tests showed that the large amount of segmented clusters produced by the algorithm were too difficult to interpret and to compare between images.

The final step was to validate the resulting clusters that were spectrally segmented. Validation required a base map from which ‘known’ clusters could be compared to with those derived from the original coarse spatial resolution VGT imagery and the generated finer spatial resolution optical-like imagery. The base map used was derived by segmenting the HRVIR imagery and considered as the real clusters because it was at the wanted scale of inference.

Validation of the generated images occurred in three ways. A first validation criterion was the ability to produce land-cover clusters that were comparable to

clusters based on the HRVIR imagery in spectral feature space. The second was to determine whether the total percent covered by each spectral cluster was equal to the total percent covered by the clusters computed from the HRVIR imagery which was deemed the ‘reality’. The expectation was that the generated fine spatial resolution imagery be similar to that which is observed by the HRVIR instrument. The final validation procedure compared mapped land-cover areas at both the 1:250 000 and 1:50 000 map scales to the segmentation results. The 1:250 000 data was based on the Canada Land Inventory level II UTM digital data while the 1:50 000 data was based on digitised topographic maps.

Chapter 5 – Generated Finer Spatial Resolution Images Based on Coarse Spatial Resolution Input Parameters

The first generated fine spatial resolution optical-like images were based on phase I parameters originating directly from the coarse spatial resolution VGT imagery. The computed image statistics based on the generated phase I images were very similar to those of the original VGT imagery suggesting that a change of spatial scale did not take place. The sequential simulation algorithm LVM option produced qualitatively better imagery than the co-simulation option. The results of this first attempt are provided below and figures not presented in the text can be found in the appendix.

5.1 Coarse Spatial Resolution Data Analysis

Phase I simulations required:

1. VGT imagery
2. VGT image first order statistics
3. Variogram model parameters based on the VGT imagery

5.1.1 The VGT imagery

Image summary statistics for each of the four study sites are presented below (table 5.I). The summary statistics were based on 225 samples (n = 225) because each coarse spatial resolution study site image covered a total area of 15 x 15 pixels.

In general the four study sites could be easily differentiated from each other based on their summary statistics. The general trend seemed to be that the urban site A produced overall the lowest reflectance values. This can be due to the fact that all three other study sites had considerably more vegetation and/or had less water than at site A. Sites B and C had the highest mean and median values for both the red and SWIR channels (channels 2 and 4). The NIR channel with the highest mean and median values was found in the site D image. The maximum values for each channel were distributed between the three sites B, C and D. It was not a surprise that all the minimum values computed for the entire data set were found on the site A image (table 5.I). The standard deviation was presented along with the coefficient of variation statistic to measure the variability of the different images. Overall data variability was greatest on the urban site A image. This was most likely due to spectral heterogeneity found within the urban landscape at study site A. However the general trend across all study sites was that channel 2 (red) was the most variable. The differences in mean and median statistics were also fairly small for sites B through D (table 5.I).

The correlation statistic was also computed between all pairs of channels for each study site (table 5.II). The correlation information was essential for the co-simulating algorithm when generating the spectral bands. Most channel combinations provided a fairly strong correlation. The urban study site A exhibited strong positive correlation between all of the spectral channels. Sites B through D exhibited a negative correlation between channels 2 and 3 with site C having the strongest (-0.74) and site B the weakest (-0.05). The strongest correlation values were computed

between channels 2 and 4 for all study sites. Although the rank correlation coefficient was computed for all pairs of channels, the results were not presented for two reasons: a) the co-simulation algorithm cannot use rank correlation values due to the data transformation and b) the rank correlation generally showed weaker relationships most likely caused by the loss of information in computing the statistic.

Table 5.I – Summary statistics for study sites A through D (n = 225). All statistics except the coefficient of variation are in reflectance units (percent).

		Mean	Median	max	min	Std dev	coef var
Site A	Channel 2	5.68	6.25	8.05	0.40	1.92	34%
	Channel 3	5.55	5.95	8.65	0.80	1.69	31%
	Channel 4	5.83	6.55	8.00	0.45	1.82	31%
Site B	Channel 2	7.87	8.10	11.50	1.80	1.74	22%
	Channel 3	7.74	7.85	9.60	3.30	0.87	11%
	Channel 4	8.70	8.95	10.75	2.15	1.18	14%
Site C	Channel 2	7.09	7.40	11.00	2.10	2.09	29%
	Channel 3	8.62	8.60	10.75	6.70	0.85	10%
	Channel 4	8.70	8.80	11.60	6.20	1.06	12%
Site D	Channel 2	5.32	5.35	9.95	2.55	1.49	28%
	Channel 3	9.16	9.25	10.95	6.90	0.79	9%
	Channel 4	7.88	7.85	9.55	5.10	0.84	11%

Table 5.II also presents the results of a t-test computed on the correlation coefficients. All but the site B channel 2 vs. channel 3 correlation coefficients rejected the null hypothesis (i.e. the correlation was not different than zero). The presence of strong correlation indicates that in general there is redundancy of information between all channels. The site B channel 2 vs. channel 3 correlation of determination only explained far less than 1% of the variability between the two channels, which was also a very good indication that the two channels were independent.

Table 5.II – Computed correlation statistics between all pairs of channels for the four study sites and their statistical significance based on the t-test of a correlation coefficient.

	Channels	Correlation	90%	95%	99%
Site A	2 vs. 3	0.75	reject	Reject	reject
	2 vs. 4	0.91	reject	reject	reject
	3 vs. 4	0.93	reject	reject	reject
Site B	2 vs. 3	-0.05	cannot	cannot	cannot
	2 vs. 4	0.78	reject	reject	reject
	3 vs. 4	0.48	reject	reject	reject
Site C	2 vs. 3	-0.74	reject	reject	reject
	2 vs. 4	0.76	reject	reject	reject
	3 vs. 4	-0.26	reject	reject	reject
Site D	2 vs. 3	-0.35	reject	reject	reject
	2 vs. 4	0.71	reject	reject	reject
	3 vs. 4	0.29	reject	Reject	reject

Histograms were computed for each channel of the study sites (figures 5.1 and 5.2). Graphically the histograms also reveal that the red channel images were the most variable because they had the widest distribution. The computed standard deviation statistics provided in table 5.I also supported this fact. Overall, the shapes of the histograms appeared normally distributed except for the site A histograms. The channel 2, site A histogram revealed a large spike to the left of the distribution that was associated with the large percentage of water covering the image and thus skewed the distribution. The same phenomenon was observed in the third and fourth channels, however not as apparent because of the small area of water that was covering those images.

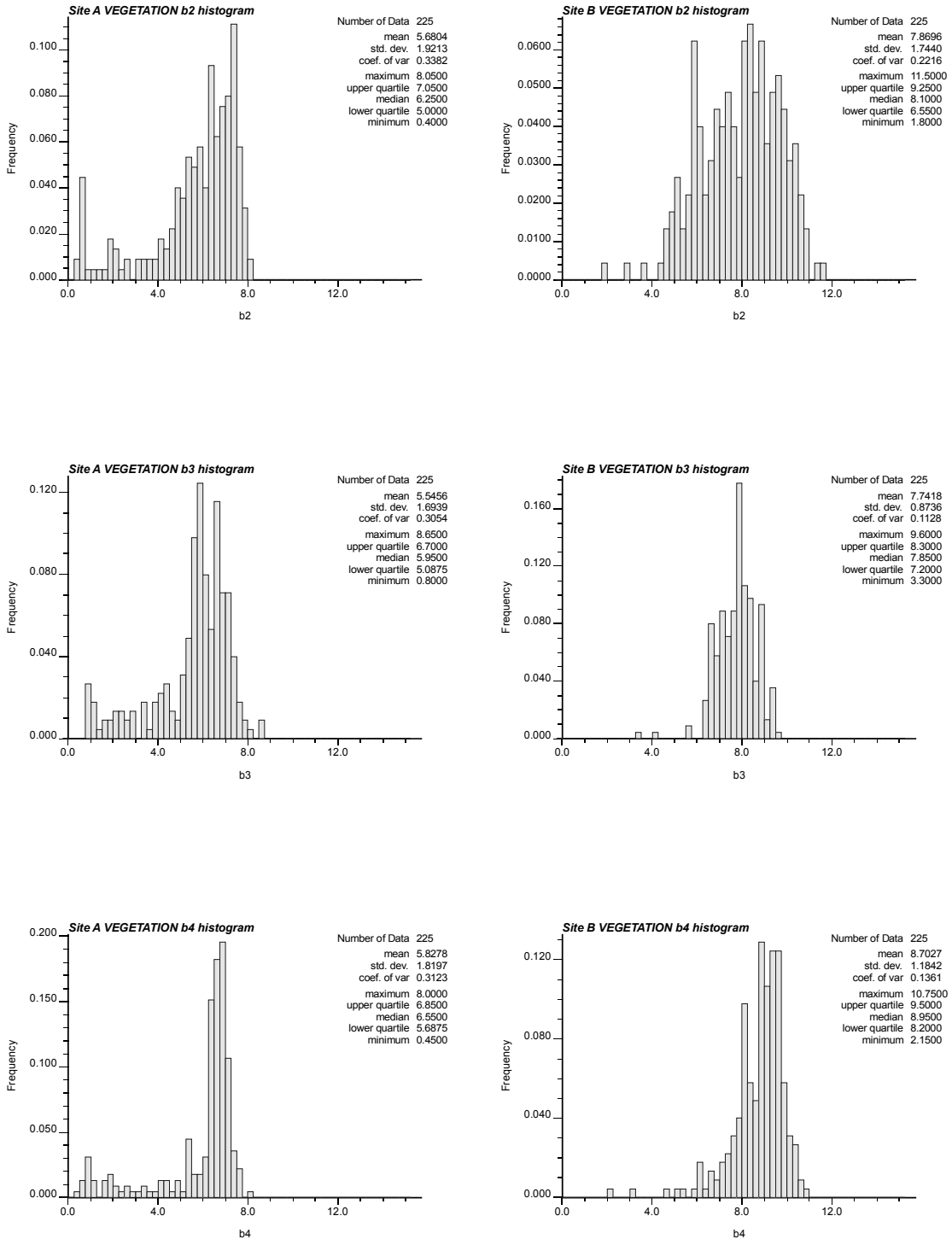

Figure 5.1 – Histograms of the study sites A (left side) and B (right side). All three spectral channels are shown for each image (from top to bottom).

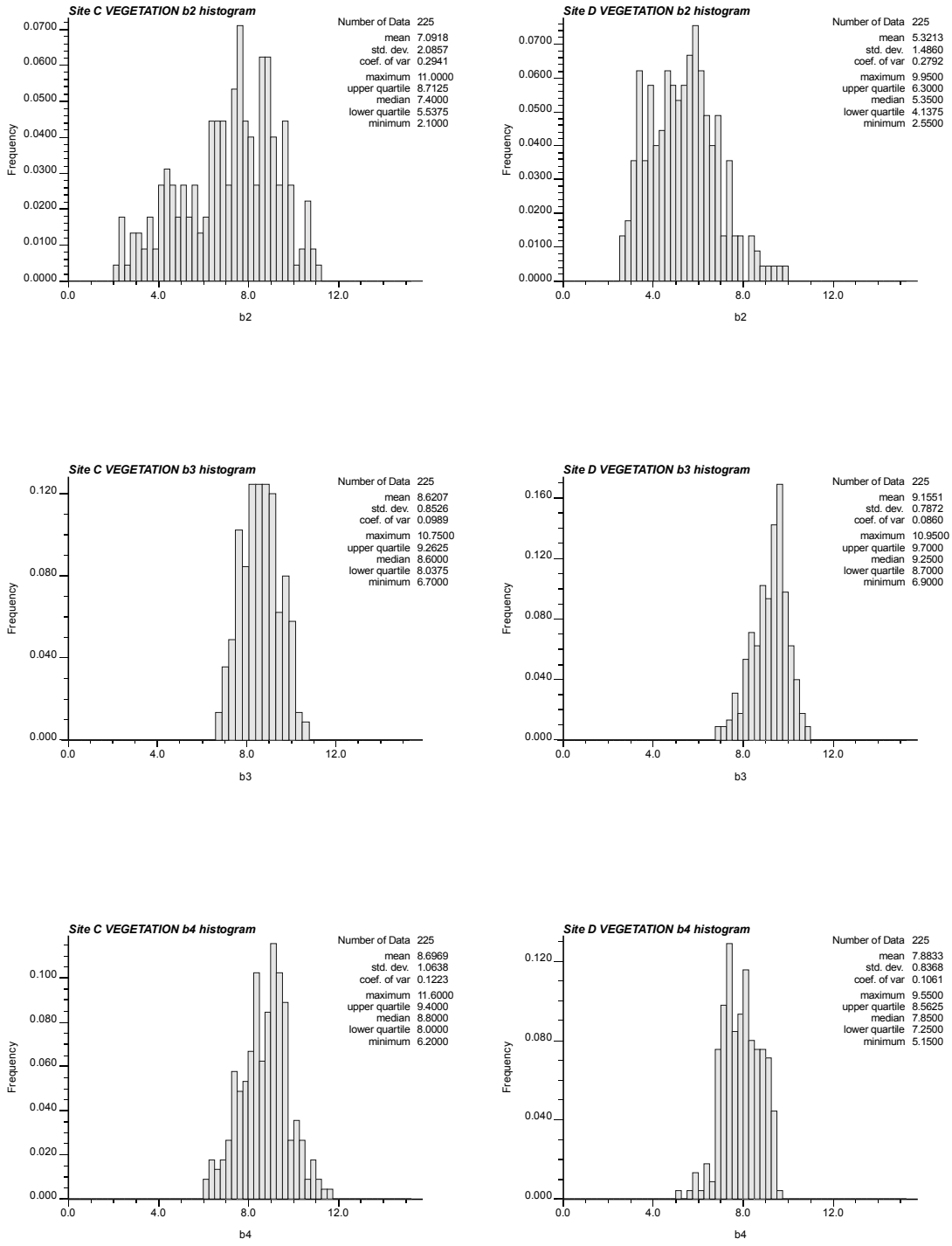

Figure 5.2 – Histograms of the study sites C (left side) and D (right side). All three spectral channels are shown for each image (from top to bottom).

5.1.2 The VGT image variogram

The experimental variogram was used to compute the spatial variability of each of the four study site images by channel. Two directional variograms (0° and 90°) and an omni-directional variogram were computed. Figure 5.3 illustrates how the variogram directions were computed.

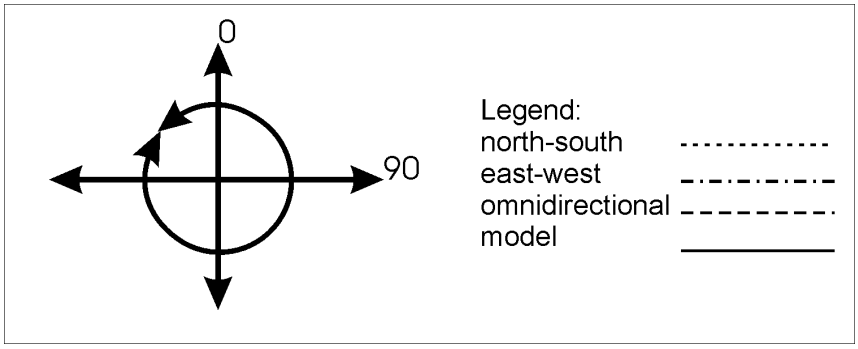

Figure 5.3 – The experimental variogram was computed for all the coarse spatial resolution images in two directions: north-south (0°) and east-west (90°), and in all directions (omni-directional variogram, circular arrow). The variogram legend is found on the right side of the figure.

The computed variograms based on the coarse spatial resolution images are presented in figures 5.4 and 5.5. Distance was computed in terms of pixels. Therefore, a single pixel is equal to a lag (distance) of 1 km. The largest lag for which the variance was computed was 10 km (over a maximum of 15 km) in order to ensure a sufficient amount of data pairs for the statistic to be viable.

In general the computed variograms derived from the coarse spatial resolution imagery could be considered anisotropic (i.e. the spatial variability depends on direction). For sites A through C, the east-west directional variograms exhibited a higher sill in all channels, while the north-south direction exhibited the highest sill for study site D. The omni-directional variograms were always found to be centred between the two directional variograms. This expected behaviour was due to the fact that the omni-directional variogram can be considered as an average of the two directional components.

The site A red channel experimental variogram (figure 5.4, top left) exhibited a small sill before continuing to increase. This was the only channel for the site A image where a sill was observed. The remaining two channels (NIR and SWIR) neither the east-west oriented nor the omni-directional variogram exhibited a definite sill. Only the north-south oriented variogram exhibited an apparent sill for the study site A (channels 3 and 4). The lack of a well defined sill for site A was most likely due to the variable nature of the urban scene. The city core was located in the lower right section of the image. The residential sections of the city were more pronounced as the distance from the core increased. This however did not include the many pockets of industrial areas that covered the entire region. Such a rich texture of land-cover was most likely the driving force behind the spatial variability still present at distances equal and more than half the image size. Thus, the idea that a spatial trend underlied the urban imagery (study site A) was dismissed because it was the nature of

the ground scene itself that caused the steady increase in variance with distance and not some underlying phenomenon.

A variogram with no apparent sill was generally not observed on the images of the other study sites. Only the channel 3 image of study site D also exhibited such behaviour. The other computed variograms (for study sites B through D) all reached a definitive sill. This indicated that pixel values at larger lags were not related.

As mentioned above, the computed 90° directional variogram sill was highest based on the images of study sites A through C compared to the 0° directional variogram sill. The anisotropy reversed for all image channels of study site D. This type of phenomenon had been previously encountered in very coarse spatial resolution image data (Bielski 1997) and was attributed to the sensor geometry rather than the ground scene itself. In order to minimize the differences due to the sensor geometry and also to simplify the modelling of the experimental variograms, the omni-directional variogram was chosen as the measure of spatial variability throughout all the study sites.

In total, 16 variogram models were adjusted automatically to the experimental variograms using Pardo-Iguzquiza's (1999) automatic fitting program (Figures 5.4 and 5.5 – solid line). The model variogram parameters are presented in table 5.III. The spherical model was fitted to all of the computed omni-directional experimental variograms.

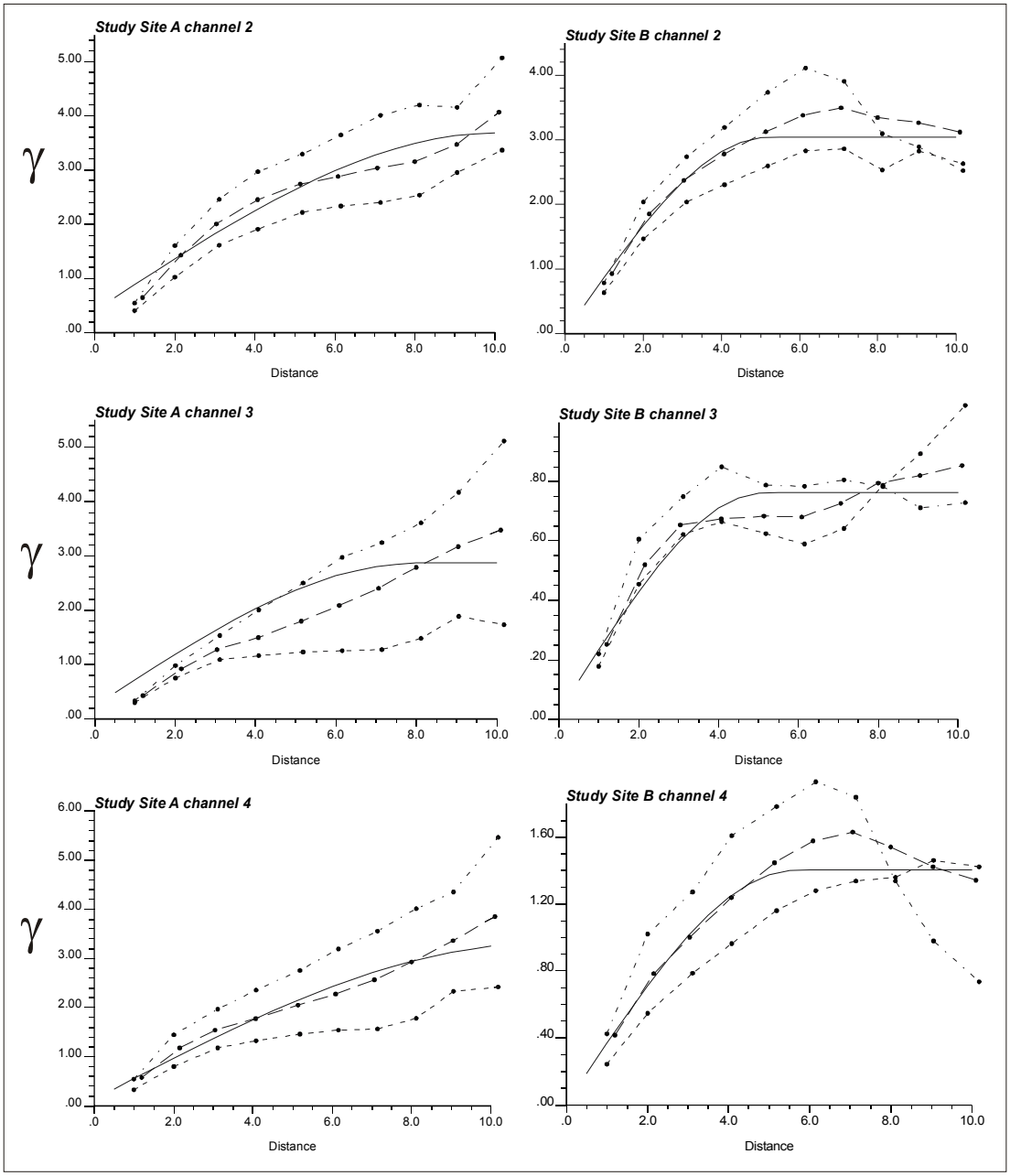

Figure 5.4 – Experimental variograms for sites A (left side) and B (right side). The variograms were computed on each channel in 2 directions (north-south and east-west) and in all directions (omni-directional variogram). Note that the abscissa scale is not constant.

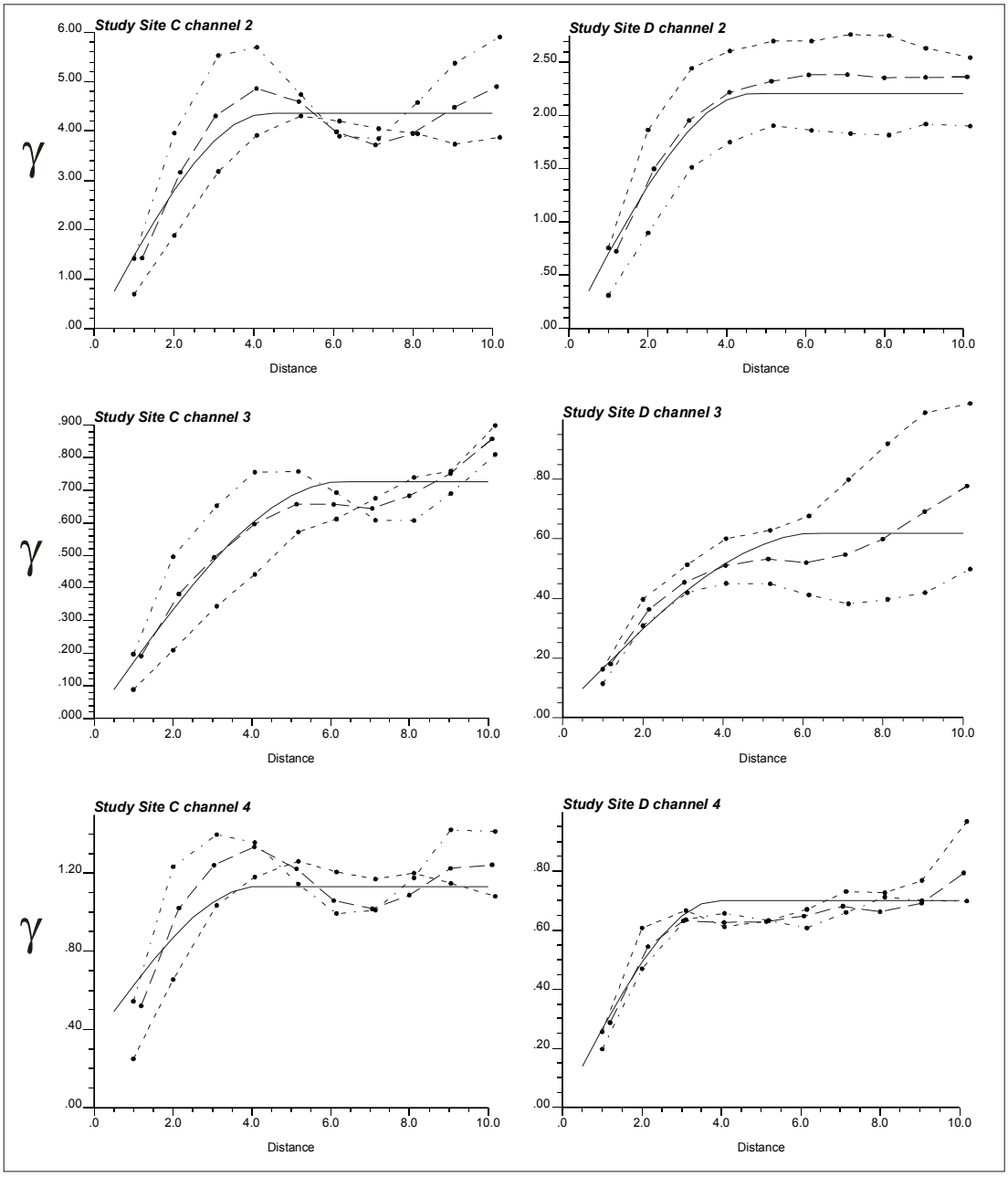

Figure 5.5 – Experimental variograms for sites C (left side) and D (right side). The variograms were computed on each channel in 2 directions (north-south and east-west) and in all directions (omni-directional variogram). Note that the abscissa scale is not constant.

Table 5.III – Variogram model parameters based on the computed omni-directional coarse spatial resolution image experimental variogram. A single spherical model was fitted automatically and the range parameter is given in km.

		Nugget	relative nugget	sill	range
Site A	Channel 2	0.40	12%	3.29	10.11
	Channel 3	0.23	9%	2.64	8.08
	Channel 4	0.14	4%	3.17	11.31
Site B	Channel 2	0.00	0%	3.04	5.20
	Channel 3	0.02	3%	0.74	5.17
	Channel 4	0.00	0%	1.40	5.68
Site C	Channel 2	0.00	0%	4.35	4.33
	Channel 3	0.00	0%	0.73	6.32
	Channel 4	0.35	45%	0.78	4.15
Site D	Channel 2	0.00	0%	2.21	4.63
	Channel 3	0.03	4%	0.59	6.35
	Channel 4	0.01	1%	0.69	3.92

The majority of the fitted variogram-model nugget parameters were very close to zero. Previous studies indicated that satellite based remotely sensed imagery tended to have low nugget values. However, a low nugget value does not provide enough information about the model variogram itself. Therefore, the relative nugget was computed which gave a better idea of the influence of the nugget effect. The relative nugget is the proportion of the nugget to the sill value. The highest relative nugget was computed for channel 4, study site C at 45%. Although this seemed pretty high, the closest relative nugget value was only 12% for channel 2 at study site A. All other relative nugget values were below 10% with almost half being less than 1%.

The largest range parameters were found at the study site A where all of the range parameters were above 8 km. For the other study sites, the highest range parameter was approximately 6.3 km, fitted to the channel three images for study

sites C and D. The lowest computed range parameter was adjusted to channel four of study site D. No trends were identified between the computed channel ranges and study sites.

The highest sill parameters were adjusted to channel 2 for all of the study sites. This was an expected result because channel 2 also consistently exhibited the largest variance. The largest difference however between the sills of individual channels was observed at sites B through D. The urban site (A) had comparable sill values ranging only between 2.6 and 3.3.

5.2 Phase I LVM Option Results

The necessary SGSIM algorithm parameters were obtained from the computed coarse spatial resolution statistics. The first stochastically generated images were based on the LVM option. The parameter file for this and for all subsequent generated images is available in the appendix. The coarse spatial resolution VGT imagery was the conditioning data. The LVM based generated finer spatial resolution images are presented in figure 5.6.

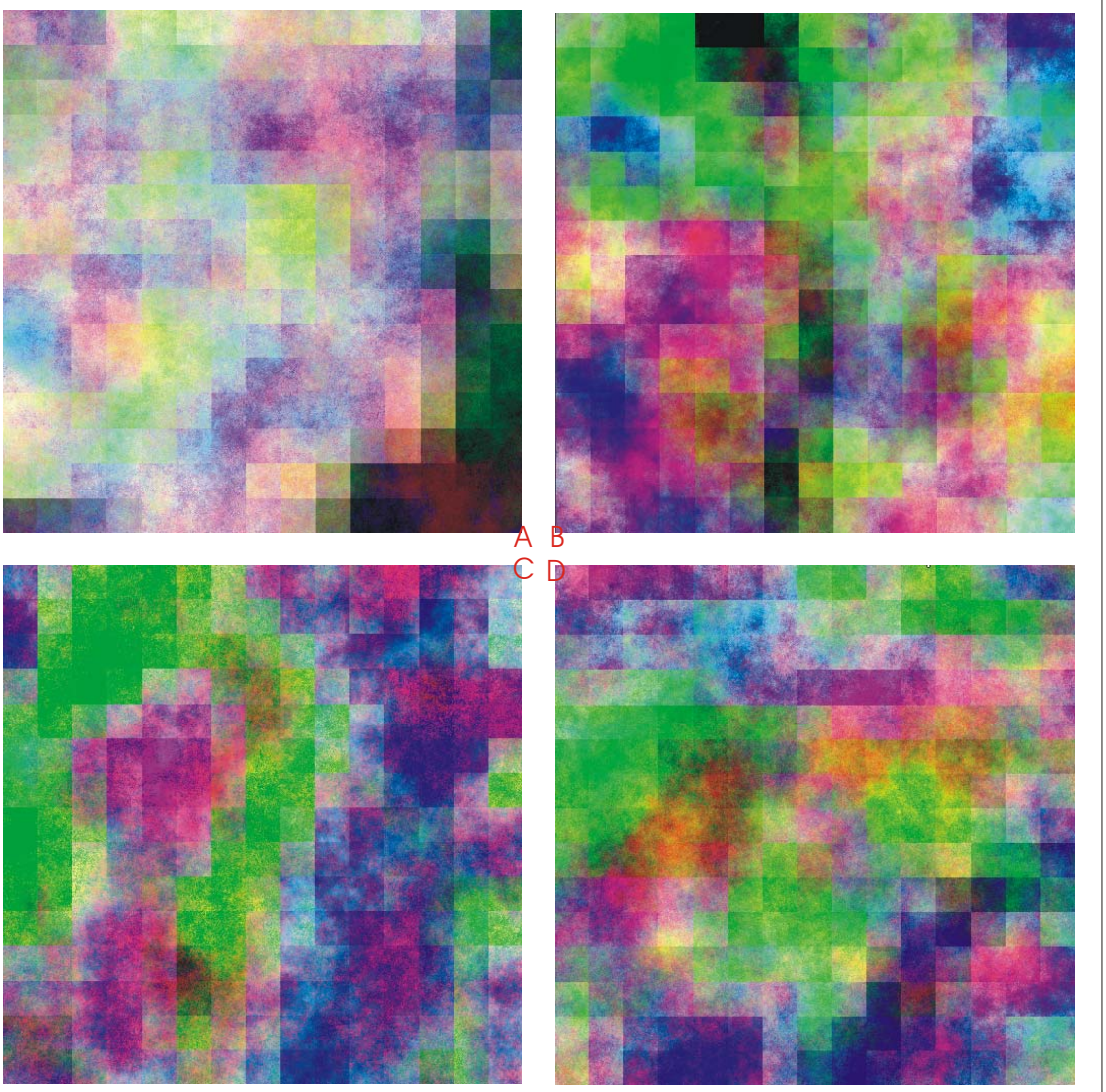

Figure 5.6 – Phase I generated finer spatial resolution images using sequential gaussian simulation and the LVM option for study sites A through D.

The generated finer spatial resolution imagery was quite fascinating because one still could distinguish the coarse spatial resolution pixel borders that conditioned the simulation and provided the local means for the 1000 x 1000 m pixel areas. The generated image colours are quite similar to those that were observed in the original

coarse spatial resolution images. The computed statistics for the generated finer spatial resolution images are provided below (tables 5.IV and 5.V).

Table 5.IV – Phase I summary statistics based on the LVM option generated finer spatial resolution imagery. All statistics except the coefficient of variation are in reflectance units (percent).

		Mean	Median	max	min	std dev	coef var
Site A	Channel 2	5.89	6.36	10.83	0.00	1.93	33%
	channel 3	5.66	6.01	10.37	0.00	1.82	32%
	channel 4	6.08	6.59	9.67	0.00	1.78	29%
Site B	channel 2	7.55	7.66	13.58	0.34	1.88	25%
	channel 3	7.72	7.77	10.93	2.06	1.09	14%
	channel 4	8.68	8.78	12.51	1.23	1.51	17%
Site C	channel 2	7.05	7.24	12.08	1.40	2.06	29%
	channel 3	8.37	8.32	12.65	4.51	1.13	14%
	channel 4	8.73	8.74	14.76	2.84	1.38	16%
Site D	channel 2	5.06	5.09	10.70	0.00	1.86	37%
	channel 3	9.11	9.13	13.18	4.95	1.09	12%
	channel 4	7.96	7.97	12.46	3.19	1.21	15%

Table 5.V – Phase I correlation statistics between channels of the generated finer spatial resolution imagery based on the LVM option.

	channels	correlation
Site A	2 vs. 3	0.64
	2 vs. 4	0.77
	3 vs. 4	0.78
Site B	2 vs. 3	-0.03
	2 vs. 4	0.49
	3 vs. 4	0.20
Site C	2 vs. 3	-0.57
	2 vs. 4	0.51
	3 vs. 4	-0.27
Site D	2 vs. 3	-0.23
	2 vs. 4	0.36
	3 vs. 4	0.04

The above computed statistics based on the generated finer spatial resolution images using the LVM option were comparable to the original VGT image statistics. The mean and median statistics (table 5.IV) were very similar (but not exact). The greatest change in the mean was 0.32 for channel 2, study site B where the mean value dropped. The change in the mean was not always negative between the original VGT data and the generated images based on the LVM option. The study site A experienced a rise in the mean that ranged between 0.11 and 0.25. All the other study sites encountered a drop in the mean except for channel 4, study sites C and D which were very small (0.03 and 0.08 respectively).

The median values (table 5.V) for the most part acted in the same manner as the changes observed with the mean. The greatest change again occurred for channel 2, study site B with a change of 0.44. The study site A median values all increased but not with the same magnitude as the mean values ranging between 0.04 and0.11. All the other study sites experienced a decrease in the median except for channel 4, study site D. An interesting trend was also observed in the magnitude of change between the mean and median values. The study site A median values had a greater magnitude of change then the mean values. This was reversed for the other study sites where the median exhibited a greater magnitude of change then the mean.

The resulting minimum and maximum values (table 5.IV) also differed from the original VGT image data. The maximum values in every case increased and the minimum values decreased for all study sites. The range of change for the maximum

value was between 3.16 and 0.75. For the minimum values the range of change was between 3.36 to 0.4.

Since there was a change in the minimum and maximum values the standard deviation statistic also differed. Comparing the differences in the coefficient of variation, the changes were overall quite small. The greatest change was 9% for channel 2 of study site D. However, all the other coefficients of variations had changes smaller than 4 % compared to the original VGT imagery.

Differences in the correlation coefficient between spectral channels of the different study site images were also observed. There was no change in sign for the correlation coefficients. The greatest change was 0.35 (channel 2 vs. 4, study site D) while the smallest change was 0.01 (channel 3 vs. 4, study site C). In all cases the correlation between channels weakened compared to the computed correlation based on the coarse spatial resolution VGT imagery. Furthermore, all these weakened correlation coefficients were statistically different from zero.

The histograms presented in figures 5.7 and 5.8 were computed from the generated images using the LVM option. These histograms were visibly smoother than their coarse spatial resolution counterparts. This was in part due to the increase in the number of data presented. Each VGT image study site was made up of only 225 pixels, while the generated images were made up of 562500 pixels. The smoothing effect caused by the increase in the number of values also seemed to mask some details that were previously apparent in the coarse spatial resolution image

computed histograms. For example, spikes in the histogram observed in channel 4 of study sites C and D were filled in. Another interesting aspect of the generated images histograms was the variability in frequencies between the coarse and finer spatial resolution images. The study site A histograms all had a peak to the left of the mean that was produced by the presence of water in the scene. For channel 2, the frequency increased for the mean values while it decreased for the water peak in the finer generated image. Whereas, channel 3 and 4 overall frequencies dropped compared to the coarse spatial resolution VGT histograms. Such changes in frequency were observed for all of the histograms. The cause of this change of frequency seemed to be linked to the manner in which histogram 'holes' were filled with the stochastic simulation algorithm. By filling these holes in the distribution, the histogram became smoother in nature and therefore changed the overall distribution of frequencies.

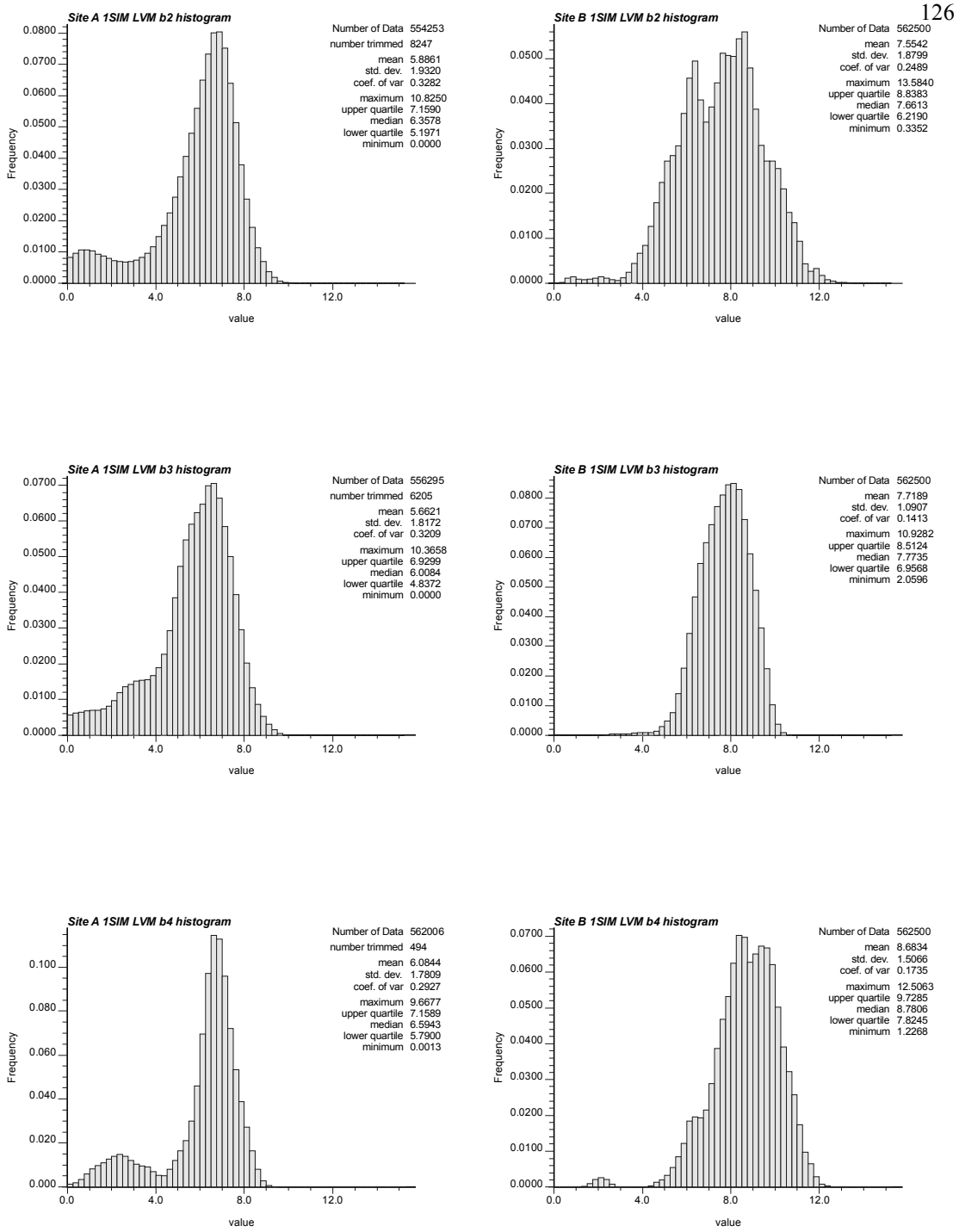

Figure 5.7 – Phase I computed histograms based on the generated finer spatial resolution imagery with the LVM option. Study sites A (left side) and B (right side) are presented with all image channels (from top to bottom).

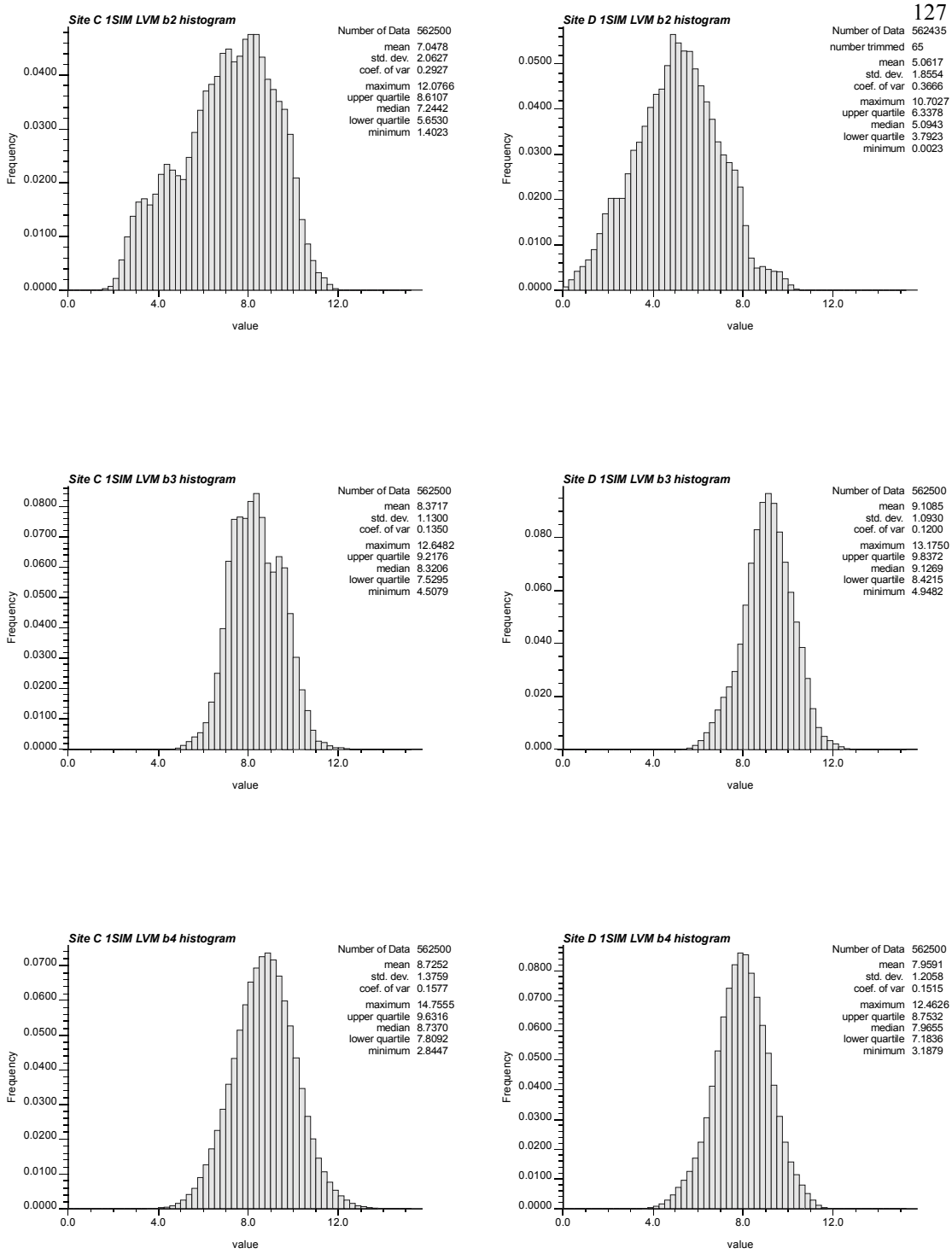

Figure 5.8 – Phase I computed histograms based on the generated finer spatial resolution imagery with the LVM option. Study sites C (left side) and D (right side) are presented with all image channels (from top to bottom).

5.3 Phase I LVM Option Results with Residual Variogram

The LVM approach was again tested this time using the variogram of residuals as the algorithm input. The variogram of residuals (figures 5.9 and 5.10) generally have a similar shape to the experimental variogram of the VGT image data. It is primarily the tail ends of the variograms that differ: the residual variograms tappered off while the experimental variograms continued to increase (e.g. Site A – channel 3).

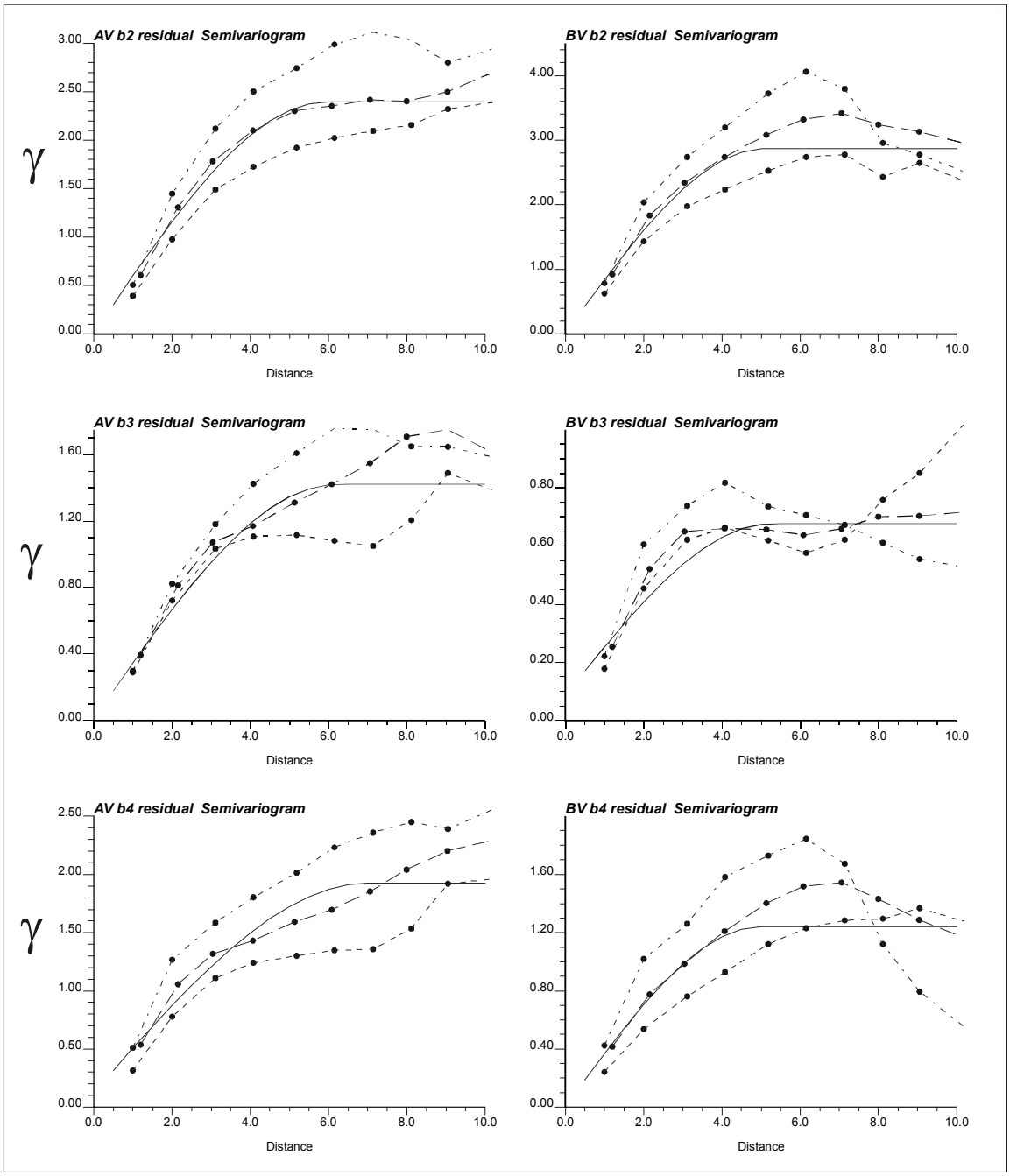

Figure 5.9 – The variograms of residuals based on the study sites A and B VGT images.

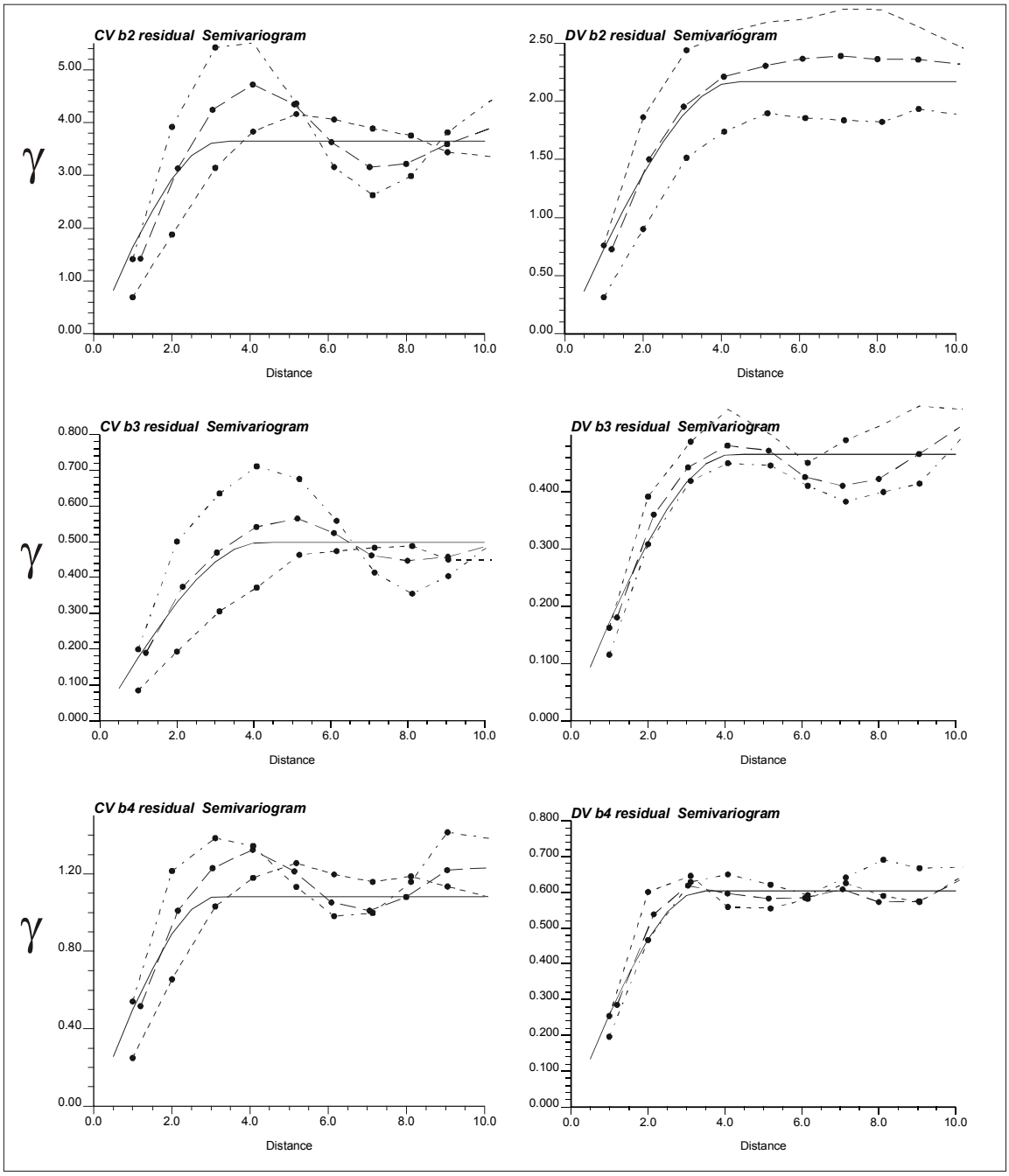

Figure 5.10 – The variograms of residuals based on the study sites C and D VGT images.

The resulting model variogram parameters did provide evidence of the differences between the experimental variogram and the variogram of residuals (Table 5.VI). Generally the nugget of the variogram of residuals was also small

compared to the sill. This is evidenced by the small relative nugget values (ranging from 0 to 15 percent). Such behaviour was also observed in the model parameters computed from the experimental variogram. The sill values were consistently lower than those of the VGT model parameters but the sill ranking order matched that of the VGT model parameters. The range parameter was quite different for the study site A images with all of the ranges of the variogram of residuals being quite a bit lower than those of the VGT data itself. The study site B on the other hand variogram of residuals range parameters were quite similar while the study sites C and D were only slightly lower.

Table 5.VI – Model parameters for the variogram of residuals.

		Nugget	Relative nugget	sill	range
Site A	Channel 2	0.0005	0%	2.3924	5.94
	Channel 3	0.0084	1%	1.4124	6.20
	Channel 4	0.1247	7%	1.8003	7.03
Site B	Channel 2	0.0059	0%	2.8640	5.10
	Channel 3	0.0864	15%	0.5903	5.25
	Channel 4	0.0013	0%	1.2404	5.00
Site C	Channel 2	0.0022	0%	3.6388	3.25
	Channel 3	0.0009	0%	0.4974	4.19
	Channel 4	0.0047	0%	1.0778	3.17
Site D	Channel 2	0.0006	0%	2.1705	4.41
	Channel 3	0.0122	3%	0.4533	4.19
	Channel 4	0.0009	0%	0.6030	3.41

With these model parameters a new set of finer spatial resolution images were generated using the VGT imagery as the locally varying mean (phase I) (figure 5.11). The resulting images were visually similar to those of the initial attempt. The reason for this similarity is twofold: a) the form of the variogram of the residuals was quite similar to that of the experimental variogram used initially and b) the locally varying

mean data was again the coarse spatial resolution VGT imagery. The distinctive blocks that are the coarse spatial resolution of the VGT imagery were again apparent.

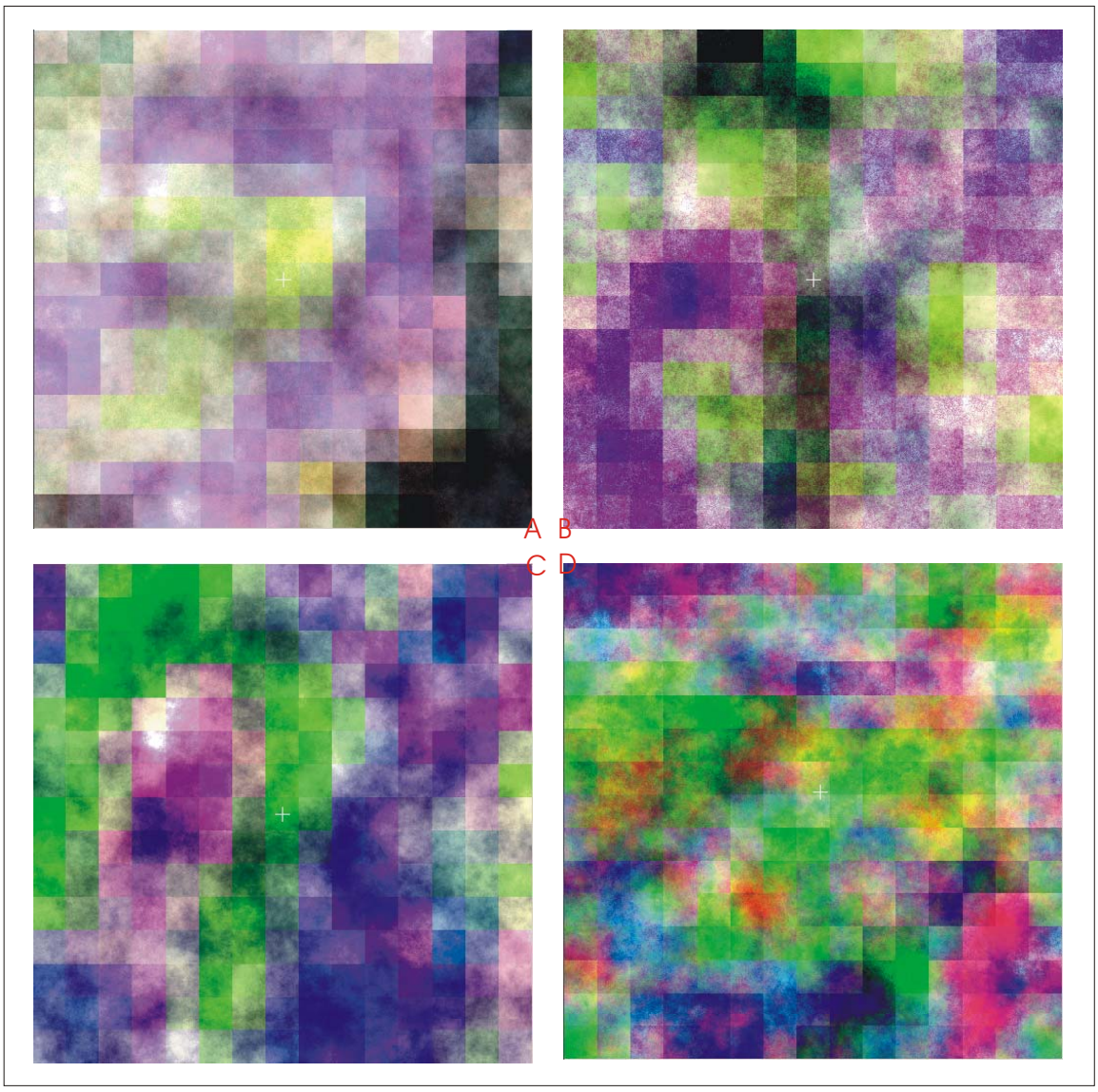

Figure 5.11 – Phase I generated finer spatial resolution images using sequential gaussian simulation and the LVM option with the variogram of residuals for study sites A through D.

Summary statistics and correlation coefficients of the generated finer spatial resolution images are presented in tables 5.VII and 5.VIII. As expected the summary statistics were quite similar to those of the original VGT imagery. Some differences were observed in the correlation coefficients of the generated imagery and those of the original VGT imagery. The study site A image correlation was almost identical to that of the VGT imagery. The study site B, channel 2 vs. 3 correlation was not negative as was observed in the VGT imagery itself, but was still quite weak while the other channel pairs had stronger computed relationships. The study site C channel 2 vs. 3 relationship remained negative however was slightly weaker. The channel 2 vs. 4 relationship was unchanged while the sign of the channel 3 vs. 4 relationship changed sign. The last study site, D, showed weakened relationships for all pairs of channels compared to the VGT data.

Table 5.VII – Phase I summary statistics based on the LVM option generated finer spatial resolution imagery.

		mean	median	Max	min	std dev
Site A	Channel 2	5.68	6.03	9.70	0.00	1.91
	Channel 3	5.55	5.80	10.55	0.00	1.79
	Channel 4	5.84	6.29	10.03	0.00	1.88
Site B	Channel 2	7.87	8.09	13.08	1.06	2.00
	Channel 3	7.76	7.81	12.39	2.00	1.31
	Channel 4	8.71	8.92	12.83	1.42	1.58
Site C	Channel 2	7.10	7.39	13.33	0.00	2.20
	Channel 3	8.63	8.64	12.80	4.79	1.23
	Channel 4	8.71	8.70	14.38	3.54	1.37
Site D	Channel 2	5.29	5.36	10.95	0.03	1.76
	Channel 3	9.31	9.37	12.96	5.40	1.10
	Channel 4	7.79	7.80	12.04	2.87	1.14

Table 5.VIII – Phase I correlation coefficients between channels of the generated finer spatial resolution imagery based on the LVM option.

	channels	correlation
Site A	2 vs. 3	0.753
	2 vs. 4	0.904
	3 vs. 4	0.928
Site B	2 vs. 3	0.287
	2 vs. 4	0.836
	3 vs. 4	0.679
Site C	2 vs. 3	-0.254
	2 vs. 4	0.765
	3 vs. 4	0.31
Site D	2 vs. 3	-0.195
	2 vs. 4	0.403
	3 vs. 4	0.117

The histograms of the generated finer spatial resolution images were also computed (appendix). Their distribution was similar to that what was computed in the original attempt (section 5.2). The similarity of the results suggests that even though the variogram of the residuals differed from that of the experimental variograms, their shape was similar enough not to make any significant differences between the generated images.

5.4 Phase I Co-Simulation Results

The finer spatial resolution images could also be generated using a co-simulation approach. The co-simulation technique requires that each variable (in this case a spectral channel) can be simulated one after another as long as it is done conditionally to the previous simulated images (Gomez-Hernandez and Journel 1993; Almeida and Journel 1994). Therefore, a channel ordering must be applied which was based on the available coarse spatial resolution VGT data. The first channel generated

was the image with the greatest spectral variability. Variability was an important concern because one does not want to limit the other simulations by starting with an image with very little variability. Since variability was also a good indicator of the amount of information, it was expected that the channel with the highest spectral variance would therefore carry the most information. The second criterion was correlation. Highly correlated channels were paired for co-simulation. Table 5.IX presents the order in which the images were generated. Channel 2 (red band) was the initial channel because the computed variability was always the highest.

Table 5.IX – Phase I spectral channel co-simulation ordering based on coarse spatial resolution VGT image data.

	Initial channel	Co-simulation	Co-simulation
Site A	2	2 vs. 4	4 vs. 3
Site B	2	2 vs. 4	4 vs. 3
Site C	2	2 vs. 3	2 vs. 4
Site D	2	2 vs. 3	2 vs. 4

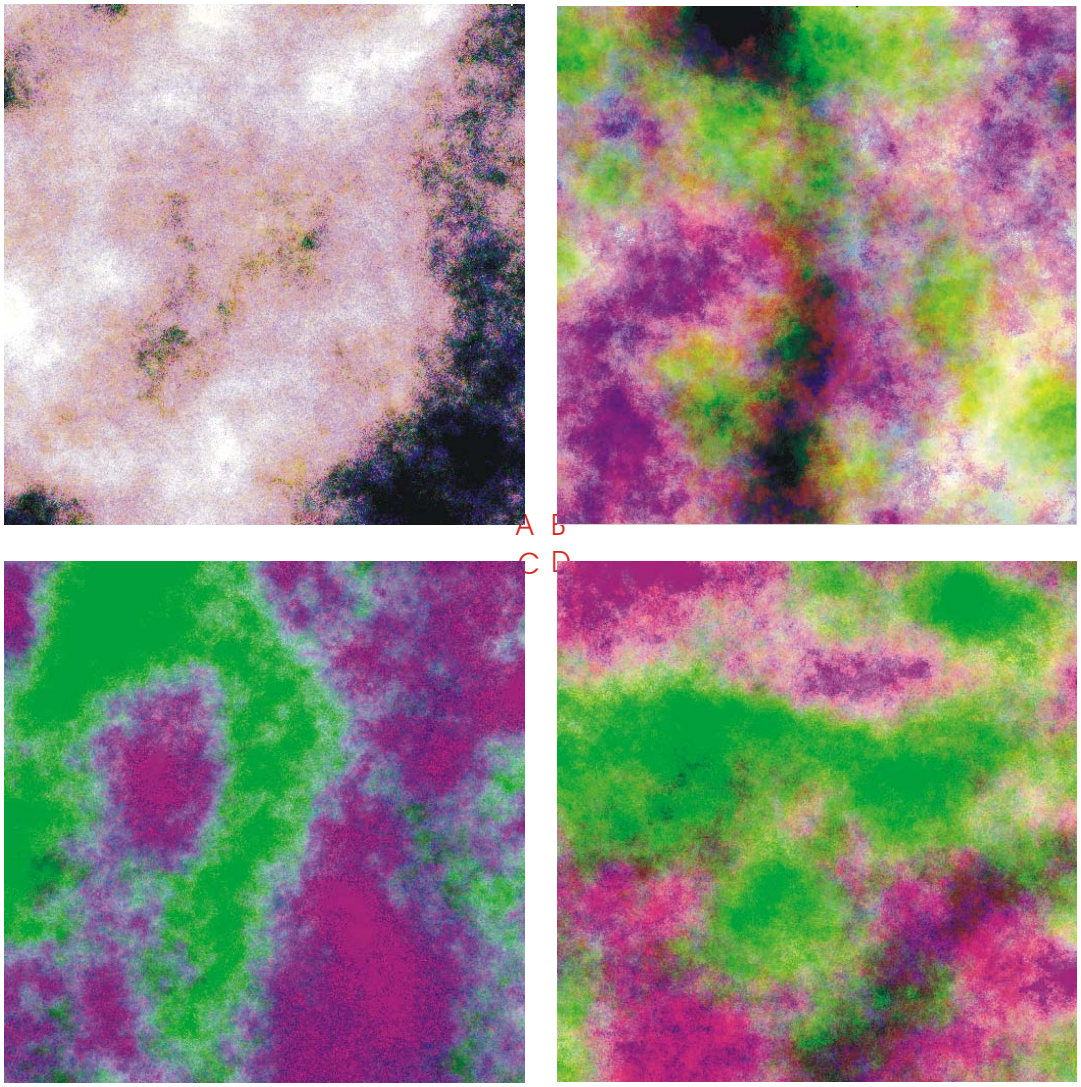

Figure 5.12 – Phase I generated finer spatial resolution images using the sequential gaussian algorithm with the co-simulation option.

Figure 5.12 presents the co-simulated finer spatial resolution imagery. These generated images lack the strong conditioning that was observed using the LVM option and resulted in very diffuse images. The summary statistics for this set of generated images are presented in table 5.X. The generated co-simulation images were very similar to the original coarse spatial resolution VGT summary statistics.

The mean value varied only slightly compared to the VGT image mean. The largest change in the mean value was only ±0.05. The median also did not vary significantly with the largest difference compared to the VGT median being only 0.10. These variations were much smaller than those found in the generated imagery using the LVM option. The maximum and minimum values also varied very little. Both measures only varied at the most by ±0.05. Therefore, it was no surprise that the variance statistics for the generated co-simulation images also did not change significantly. The greatest change in the coefficient of variation that was observed was only by 1%.

The correlation statistics also provided some insight into the generated finer spatial resolution images (table 5.XI). The observed correlation statistics increased compared to those computed directly from the VGT imagery, i.e. a stronger correlation coefficient was computed for the relationships between channels in the majority of cases. The correlation coefficient weakened only in two cases, channels 2 vs. 4 and channel 3 vs. 4 of the study site A images. Even more interesting was the fact that the sign of the relationship changed for two of the generated finer spatial resolution images, channels 2 vs. 3 for study site B and channels 3 vs. 4 for study site D. The greatest increase in magnitude was detected for the correlation between channels 3 vs. 4 at study site D.

Table 5.X – Phase I image statistics based on the co-simulation generated finer spatial resolution imagery. All statistics except the coefficient of variation are in reflectance units (percent).

		Mean	Median	max	min	std dev	coef var
Site A	Channel 2	5.68	6.31	8.05	0.40	1.94	34%
	Channel 3	5.51	5.95	8.60	0.80	1.79	33%
	Channel 4	5.83	6.55	8.00	0.45	1.85	32%
Site B	channel 2	7.83	8.10	11.50	1.80	1.73	22%
	channel 3	7.71	7.85	9.60	3.30	0.85	11%
	channel 4	8.66	8.95	10.75	2.15	1.26	15%
Site C	channel 2	7.14	7.50	11.00	2.10	1.99	28%
	channel 3	8.59	8.52	10.75	6.70	0.86	10%
	channel 4	8.70	8.80	11.60	6.20	1.32	15%
Site D	channel 2	5.27	5.22	9.95	2.55	1.45	28%
	channel 3	9.11	9.25	10.95	6.90	0.80	9%
	channel 4	7.88	7.85	9.55	5.15	0.94	12%

Table 5.XI – Phase I computed correlation coefficients based on the co-simulation generated finer spatial resolution imagery.

	channels	Correlation
Site A	2 vs. 3	0.87
	2 vs. 4	0.88
	3 vs. 4	0.92
Site B	2 vs. 3	0.26
	2 vs. 4	0.81
	3 vs. 4	0.59
Site C	2 vs. 3	-0.80
	2 vs. 4	0.88
	3 vs. 4	-0.72
Site D	2 vs. 3	-0.47
	2 vs. 4	0.89
	3 vs. 4	-0.35

For each study site, the generated spectral channel histograms are presented in figures 5.13 and 5.14. Visually comparing the co-simulation generated histograms to the original VGT image histograms showed very little difference. The peaks of the distribution were very well matched to those of the VGT data. In the tail sections of

the co-simulation derived histograms, some subtle differences were observed. Since the original VGT image data was only comprised of 225 pixels for every study site, the tails of the distributions only had a few values thereby leaving holes in some of the histograms. The co-simulated images on the other hand are made up of a many more pixels and filled in the holes in the distribution with values that had fairly small frequencies. This phenomenon was well illustrated on the study site B histograms left tail.

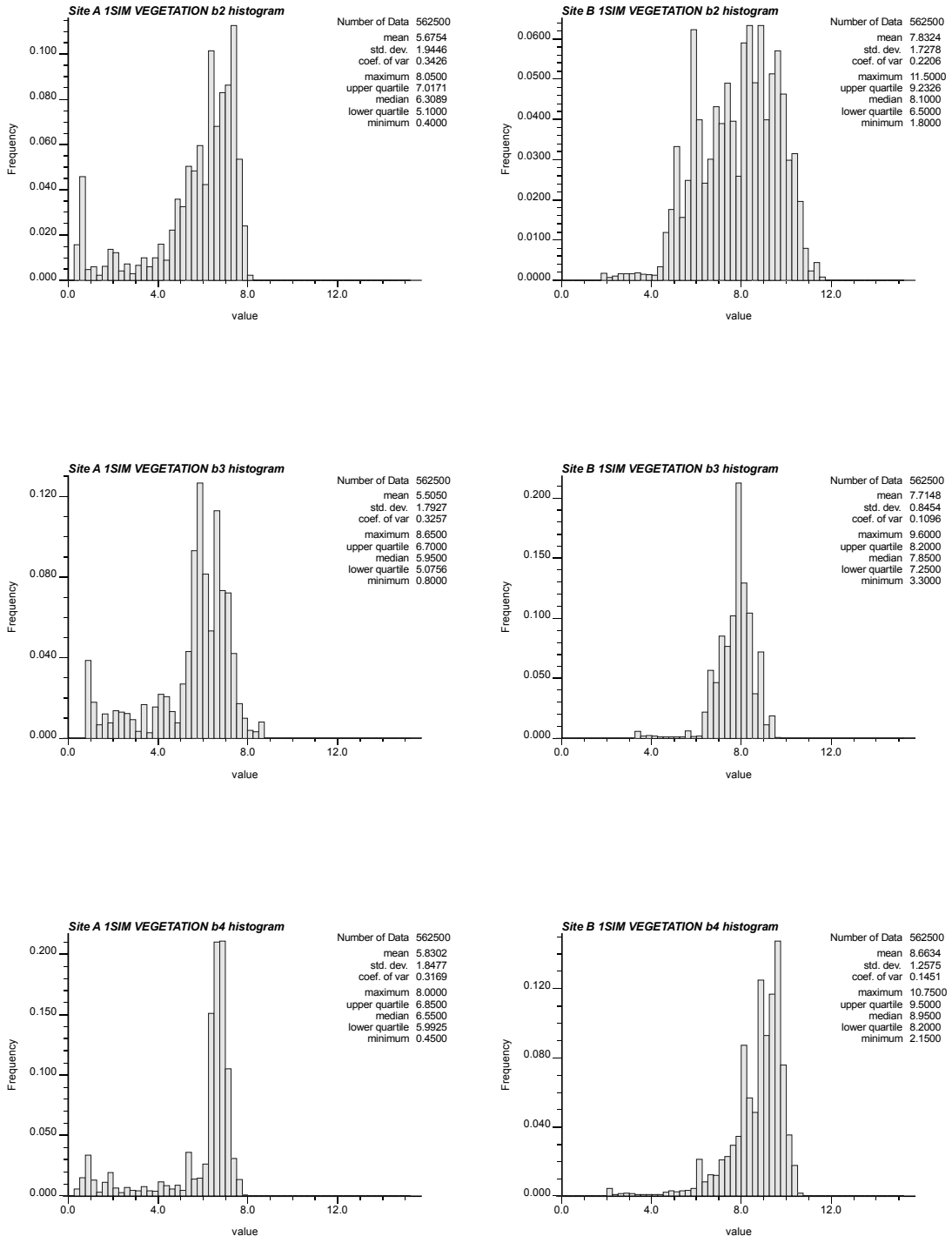

Figure 5.13 – Single realisation co-simulation histograms of the spectral channels based phase I input parameters for study sites A (left side) and B (right side).

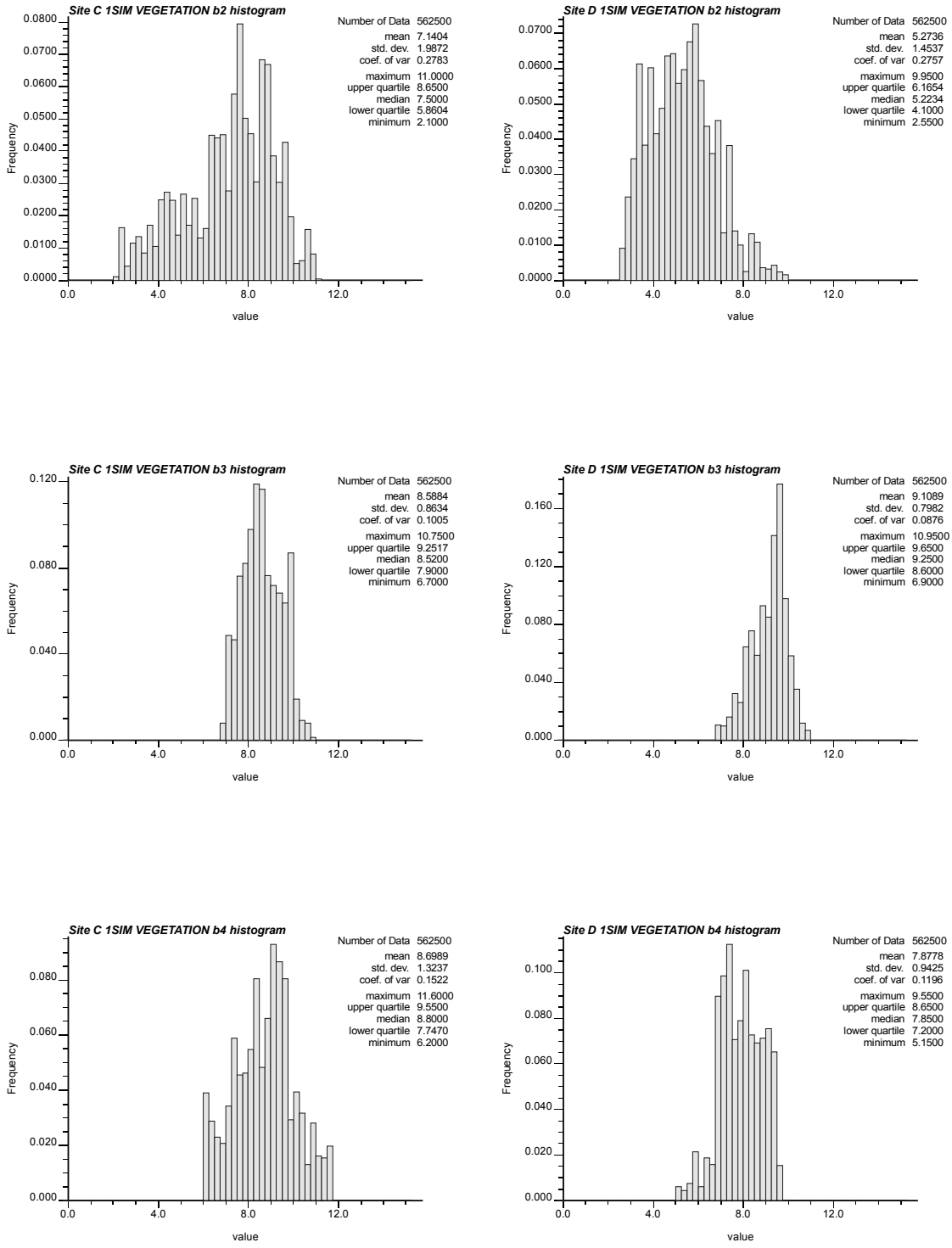

Figure 5.14 – Single realisation co-simulation histograms of the spectral channels based on phase I input parameters for study sites C (left side) and D (right side).

5.5 Results from a Series of Realisations

Using the co-simulation approach, a set of 50 realisations of each channel was generated for each study site. Due to the fact that all 50 generated images could not be examined individually because of the sheer volume of data, summary statistics were computed across all 50 realisations. Across the 50 realisations the E-type estimate, 10^{th}, 50^{th} and 90^{th} percentiles were computed and false colour composite images were produced based on these summary statistics (figures 5.15 to 5.18). The false colour images were produced with blue = channel 2 statistic, green = channel 3 statistic and red = channel 4 statistic.

Generally the images based on the statistics computed across all 50 realisations were visually similar to the co-simulation generated finer spatial resolution image (single realisation). The diffuse nature of the imagery persisted even when computing 50 realisations. However, the single realisation image did have a greater range of colours. This indicated more variability between the channels than what was seen on the images generated from 50 realisations. The observed variability in the single realisation was not present in the statistically based images because the statistical values are more likely to be similar in certain areas across the 50 realisations.

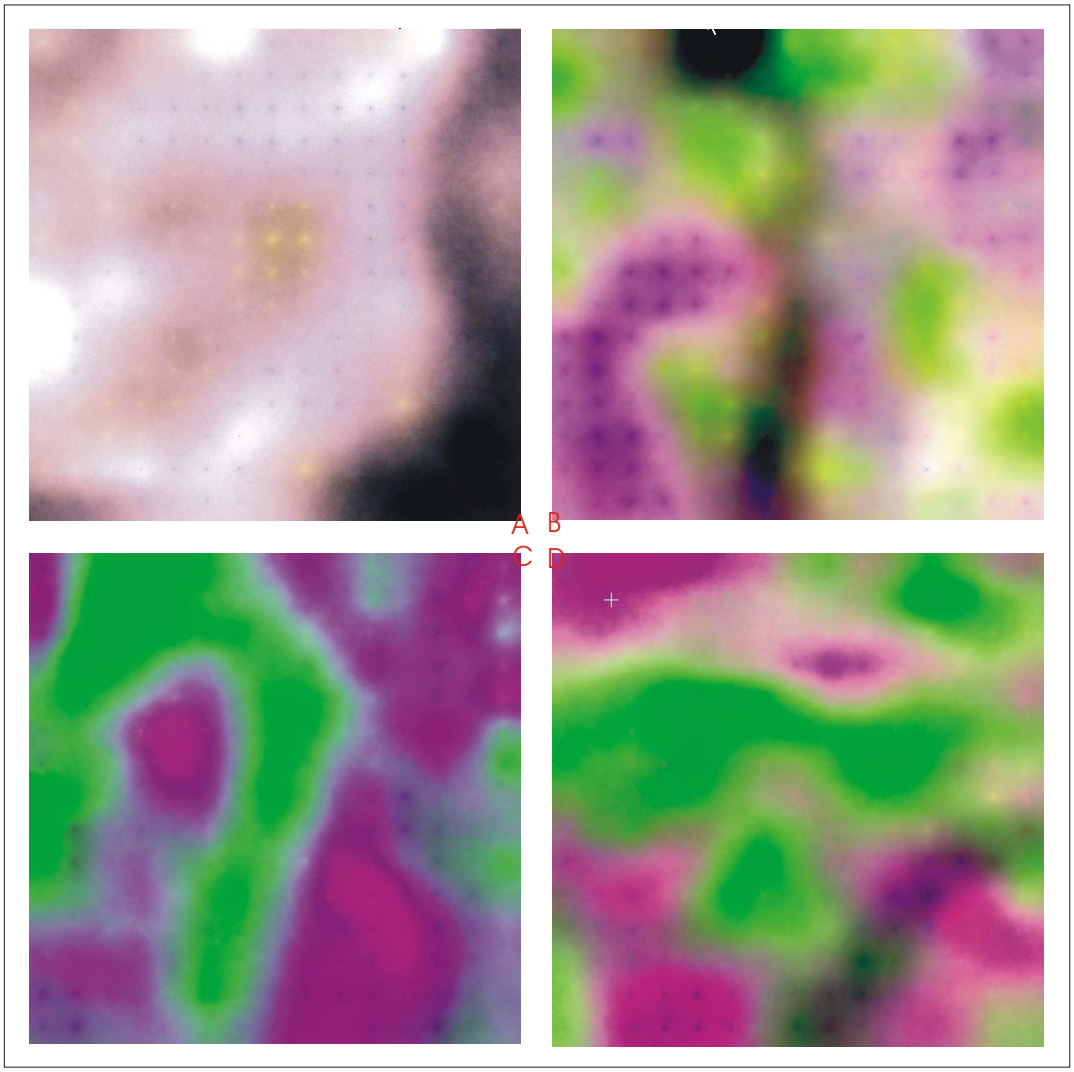

Figure 5.15 – Phase I E-type statistic presented in false colour based on 50 realisations.

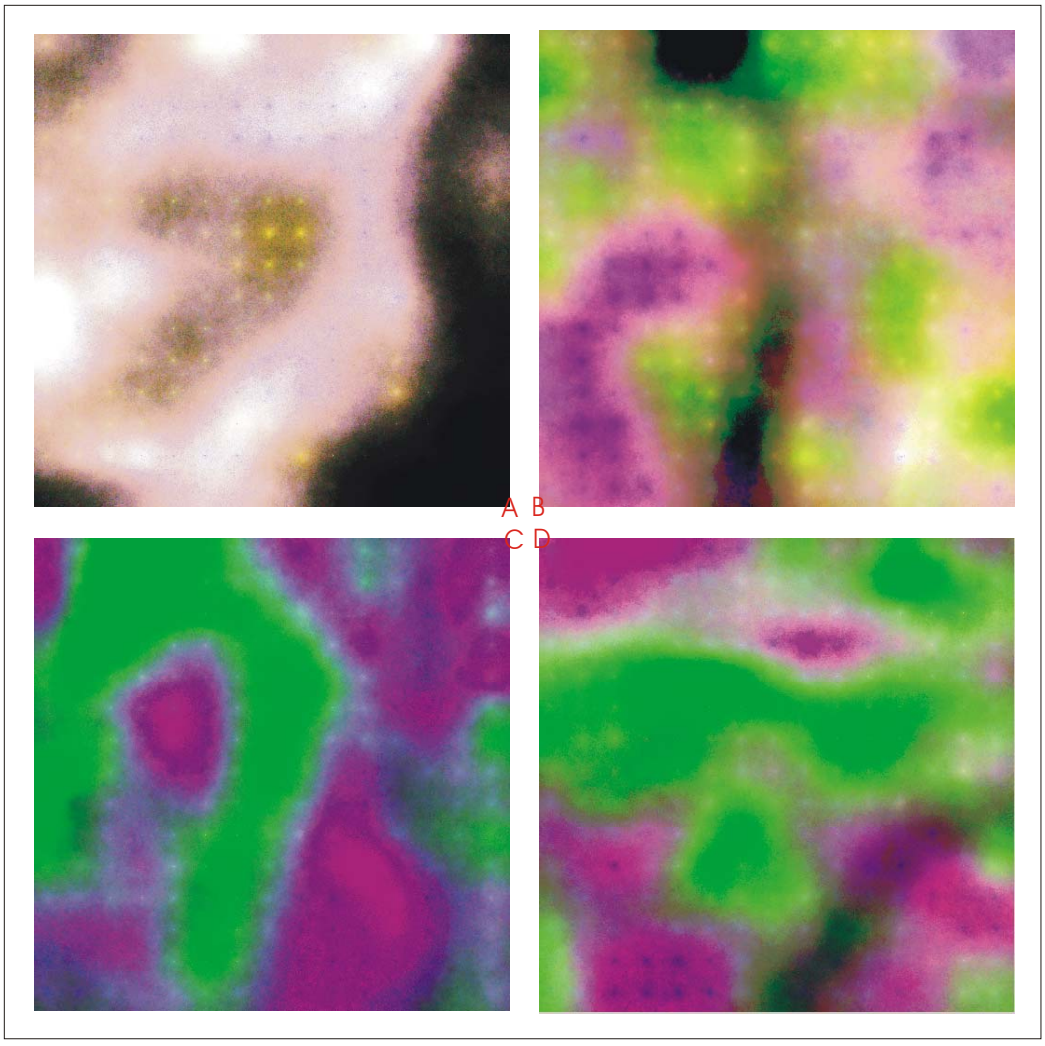

Figure 5.16 – Phase I 10th percentile statistic presented in false colour based on 50 realisations.

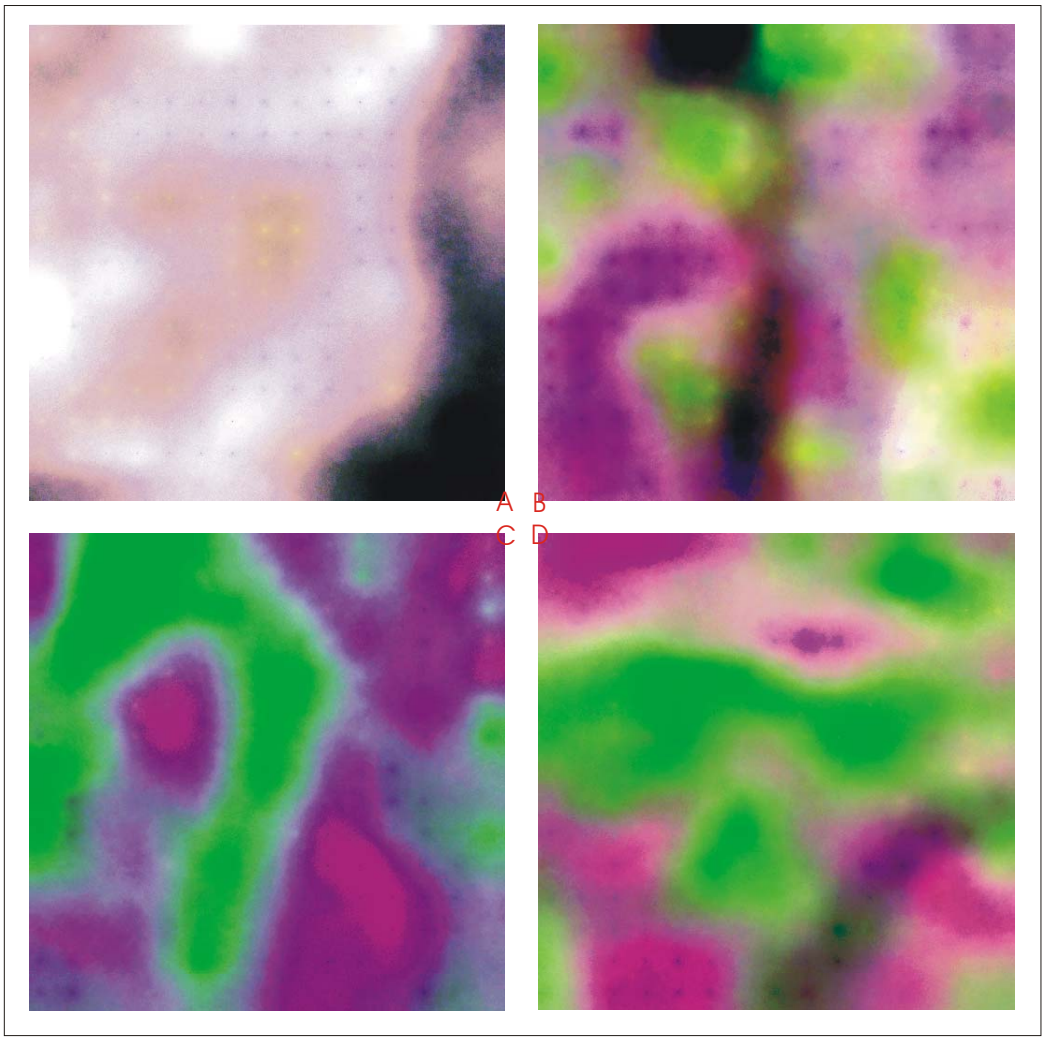

Figure 5.17 – Phase I median statistic presented in false colour based on 50 realisations.

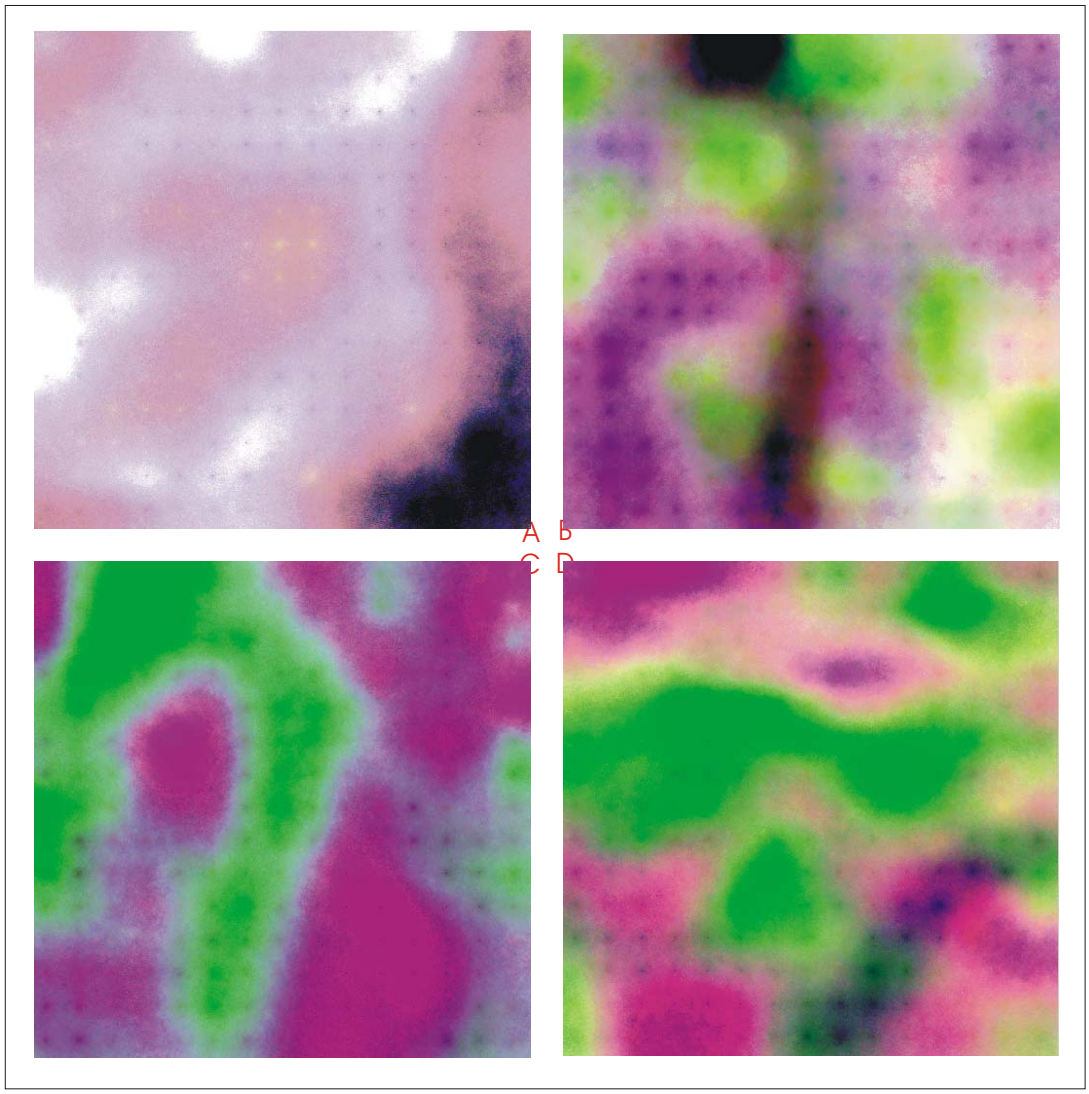

Figure 5.18 – Phase I 90th percentile statistic presented in false colour based on 50 realisations.

The statistically based generated images produced dots that are in a grid formation. This phenomenon was certainly caused by the conditioning data because

of the grid like formation of the dots. The statistically based images produced such a pattern because simulated pixels in the vicinity of these points were conditioned by the VGT data. Proximity to the conditioning data resulted in a stronger dependence that is not apparent in a single realisation (because of the random visit sequence) but was apparent over 50 realisations. Therefore over 50 realisations, any particular node in the vicinity of a conditioning node would have a distribution of values that was much less variable than pixels found further away. As such, the histogram of these nodes tended to vary less.

The computed summary statistics across the 50 realisations are presented in tables 5.XII through 5.XV with expected results. The E-type estimate computed across the 50 realisations showed overall very little change compared to the original VGT statistics. The mean of the E-type estimate varied only slightly with a maximum change of only 0.05 for channel 2 of study site D. The median varied a little more with a maximum of 0.16 for the same image. The maximum and minimum values of the distribution derived from the E-type estimate image showed no change except for the channel 4 of study site D where the minimum increased by only 0.05. However, very slight changes were observed in the coefficient of variation with the greatest change being only 4%.

The median image based on the 50 realisations also did not change statistically compared to the original VGT image data. The mean and median values for this image changed by a maximum of 0.08 and 0.13 respectively. Again, the

minimum and maximum values did not change except for channel 4 of study site D. For the median image the coefficient of variation only changed a maximum of 3%.

The 'extreme' distribution statistics differed significantly from those of the E-type estimate and mean because the results were taken from the lower and upper quantiles of the distribution. Looking at the means computed based on the 10^{th} percentile image, the values were always lower and the change varied between 0.35 (channel 3 site D) and 1.26 (channel 2 site A). All the median values were also lower than their VGT image counterparts varying between 0.20 (channel 4 site A) and 1.15 (channel 2 site A). The minimum values of the 10^{th} percentile image distribution did not vary much at all, however the maximum values decreased only in the site A image. All the other study sites did not have any change in their maximum values compared to the original course VGT image data. The variance of the distribution for these particular images did increase overall with a maximum observed at channel 2 study site A of 15%.

The final images of this set of realisations were based on the 90^{th} percentile. This set of images exhibited a general increase in the mean and median statistics except for channel 3, study site C for the median where it decreased by 0.05. The increase in the mean ranged between 0.29 and 1.03 and for the median between 0.27 and 1.06. The minimum and maximum values did not vary from those of the original VGT data except for a small change in channel 4, study site D where the minimum increased by 0.05. The coefficients of variation decreased at a maximum of 16% for channel 2 study site A.

The differences exhibited in the 10th and 90th percentile statistics compared to the coarse spatial resolution VGT image statistics were expected. The 10th percentile distribution should generally be made up of lower values than the average because the statistic comes from the lower end of the distribution. The same reasoning can be applied to the 90th percentile where higher than average mean and median values were observed because the statistic necessarily was biased towards the higher end of the distribution.

Table 5.XII – The E-type summary statistics based on 50 realisations. All statistics except the coefficient of variation are in reflectance units (percent).

E-Type		mean	Median	Max	min	std dev	coef var
Site A	Channel 2	5.64	6.16	8.05	0.40	1.69	30%
	Channel 3	5.51	5.99	8.65	0.80	1.64	30%
	Channel 4	5.84	6.55	8.00	0.45	1.68	29%
Site B	channel 2	7.86	8.02	11.50	1.80	1.57	20%
	channel 3	7.71	7.80	9.60	3.30	0.79	10%
	channel 4	8.67	8.91	10.75	2.15	1.18	14%
Site C	channel 2	7.08	7.38	11.00	2.10	1.87	26%
	channel 3	8.59	8.51	10.75	6.70	0.82	10%
	channel 4	8.70	8.74	11.60	6.20	1.12	13%
Site D	channel 2	5.27	5.19	9.95	2.55	1.33	25%
	channel 3	9.13	9.30	10.95	6.90	0.73	8%
	channel 4	7.86	7.87	9.55	5.15	0.86	11%

Table 5.XIII – The 10th percentile summary statistics based on 50 realisations. All statistics except the coefficient of variation are in reflectance units (percent).

1st quantile		mean	median	max	min	std dev	coef var
Site A	channel 2	4.42	5.10	4.42	0.40	2.17	49%
	channel 3	4.70	5.47	4.70	0.80	1.89	40%
	channel 4	5.15	6.35	5.15	0.45	2.13	41%
Site B	channel 2	7.09	7.05	11.50	1.80	1.65	23%
	channel 3	7.29	7.36	9.60	3.30	0.90	12%
	channel 4	8.24	8.51	10.75	2.15	1.41	17%
Site C	channel 2	6.07	6.40	11.00	2.10	2.00	33%
	channel 3	8.27	8.20	10.75	6.70	0.82	10%
	Channel 4	7.79	7.75	11.60	6.20	1.09	14%
Site D	Channel 2	4.59	4.41	9.95	2.55	1.24	27%
	Channel 3	8.73	8.93	10.95	6.90	0.80	9%
	Channel 4	7.34	7.28	9.55	5.15	0.93	13%

Table 5.XIV – The median summary statistics based on 50 realisations. All statistics except the coefficient of variation are in reflectance units (percent).

5th quantile		mean	median	max	min	std dev	coef var
Site A	channel 2	5.76	6.32	8.05	0.40	1.79	31%
	channel 3	5.55	5.95	8.65	0.80	1.69	31%
	channel 4	5.90	6.55	8.00	0.45	1.75	30%
Site B	channel 2	7.87	8.10	11.50	1.80	1.60	20%
	channel 3	7.72	7.85	9.60	3.30	0.80	10%
	channel 4	8.69	8.92	10.75	2.15	1.17	14%
Site C	channel 2	7.11	7.45	11.00	2.10	1.92	27%
	channel 3	8.59	8.51	10.75	6.70	0.83	10%
	channel 4	8.70	8.80	11.60	6.20	1.16	13%
Site D	channel 2	5.26	5.22	9.95	2.55	1.34	26%
	channel 3	9.13	9.32	10.95	6.90	0.74	8%
	channel 4	7.87	7.85	9.55	5.15	0.87	11%

Table 5.XV – The 90th percentile summary statistics based on 50 realisations. All statistics except the coefficient of variation are in reflectance units (percent).

9th quantile		Mean	median	max	Min	std dev	coef var
Site A	channel 2	6.71	7.09	8.05	0.40	1.24	0.18
	channel 3	6.26	6.62	8.65	0.80	1.41	0.23
	channel 4	6.43	6.82	8.00	0.45	1.34	0.21
Site B	channel 2	8.61	8.82	11.50	1.80	1.48	0.17
	channel 3	8.12	8.14	9.60	3.30	0.72	0.09
	channel 4	9.07	9.25	10.75	2.15	0.98	0.11
Site C	channel 2	8.07	8.46	11.00	2.10	1.72	0.21
	channel 3	8.91	8.55	10.75	6.70	0.82	0.09
	channel 4	9.61	9.59	11.60	6.20	1.14	0.12
Site D	channel 2	5.98	5.95	9.95	2.55	1.43	0.24
	channel 3	9.51	9.61	10.95	6.90	0.67	0.07
	channel 4	8.36	8.48	9.55	5.15	0.80	0.10

Figures 5.19 through 5.26 present the histograms computed from the generated images based on the statistics across all 50 realisations. The histograms based on the E-type statistic images all visually approximated the histograms derived from the coarse spatial resolution VGT imagery. Their appearance was much smoother in nature but was not as smooth as those produced by the images generated with the LVM option. The median images also resembled the original VGT image histograms however their frequency distribution was much higher thereby producing higher peaks than was observed in the E-type statistic images. The most notable example of this was in the left tail of the distribution for study site A, channels 2 and 3. Here the frequency of the low reflectance values was twice as high than those of the E-type estimate for channel 2.

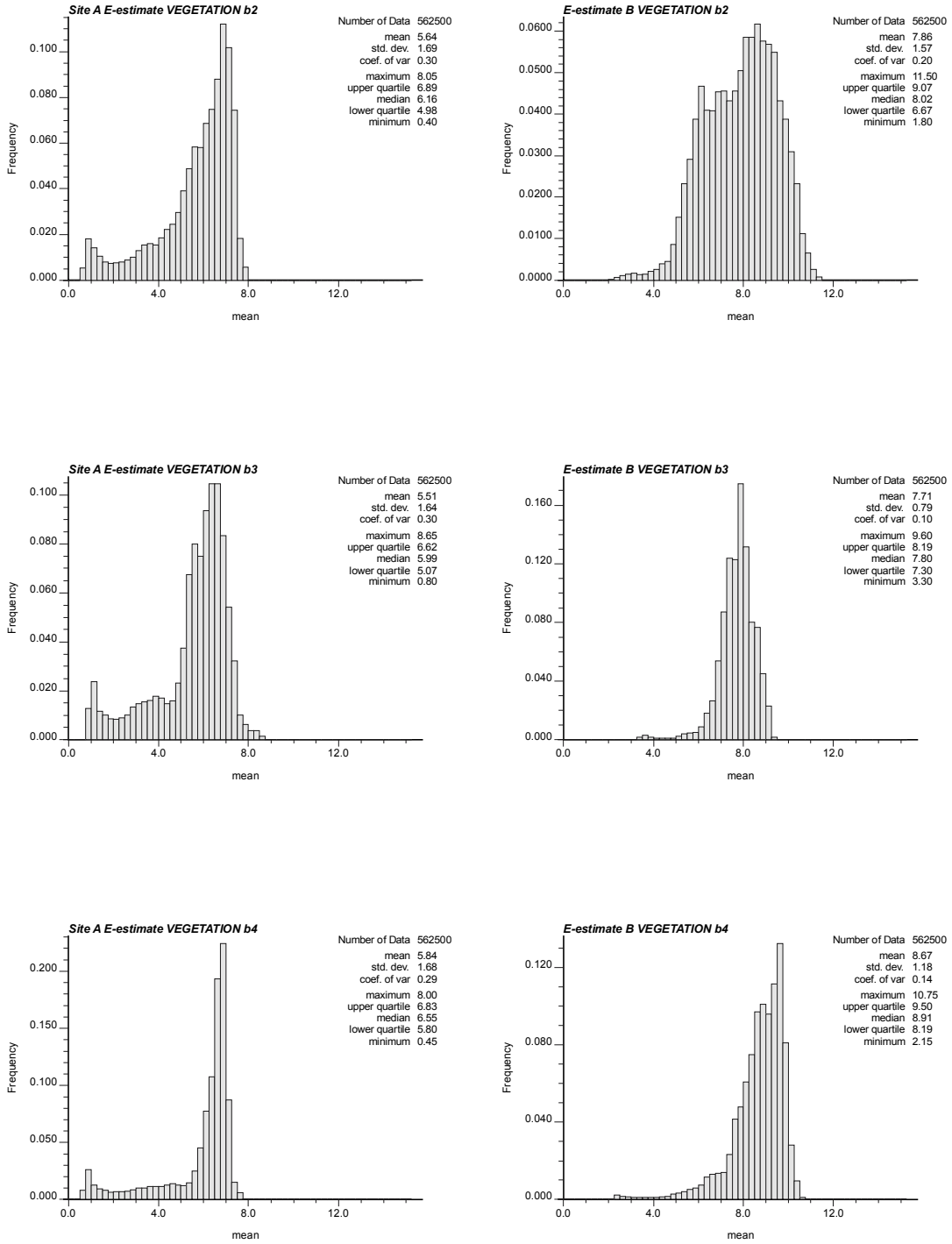

Figure 5.19 – Histograms computed from the E-type estimate images based on the set of 50 realisations for sites A (left side) and B (right side).

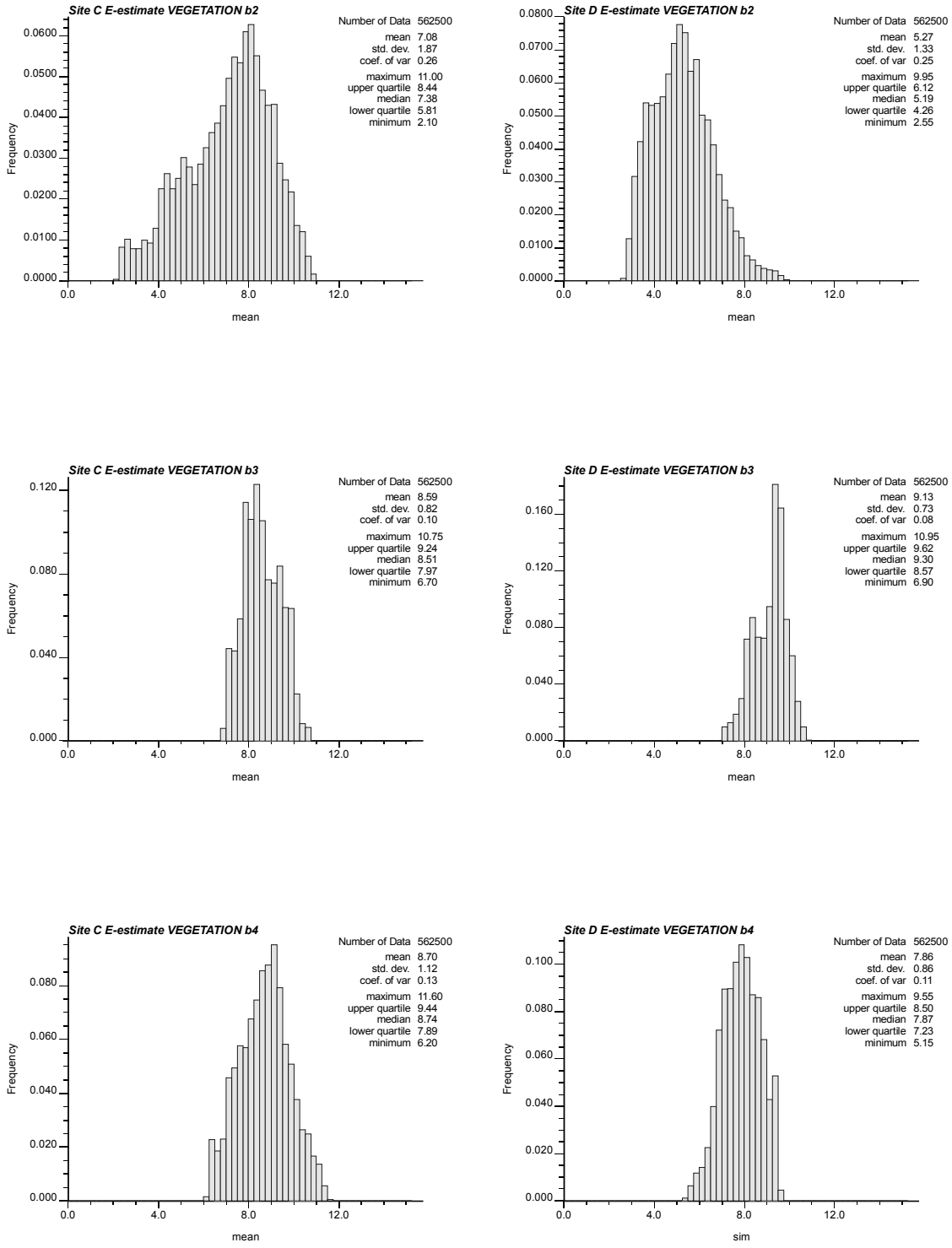

Figure 5.20 – Histograms computed from the E-type estimate images based on the set of 50 realisations for sites C (left side) and D (right side).

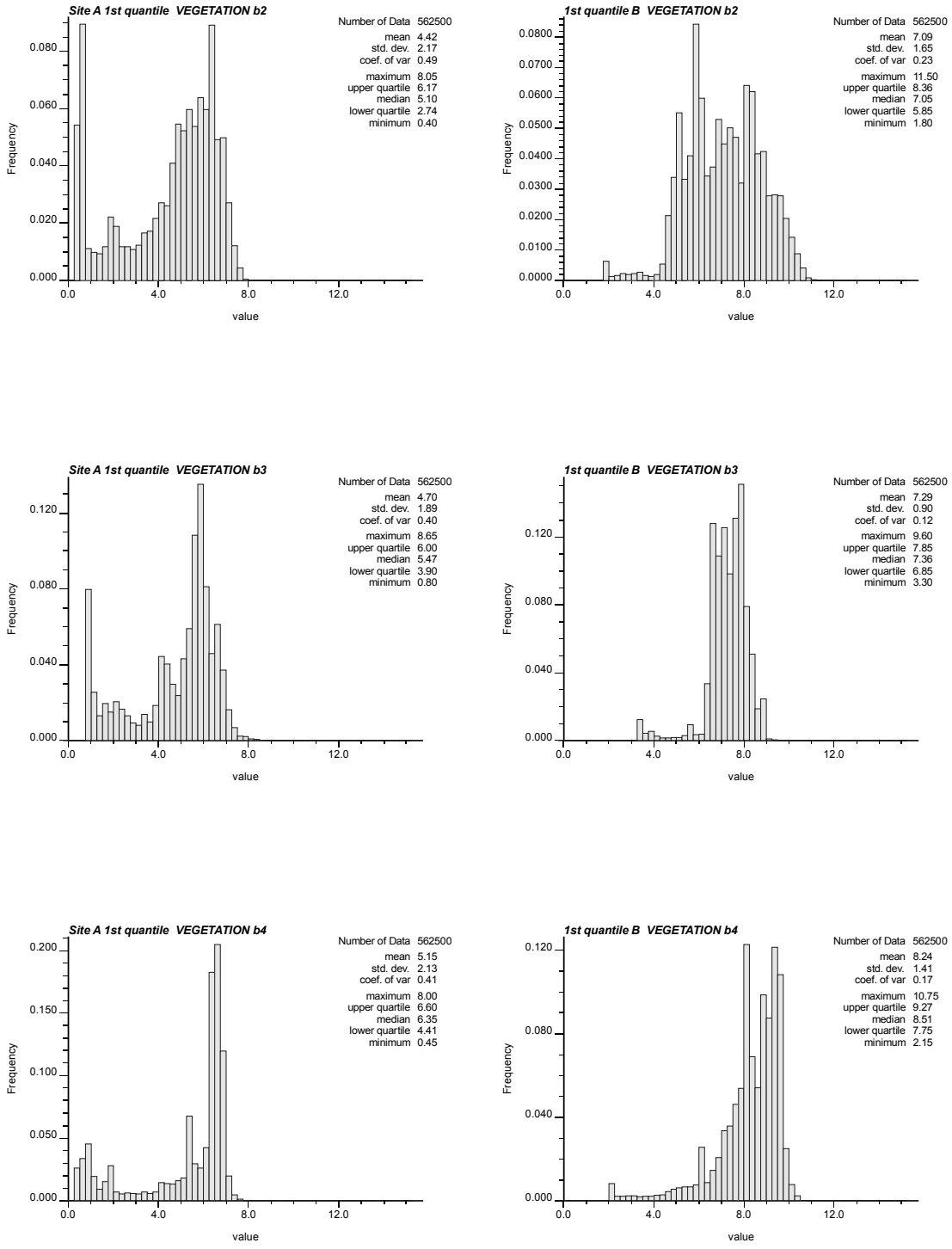

Figure 5.21 – Histograms computed from the 10th percentile images based on the set of 50 realisations for sites A (left side) and B (right side).

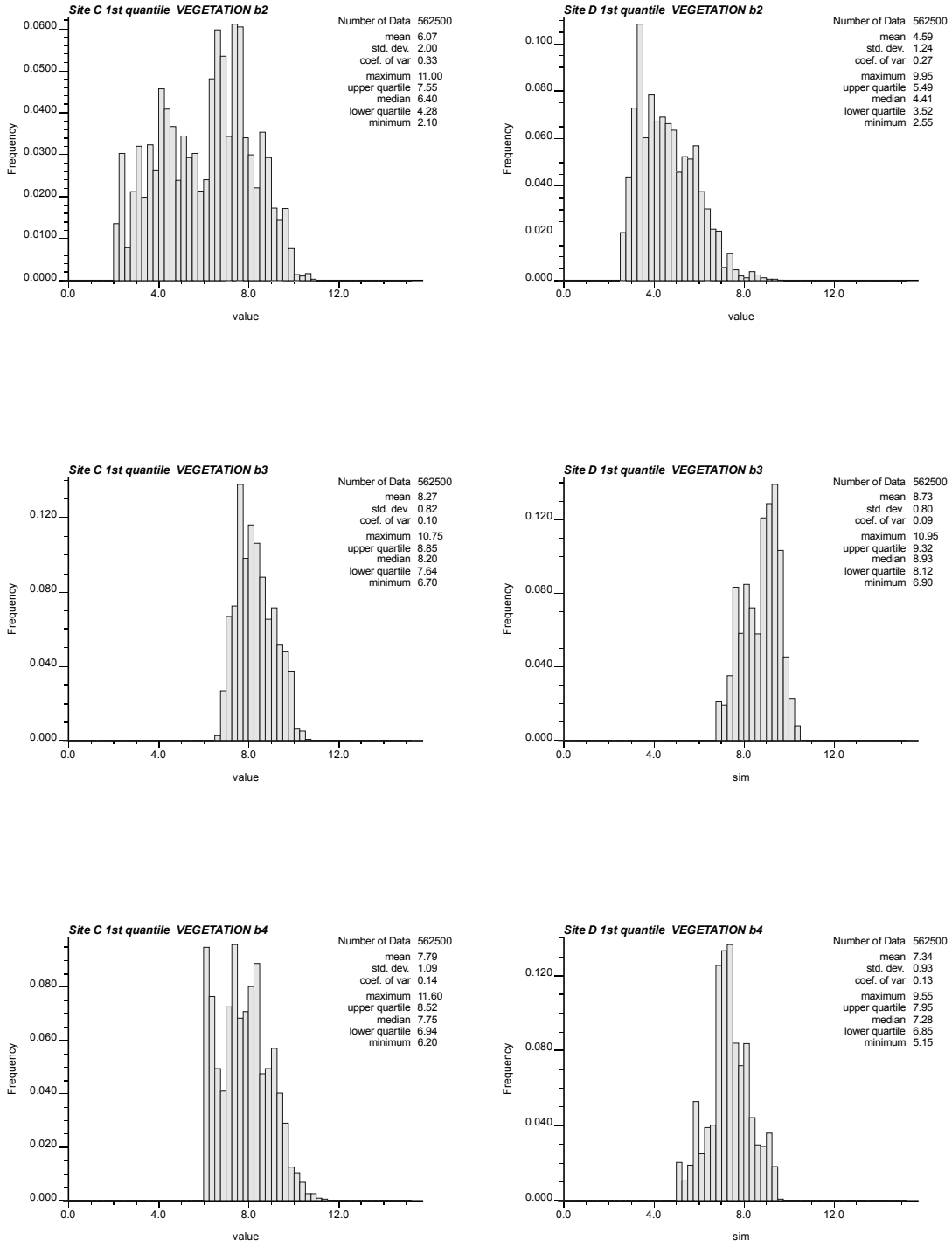

Figure 5.22 – Histograms computed from the 10th percentile images based on the set of 50 realisations for sites C (left side) and D (right side).

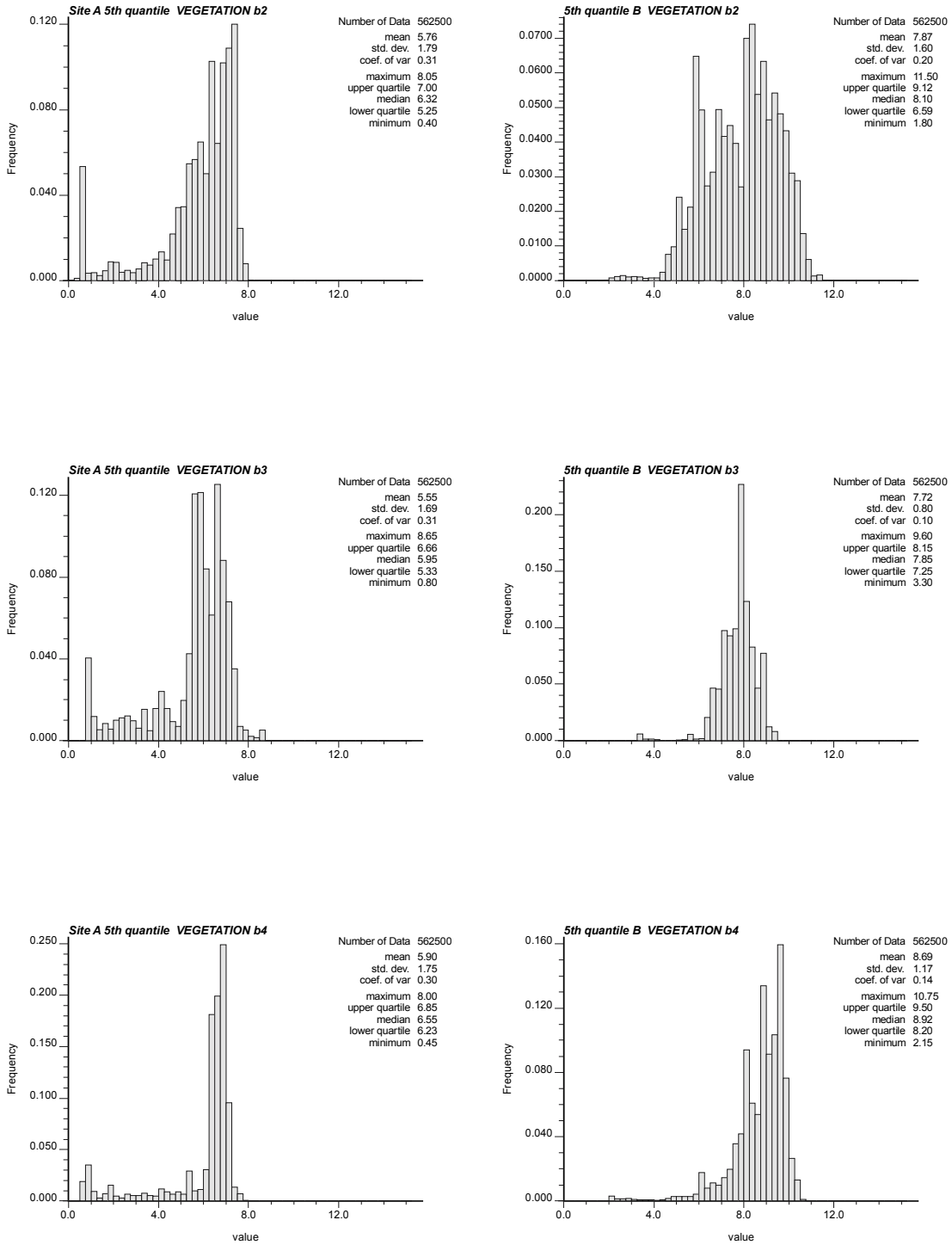

Figure 5.23 – Histograms computed from the median images based on the set of 50 realisations for sites A (left side) and B (right side).

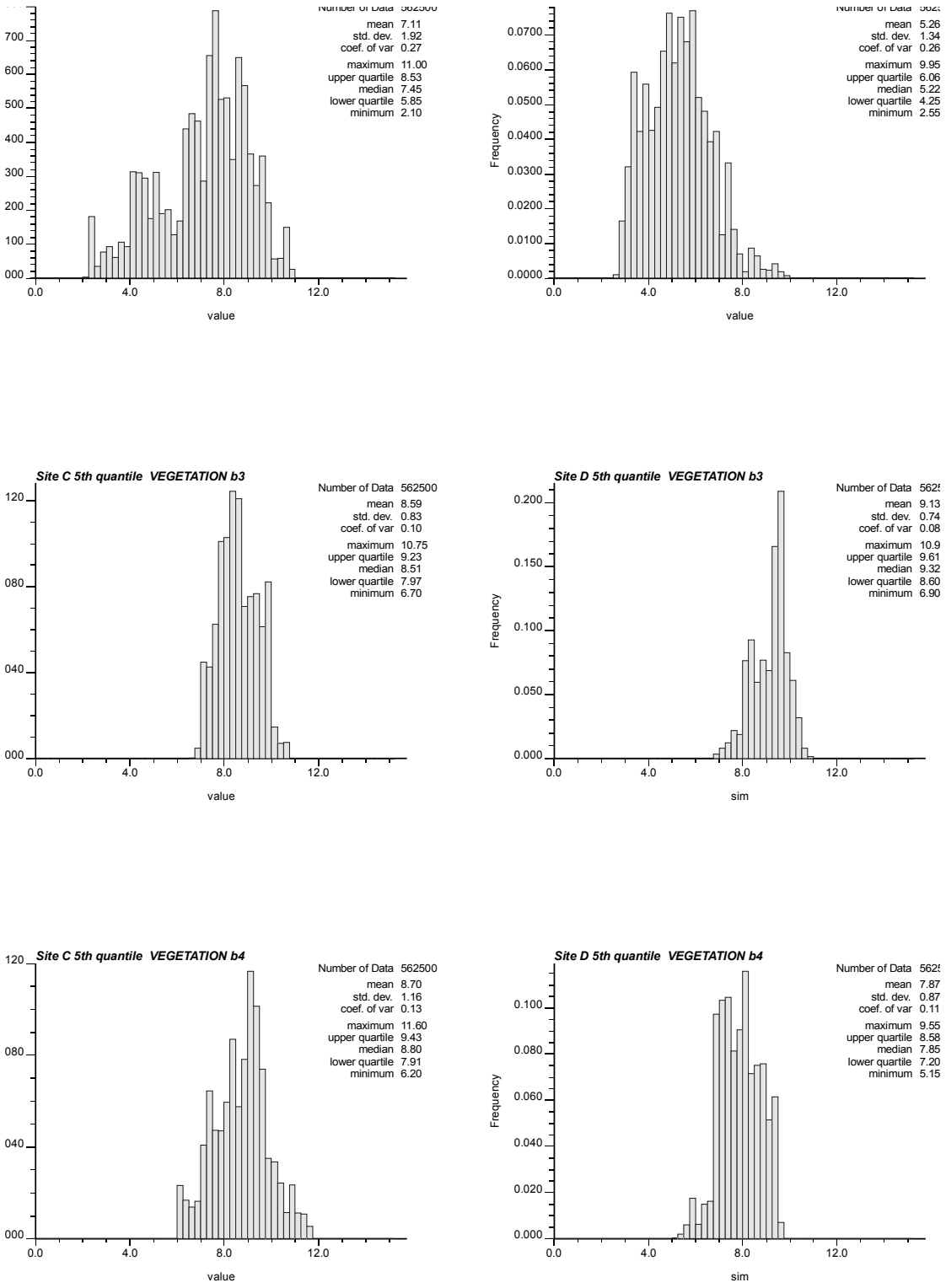

Figure 5.24 – Histograms computed from the median images based on the set of 50 realisations for sites C (left side) and D (right side).

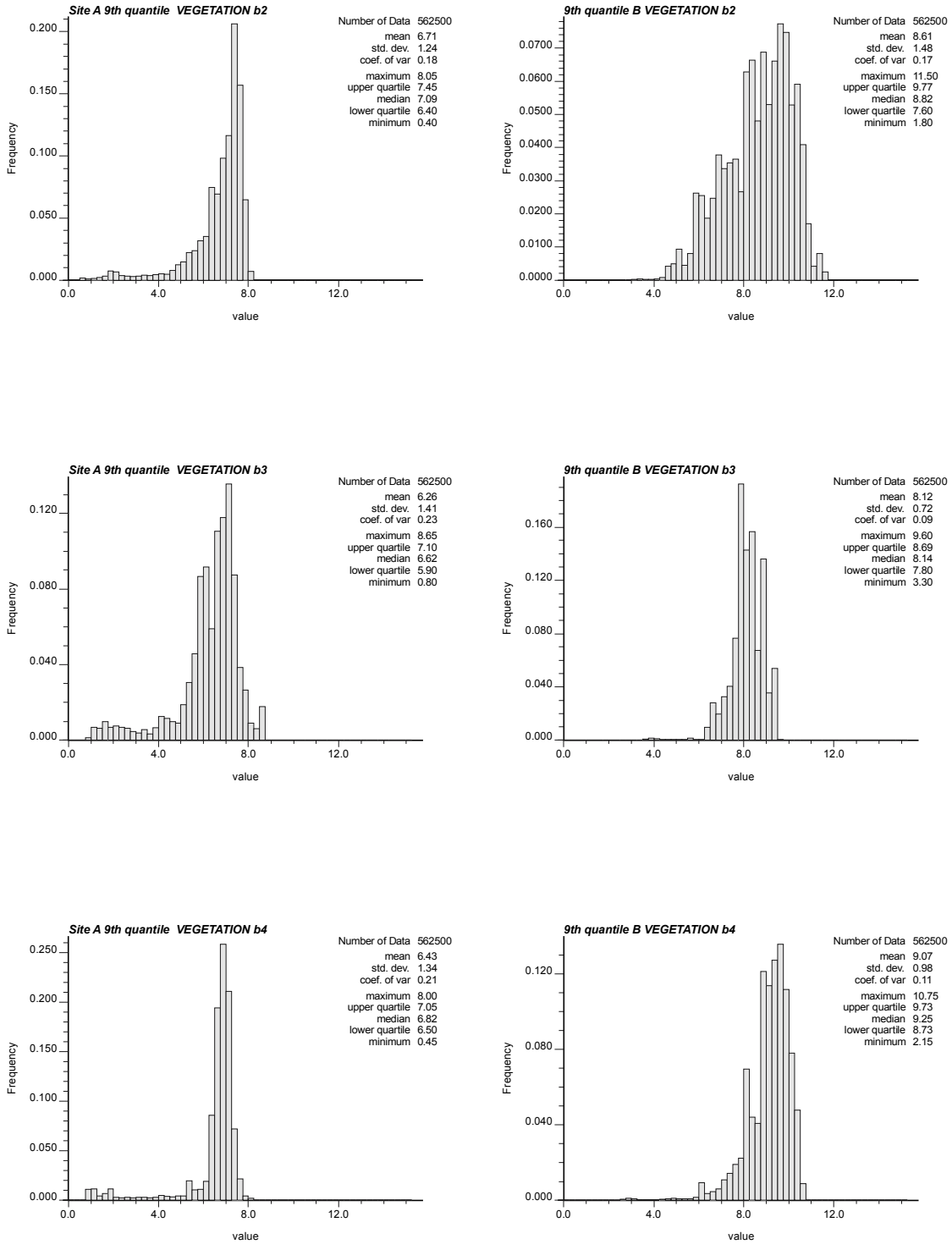

Figure 5.25 – Histograms computed from the 90th percentile images based on the set of 50 realisations for sites A (left side) and B (right side).

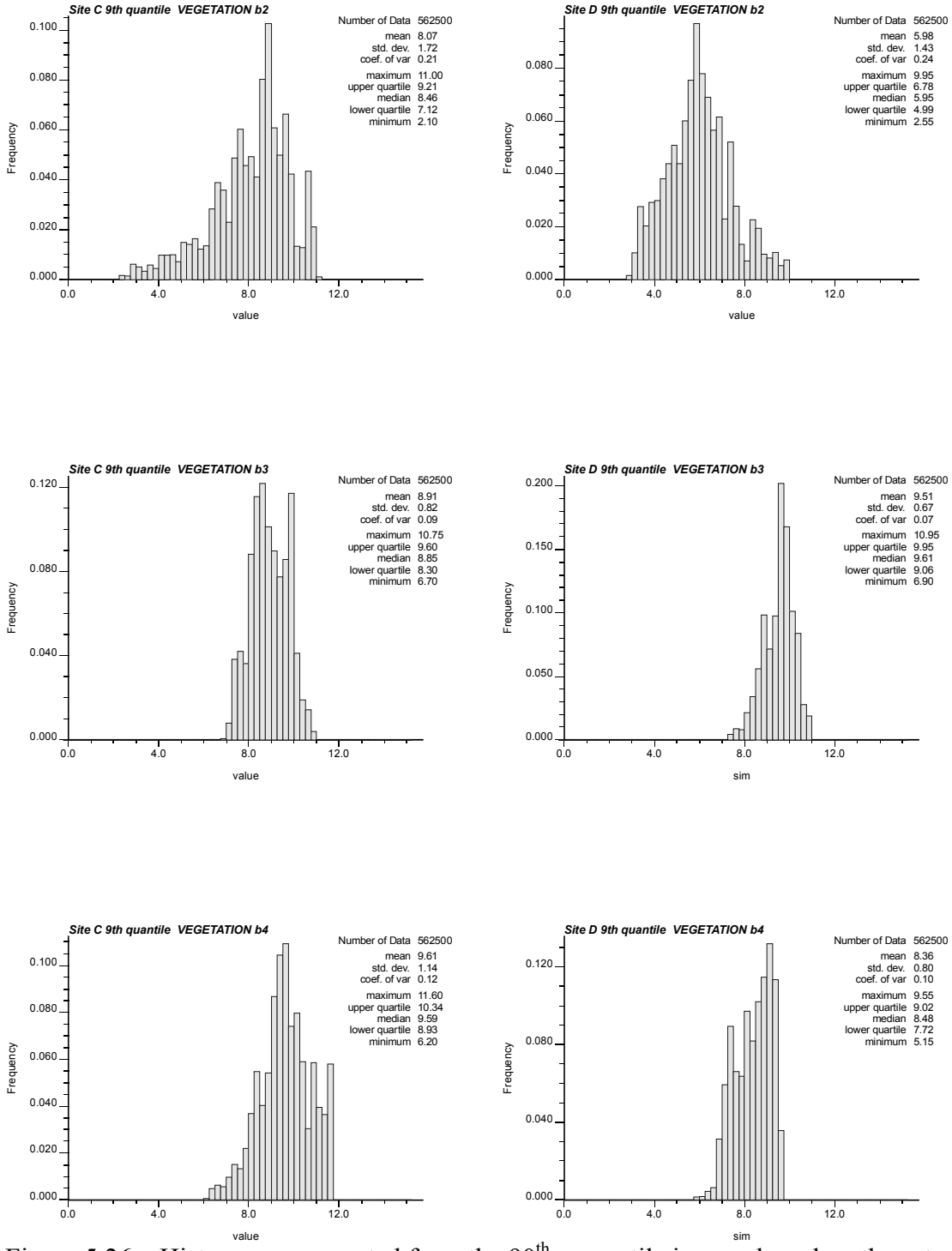

Figure 5.26 – Histograms computed from the 90th percentile images based on the set of 50 realisations for sites C (left side) and D (right side).

The 10^{th} and 90^{th} percentile images depicted the distribution of the extreme values over the 50 realisations. These distributions did not mimic those of the coarse spatial resolution VGT image data or those of the mean and median histograms described in the previous paragraph. The 10^{th} percentile histogram clearly showed an increase in the lower range of reflectance values. A very good example was channel 2 of study site A where the lower peak had almost the same frequency as that of the median value computed from the VGT image data. In general what was observed is that the distribution shifted to the left. This was most obvious for channel 2 of study sites C and D. The opposite was observed for the 90^{th} percentile images. The study site A images lower bump almost disappeared for all three channels. Due to this shift, the channel 2 frequencies close to the mean almost doubled compared to those of the original VGT histogram. This shift of frequency distribution toward the right was also very pronounced in the images of study sites B through D.

5.6 Discussion of Phase I Results

Phase I produced results inline with expectations, that is, the summary statistics were similar to those of the original VGT imagery. This included the fact that the computed overall statistics based on the different types of generated finer spatial resolution imagery were similar to those based on the original coarse spatial resolution VGT imagery.

The generated finer spatial resolution images were visually different than the VGT image, specifically the range of colours and the diffuse nature of the imagery. In essence, the generated imagery could be considered as new images. They were new in the sense that their spatial resolution was very different from that of the VGT image. However, they still shared comparable summary statistics and at this point it is difficult to determine whether the generated imagery was related to the actual ground scene. The fact that the coarse and generated imagery statistics were so similar implies that they were not related to the actual ground scene. In theory, study sites A through D images at the finer spatial resolution (20m) should at least have higher variability than the original VGT images.

With this in mind, one must consider the spatial scale of observation and inference. From the computed statistics it was clear that the desired change in spatial scale did not occur as desired. A change in spatial resolution did occur which in itself was a change of scale, however the scale of inference (based on the generated imagery) could never be associated with the real ground scene. It cannot be associated with the real ground scene because the simulations were based on coarse spatial resolution image statistics. Therefore, the sequential gaussian simulation algorithm generated what could be considered as an image whose scale of observation is that of a VGT sensor but re-sampled to a finer grid. When changing the spatial scale of observation from coarse resolution to fine, the expectation was that the overall variance, at least, would increase. In reality, the differences in the summary statistics between the 20 m HRVIR and 1000 m VGT images was quite

large. Changes in variance can be considered the most important factor when changing spatial scales.

The generated finer spatial resolution imagery however was still quite interesting. The generated images based on the LVM option produced an image whose conditioning coarse spatial resolution VGT image footprint could still be discerned. Even more interesting was the fact that no relationship between bands was utilised to produce the generated finer spatial resolution imagery. Each spectral channel was simulated individually based only on the conditioning VGT data and yet a correlation coefficient was computed between the generated channels that was similar to those found based on the VGT image data. It seemed that the conditioning VGT image data had a strong enough influence to impose an inter-channel correlation that was similar to that found at the coarse spatial resolution.

The same spectral objects as identified in the HRVIR imagery could not be created. For example, roads, parks, rivers, buildings and so on can be readily recognised on the HRVIR imagery but in general the generated images reproduced at a finer spatial resolution the original VGT spectral objects. This behaviour is due to the aggregation effect of the coarse spatial resolution VGT sensor. Spatial location information is not available from the VGT image data for spatial resolutions finer than 1 km and is impossible to deduce this information directly from the coarse spatial resolution data. Such information could only be available from secondary sources. However, even though the location of objects cannot be distinguished, one

should be able to cluster similar spectral signatures and thus extract spectral objects and derive land-cover information.

The relationship between spectral channels is an important characteristic for the detection of object spectral signatures. If one was able to predict the spectral relationship between bands then there would be a greater chance that the generated finer spatial resolution imagery would be successful in extracting products that are more in tune with real ground scene characteristics. However, the spectral relationship could also change depending on the spatial resolution. The LVM option did not require the correlation to be known between channels because each band was simulated separately. The co-simulation option, however, required additional information on the correlation between channels to guide the realisations. The input correlation parameters were derived directly from the VGT imagery and for this reason the resulting simulations also had similar correlation between channels. The question still remains as to whether one should expect that finer spatial resolution imagery have the same spectral relationship that is found at the coarse spatial resolution. In my opinion, the relationship between bands will change depending on the spatial resolution because as the spatial resolution becomes finer, the variability of the data also increases producing new inter-band relationships. As a result, the actual expected relationship between spectral channels would be difficult to predict, i.e. the direction or magnitude of the change in correlation is not very clear. The coarse spatial resolution channel correlation however, should be used as an indicator of the possible spectral relationship at a finer spatial resolution.

The co-simulation algorithm required the relationship between simulated spectral channels to be known. This relationship is present because spectral data is not a random process but rather it is a process related to the object or phenomenon being recorded by the sensor. In theory, generating spectral channels separately should produce spectral entities that could be considered random and with no 'real world' equivalent. However, as was seen in the LVM case, the strong conditioning influence of the VGT data maintained a similar correlation between the generated spectral image channels even though the channels were simulated separately.

The correlation statistic used in the SGSIM algorithm assumed a linear relationship between spectral channels but the spectral relationship was not necessarily linear. Therefore, even poor linear relationships between spectral channels might influence the simulation process by also not allowing the channels to have a linear relationship. The relationship between spectral channels is very important for image segmentation. Segmentation is dependent on the relationship between the spectral channels because it takes place in spectral feature space.

The last generated images were based on a set of 50 realisations. Each resulting image was based on either the E-type, median, 10^{th} or 90^{th} percentile statistic computed across all generated images. This exercise provided insight into the differences between realisations and the 10^{th} and 90^{th} percentile images revealed the extreme possibilities that the sequential gaussian simulation algorithm could produce as well as provide a type of image confidence range. The results showed that over 50 realisations, no major deviations occurred.

Chapter 6 – Generated Finer Spatial Resolution Images Based on Derived Finer Spatial Resolution Input Parameters

The goal of phase II was to generate finer spatial resolution imagery whose statistics matched those that could be expected to be observed at a spatial resolution of 20 m. This particular phase required that the input parameters be more in tune with the intended 20 m finer spatial resolution. The parameters deemed most important during a change of spatial resolution were the variogram and histogram parameters. The variogram provided information about the spatial variability while the histogram provided information on the change in the distribution of values. The expected outcome was that the generated finer spatial resolution images would be more variable than those of the VGT images. The amount of change in variability depended on the underlying ground scene.

6.1 Available Fine Spatial Resolution Data

If only coarse spatial resolution image data was available, then the phase II input parameters would have to be derived from the available data with no way to verify the validity. However, HRVIR images were available and the actual fine spatial resolution derived data could be verified for the four study sites. These HRVIR images were considered as point samples compared to the very coarse VGT data. Table 6.I presents the computed statistics based on the HRVIR imagery.

Table 6.I – Computed HRVIR summary statistics for study sites A through D (n = 5625000). Except for the coefficient of variation, all statistics are in reflectance units (percent).

		Mean	Median	max	min	std dev	Coef var
Site A	Channel 2	9.49	9.85	37.33	2.35	2.95	31%
	Channel 3	17.85	17.55	79.62	0.31	7.46	42%
	Channel 4	15.41	16.05	63.69	0.25	5.13	33%
Site B	Channel 2	10.97	10.73	37.33	2.50	4.06	37%
	Channel 3	23.51	22.57	79.62	0.31	6.83	29%
	channel 4	21.03	21.06	63.69	1.25	4.75	23%
Site C	channel 2	10.45	9.85	37.03	3.23	4.43	42%
	channel 3	25.72	24.77	55.80	0.31	6.68	26%
	channel 4	21.31	20.81	52.65	1.76	5.04	24%
Site D	channel 2	8.64	7.35	37.33	2.50	3.82	44%
	channel 3	27.61	27.27	79.62	0.31	6.37	23%
	channel 4	19.91	19.06	63.69	0.25	4.64	23%

As expected, the HRVIR image summary statistics differed from those of the coarse spatial resolution image. All the mean and median values were found to be greater than that of the VGT data. For the mean the differences ranged from 3.10 to 18.45 while the differences in the median ranged from 2.0 to 18.02. Another obvious difference between the VGT and HRVIR statistics was the maximum value. The maximum values for all channels increased substantially ranging from 25.83 to 70.97 for channel 3 of study site A. The minimum values did not have such a substantial change compared to the maximum values. Three channels had higher minimum values (channel 2, site A; channel 2, site B; channel 2, site C) while the others were all lower.

The coefficient of variation of the HRVIR image data was greater than that of the VGT image data. The difference in the variability of the distribution was not that

significant in all cases. Channel 4, study site A exhibited the smallest difference in the coefficient of variation of only 2% while the largest difference was exhibited by channel 3, study site B with a total of 18% compared to the same VGT channel.

Table 6.II – Computed correlation coefficients based on the HRVIR image data.

	Channels	Correlation
Site A	2 vs. 3	0.17
	2 vs. 4	0.65
	3 vs. 4	0.79
Site B	2 vs. 3	-0.32
	2 vs. 4	0.73
	3 vs. 4	0.29
Site C	2 vs. 3	-0.52
	2 vs. 4	0.80
	3 vs. 4	-0.04
Site D	2 vs. 3	-0.49
	2 vs. 4	0.77
	3 vs. 4	-0.03

Examining table 6.II that presents the computed correlation coefficient of the HRVIR imagery showed many weak linear relationships between spectral channels. Out of all the channel combinations, only four had a strong correlation (i.e. are significantly above 0.5) and no pattern to this strong correlation seemed to be present. There were also some negative relationships computed. The strongest correlation was found at study site C between channels 2 and 4 (0.80) while the weakest relationships were found between channels 3 vs. 4 at study sites C (-0.04) and D (-0.03). When only looking at study sites B through D, the strongest correlation was always between channels 2 and 4. All the correlation coefficient values were statistically significant.

The correlation between spectral channels was very different from that observed in the VGT images. For study site A, the correlation statistic decreased quite dramatically between channels 2 and 3. There was also a decrease in the correlation between the other channels for the study site A, however the relationship remained fairly strong. For study site B, the correlation strengthened for channels 2 and 3, which was weaker between the same VGT image channels. The correlation weakened slightly between the other channel pairs of study site B. For study site C, the correlation increased between channels 2 and 4, and channels 3 and 4 for study site D. All other channel correlation showed a decrease for study sites C and D.

The sign of the relationships between channels of the HRVIR images was for the most part similar to that of the VGT image data. The exception being study site D channels 3 and 4 where the sign changed from positive (VGT) to negative (HRVIR). However, in both cases the relationship was very weak. Overall, the largest correlation variation observed was 0.58 and the smallest was 0.04.

The differences in the correlation between channels of the HRVIR and VGT images were difficult to derive because no model was available a priori for such relationships. Therefore, the computed correlation coefficients based on the fine spatial resolution HRVIR image data itself were used as input parameters to the phase II simulations.

Figures 6.1 and 6.2 present the computed histograms based on the HRVIR images. The sheer number of data points (n = 562500) produced a smoother looking

histogram than that based on the VGT imagery. The graphs were also drawn with a different range because of the higher variability of the HRVIR data distribution. The histograms themselves produced a different frequency distribution than that of the VGT histograms. For instance, the channel 2 (red band) histogram frequencies based on the HRVIR data were all higher than those of their VGT counterparts were. For channel 3 (NIR band) the frequencies were lower and for channel 4 (SWIR band) the frequencies were approximately equal. This indicated that the spatial scale of change was not uniform across the EM spectrum. This has profound implications on scale change because it means that a single model cannot be used for all of the spectral bands in question. Such differences in the distribution could also explain the changes that were observed in the correlation coefficients.

The shapes of the histograms were also quite different from those based on the VGT imagery. The channel 2 histograms of study sites C and D were especially different because the highest frequencies were found to the left of the distribution instead of the right as was seen in the VGT histograms.

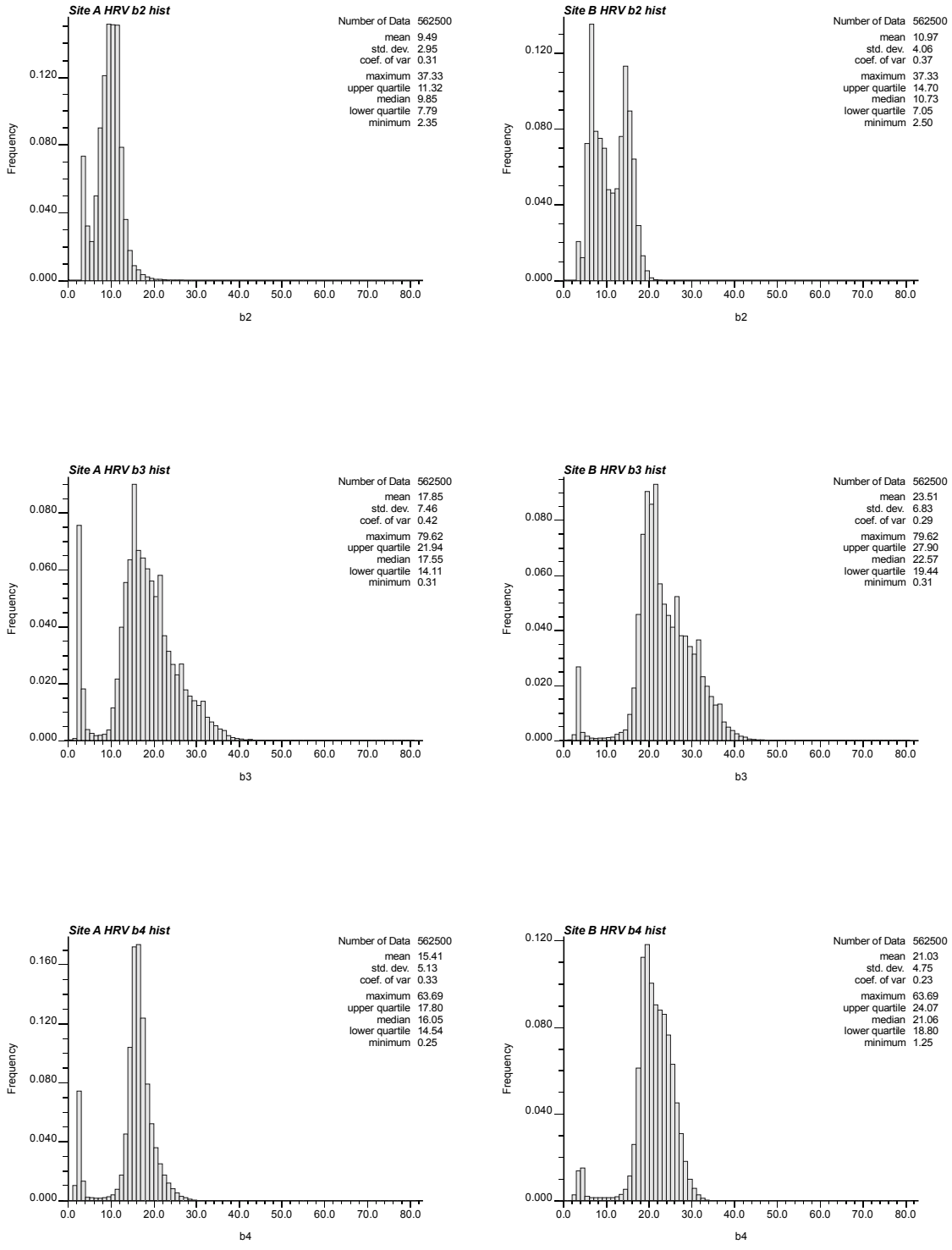

Figure 6.1 – Computed histograms based on the HRVIR images of study sites A (left side) and B (right side).

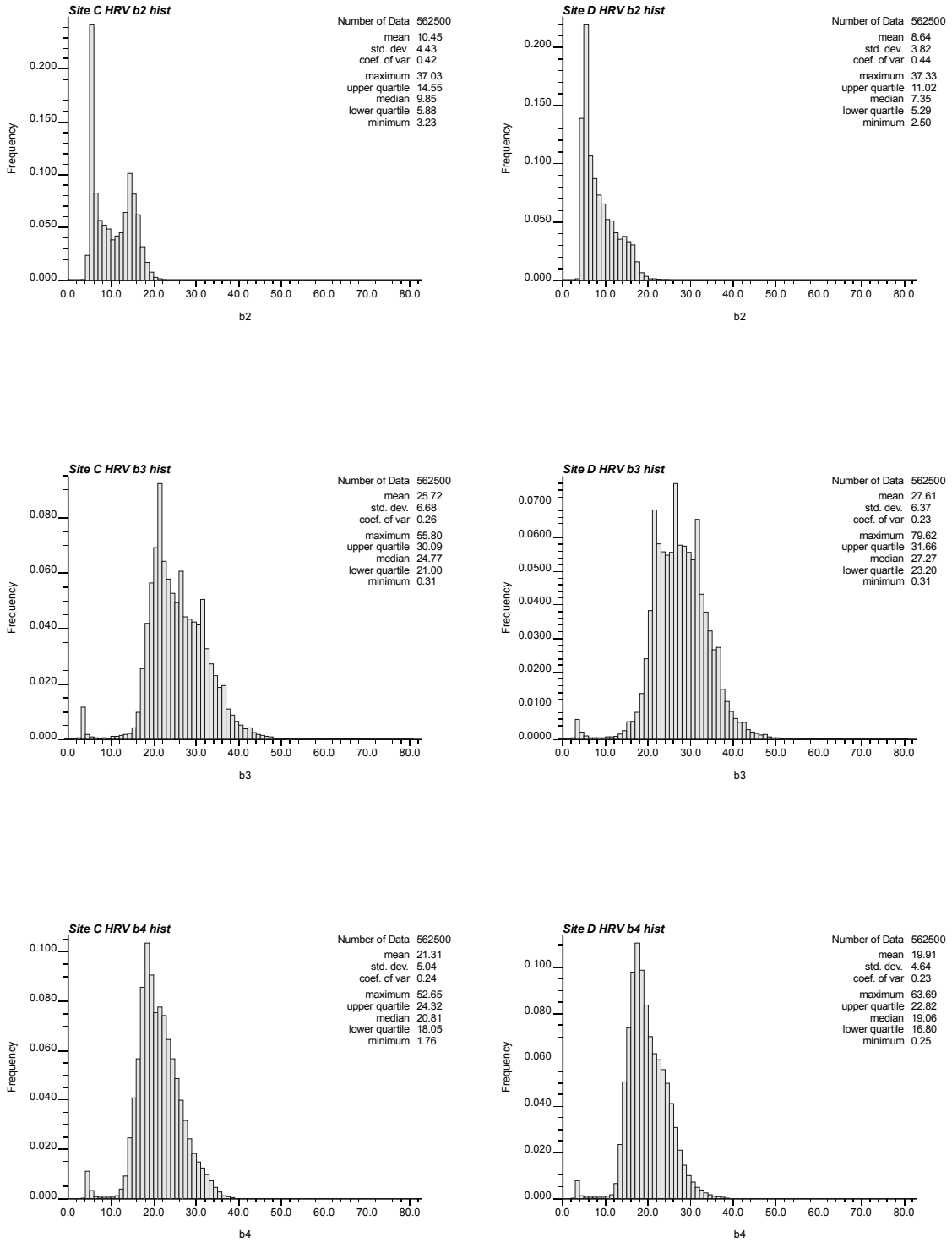

Figure 6.2 – Computed histograms based on the HRVIR images of study sites C (left side) and D (right side).

The experimental variograms were computed on the fine spatial resolution HRVIR imagery (legend: figure 6.3, figures 6.4 and 6.5). Although each study site was quite small, the large number of data points (n = 562500) associated with each HRVIR image produced long computing times. For this reason it was decided that the experimental variogram be computed only in two directions (north-south and east-west) and thus the omni-directional variogram was not computed. The lag was based on the pixel where a pixel was equal to 20 m.

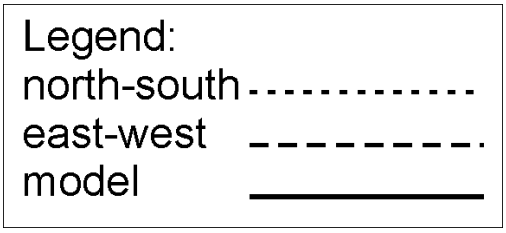

Figure 6.3 – Legend for the experimental variograms based on the HRVIR imagery (figures 6.4 and 6.5).

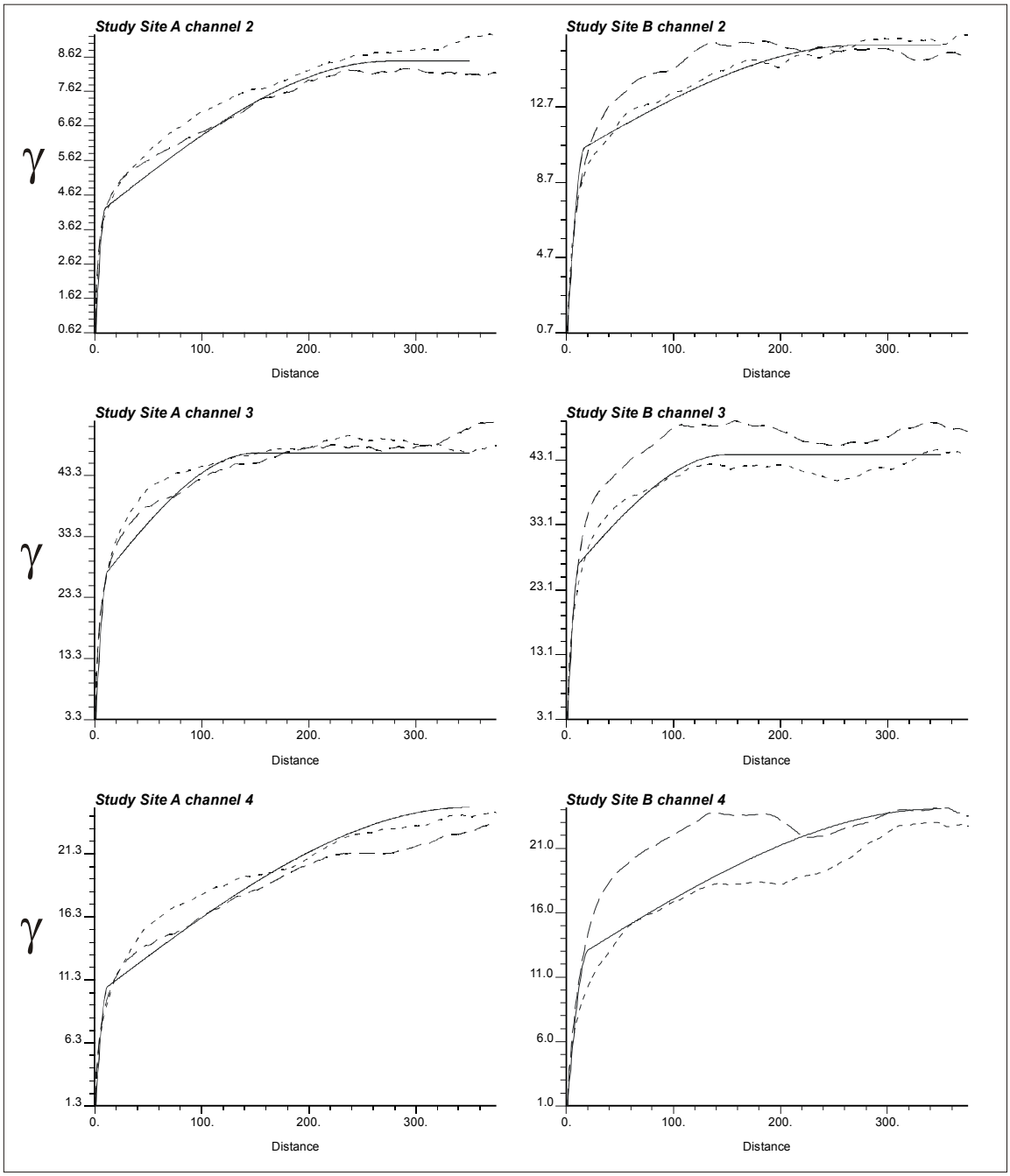

Figure 6.4 – Experimental and model (visual fit) variograms based on the HRVIR fine spatial resolution imagery for study sites A (left side) and B (right side). Distance is shown in pixels where 1 pixel is equal to 20 m (Note the abscissa axis is not constant).

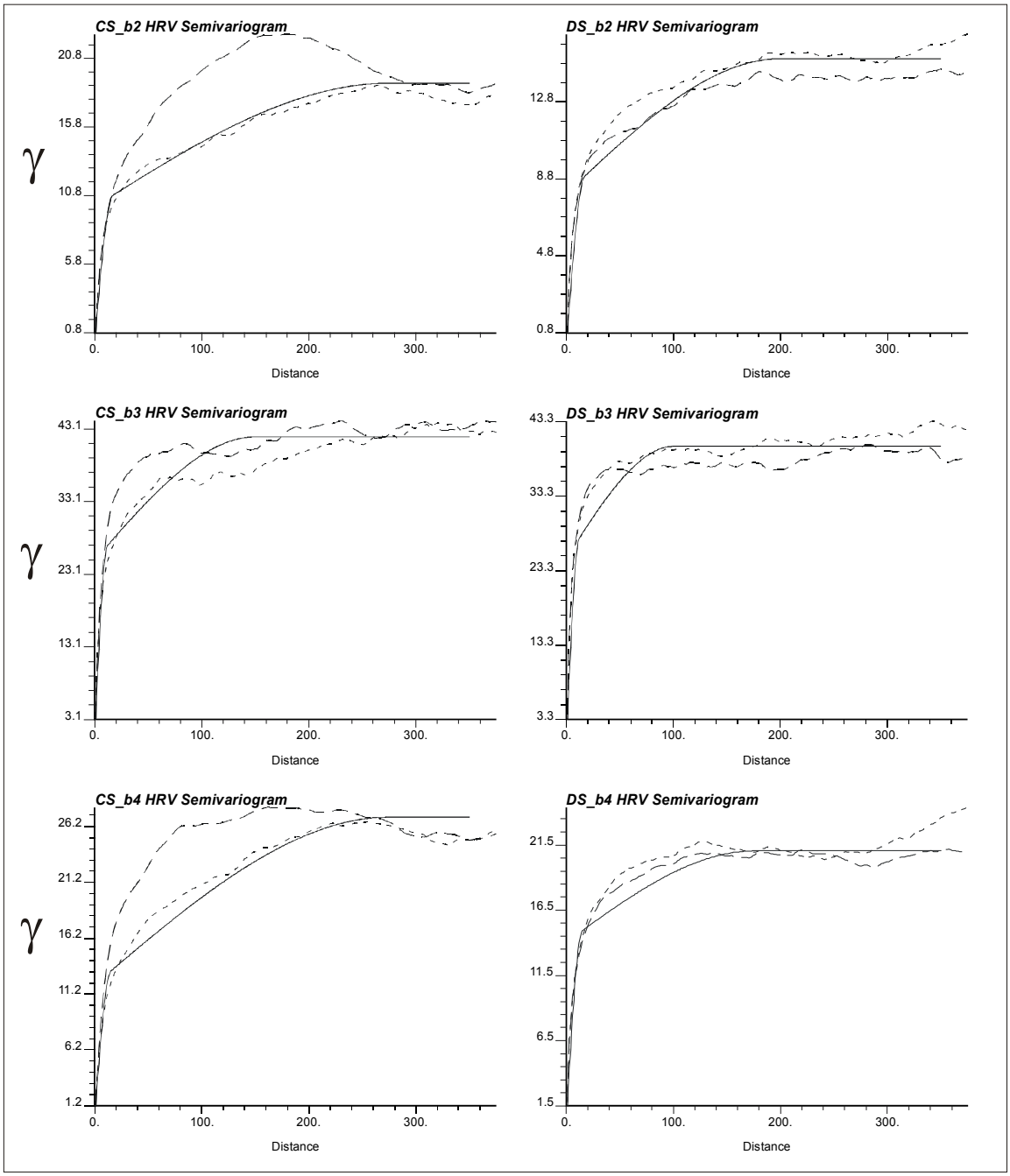

Figure 6.5 – Experimental and model (visual fit) variograms based on the HRVIR fine spatial resolution imagery for study sites C (left side) and D (right side). Distance is shown in pixels where 1 pixel is equal to 20 m (Note the abscissa axis is not constant).

The HRVIR experimental variograms were unlike their VGT counterparts. The most striking difference was the fine scale variability that was captured by the experimental variogram. Such fine scale variability was not apparent in the coarse spatial resolution VGT imagery because of the large lag. A secondary scale of spatial variability was also observed over longer distances. The fine scale variability occurred within a distance of 20 pixels (400 m). Such fine scale variability cannot be attained using the VGT imagery because the smallest distance (spatial resolution) is 1000 m.

Note that the directional component of the experimental variograms was not as pronounced based on the HRVIR imagery as those based on the VGT imagery. Only channels 2 and 4 of study sites B and C hinted at an anisotropic behaviour.

Due to the different scales of spatial variability observed in the experimental variograms computed from the HRVIR imagery, an automatic fitting procedure was not used to fit a model. Instead a variogram model was fit visually to the experimental variogram data. The resulting model parameters are presented in table 6.III. The basic models used for both fine and coarse scale spatial variability was the spherical model. The maximum lag computed in each direction was only 6800 m but that was sufficient distance to reach a sill in all cases.

The smallest lags of the experimental variogram (figures 6.3 and 6.4) all began at the origin. Therefore, the nugget values were all set to zero, i.e. no nugget effect. The fine scale variability was captured with the first model where the sill

values ranged between 4 and 25. The channel 3 sill value was always 25 across all the study sites while the study site A, channel 2 had the lowest sill value associated with the fine scale model. The range parameters associated with the fine scale variability were also very small. They ranged between 10 pixels (200 m) and 20 pixels (400 m). Here the channel 3 range parameters were also all equal to 12 pixels across all four study sites. The channel 2 range parameters were equal to 17 for the study sites B through D. While the study site A had the lowest overall range parameters for the first model.

Table 6.III –Model variogram parameters adjusted to the experimental variogram of the HRVIR image. The range values are shown in pixels where a pixel is equal to 20 m. The spherical model was used throughout. The model 1 parameters describe the fine scale variability while the model 2 parameters describe the coarse scale variability.

			Model 1		Model 2	
		nugget	Sill	Range	Sill	Range
Site A	channel 2	0.0	4.0	10.0	4.5	275.0
	channel 3	0.0	25.0	12.0	22.0	150.0
	channel 4	0.0	10.0	12.0	15.0	350.0
Site B	channel 2	0.0	10.0	17.0	6.0	275.0
	channel 3	0.0	25.0	12.0	19.0	150.0
	channel 4	0.0	12.0	20.0	12.0	350.0
Site C	channel 2	0.0	10.0	17.0	9.0	275.0
	channel 3	0.0	25.0	12.0	17.0	150.0
	channel 4	0.0	12.0	15.0	15.0	275.0
Site D	channel 2	0.0	8.0	17.0	7.0	200.0
	channel 3	0.0	25.0	12.0	15.0	100.0
	channel 4	0.0	14.0	15.0	7.0	175.0

The second model was based on the coarse scale spatial variability. The sill parameters ranged between 8.5 and 47. The channel 3 sill values were the highest across all the study sites while the channel 2 sill values were consistently the lowest. The range parameters for the second model were all much higher than those of the first model with values ranging between 100 pixels (2000 m) and 350 pixels (7000 m). Looking back at the range model parameters computed from the VGT data, the range values spanned between approximately 4000 m and 11 km.

6.2 Phase II Input Parameters

When only coarse spatial resolution data is available, one must be able to derive global statistics that are associated with the fine spatial resolution imagery that is to be generated. The stochastic imaging phase II parameters were an initial attempt at deriving finer spatial resolution spatial variability and distribution statistics based on the available VGT imagery. This proved to be more difficult than expected.

One of the key goals of phase II was to derive the model variogram parameters at the finer spatial resolution, i.e. the point variogram. In theory, it is possible to derive the point variogram from the regularised variogram and vice versa (Clark 1977, Collins and Woodcock 1999). The resulting models were compared to the computed HRVIR and VGT variograms where the HRVIR image was considered as the 'point' variogram and the VGT was considered as regularised. The variogram, which was calculated on one type of support, will not be the same as that calculated on another, i.e. the HRVIR and VGT variograms should be different. The process of

averaging the EM signal across the spatial resolution will influence the shape and behaviour in such a manner that an indirect method must be used to derive the theoretical model for the point variogram necessary for further analysis and estimation (Clark 1977). It is only by finding the punctual variogram or some reasonable approximation to it, that we can see the effect of changing the spatial resolution in the range of interest and it must be done by trial and error (Atkinson and Curran 1995).

A first attempt was made using Clark's (1977) method to derive the point variogram model parameters based on the VGT variogram models. This method consistently produced model parameters that were much lower than those directly computed from the HRVIR experimental variograms. For this reason these results were not considered satisfactory. Another attempt was made using the Collins and Woodcock (1999) algorithm. However, applying the Collins and Woodcock (1999) algorithm also produced erroneous results. The resulting regularized variograms were all much flatter (i.e. the sill values were again very much lower) than those computed directly from the VGT imagery. It was therefore decided that the variogram model parameters computed directly from the HRVIR imagery be used to generate the phase II finer spatial resolution images.

The sequential gaussian simulation algorithm also required parameters that describe the distribution of the derived phase II finer spatial resolution data. This primarily entails estimating the minimum and maximum of the distribution. Although the actual minimum and maximum values were known based on the original HRVIR

imagery, this information was not used directly in phase II because the distributions did not have the same mean. Instead a simple procedure was devised in order to estimate the minimum and maximum values based on the available HRVIR and VGT data.

The standard deviation (SD) in this case was known for all channels of the coarse spatial resolution data set and was a measure of the spread of the distribution. Theoretically, the point variogram model parameters can be estimated based on the available coarse spatial resolution data. Once the point model variogram parameters are known, the sill parameter can be used as an estimate of the total variance over the given extent and from this the SD can easily be computed. With the SD known for the point imagery to be generated a new minimum and maximum value can be derived by considering the mean to be invariant across spatial resolutions (Isaaks and Srivastava 1989). Examining the available phase II data showed that each channel variance for the HRVIR imagery was close to the sill value of the modeled HRVIR variograms. On the other hand, comparing the HRVIR and VGT imagery revealed differences in the mean values. Therefore, a methodology was devised to try and normalize for the differences in mean between the fine and coarse spatial resolution images.

The wanted parameter was the SD of the VGT data at a spatial resolution of 20 m. A simple relationship between the VGT and HRVIR SD at both 20 m and 1000 m spatial resolutions was devised to find this wanted parameter.

$$\frac{\text{SD VGT 1km}}{\text{SD HRVIR 1km}} = \frac{\text{SD VGT 20m}}{\text{SD HRVIR 20m}}$$

From the available data the SD was known for the VGT data at 1 km and HRVIR data at 20 m. However, at least a third value must be known to solve the relationship. This third value was derived from the HRVIR images by coarsening (using an averaging procedure) the spatial resolution to 1 km and computing the SD on the coarse spatial resolution HRVIR data.

Having the SD for the VGT data at a theoretical 20 m spatial resolution allowed for the derivation of new minimum and maximum values. The minimum and maximum values were computed by multiplying the above result (i.e. SD VGT at 20m) by two standard deviations, which is equal to 1.96. The resulting value provided a basis for a 'normal' distribution range. This value was then added to the mean of the original VGT data to compute the maximum value and subtracted from the mean to compute the minimum. Since negative values were not possible for reflectance, all negative values were set to zero. None of the maximum values ever reached the 100% (reflectance). The resulting values can be found in the phase II parameter files (appendix).

6.3 Phase II LVM and Co-Simulation Results

Phase II was based on fine spatial resolution input parameters to the sequential gaussian simulation algorithm. The first images were generated using the LVM option and conditioned to the VGT imagery (figure 6.6).

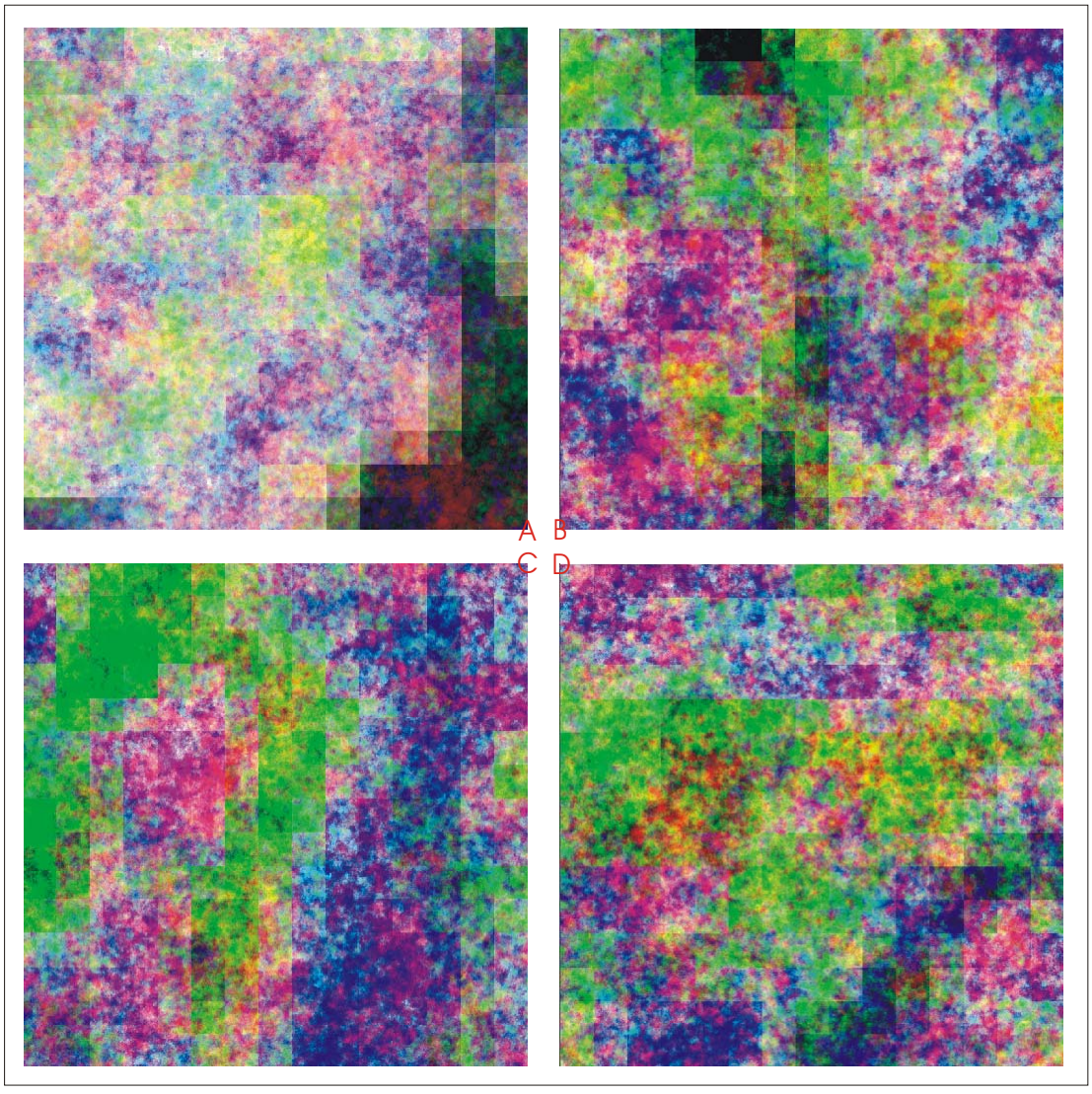

Figure 6.6 – Phase II generated finer spatial resolution imagery using the LVM option.

The generated imagery using the LVM option and phase II parameters possessed a very distinct association with the conditioning coarse spatial resolution VGT imagery. The apparent blocks were the limits that delineated the coarse spatial resolution VGT pixel. However, the grain of this imagery was finer and less diffuse than the phase I generated imagery using the LVM option. The summary statistics associated with these images are presented below (table 6.IV).

Table 6.IV – Summary statistics for the phase II generated images using the LVM option.

		Mean	Median	max	Min	std dev	coef var
Site A	channel 2	5.88	6.29	11.60	0.00	1.98	34%
	channel 3	5.62	5.95	11.02	0.00	1.90	34%
	channel 4	6.03	6.48	10.63	0.00	1.86	31%
Site B	channel 2	7.77	7.85	15.66	0.01	1.94	25%
	channel 3	7.73	7.77	13.05	0.99	1.27	16%
	channel 4	8.70	8.86	13.09	0.36	1.50	17%
Site C	channel 2	7.11	7.32	12.95	0.05	2.13	30%
	channel 3	8.59	8.59	13.72	3.10	1.31	15%
	channel 4	8.73	8.74	14.24	3.42	1.37	16%
Site D	channel 2	5.23	5.19	12.27	0.00	1.85	35%
	channel 3	9.06	9.10	14.16	3.62	1.24	14%
	channel 4	7.96	7.98	13.10	2.26	1.33	17%

The summary statistics computed from the phase II generated images using the LVM option were quite similar to those of the VGT imagery. The mean and median values varied only slightly from those of the VGT imagery. The mean changed by a maximum of 0.20 for channel 4, study site A. The median values also barely changed with a maximum difference of 0.25 for channel 2, study site B. Differences in the minimum and maximum statistics were much more evident. All of the maximum values increased and all the minimum values decreased compared to

the VGT statistics. The change in the maximum values ranged between 1.95 (channel 2, study site C) and 4.16 (channel 2, study site B). From the above table many minimum values were set to zero with the greatest change of 3.60 for channel 3, study site C. This change in minimum and maximum values however was expected because the phase II algorithm parameters were set to these new values. The coefficient of variation changed very little. The highest computed change was only 7%.

The generated imagery statistics were also compared to the HRVIR image statistics. This comparison should be taken with a grain of salt because of the different radiometric scales of the two images. The changes in the mean and median values had quite a large range. However, in all cases the mean and median of the HRVIR imagery was greater than that of the generated phase II imagery using the LVM option. The mean ranged between 3.20 and 18.55 while the median ranged between 2.16 and 18.17. The greatest differences for the mean and median in both cases was for channel 3, study site D. The maximum values showed the greatest differences and in all cases the HRVIR had the highest values. These values differed from 21.67 to 68.60. The differences in the minimum values were not as significant and actually showed decreases i.e. the phase II minimum was higher than the HRVIR minimum. The correlation coefficients also differed. The coefficient of variation for channel 2, study site A, was higher for the phase II imagery by 3%. In all other occurrences the coefficient of variation was lower and the differences ranged between 2% and 13%.

The correlation coefficients were computed between channels of the phase II images (table 6.V) and all were statistically significant to α=5. Study site A showed strong correlation between all bands however, the other study sites showed poor correlation. For study sites B through D, the correlation between channels 2 and 4 was consistently higher. All correlation between channels 2 and 3 for study sites B through D had a negative relationship as well as channels 3 and 4 of study site C.

The phase II image correlation was weaker when compared to the VGT data. This was likely due to the greater local variability found in the generated images using the LVM option. On the other hand, the correlation coefficient compared to the HRVIR imagery was variable and ranged in magnitude between 0.05 and 0.40.

Table 6.V – Computed correlation coefficients for the phase II generated images using the LVM option.

	Channels	Correlation
Site A	2 vs. 3	0.56
	2 vs. 4	0.70
	3 vs. 4	0.70
Site B	2 vs. 3	-0.06
	2 vs. 4	0.49
	3 vs. 4	0.22
Site C	2 vs. 3	-0.47
	2 vs. 4	0.47
	3 vs. 4	-0.15
Site D	2 vs. 3	-0.19
	2 vs. 4	0.37
	3 vs. 4	0.10

The phase I and phase II generated images based on the LVM option exhibited very similar tendencies. The differences (±) in the mean and median were at

most 0.22 for the mean and 0.27 for the median. The minimum and maximum values were of course lower and higher respectively because of the derived parameters used in the phase II generated imagery. A slight increase in the coefficient of variation was observed from phase I to phase II generated images with a change between 1% and 2% except for the channel 4 for study sites B and C where no change was observed and channel 2, study site D where a decrease of 2% was observed.

Histograms were computed from the phase II LVM option generated images (appendix). Visually they were smooth and the distribution, especially for the histograms of study sites B through D, was quite normal. The study site A histograms showed an extended tail to the left of the graph. These histograms resemble the phase I histograms computed from the images using the LVM option. However, it should be noted that there were many negative numbers generated through the simulation process that were set to zero (because a negative reflectance does not exist) and therefore the number of data in the histograms varied from channel to channel.

The co-simulation option of the sequential gaussian simulation algorithm was also used with phase II parameters. As in phase I, the simulation ordering was necessary and based on the HRVIR image correlation. The phase II co-simulation did not have the same ordering as the phase I co-simulation because the greatest variability was found in the channel 3 (NIR band) and therefore was the first channel to be simulated in every case. The ordering of the co-simulations was therefore also modified (table 6.VI).

The phase II single realisation co-simulations are presented in figure 6.7. The images did not appear as diffuse as their phase I counterparts giving the appearance of much more local variability. These images were however different from those generated using the LVM option. Making use of the phase II parameters however did not improve the ability to localise familiar objects that would be normally detected at a 20 m spatial resolution. Summary statistics for these phase II single realisation co-simulated images are presented in table 6.VII.

Table 6.VI – Phase II co-simulation ordering based on HRVIR image correlation.

	Initial channel	Co-simulation	Co-simulation
Site A	3	3 vs. 4	4 vs. 2
Site B	3	3 vs. 2	2 vs. 4
Site C	3	3 vs. 2	2 vs. 4
Site D	3	3 vs. 2	2 vs. 4

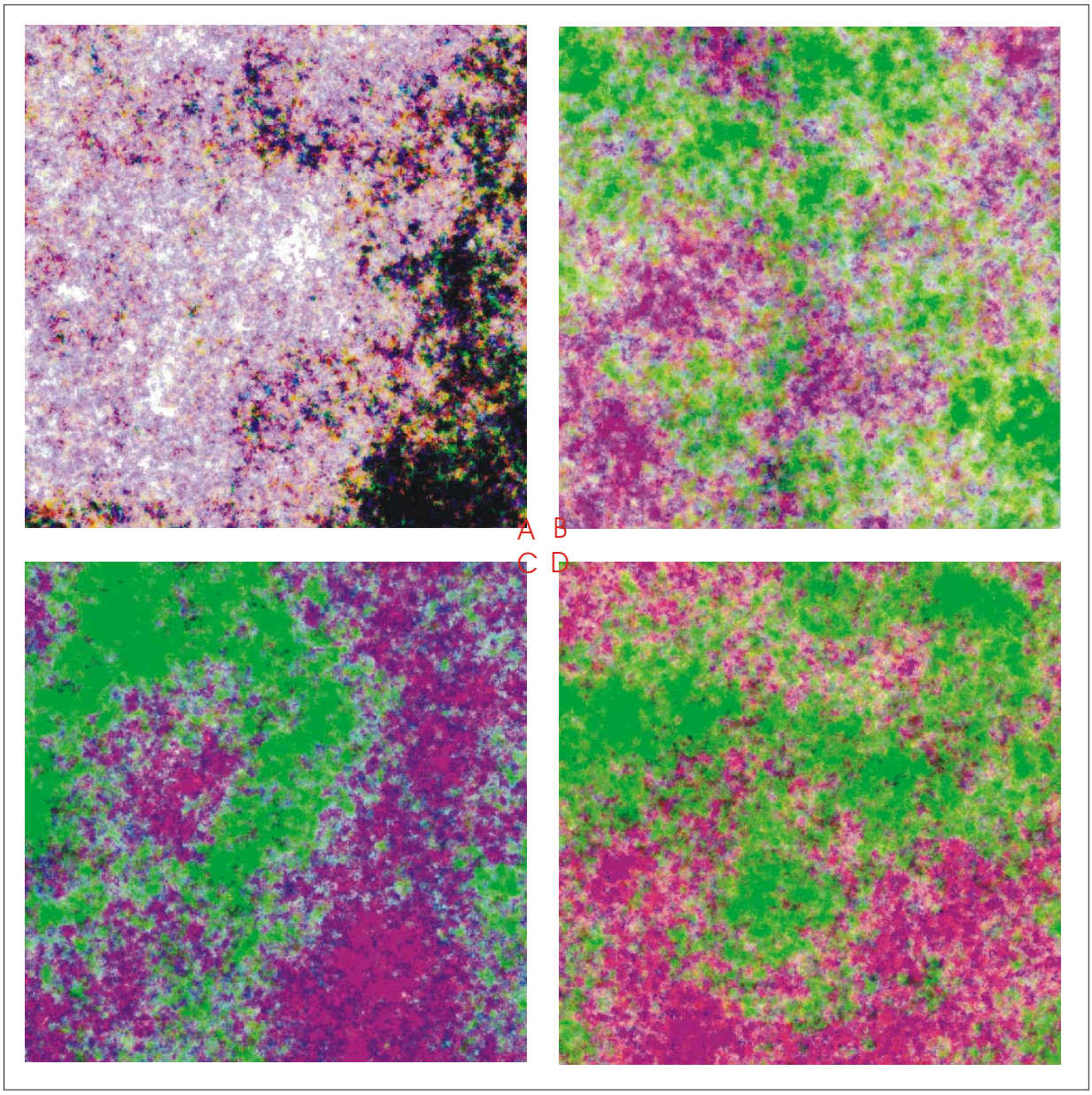

Figure 6.7 – Phase II single realisation co-simulated imagery of study sites A through D.

The mean and median statistics computed from the phase II single realisation co-simulated images were very similar to those of the original VGT images. The mean was generally higher for the original VGT imagery by a maximum of 0.19 except for channel 2 and 4 of study site D whose means were 0.01 less than the phase

II co-simulated imagery. The median was also almost invariable (with a maximum change of 0.15).

The minimum and maximum values however differed quite significantly from the original VGT values as expected. The minimum values were consistently lower and the maximum values were consistently higher than those from the VGT image because the parameters were set in this manner. The maximum values increased between 2.85 and 11.85 while the minimum values decreased a little less, between 0.4 and 6.90. All the correlation coefficients increased in the phase II generated images by 1% to 11%.

Strong differences were found between the phase II and HRVIR summary statistics. The phase II co-simulated imagery showed mean and median values that were very different from those based on the HRVIR data. The mean was consistently lower by 3.19 to 18.56 and the median was lower by 2.05 to 18.02 than the HRVIR statistics. Even with the adjusted phase II maximum values, the HRVIR images had much higher maximum values than those of the phase II single realisation images did. The change in the maximum values varied between 21.27 for channel 2, study site C and 59.12 for channel 3, study site A. The minimum values for the phase II single realisation images, on the other hand, were all lower than their HRVIR counterparts ranging from 0.25 to 3.23. The coefficients of variation for study sites B through D of the phase II single realisation images were all lower than that of the HRVIR imagery. The study site A images however showed an increase in the coefficient of variation

for channels 2 and 4 of 11% and 3% respectively while channel 3 showed no change compared to the HRVIR statistics.

Changes were also observed between the phase I and phase II single realisation co-simulated images. For the mean and median statistics, differences were very slight and ranged between 0.01 and 0.15 for the mean and to a maximum of 0.09 for the median. Much greater differences were found between the maximum values for which the phase II images were all higher. The minimum values of the phase II images were all lower than those generated using the phase I parameters. As a consequence, the coefficients of variation also differed between the two generated images having either no change (channel 4 study sites B and C) or an increase in the coefficient of variation in the phase II based imagery to a maximum of 9%.

Table 6.VII – Phase II single realisation co-simulated imagery summary statistics.

		Mean	median	max	min	std dev	coef var
Site A	Channel 2	5.53	6.40	11.50	0.00	2.32	42%
	Channel 3	5.36	5.95	20.50	0.00	2.27	42%
	Channel 4	5.71	6.55	15.94	0.00	2.05	36%
Site B	Channel 2	7.78	8.07	15.30	0.40	1.93	25%
	Channel 3	7.68	7.80	21.13	0.00	1.32	17%
	Channel 4	8.68	8.91	17.99	0.01	1.28	15%
Site C	Channel 2	7.09	7.50	15.76	0.00	2.42	34%
	Channel 3	8.60	8.55	21.71	0.00	1.50	17%
	Channel 4	8.69	8.80	18.56	0.01	1.28	15%
Site D	Channel 2	5.33	5.30	12.80	0.00	1.70	32%
	Channel 3	9.05	9.25	21.64	0.00	1.57	17%
	Channel 4	7.89	7.87	16.98	0.00	1.18	15%

Table 6.VIII – Phase II single realisation co-simulated images computed correlation coefficients.

	channels	correlation
Site A	2 vs. 3	0.73
	2 vs. 4	0.80
	3 vs. 4	0.81
Site B	2 vs. 3	-0.42
	2 vs. 4	0.76
	3 vs. 4	-0.35
Site C	2 vs. 3	-0.63
	2 vs. 4	0.86
	3 vs. 4	-0.60
Site D	2 vs. 3	-0.57
	2 vs. 4	0.81
	3 vs. 4	-0.55

The computed correlation coefficients based on the phase II single realisation co-simulated images were fairly strong across the board (table 6.VIII). The weakest correlation were found between channels 2 and 3, and 3 and 4 of study site B while the highest were found at the study site A. All computed correlation were again statistically significant at α=0.05. Comparing these results with those of the coarse spatial resolution VGT data, it is observed however that the correlation differences do not have any particular pattern. For example, the study site A correlation were all lower than their VGT counterparts while study site D consistently had higher correlation compared to their VGT counterparts. Some changes in sign were also observed compared to the VGT images. In both cases, the channel 3 and 4 correlation reversed sign for the study sites B and D.

The phase II single realisation co-simulated correlation parameters used to generate the images were based on the HRVIR image correlation but were consistently higher than those of the HRVIR images were. Differences in the correlation coefficients ranged between 0.02 and 0.64. A sign change also occurred between channels 3 and 4 at study site B.

Comparing correlation coefficients between phase I and phase II single realisation co-simulated images, the study sites A and C phase II correlation were all lower than the phase I generated relationships. For the study site B, the sign changed for both channel 2 and 3, and 3 and 4 correlation. Furthermore, the magnitude of the relationships increased between channels 2 and 3 while it decreased for the others. Looking at study site D, the relationship between channels 2 and 4 decreased and increased for the other relationships compared to the phase I statistics.

The histograms were computed for the phase II single realisation co-simulated images (appendix). Their distribution appeared irregular compared to the phase II LVM option images, which were very smooth. The study site A histograms visually appeared to be similar in shape to the VGT histograms. However, the channel 2 and 3 histograms had higher frequencies in both cases compared to those of the VGT histograms. Overall, this effect was seen across all study sites when comparing to the VGT histograms. An interesting feature to note was the very low frequency tails of the distributions in study sites B through D. The channel 2 histograms had this tail on both sides of the distribution and was the result of the back transformation. The phase

II histograms did not resemble the HRVIR histograms, but on the other hand were very similar to the phase I single realisation co-simulation histograms.

The co-simulation option was also used to generate 50 realisations based on the phase II input parameters. A single image was generated from these 50 realisations by computing the E-type estimate, median, 10^{th} and 90^{th} percentile (appendix). These images appeared more diffuse than that of a single realisation. The dot phenomenon that was observed in the same images based on the phase I parameters also appeared in these images. Summary statistics were computed on the resulting images (tables 6.IX to 6.XII).

Table 6.IX – The E-type summary statistics based on 50 realisations.

E-type		mean	median	Max	min	std dev	coef var
Site A	channel 2	5.54	6.24	8.60	0.29	1.81	33%
	channel 3	5.38	5.66	11.83	0.68	1.54	29%
	channel 4	5.71	6.27	9.47	0.45	1.51	26%
Site B	channel 2	7.83	7.79	12.30	1.80	1.16	15%
	channel 3	7.70	7.74	12.46	3.17	0.82	11%
	channel 4	8.69	8.73	11.53	2.15	0.80	9%
Site C	channel 2	7.04	7.34	11.89	1.89	1.83	26%
	channel 3	8.61	8.59	13.99	4.75	0.88	10%
	channel 4	8.69	8.83	11.80	4.77	0.99	11%
Site D	channel 2	5.33	5.14	10.08	2.25	1.19	22%
	channel 3	9.11	9.22	13.64	5.16	0.84	9%
	channel 4	7.88	7.84	11.96	4.94	0.76	10%

Table 6.X – The 10th percentile summary statistics based on 50 realisations.

1st quantile		mean	median	max	min	std dev	coef var
Site A	channel 2	3.85	4.80	8.05	0.00	2.29	59%
	channel 3	3.35	3.39	8.65	0.01	2.04	61%
	channel 4	4.18	5.22	8.00	0.05	2.37	57%
Site B	channel 2	5.89	5.77	11.50	0.65	1.29	22%
	channel 3	6.58	6.70	9.60	0.11	1.11	17%
	channel 4	7.55	7.73	10.75	0.79	1.26	17%
Site C	channel 2	4.94	4.76	11.00	0.06	2.01	41%
	channel 3	7.49	7.53	10.75	0.12	1.02	14%
	channel 4	7.71	7.86	11.60	0.35	1.09	14%
Site D	channel 2	3.88	3.54	9.95	0.18	0.98	25%
	channel 3	7.97	8.18	10.95	0.04	1.14	14%
	channel 4	6.98	7.05	9.55	0.12	0.83	12%

Table 6.XI – The median summary statistics based on 50 realisations.

5th quantile		mean	median	max	min	std dev	coef var
Site A	channel 2	5.71	6.49	8.05	0.32	2.02	35%
	channel 3	5.53	5.95	8.65	0.80	1.62	29%
	channel 4	5.93	6.57	8.00	0.45	1.68	28%
Site B	channel 2	7.90	8.02	11.50	1.80	1.24	16%
	channel 3	7.73	7.83	9.60	3.30	0.67	9%
	channel 4	8.83	8.55	10.73	2.15	0.69	8%
Site C	channel 2	7.12	7.55	11.00	2.10	1.96	28%
	channel 3	8.58	8.55	11.95	6.70	0.75	9%
	channel 4	8.70	8.90	11.60	6.20	0.94	11%
Site D	channel 2	5.25	5.15	9.95	2.55	1.22	23%
	channel 3	9.15	9.32	10.95	6.90	0.67	7%
	channel 4	7.90	7.80	11.39	5.15	0.71	9%

Table 6.XII – The 90th percentile summary statistics based on 50 realisations.

9th quantile		mean	Median	max	min	std dev	coef var
Site A	Channel 2	6.96	7.43	11.43	0.40	1.30	19%
	Channel 3	7.05	7.05	20.38	0.80	1.38	20%
	Channel 4	6.89	7.00	15.55	0.45	0.83	12%
Site B	Channel 2	9.68	9.75	14.99	1.80	0.96	10%
	Channel 3	8.72	8.75	20.84	3.30	0.96	11%
	Channel 4	9.63	9.60	16.70	2.15	0.56	6%
Site C	Channel 2	8.97	9.29	15.49	2.10	1.56	17%
	Channel 3	9.72	9.70	21.62	6.70	1.23	13%
	Channel 4	9.64	9.64	17.43	6.20	0.98	10%
Site D	Channel 2	6.92	6.69	12.66	2.55	1.41	20%
	Channel 3	10.15	10.10	21.57	6.90	1.14	11%
	Channel 4	8.76	8.81	16.72	5.15	0.79	9%

Some slight differences were observed between the E-type estimate and median images. Generally the E-type estimate images mean and median values were lower. On the other hand, the maximum values were higher than those of the median images were. The minimum values of the E-type images were equal or lower than the median images. The coefficient of variation differed by a maximum of 2%.

The 10^{th} percentile images mean and median statistics were all lower than that of the E-type estimate image as expected. The maximum values as well as the minimum values were also lower. The coefficient of variation tended to be higher for the 10^{th} percentile image with the study site A values ranging between 26% and 32% higher while the other study sites ranged between 2% and 15% higher than the E-type estimate image. The opposite results were observed with the 90^{th} percentile image statistics. The mean, median, maximum and minimum statistics were all higher than the other generated images as expected. The study site A again had the greatest changes in the coefficient of variation that were this time lower (ranging from 9% to 14%) than those of the E-type estimate image. Only one other channel had such a large difference (9%) compared to the E-type estimate images and that was channel 2, study site C. The other study sites saw their coefficient of variation changed by a maximum of only 5%.

Even with the phase II parameters used in the co-simulation algorithm, the resulting statistics were still similar to those of the VGT imagery. For instance, the E-type estimate images mean and median values match those of the VGT imagery with

variations in the mean being at most 0.17 and in the median 0.31. The median image statistics generated using the phase II parameters also only varied by 0.13 in the mean and 0.40 in the median (channel 4, study site B). These differences in the central tendency of the distribution were very slight compared to the VGT imagery. The maximum values of the phase II imagery were greater than the VGT imagery because the parameters were set to those values. The coefficient of variation statistic was reduced by a maximum of 7% compared to the VGT data. The median images were very similar overall to the VGT images.

Histograms were computed for the E-type estimate, median, 10^{th} and 90^{th} percentile images (appendix). These histograms were generally smoother than the single co-simulated images but not as smooth as those based on the LVM option images. When comparing these histograms to the original VGT data, the median images histograms matched quite well. The E-type estimate histograms had similar overall distributions but were smoother.

It came as no surprise that the 10^{th} and 90^{th} percentile image histograms did not look anything like the original VGT image histograms. The 10^{th} percentile histograms tended to have a more negatively skewed distribution while the 90^{th} percentile images tended to have a more positively skewed distribution. The 10^{th} and 90^{th} percentile image histograms also had long tails that were not apparent in the mean and median image histograms. The long tails were extreme values (either positive or negative) and thus only appeared in the 10^{th} and 90^{th} percentile image histograms. The normal back-transformation model caused the low frequencies of

these tails because missing values must be extrapolated in order to fit the minimum and maximum parameters specified to the algorithm when converting the simulated values back to reflectance.

The lack of similarity was easily perceived between the HRVIR image histograms and the generated phase II images. Differences in the histograms of the generated phase I and phase II images were apparent providing evidence that the input parameters did change the resulting imagery.

6.4 Discussion

The goal of phase II was to generate finer spatial resolution optical-like imagery using the sequential gaussian simulation algorithm with input parameters that were more in tune with the desired final products at 20 m spatial resolution. The fact that an image was generated does not mean that the goal was reached. These generated images must satisfy certain scale criteria in order to be useful in the remote sensing context and their appropriateness evaluated. In phase I, the results clearly demonstrated the statistical similarity between the generated and VGT imagery. Phase II results were resembled those of the VGT imagery because of the difficulty in deriving the finer spatial resolution statistical input parameters and the dependence on the VGT conditioning imagery.

Phase II results failed to reproduce the wanted HRVIR image statistics as it was hoped. The modified input parameters for phase II were the model variogram

parameters and the distribution parameters. The point model variogram of the VGT data was taken from the HRVIR imagery, considered as point samples compared to the coarse spatial resolution VGT imagery. The first attempt at finding the punctual variogram model parameters using Clark's (1977) method failed to produce results that were similar to the HRVIR image based experimental variogram. An algorithm developed by Collins and Woodcock (1999) was also applied to deduce the punctual model variogram based on regularised variogram model information and again did not produce the expected HRVIR model variograms.

The HRVIR images were assumed throughout to be point measurements compared to the VGT imagery because of the great differences in spatial resolution. This assumption was necessary to validate the derived fine spatial resolution statistics. If this assumption was true then the current available tools that were used to determine the punctual variogram model from coarse spatial resolution data were imprecise because they resulted in coarse spatial resolution model variograms that were different from those observed in the VGT imagery. Otherwise, the tools were correct but the assumption that the HRVIR imagery was the point sample imagery is invalid. In both cases more study must be done in order to verify these statements.

Regarding this issue, Collins and Woodcock (1999) describe some general obstacles when using real (coarse and fine spatial resolution) images. The viewing and illumination conditions can have significant impact on the scene spatial structure, affecting both the magnitude and isotropy of spatial dependence. Also the atmosphere in most cases is a major factor to be considered. Furthermore, the PSF is not constant

across all scan angles and this is most prominent for sensors with very large swath widths such as the VGT sensor. For the most part, these obstacles were avoided in this study by using the SPOT 4 satellite where both the HRVIR and VGT sensors are on the same platform. Having images taken at the same time the atmospheric differences were negligible. Furthermore, as the chosen study sites images were close to nadir, viewing and illumination angle differences were minimised. Therefore, in this case it would appear that the sensor PSF would be the most influential variable and therefore skew the regularisation procedures. The fact that the HRVIR and VGT sensors have different spectral extents was important, however it would not influence the regularisation of the spatial variability as greatly as the sensor PSF could. The PSF defines the characteristics of the image of a point source formed by an optical system. An accurate model of the PSF of coarse spatial resolution sensors such as AVHRR or VGT is difficult to determine due to the unknown contributions of atmospheric and view angle effects, deviations from preflight optical characteristics, and along-track and cross-track asymmetry (Moreno and Melia 1994). Remotely sensed measurements are not simple averages of radiance within a sensor's field of view, and this field may not be rectangular (as is often implicitly assumed when averaging pixels). Instead, sensor optical and electronic effects cause scene radiance to be weighted differently according to its relative spatial position. Using a simple averaging process is equivalent to assuming that the PSF has the form of a simple square wave. Few if any studies have explicitly assessed the impact of modelling the remote sensing process using such assumptions (Collins and Woodcock 1999).

The need for the phase II punctual variogram model parameters left little choice but to adopt the HRVIR imagery parameters directly. This decision was made knowing that there was a difference in the radiometric extent between the sensors because the simulation algorithms only required the shape of the punctual variogram model and not the sill values themselves. This was achieved by normalising the model to a variance of one.

Phase II also required parameters that described the distribution of the wanted finer spatial resolution data. Specifically, the minimum, maximum and the normal score transform file were the most important. The minimum and maximum values provide the sequential gaussian simulation algorithm with the extent of the distribution of values while the normal score transform file provides the information to convert the actual image data to and from the standard normal distribution. The input parameter minimum values did resemble the HRVIR images minimum values but the derived phase II maximum values were much lower than those observed in the HRVIR imagery. The manner in which these parameters were derived was obviously inadequate and a method should be used that is based on the knowledge of the HRVIR sensor itself rather then pure statistics.

The back-transformation file in phase II was based on the VGT data and therefore the simulated values necessarily resembled the VGT distribution. The fact that the minimum and maximum values were changed and the transformation file was not, was the reason why the generated imagery histograms tended to have such long tails with low frequencies. These long tails were caused by the extrapolation of the

simulated values to reach the minimum and maximum values imposed by the input parameters that were lower than the minimum and higher than the maximum values of the conditioning VGT back-transform file. Future work should concentrate on also correcting the back-transformation file to the finer spatial resolution output desired. Isaaks and Srivastava (1989) present some possible techniques that could help adapt the back-transform file where the mean of the distribution remains unchanged and the variance is adjusted by some factor (called variance adjustment factor). The effect of support on the back-transform file distributions symmetry is related to the entropy, or the connectedness of extreme values. Entropy is not adequately described by the variogram and therefore our a priori knowledge of the underlying scene will help judge the expected degree of symmetrization. Qualitative information about the spatial arrangement of values must be brought to bear on the problem. If past experience in similar environments suggests that the extreme values were poorly connected, then we should choose a procedure that implicitly increases the symmetry of the distribution as the support increases. If the extreme values tend to be well connected, then we might prefer a procedure that does not implicitly symmetrize the distribution (Isaaks and Srivastava 1989). According to Zhang et al. (1990), unfortunately, all of these methods to adjust the distribution depend on unverifiable assumptions about how the distribution changes as the support increases and they also require knowledge of certain parameters that are difficult to estimate precisely.

Each new generated image was exactly the same size and equivalent to the SPOT 4 HRVIR study sites, i.e. the spatial resolution was 20 m and the image grid was 750 pixels x 750 pixels. A change of scale occurred when generating these finer

spatial resolution images because the spatial resolution changed from that of 1000 m to 20 m. Is stationarity guaranteed when the change of spatial scale involved a change of spatial resolution? Without knowledge of the underlying finer spatial resolution variability one cannot make this decision a priori. More importantly, one must consider whether the stochastic imaging algorithm used to generate the imagery was capable of producing non-stationary imagery. Looking over the results from both phase I and II, it appeared that the sequential gaussian simulation algorithm was not capable of generating non-stationary data because the resulting overall statistics were similar. The HRVIR study sites produced different overall statistics however; the area was still deemed stationary.

One of the goals of the generated finer spatial resolution images was to increase the certainty of the information that was extracted from them. This increased certainty was based on the notion that finer spatial resolution brings better accuracy. However, the uncertainty about the phase II input parameters must also play an important part in the total error. As a result, the manner in which the phase II parameters were derived must be improved in order to increase the certainty of the final product. The total error however, cannot be assessed until the real values are known and compared to the generated finer spatial resolution data.

Estimation of the punctual variogram is error-prone. There is nothing inherent in the algorithm to prevent estimation of variance for spatial resolutions finer than the original data. In fact, if the punctual variogram is known, variance at any resolution can be determined accurately. The problem is the greater difficulty of estimating the

punctual variogram from coarse data. Estimates of variance at fine scales are affected by such problems. In practice, there is no way to tell whether the punctual variogram has been estimated precisely. This uncertainty undermines confidence in fine-scale estimates made from coarse-scale data. At best, such estimates constitute reasonable guesses based on the available information, but their accuracy cannot be confirmed in practice. More experience may lead to a general rule regarding the range of resolutions over which estimates remain valid (Collins and Woodcock 1999).

In phase II, 50 realisations were used to generate statistical imagery based on the E-type estimate, median and 10^{th} and 90^{th} percentiles. The resulting statistics demonstrated the resemblance of the phase II generated images to those of phase I. Even over 50 realisations the stochastic images did not differ significantly from those of the phase I images.

Based on the results, it was obvious that the input parameters were very important because they drive the simulation. Incorrect or inappropriate input parameters would still generate a finer spatial resolution image. However, such data would be useless for any land-cover information extraction. Therefore, if the input parameters were not at the correct spatial scale, then neither would the resulting imagery. The testing of this idea would require generating imagery based entirely on known fine spatial resolution statistical parameters and comparing the results to generated images based on coarse spatial resolution statistics. For example, the HRVIR image statistics and phase I statistics could be used. Furthermore, both conditional and unconditional simulations should be investigated in order to observe

the influence of the conditioning data on the resulting imagery. The expectation would be that better input parameters would yield better results.

Many new parameters were derived and introduced into the simulation process in phase II. However, the resulting generated finer spatial resolution imagery did not differ significantly from those of phase I as was hoped. Before any definitive conclusions can be made, further study into the uncertainty in the use or derivation of the phase II parameters is required.

Chapter 7 – Generated Finer Spatial Resolution Images with the Help of SAR Imagery

A 20 m spatial resolution image such as HRVIR provides imagery with spatial detail that is ideal for local level land-cover projects because objects are easily identified. The previously generated phase I and II finer spatial resolution imagery was visually difficult to interpret because of the lack of familiar objects. The stochastic nature of the generated images produced an almost featureless product because there was no way of knowing the spatial arrangement or location of spectral objects prior to simulation. Location information was needed to fix simulated values to geographic positions that better represent the actual ground scene variability.

Spatial location information can be taken from other types of imagery. RADARSAT SAR imagery can be recorded at a spatial resolution of 100 m that covers an area approximately 500 km x 500 km. The SAR can record ground scenes in a variety of conditions where optical sensors are unusable. In addition, RADARSAT ScanSAR is able to revisit areas of interest on a regular basis with a small time step. As such, RADARSAT ScanSAR imagery was considered as a complimentary source of imagery for the VGT imagery. However, the amount of information that can be potentially extracted from a single band SAR image is much less than from a multi-spectral image with an equivalent spatial resolution. Moreover, the SAR images visual characteristics are unfamiliar to the human eye hindering interpretation and information extraction. This imagery nevertheless can record the

same ground scene providing information on object location at a spatial resolution that is much finer than that of the VGT imagery.

Phase III used RADARSAT ScanSAR wide imagery to condition the generated finer spatial resolution imagery to improve the visual output. The influence of the SAR data greatly improved the visual output of the generated finer spatial resolution imagery however the correlation between visible and SAR data was poor and ultimately arbitrarily increased.

7.1 Conditioning with RADARSAT-1 SAR Imagery

In phase III, a new image data set was introduced: RADARSAT ScanSAR wide. Summary statistics for the study sites relating to the single band SAR data are presented in table 7.I. The RADARSAT ScanSAR wide imagery was resampled to a 20 m spatial resolution when geometric corrections were applied. Therefore, the summary statistics were based on 562500 sample pixels (n = 562500) just like the original HRVIR imagery which covers a total area of 750 x 750 pixels.

Table 7.I – Summary statistics based on the RADARSAT ScanSAR imagery recorded for each of the study sites (n = 562500). The mean, median, maximum and minimum values are in radar backscatter values (units sigma naught).

	Mean	median	max	Min	std dev	coef var
Site A	0.45	0.42	0.98	0.00	0.21	46%
Site B	0.29	0.27	0.93	0.00	0.13	44%
Site C	0.29	0.26	0.93	0.00	0.11	39%
Site D	0.35	0.34	0.99	0.05	0.12	33%

The highest mean and median values were computed for study site A at 0.45 and 0.42 respectively. Study site D showed slightly lower mean and median values while study sites B and C had equal mean values. The median values for study sites B and C were very similar with only a difference of 0.01. For the SAR data, the computed median values were consistently lower than the mean. The opposite was observed in the summary statistics of the visible image data.

SAR backscatter values range between 0 and 1. Sites A through C all had minimum values that were equal to zero while the study site D had a slightly higher minimum value of 0.05. The highest value was computed for the study site D (0.99) while study sites B and C had the lowest maximum values of 0.93.

The SAR imagery is physically different from VGT and HRVIR imagery so direct comparison of the summary statistics was meaningless. The coefficient of variation statistics for the SAR imagery ranged between 33% for study site D and 46% for study site A. For the most part, the SAR coefficient of variation statistics were higher than those computed for any of the VGT bands, except for study site A, channel 2 with a correlation of 34%. The HRVIR coefficients of variation were a little stronger than the VGT coefficients and therefore more comparable to the SAR computed coefficient of variation statistics.

As in phase I and II, the co-simulation algorithm required information on the correlation between the conditioning and simulated data. The HRVIR imagery was used to compute the correlation between visible and SAR data (table 7.II) because the

spatial resolution of the VGT imagery was too coarse. The goal of computing the correlation coefficients between the optical and SAR image data was to determine the linear relationship between the optical and SAR bands. The VGT data was not used because of the large differences in spatial resolution that would produce a range of variations (100 pixels) for every one VGT pixel. Such a comparison would not adequately describe the relationship between the optical and SAR data. Furthermore, one wants to know the relationship between optical and SAR image data at the fine spatial resolution which is being simulated.

Table 7.II – Computed correlation coefficients between the RADARSAT SAR image and the HRVIR imagery.

	Channels	Correlation
Site A	2 vs. SAR	0.41
	3 vs. SAR	0.12
	4 vs. SAR	0.28
Site B	2 vs. SAR	-0.29
	3 vs. SAR	0.23
	4 vs. SAR	-0.14
Site C	2 vs. SAR	-0.48
	3 vs. SAR	0.28
	4 vs. SAR	-0.38
Site D	2 vs. SAR	-0.23
	3 vs. SAR	0.09
	4 vs. SAR	-0.21

All pairs produced weak correlation coefficients. The computed t-test resulted in rejecting the null hypothesis (indicating that the channels are dependent) at α = 0.1, 0.05 and 0.01. The magnitude of the relationships ranged between 0.48 for study site C, channel 2 vs. SAR and 0.09 for study site D, channel 3 vs. SAR. Negative relationships were also computed between channel 2 and SAR, and channel 4 and

SAR for study sites B through D. Study site C produced the strongest relationships compared to the other study sites.

The computed correlation between the HRVIR and SAR image data are expectedly quite different than that what was observed between pairs of optical channels. The computed coefficients of correlation for the VGT imagery were generally much higher except for study site B, where the channel 2 vs. 3 correlation was much lower. The sign of the relationships were also different compared to the SAR correlation results and those based on the VGT image data. When compared to the HRVIR correlation coefficient results, the differences were much more varied and in many cases not as extreme.

Such weak correlation coefficients (all were less than 0.5) would have little effect on conditioning the realisations (NACOG 2000). The general trend that was observed however, showed that the red band (or channel 2) always produced the strongest relationship with the SAR data. The red channel was therefore chosen as the first channel to be generated. However, in order to increase the conditioning influence of the RADARSAT ScanSAR data on the resulting realisations, the magnitude of the relationship was arbitrarily increased to 0.75. The sign of the relationship however remained as in table 7.II.

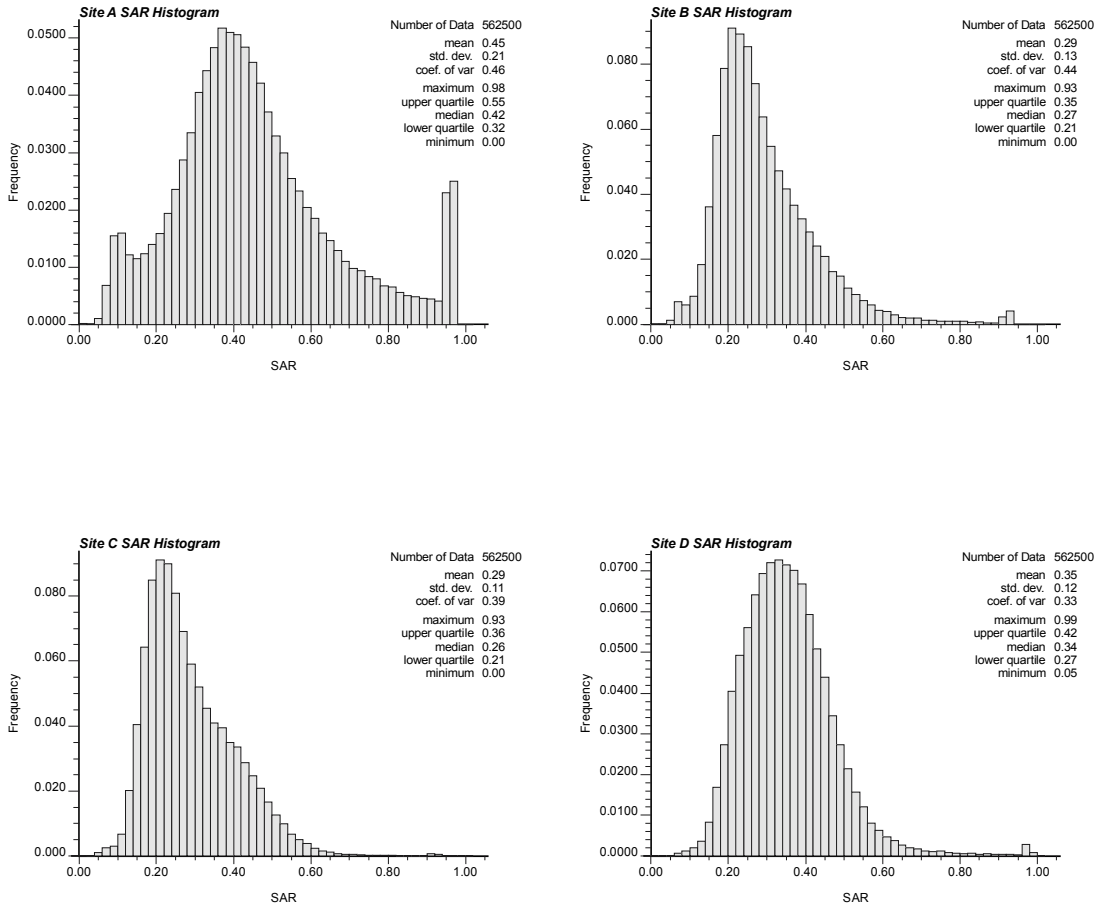

Figure 7.1 – Histogram of the RADARSAT ScanSAR wide imagery.

For each of the study sites, the histogram of the RADARSAT ScanSAR wide images was computed (figure 7.1). Their overall shape was smooth and all study sites exhibited a long positive tail. The histogram based on study site A exhibited a sudden and notable peak at the extreme right. The other study sites (especially B and D) also have slight increases in the frequencies around their maximum values. The urban nature of the ground scene of study site A caused the sudden spike to the right of the distribution. The strong signal return was caused by structures that simulate corner reflectors. A second peak developed to the left of the distribution because of the large area covered by water within the study site A. Water scatters the EM radiation in the

centimetre region where SAR signals are recorded and therefore the signal return is weaker (specular reflection). The positive skew observed in all the SAR histograms pushed the median statistic below the mean value across all study sites.

The phase III simulations began by co-simulating the fine spatial resolution channel 2 with the help of the RADARSAT ScanSAR wide imagery. The other channels were simulated in the same manner as in phase II. Table 7.III presents phase III co-simulation ordering. The input parameters otherwise were the same as in phase II.

Table 7.III – Spectral channel co-simulation ordering based on RADARSAT ScanSAR wide and VGT image data.

	Initial co-simulation	Co-simulation	Co-simulation
Site A	SAR vs. 2	2 vs. 4	4 vs. 3
Site B	SAR vs. 2	2 vs. 4	4 vs. 3
Site C	SAR vs. 2	2 vs. 3	2 vs. 4
Site D	SAR vs. 2	2 vs. 3	2 vs. 4

7.2 Phase III Co-Simulation Results

The sequential gaussian simulation algorithm as it was made available in the Deutsch and Journel (1999) software was unable to generate finer spatial resolution images with both the LVM and co-simulation options at the same time. Therefore, realisations using the LVM option could not be generated in phase III.

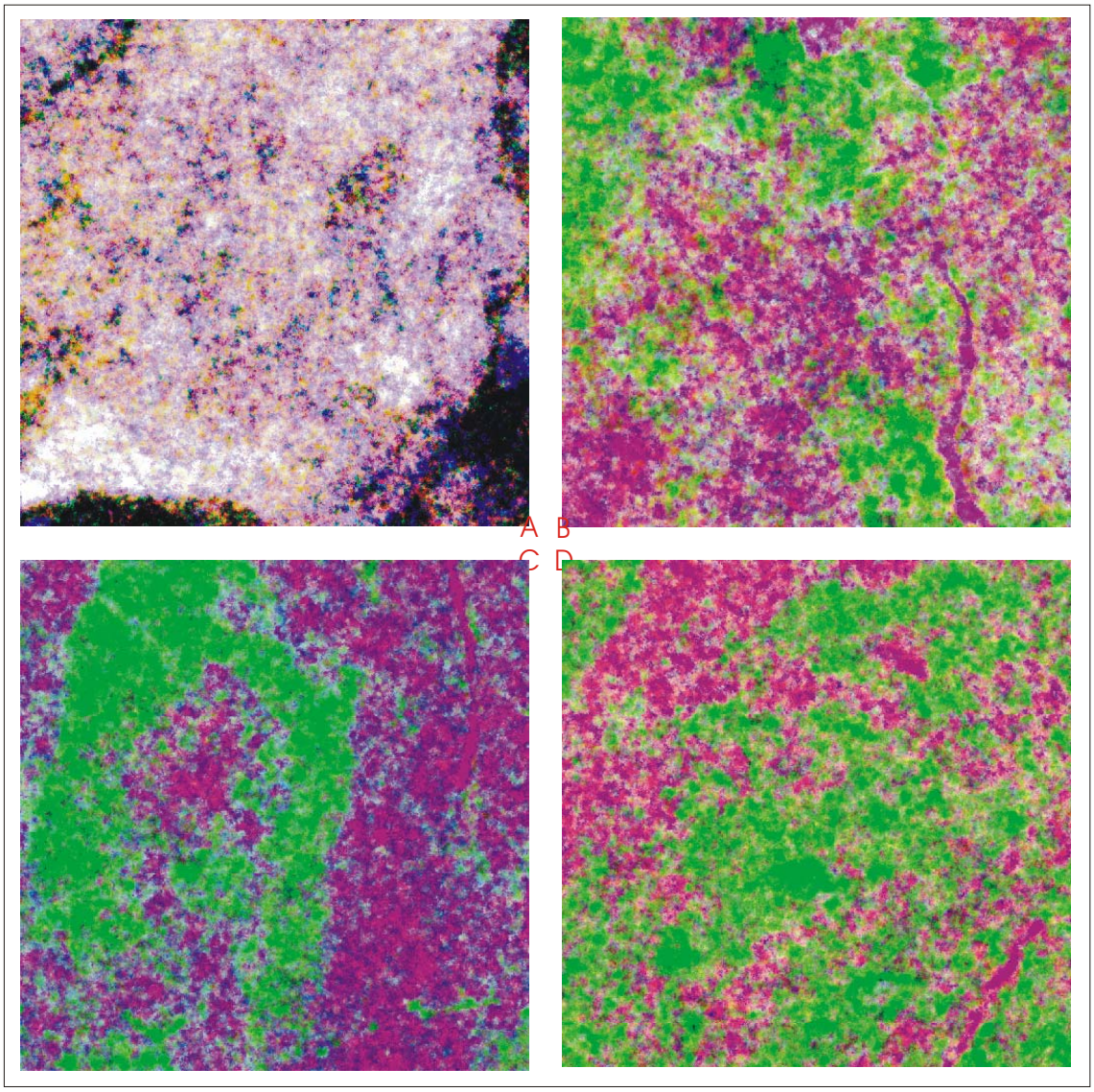

Figure 7.2 – Generated finer spatial resolution imagery conditioned with SAR imagery.

A single realisation was computed generating a multi-spectral image for each of the four study sites (figure 7.2). The resulting finer spatial resolution imagery was visually different then the phase I and II images. The most noticeable differences were the sharper boundaries that could be detected. Also, the imagery did not appear

as diffuse as in the previously generated finer spatial resolution imagery. Comparing the above output to the original HRVIR images presented in chapter 4 gives one a better appreciation of the details resulting from incorporating the SAR imagery into the simulation process.

The study site A imagery (figure 7.2), shows the contour of the Island of Montreal quite clearly. In the upper left corner a section of the Rivière-des-Prairies can be seen that separates the Island of Montreal and Laval. This river was not seen in the other generated finer spatial resolution images. The water/land interface was much less diffuse. Imagery of the island itself is also much more detailed where white areas seem to indicate built up areas while colourful regions are located where vegetation is prominent. For example, the circular region of the Mount Royal was quite easily distinguished in the upper right hand corner of the image. The overall high pixel values associated with built up areas are most likely due to the influence of the SAR imagery.

Study sites B through D were located in less urbanised regions. In the study site B image (figure 7.2), the river that runs through the middle of the image and the lake at the top do not exhibit the expected dark colour for water. However, forested and agricultural regions were quite well delineated in either green for forest or red for agricultural areas. Built up areas on the generated fine spatial resolution imagery appear as white specks. This is due to the strong influence of the SAR imagery. The horseshoe shaped forested area was well defined in the study site C image. The generated finer spatial resolution image of study site D (figure 7.2) also improved

agricultural plot delineation within the generally forested scene much better than those generated in both phase I and II. The generated images of study sites C and D also did not display the water surfaces as dark regions.

The summary statistics were computed for the single realisation images (table 7.IV). The highest mean value computed was for channel 3 of study site D while the lowest was 5.52 for channel 3 of study site A. The median value behaved similarly with the same channels having the highest and lowest computed values. Generally, study site A images produced the lowest overall mean and median values. The maximum values ranged between 21.70 for channel 3 of study site C and 11.50 for channel 2 of study site A. All the minimum values for study site A were equal to zero, while the other study sites had minimum values ranging between zero and 0.41 for channel 2, study site B.

Table 7.IV – Summary statistics for the single realisation finer spatial resolution images co-simulated with RADARSAT ScanSAR wide image data.

		mean	Median	max	min	std dev	Coef var
Site A	Channel 2	5.69	6.35	11.50	0.00	2.03	36%
	Channel 3	5.52	5.95	20.50	0.00	2.07	37%
	channel 4	5.83	6.55	15.99	0.00	1.94	33%
Site B	channel 2	7.88	8.10	15.29	0.41	1.78	23%
	channel 3	7.72	7.81	21.10	0.00	1.14	15%
	channel 4	8.69	8.95	18.01	0.02	1.27	15%
Site C	channel 2	7.08	7.53	15.66	0.03	2.17	31%
	channel 3	8.63	8.55	21.70	0.01	1.32	15%
	channel 4	8.69	8.83	18.52	0.04	1.17	14%
Site D	channel 2	5.27	6.12	12.80	0.05	1.42	27%
	channel 3	9.14	9.25	21.64	0.01	1.06	12%
	channel 4	7.90	7.85	16.98	0.00	1.07	13%

The highest coefficient of variation was found at study site A and ranged between 33% and 37%. Lower coefficients were computed for all the other study sites and ranged between 31% for channel 2 of study site C and 12% for channel 3 of study site D.

The phase III single realisation mean and median values were similar to the original VGT imagery. The maximum difference in the mean across all the study sites was only 0.05. The differences in the median statistic were a little greater with channel 2 of study site D being 0.77 higher than the VGT image median. Except for study site B, the mean and median values for channel 2 had the greatest difference compared to the original VGT imagery. All phase III maximum values were greater and all the minimum values were lower than their respective VGT image counterparts. The differences in the coefficients of variability were not very large ranging from 1% to 6% with the phase III computed coefficients being greater than their VGT image counterparts, except for channel 2 of study site D.

The mean and median values of the phase III generated finer spatial resolution images were lower than those of the HRVIR imagery were. These differences in the mean value ranged between 3.09 to 18.47 for channel 3 of study site D and the median value range between 1.23 and 18.02. The HRVIR images maximum values were all expectedly higher because the phase II input parameters where used. Differences between the two images maximum values ranged between 21.37 and 59.12. The minimum values were lower and only slightly differed from the HRVIR imagery. The coefficient of variation statistic also varied slightly. Channel 2 of study

site A was the only image where the coefficient of variation was higher than the HRVIR imagery. All other images had lower coefficient of variation statistics that ranged from no change to 17% for channel 2, study site D.

No significant differences where observed when comparing the phase II and III summary statistics. The largest differences in the mean were observed at study site A where mean values for the phase III image was greater by only 0.16. The median values generally differed even less. Only very small differences were found in the minimum and maximum values. Overall, the coefficient of variation statistic was greater for the phase II images with slight differences ranging from no change to 6%. The phase III distributions had less variability because of the added constraints of the SAR image data. The addition of the SAR conditioning data basically only resulted in decreasing the variability of the output images when looking only at the summary statistics.

The correlation coefficient statistic computed on the phase III generated images showed that the channel relationships were quite strong (table 7.V). The strongest relationship was computed for the channel 2 vs. 4 pair of study site C at 0.86 and the weakest for channel 3 vs. 4 for study site B at –0.38. All study site A correlation coefficients and channels 2 vs. 4 relationships were positive. In all cases, the relationships all rejected the t-test null hypothesis.

Almost no change was observed between the phase II and phase III correlation coefficients. For the same band combinations, the differences between the two were

between zero and 0.06 and all signs remained the same. However, the phase III correlation coefficients were all stronger than those of the HRVIR imagery.

Table 7.V – Correlation coefficient of the phase III generated images.

	Channels	Correlation
Site A	2 vs. 3	0.69
	2 vs. 4	0.74
	3 vs. 4	0.81
Site B	2 vs. 3	-0.45
	2 vs. 4	0.75
	3 vs. 4	-0.38
Site C	2 vs. 3	-0.66
	2 vs. 4	0.86
	3 vs. 4	-0.65
Site D	2 vs. 3	-0.59
	2 vs. 4	0.80
	3 vs. 4	-0.56

The phase III generated image histograms (appendix) were very similar in shape to those of the VGT imagery. Even the channel 2 histograms that were co-simulated using the SAR imagery were similar to the channel 2 histograms of the VGT imagery. The HRVIR and phase III generated finer spatial resolution histograms were not any more similar visually than the previous two attempts (i.e. phase I and II).

A second set of generated imagery was produced based on the phase III input parameters by computing statistics over a set of 50 realisations (Figure 7.3 and appendix). The order of the co-simulations was the same as that for single realisations (table 7.III).

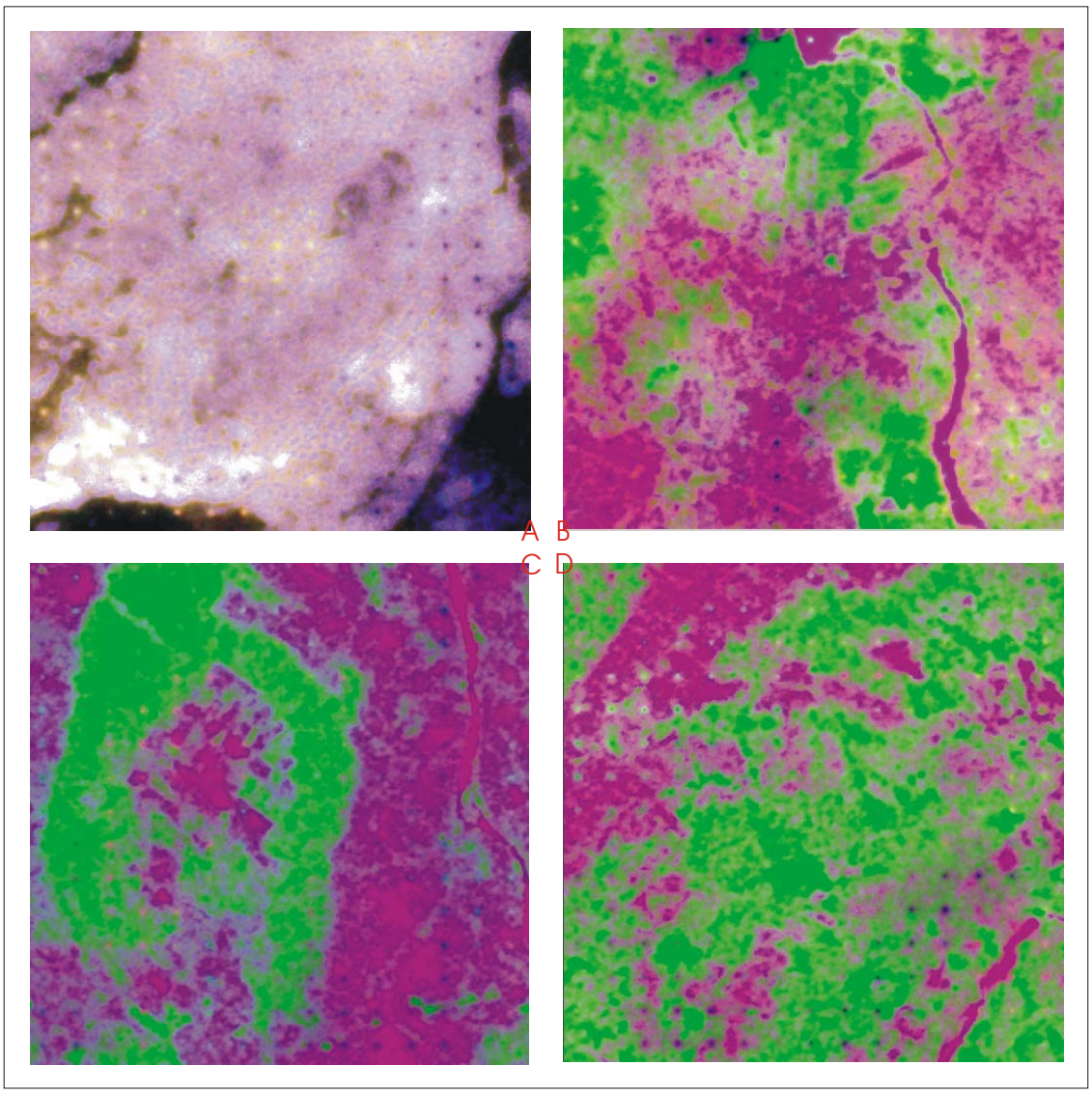

Figure 7.3 – Generated imagery computed from 50 realisations using the E-type estimate and phase III input parameters for study sites A through D.

The images based on the E-type estimate statistic (figure 7.3) produced a much better delineation of different land-cover than was observed in any of the previous simulations. Study site A of the Island of Montreal clearly displayed the water surfaces that were also observed in the fine spatial resolution HRVIR imagery

and the shoreline was strongly delineated. The Island of Montreal itself visually seems to have less variability overall than the single realisation image. Built up areas (which are also areas with a strong SAR signal) were still the brightest and vegetated areas such as the Mount Royal were not as prominent in the E-type estimate image. Another interesting effect observed in the study site A image was a type of road network. However, this is not the case and was most likely an artefact of the simulation algorithm.

The study sites B through D E-type estimate images generated different results (figure 7.3). In these images the forest and agricultural land-cover entities dominated and were strongly delineated but the range of colours had diminished overall. The variability diminished because the E-type estimate retained only the mean values across the 50 realisations. The most notable change however, was the red colour of the water land-cover, which was not dark as expected.

The median, 10^{th} and 90^{th} percentile images are found in the appendix. The median imagery resembled quite strongly the E-type estimate imagery. The images based on the 10^{th} and 90^{th} percentile showed more water and more land respectively because the water values were lower and the land values were higher.

Summary statistics (appendix) were very similar to those of the VGT imagery and as such also did not differ from the results computed from phase II. Similarly, the HRVIR image summary statistics were higher than those based on the

phase III 50 realisations. The same result was observed based on the computed histograms of the phase III generated images based on 50 realisations (appendix).

7.3 Discussion

The results presented above provide an insight into the possibilities of using RADARSAT ScanSAR wide imagery to help generate finer spatial resolution imagery. While the summary statistics did not drastically change compared to earlier attempts (phase I and phase II), the resulting images provided much better spatial detail. This resulted in imagery that was not diffuse and also provided fairly accurate object locations.

One of the first hurdles encountered in phase III was the fact that the SAR imagery did not actually have a strong linear relationship with any of the optical bands. In order for the SAR imagery to have any influence on the co-simulation, a stronger correlation was needed. As a result, the correlation was arbitrarily increased to 0.75. This correlation value was chosen arbitrarily because it could have been higher or lower than 0.75. However it was felt that a higher correlation might bias the simulation toward the SAR imagery itself and produce artefact results. More tests must be carried out in order to see how changes in the correlation affect the resulting co-simulations.

A second decision that was taken while increasing the correlation between SAR and optical bands artificially was to keep the sign of the relationship. The

highest computed correlation was between channel 2 and the SAR images however, their weak relationships ranged between –0.23 and –0.48. Artificially increasing these negative relationships also caused a negative relationship between the SAR and red band water-surface objects. Normally this is not the correct relationship because water-surface objects have a low reflectance in the red band and low return in the microwave band and as a result a positive correlation should have been observed. The total surface area taken up by water in the study sites B through D were quite small and thus did not influence the computed correlation coefficient as much as in the case of study site A. This resulted in a water object always being improperly simulated if one was to use a negative relationship. Further study is required to test whether a positive relationship should always be used when water is present and to see what effect this would have on other types of land-cover.

A second possibility would be to first process the SAR imagery even further. For example, a texture filter could be applied to the imagery and the resulting image would be used to compute the correlation coefficient. If the texture image produces a stronger linear relationship with respect to the visible image channels then the correlation value would not have to be artificially increased and the sign of the relationship would better describe the relationship between the two different types of imagery.

The generated phase III images did provide very good spatial localisation of the vegetated land-cover. The resulting images resemble quite well a fine spatial resolution image. The accuracy of this data must still be investigated if one was to use

such imagery for mapping forest and agricultural land-cover. Another outcome of including the SAR data in the generation of finer spatial resolution imagery was the appearance of built up areas. Normally in the visible spectrum, built-up areas do not appear as bright pixels because man made objects such as buildings are spectrally defined. Built up areas therefore must be spectrally different from the background to actually detect it. The generated imagery with the help of SAR imagery allows the user to spot buildings differently. The high signal return caused by man made structures in the microwave band produces very bright spots in the SAR imagery. In study site A, the result of this high return was translated into very high reflectance values producing white areas in the optical imagery. The other study sites also produced white flecks in regions where towns and buildings were expected. The negative relationship however that was used to generate the imagery at those study sites must be further investigated in order to be sure that the same land-cover type is generated throughout.

Results of the phase III implementation also showed that summary statistics were not similar to those of the HRVIR imagery. This result echoed those found during phase II. Although in phase III the appearance of the generated finer spatial resolution imagery was greatly improved the statistical similarities between the original coarse spatial resolution VGT imagery were still strong.

The RADARSAT ScanSAR imagery was used to influence the simulated output using the co-simulation approach. This approach only allowed the first optical band that was simulated to be influenced directly by the SAR imagery. Channel 2

was used in every case and the histograms of the generated finer spatial resolution red band did not show any clear signs of SAR influence because of the back-transformation. Without any significant influence on the first simulated band, the other bands (channels 3 and 4) were primarily influenced by their relationship to channel 2.

Geometric registration was an important step in phase III because the optical data had to be overlaid by the SAR data. Misregistration would cause objects to be placed in the wrong location. The water surfaces of the phase III generated images of study sites B through D appeared as red. At first, it was concluded that the cause was due to misregistration. However, after verifying the geometric registration a different reason was found i.e. the negative relationship between SAR and the red band. As a result, preparatory steps must be carefully executed and caution must be used when interpreting the stochastic imaging results.

The imagery that was produced using 50 realisations also produced some interesting results. Study site A generated finer spatial resolution imagery, especially based on the E-type statistic, produced what looked like a road network on the Island of Montreal. Although it appears to be a road network, it would be impossible that the fusion of the VGT and RADARSAT ScanSAR imagery could ever produce such fine spatial details. The cause of this effect is most likely due to the influence of the SAR imagery in an urban setting. Patterns are quite pervasive in urban settings where, for example, a residential area made up of single family homes produces a specific

pattern that can be observed in the SAR imagery. This influence generated the patterns that are observed in the generated images based on 50 realisations.

Familiar objects or entities are what allows one to classify land-cover based on remotely sensed imagery. The stochastic nature of the images produced in phase I and II were impossible to interpret directly because of the lack of familiarity. Objects or entities were not generated but rather spatial data was stochastically assigned in order to satisfy the input parameters of the stochastic imaging algorithm. The addition of SAR imagery at the wanted resolution provided the necessary data in order to place simulated values in the correct location thereby improving the resulting imagery in terms of familiarity. Without this familiarity the notion of map accuracy becomes useless in the traditional context because no two simulated images would be exactly alike.

Chapter 8 – Extracting Information from Generated Imagery

Information extraction is the most difficult part of any remote sensing investigation. At this stage detection, segmentation and classification are the processes by which information is extracted. Here the goal was to spectrally segment the generated finer spatial resolution imagery in order to compare them to the HRVIR and VGT image based spectral segments. The segmentation process was necessarily done automatically for exploratory reasons and because of the nature of the generated images. Segmentation alone does not guarantee land-cover information, however it is the first necessary step. The final step is to compare the spectral segments to known classes in order to evaluate the suitability of the generated finer spatial resolution imagery.

A fine spatial resolution image based on a recorded ground scene can be interpreted visually by a trained eye based on the knowledge of location, size, shape and tone of detectable objects. In this case, the generated finer spatial resolution imagery did not always produce images that resembled regular ground scenes because of the stochastic nature of the algorithm and the lack of spatial information when scaling-down. Therefore, knowledge of location, size and shape are not necessarily applicable to phase I and II images. Only in phase III with the infusion of RADARSAT ScanSAR imagery did the simulated output resemble a real ground scene even though artefacts were observed within the imagery.

Chapter 8 focuses on the extraction of land-cover and the calculation of the area taken up by each land-cover. Land-cover information based on coarse spatial resolution imagery does not provide the same details possible with a finer spatial resolution image. Therefore, estimates based on coarse spatial resolution imagery can be erroneous when compared to local level land-cover classes.

8.1 Automated Image Segmentation

Unsupervised image segmentation was applied to all the original and generated phase I, II and III images using all three spectral bands. Supervised methods were considered unsuitable for this application because known land-cover objects could not be defined. Among the unsupervised segmentation techniques, the K-means algorithm was chosen.

The K-means algorithm uses the spectral feature space of the three channels making up the images to find the centres of spectral clusters that are similar spectrally. The K-means algorithm only requires the user to input the maximum number of segments. For exploratory purposes, the K-means algorithm was run twice on each image. The first segmentation was based on 16 segments while the second was based on 10 segments.

The actual number of groups was decided based on viewing the original imagery. Both a lower threshold and upper threshold were decided upon because some study sites had fewer obvious land-cover classes while others had more. Too

large a number of classes were not wanted because of the difficulty that was foreseen in matching up the different segments in spectral feature space between images. The results of the segmentation are presented below. The figures are three-dimensional graphs representing the mean value of each segment for each spectral channel. Channel 2 (red band) is presented along the x axis, channel 3 (NIR band) along the y axis and channel 4 (SWIR band) along the z axis. The total number of pixels within each segmented group is shown at the location in spectral feature space as a percentage of the total. The different images were coded in order to easily identify them in the graphs (table 8.I).

Table 8.I – Codes used to identify images in the graphs.

VGT	SPOT 4 coarse spatial resolution image	HRVIR	SPOT 4 fine spatial resolution image
LVM1	LVM phase I generated image	LVM2	LVM phase II generated image
P1	Co-simulated phase I generated image	P2	Co-simulated phase II generated image
P1E	E-type estimate phase I generated image	P2E	E-type estimate phase II generated image
P1Q1	1st quantile phase I generated image	P2Q1	1st quantile phase II generated image
P1Q5	Median phase I generated image	P2Q5	Median phase II generated image
P1Q9	9th quantile phase I generated image	P2Q9	9th quantile phase II generated image
P3	SAR/co-simulated phase III generated image	P3E	SAR/co-simulated E-type estimate generated image
P3Q1	SAR/co-simulated 1st quantile generated image	P3Q5	SAR/co-simulated median generated image
P3Q9	SAR/co-simulated 9th quantile generated image		

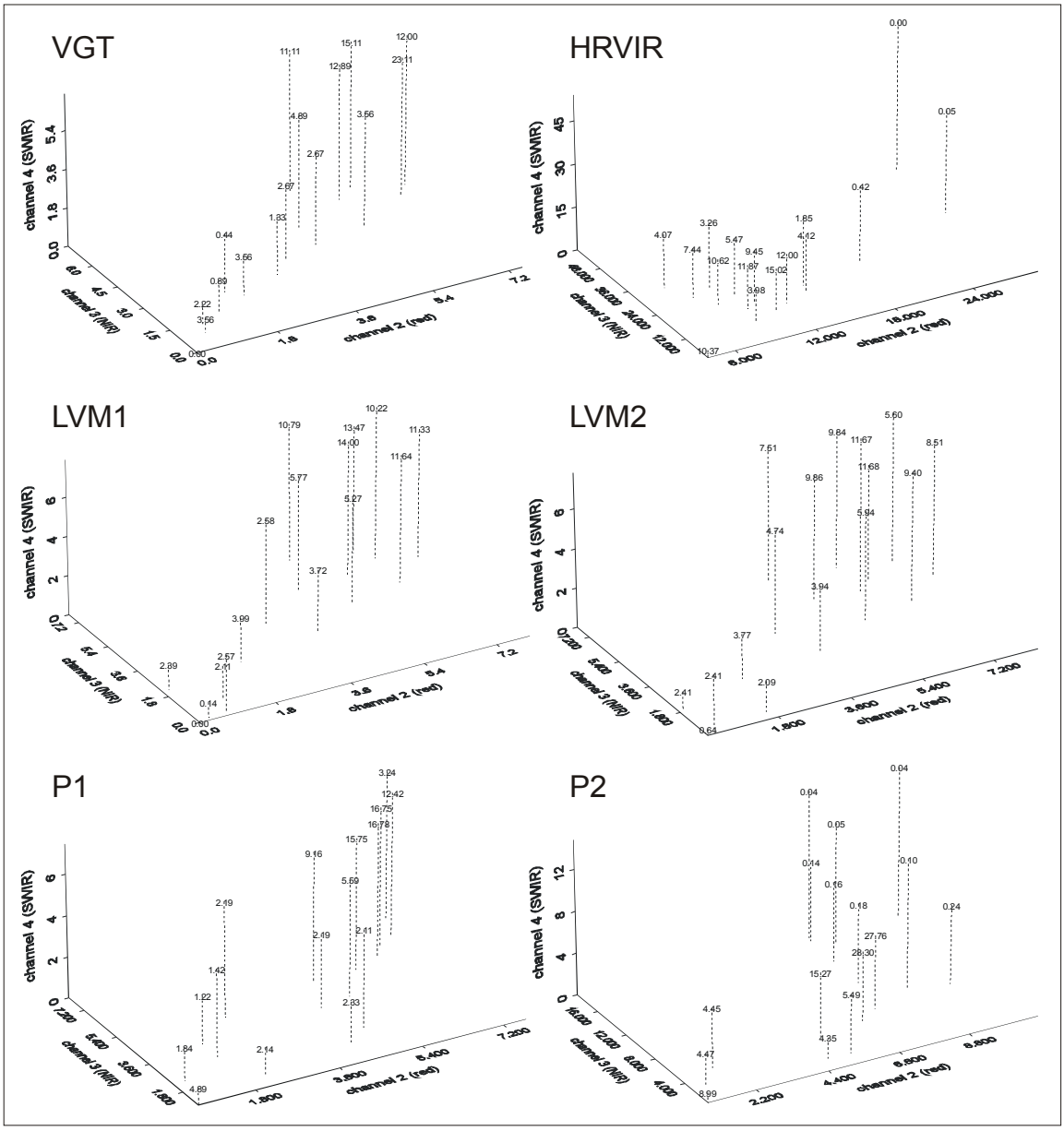

Figure 8.1 – Three-dimensional representation of the spectral groupings in spectral feature space after segmentation based on the K-means algorithm. The results shown are for study site A and a maximum of 16 groups.

The segmentation results for study site A are presented in figures 8.1 through 8.3. The segmentation of the original VGT and HRVIR are shown in the upper left

and right respectively of figure 8.1. The VGT and HRVIR spectral segments were quite different. The VGT image generated spectral groupings that have a planar trend with little variability. A generally equal distribution of groupings across all spectral values was observed. The HRVIR imagery on the other hand produced many groupings with low spectral values across all the three channels. Only three groups were observed that were made up of high spectral values.

In figure 8.1 (middle graphs) the phase I and II generated images using the LVM option are presented. The resulting segmentation of these two images produced very similar patterns. The distribution of spectral segments of the LVM phase I and II images however generally follow the planar distribution found in the VGT imagery. Differences that were observed were the many higher valued spectral segments in the LVM generated images. The bottom graphs (figure 8.1) present the co-simulated single realisation phase I and II images. The spectral segments from these images were also similar to the VGT images spectral segments.

The K-means algorithm was also used to segment the E-type estimate, median, 10^{th} and 90^{th} percentile images (figure 8.2). The segmented phase I E-type estimate imagery produced groupings that were almost perfectly planar (figure 8.2 – upper left). The phase II E-type estimate image however showed a slight curvature. The spectral segments however also tended to increase in a planar fashion beginning from segments made up of low spectral values to groups of values with high spectral values. The median generated imagery spectral segments were almost identical in

structure to those of the E-type estimate (figure 8.2). More variability in the lower spectral region could be observed in the phase II median graph.

As expected, the resulting spectral segments of the phase I and II 10^{th} percentile images differed from the E-type estimate and median segmentations. The most notable change was the higher number of pixels within the lower spectral segments. The 90^{th} percentile phase I segmentation showed a slight deviation toward the channel 2 axis compared to the E-type estimate segments. The phase II 90^{th} percentile image produced quite a pronounced shift toward the channel 2 axis before deviating again (almost perpendicularly). Note the majority of the segments were in a region where channel 2 and 4 had high spectral values but not channel 3.

The phase III results of the spectral segmentation are shown in figure 8.3. The single realisation image graph of the spectral segments differed from both the VGT and HRVIR graphs. The actual spectral segments were distributed quite unevenly. The E-type estimate segments however still had a linear effect reminiscent of the VGT image results. The median image segments were not as evenly distributed, with four groupings close to the upper limits of values for all three channels. The 10^{th} percentile segments resulted again in a planar distribution oriented in the z direction. However, the 90^{th} percentile segments mimicked those that were observed in the same phase II results.

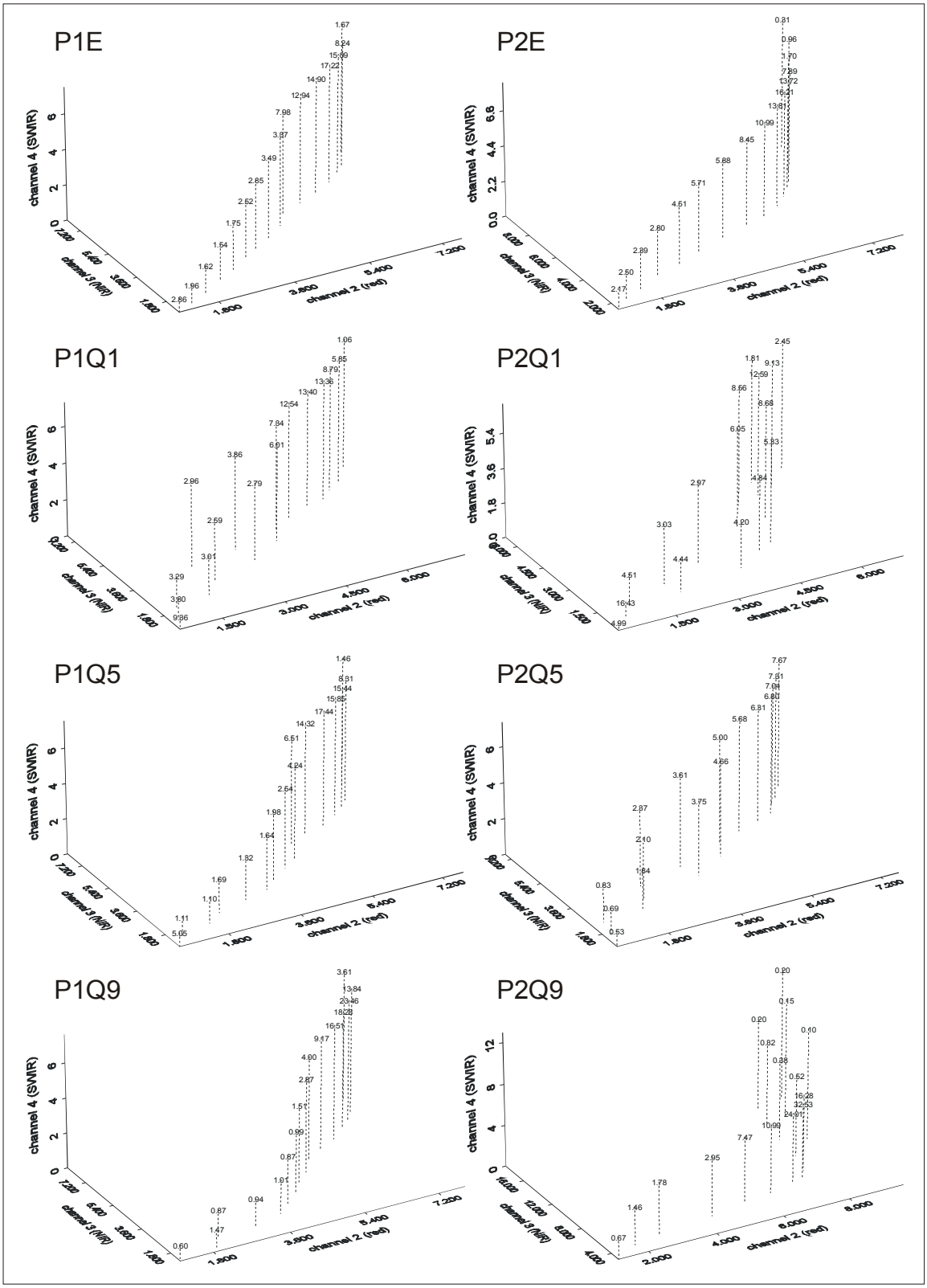

Figure 8.2 – K-means segmentation results for phase I and II statistical images. The results shown are for study site A and a maximum of 16 groups.

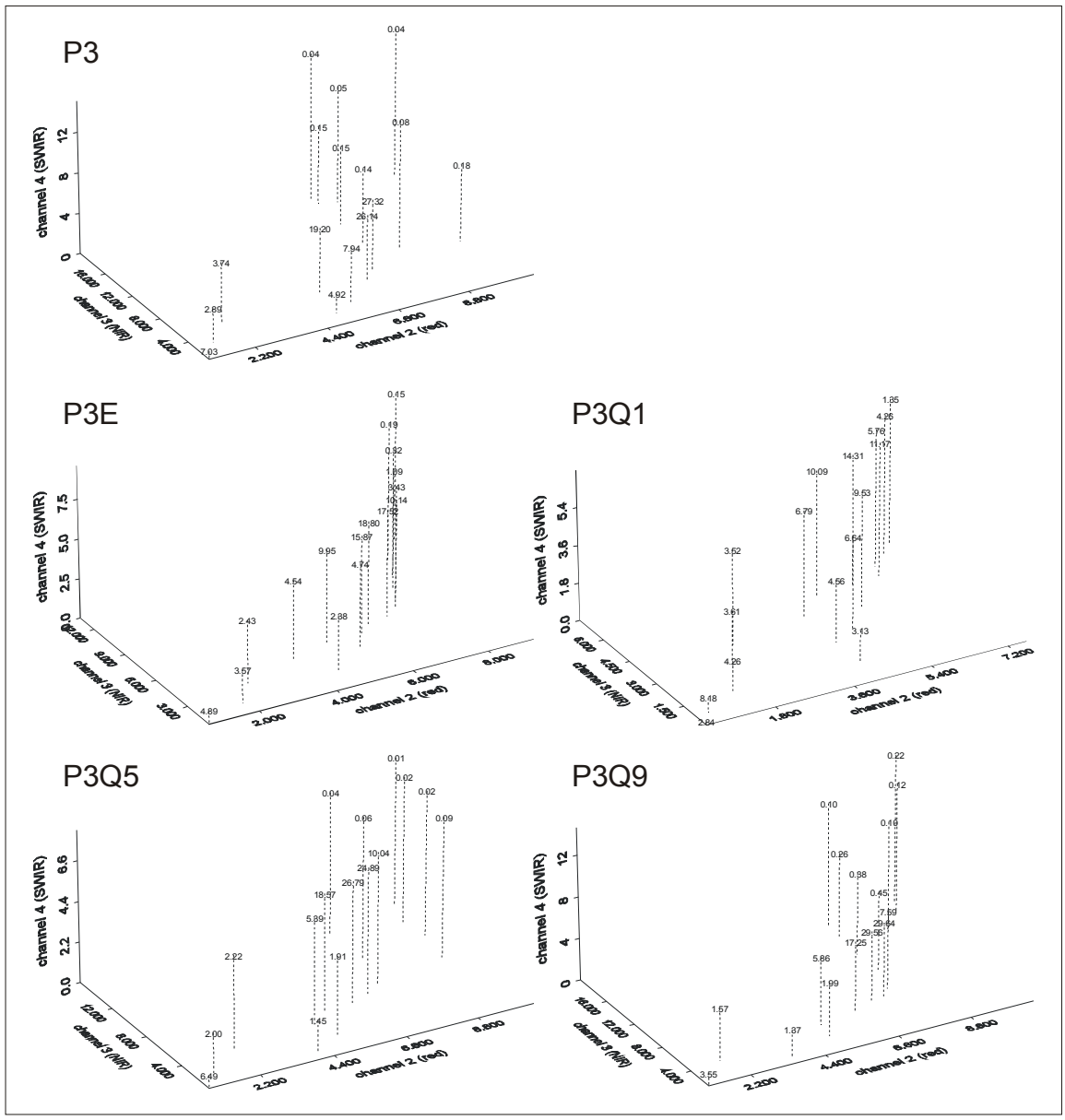

Figure 8.3 – K-means segmentation phase III results for study site A. The results shown are for study site A and a maximum of 16 groups.

The second set of segmented images for study site A was based on a maximum of 10 segments (figures 8.4 to 8.6). Again the VGT and HRVIR images did not produce the similar spectral segments, as was expected (figure 8.4). The graph

based on the VGT data showed comparable results as observed with 16 segments with a planar sequence of spectral groups. The HRVIR image on the other hand did not produce the same spectral clustering. Specifically the group of low value spectral segments was no longer present as was seen with 16 groups.

The phase I LVM based imagery with 10 spectral segments had many similarities to the VGT image output. The LVM II based imagery retained approximately the same configuration however more segments were found in the higher spectral regions. The single realisation phase I and II images resulted in a different arrangement in spectral feature space (figure 8.4) than both the VGT and HRVIR results.

Figure 8.5 presents the segmented spectral clusters of the E-type, median, 10^{th} and 90^{th} percentile images. For the most part, these diagrams behaved exactly in the same manner as those for the 16 spectral segment case. The phase III results (figure 8.6) also showed the same tendencies as the spectral segments based on 16 segments.

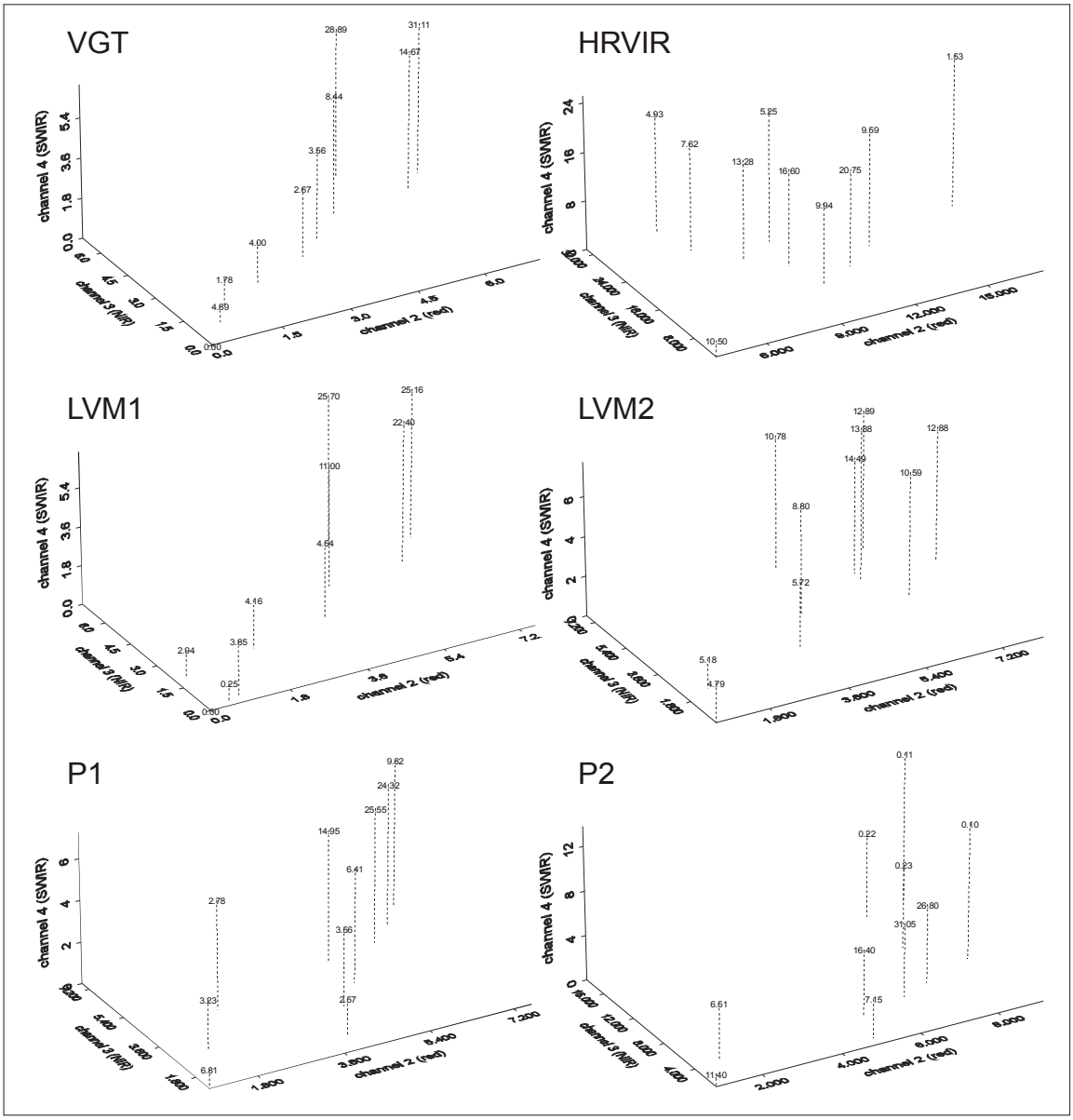

Figure 8.4 – Three-dimensional representation of the spectral groupings in spectral feature space after segmentation based on the K-means algorithm. The results shown are for study site A and a maximum of 10 groups.

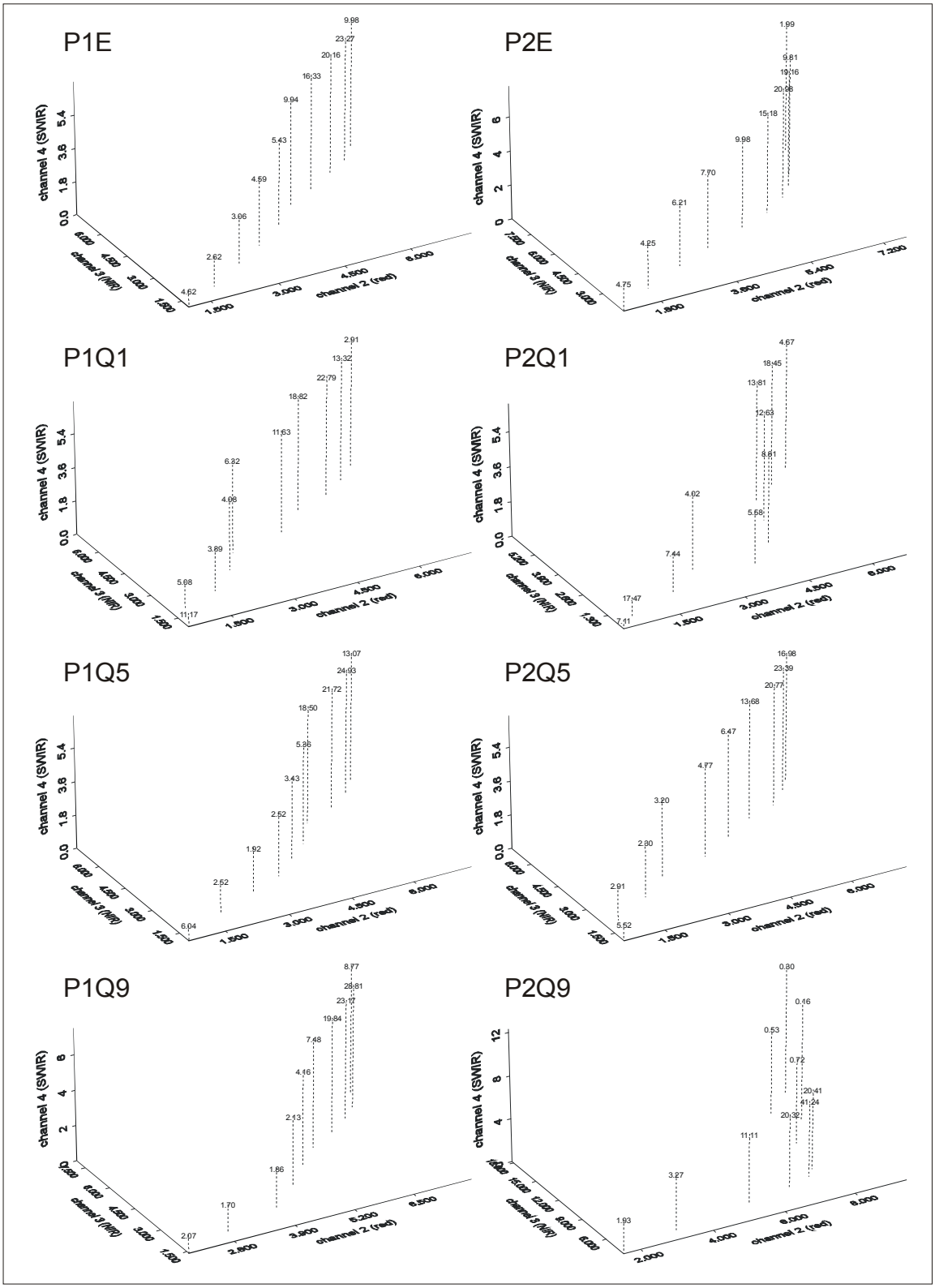

Figure 8.5 – K-means segmentation results for phase I and II statistical images. The results shown are for study site A and a maximum of 10 groups.

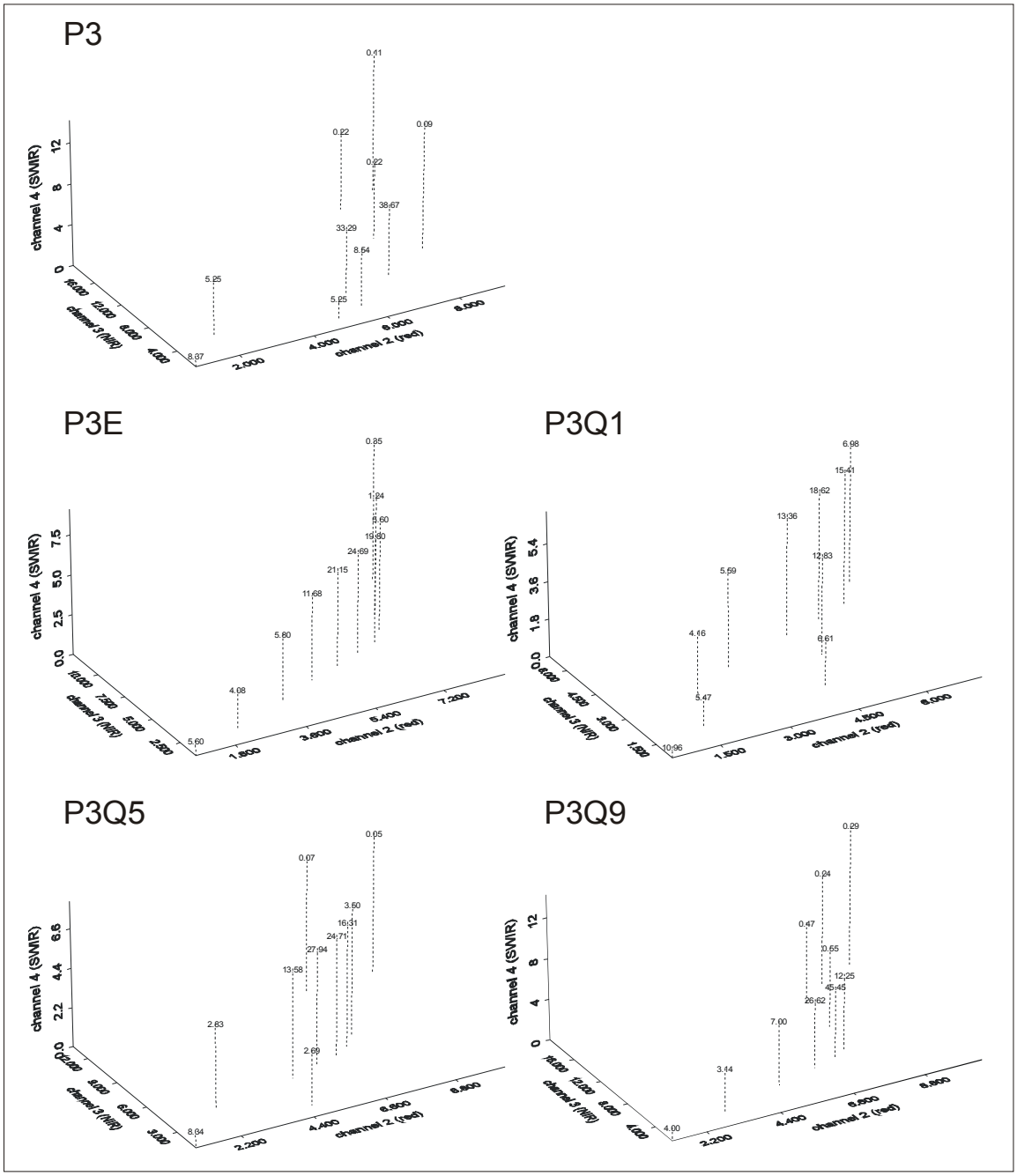

Figure 8.6 – K-means segmentation phase III results for study site A. The results shown are for study site A and a maximum of 10 groups.

The computed spectral segments based on 16 classes for study site B (an agricultural region) are presented in figures 8.7 to 8.9. The graphs of the VGT and HRVIR spectral segments again were not similar (figure 8.7). While most of the spectral clusters were found in the higher ranges for the VGT segments, the HRVIR segments were mostly concentrated in the lower spectral ranges.

The phase I LVM spectral segments resembled the VGT graph with a few more lower spectral value clusters while the phase II LVM spectral segments generally had a greater distribution of clusters in the higher spectral value region (figure 8.7). The phase I single realisation image mimicked again the VGT spectral clustering. The phase II single realisation image produced spectral clusters that varied in the channel 2/3 space with fairly high channel 4 spectral values (figure 8.7).

The phase I E-type estimate and median images spectral segments were very similar (figure 8.8). The phase II E-type image showed the majority of the segments at higher reflectance values, while the median graph spectral clusters were spread out across the channel 2/3 plane with high values in the SWIR band. The 10^{th} percentile and 90^{th} percentile based images produced different results as expected. The 90^{th} percentile images generated spectral clusters that made an ‘L’ shape in the channel 2/3 plane (figure 8.8).

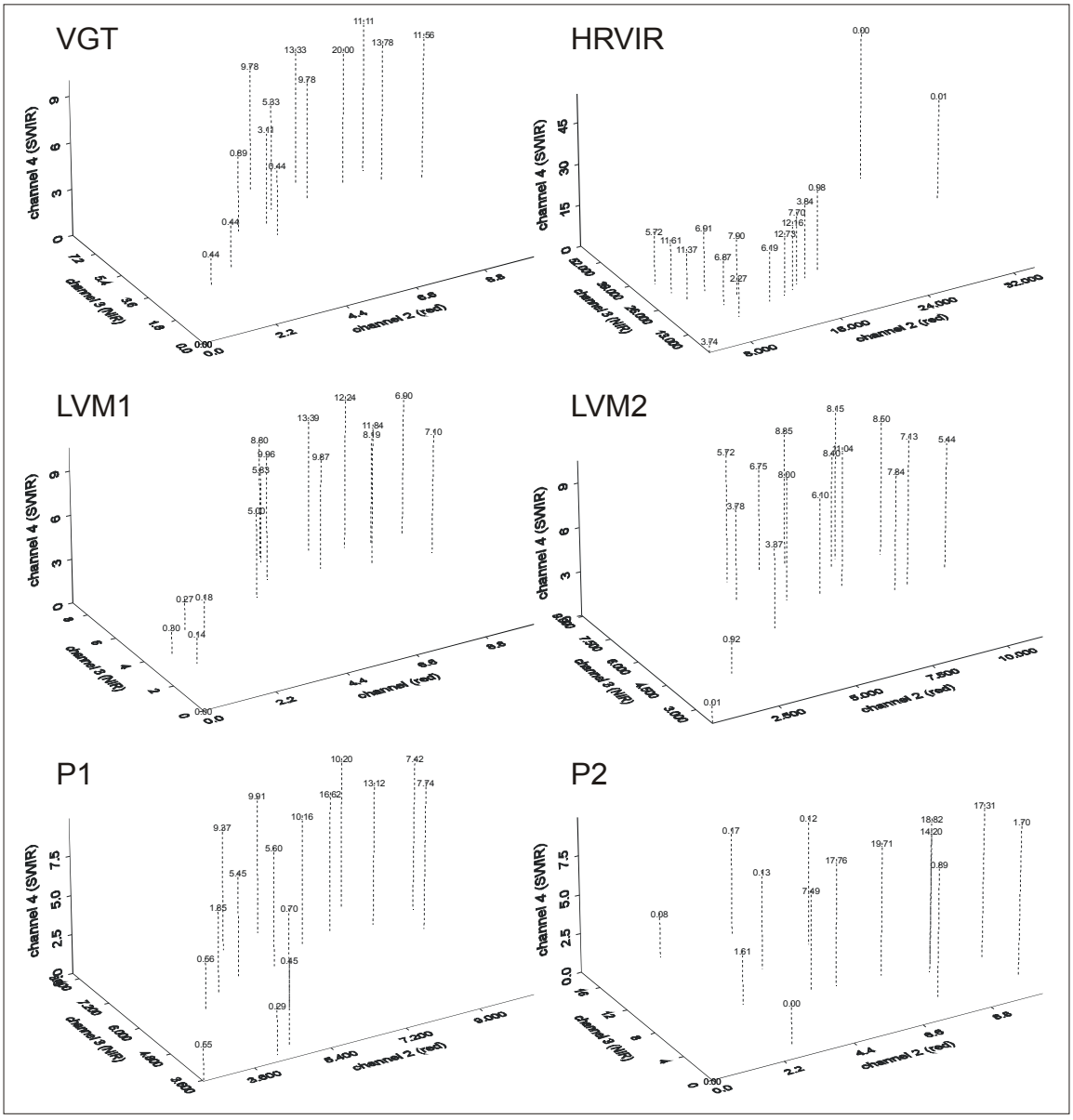

Figure 8.7 – Three-dimensional representation of the spectral groupings in spectral feature space after segmentation based on the K-means algorithm. The results shown are for study site B and a maximum of 16 groups.

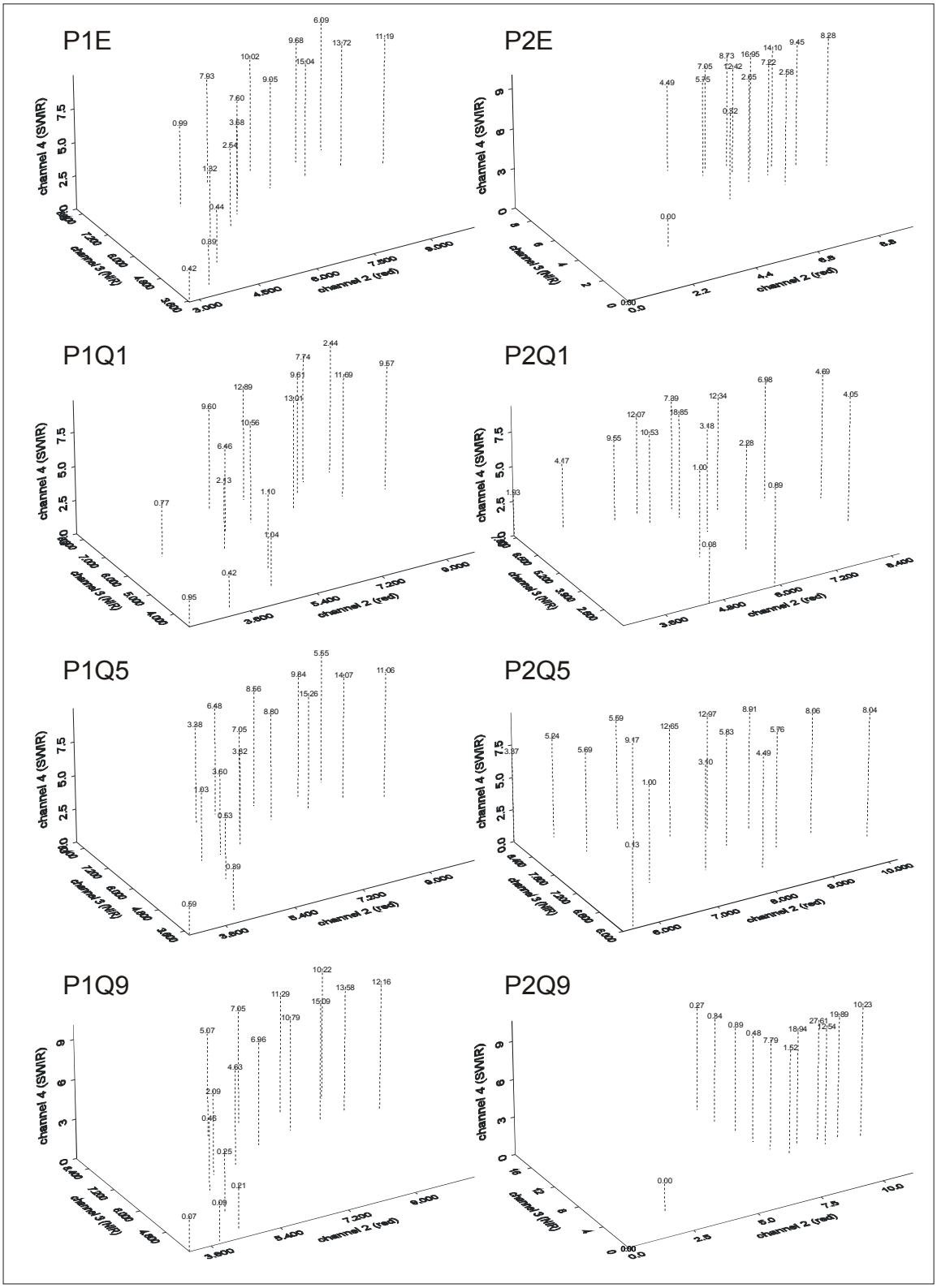

Figure 8.8 – K-means segmentation results for phase I and II statistical images. The results shown are for study site B and a maximum of 16 groups.

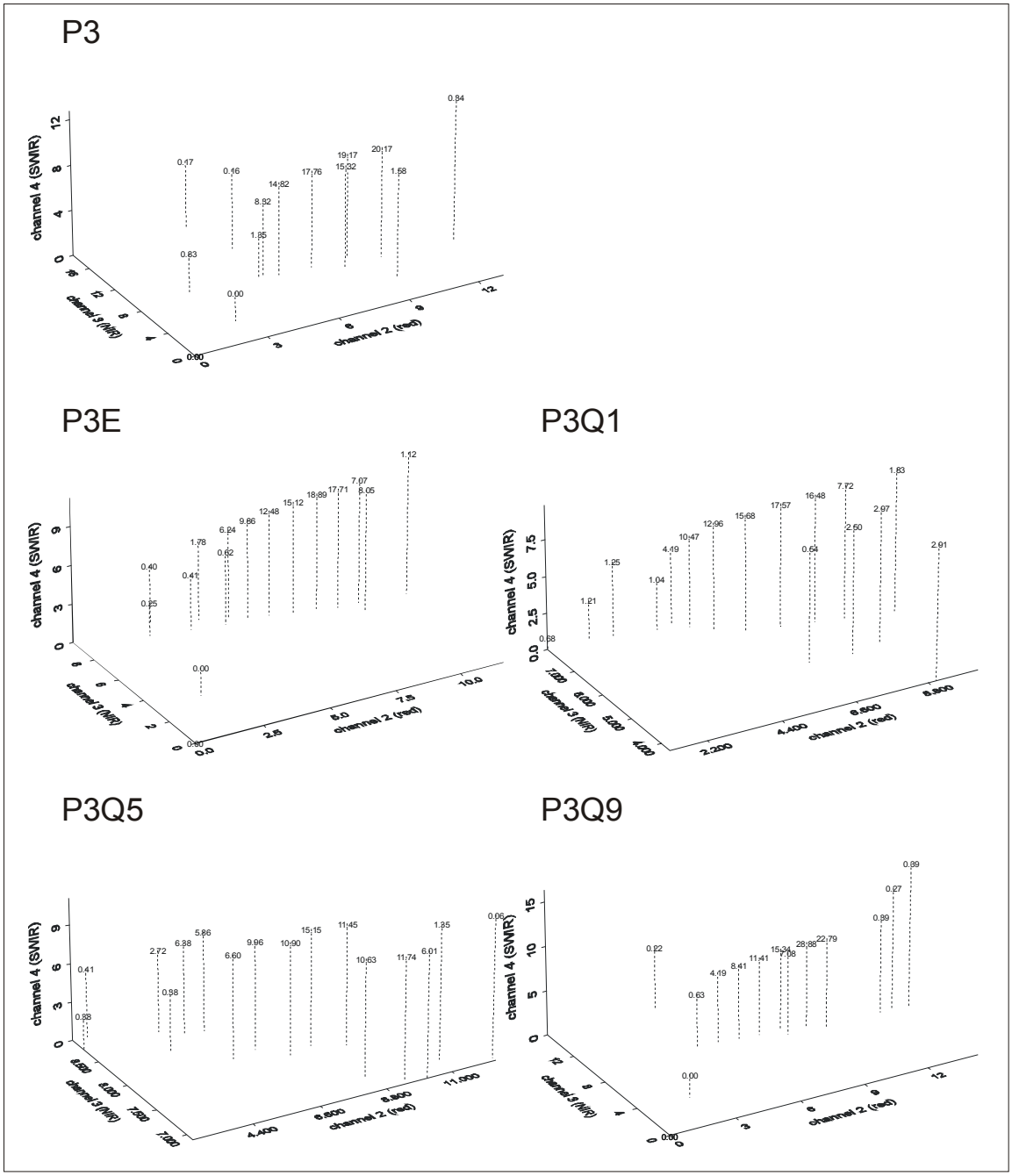

Figure 8.9 – K-means segmentation phase III results for study site A. The results shown are for study site B and a maximum of 16 groups.

The phase III imagery did not produce the same spectral segments as those observed in the phase I and II images (figure 8.9 – top). The E-type estimate and median spectral clusters were not similar either. There seemed to be a negative relationship in the median spectral segments between channels 2 and 3. The 10^{th} and 90^{th} percentiles again differed from the other phase III spectral graphs.

The study site B generated images were also segmented based on a maximum of 10 clusters. The resulting three-dimensional spectral space representations provided similar results as those found above based on 16 clusters (appendix).

Similar trends were observed for study sites C and D (appendix). Spectral segment configurations derived from the VGT and HRVIR images were always different. The phase I and II LVM based images resulted in spectral segments that were similar in form to those of the VGT imagery. Another generated image that consistently and expectedly produced similar spectral segments to those of the VGT imagery was the phase I co-simulated images. The phase II co-simulated images tended to differ from both the VGT and HRVIR images spectral segment formations and were more variable in spectral feature space then the VGT imagery. Furthermore, the differences between having segmented 10 or 16 segments was variable. Generally, the 10 segment graphics matched closely the formation based on 16 clusters. Some curious spectral cluster arrangements were observed (appendix) but these were deemed unimportant because our goal was to try and match spectral segments between the different images, which could not be done.

8.2 The Difficulty of Validation

Validation requires that known objects or pixel values be compared to those that are under study. Normally, this would be done based on location. Stochastic imaging however prevents such validation because spatial location is not preserved. This is further hindered by the fact that the generated imagery is segmented differently depending on the manner in which it was generated. The previous section demonstrated the difficulty with which to match spectral segments between different images.

The fact that spectral classes could not be linked between the different images led to the need for a different kind of comparison. From the above figures one could see that even though different images were generated spectrally, segmentation of the data was possible. Therefore the clustered data was compared by the total percentage per segment, i.e. each segment was ranked by the total percent area. Ranking the data compared the segments based on total area.

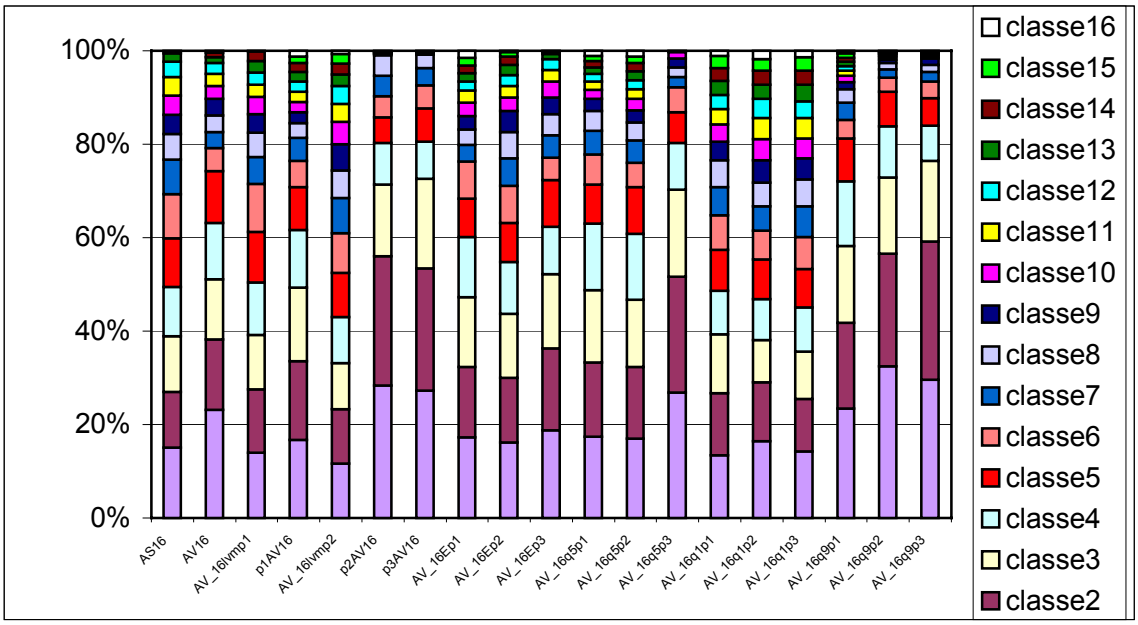

Figure 8.10 – Ranked spectral segments based on the pixel count. The results shown are for study site A and a maximum of 16 groups.

Figure 8.10 presents the ranked segments for each of the generated images for study site A using 16 classes. The largest spectral segment was in purple and found at the bottom of the graph. Comparing only the largest spectral segments, one can immediately see the large disparity between each of the images compared to the 'true' image, that of the HRVIR image (AS16 – figure 8.10). The graph also showed that not all images necessarily had 16 segments or at least some segments contained very few pixels. This was quite obvious with the phase II and phase III based single realisation images.

Comparing spectral segments in this manner helped see how much cover each segment occupied. Any change in the percentage of cover (i.e. a segment is made up

of more or less number of pixels) would generate a graph that is different from the HRVIR 'ideal'. The HRVIR image was the first graphic on the left in figure 8.10. The original VGT (AV16 – 8.10) image showed that the largest portion of segments was greater by just under 10% compared to the HRVIR image. A difference of 10% on the VGT image was equal to 22.5 pixels. That was quite a large difference considering it was the segment with the greatest number of pixels. The graphic clearly showed the variability in spectral segments among the generated images. Only the VGT image had a different spatial resolution (1000 m). All the other images were based on a 20 m spatial resolution.

From figure 8.10, the generated image that most resembled the HRVIR spectral segments was the phase I LVM based image. For the most part the larger segments were fairly similar in terms of the number of pixels each segment contained. Some differences were observed in the smaller sized spectral segments. The largest differences were observed in the images that were generated using the co-simulation approach. Both phase I and II single realisation images had over estimated the percentage of the largest segments compared to the HRVIR data. This was not however true for the post-processed based imagery where only the median and 90th percentile images had segment percentages that were much greater than that of the HRVIR imagery.

The bar graphs (8.10) alone will not provide land-cover information that is required. Figure 8.11 presents the images based on the spectral segments. The pseudo colours were the same as those presented in figure 8.10. Comparing the VGT and

HRVIR images clearly showed the difference in not only the detail that was available but also in the manner in which the images were segmented and the total area each segment encompassed. A very clear example was the area taken up by water. In the VGT scene, water was coloured blue while in the HRVIR image it was red. In this particular case it seemed that the blue and red segment traded places.

The generated finer spatial resolution images were very much different from both the coarse VGT and fine HRVIR spatial resolution images. Although the phase I LVM based image still had overtones of the large pixels of the VGT image the segmentation clearly showed that location was not necessarily maintained. This was even more obvious in the phase II LVM based image where the spectral segmentation was spatially dissimilar to the VGT image.

The phase I and II generated co-simulation images were even more difficult to decipher because of the many small clusters that peppered the study site A. These images produced spectral segments unlike any other image. The phase III co-simulated imagery however did seem to localise the land-cover segments in a manner similar to the HRVIR images. This was surprising because the spectral segment rankings of the HRVIR and phase III single realisation images were quite different.

The post-processed based images were very different (figures 8.12 and 8.13). They were different because the spectral segments did not seem to be based on the underlying scene. A general trend could also be observed where the complexity of the simulations increased with the input parameters. The phase I imagery was based on

the VGT input parameters which were very coarse and therefore the output images were also course. These images resembled smoothed maps just like the VGT image. The phase II imagery on the other hand had fine spatial scale input parameters that obviously had a local effect on the resulting simulations. Finally, the phase III images showed the most variability with the inclusion of SAR data. This tendency was observed across all the computed statistics.

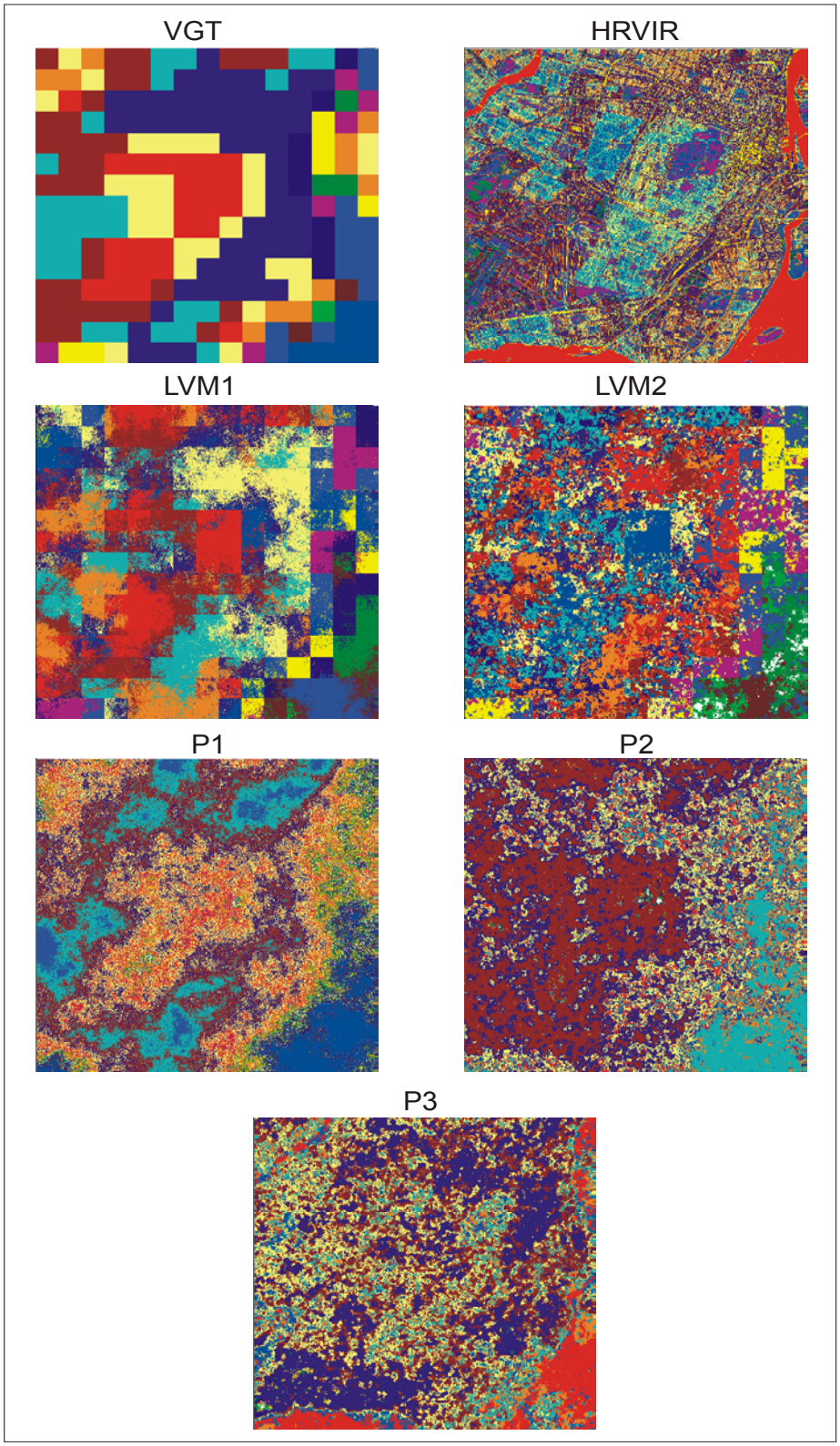

Figure 8.11 – Classified spectral segments based on percent cover of study site A with 16 classes (single realisation images).

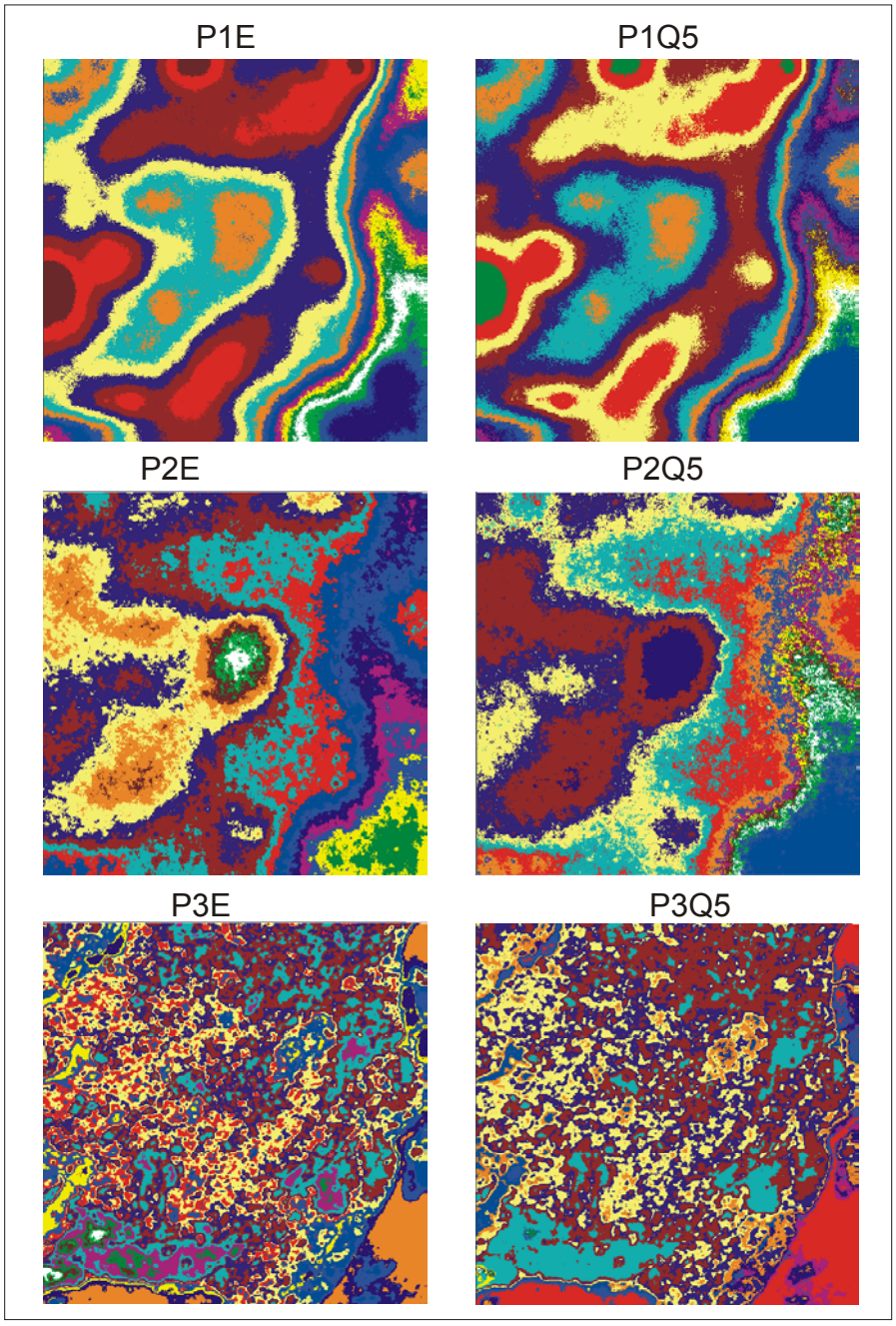

Figure 8.12 – Classified spectral segments based on percent cover of study site A with 16 classes (E-type estimate and median images).

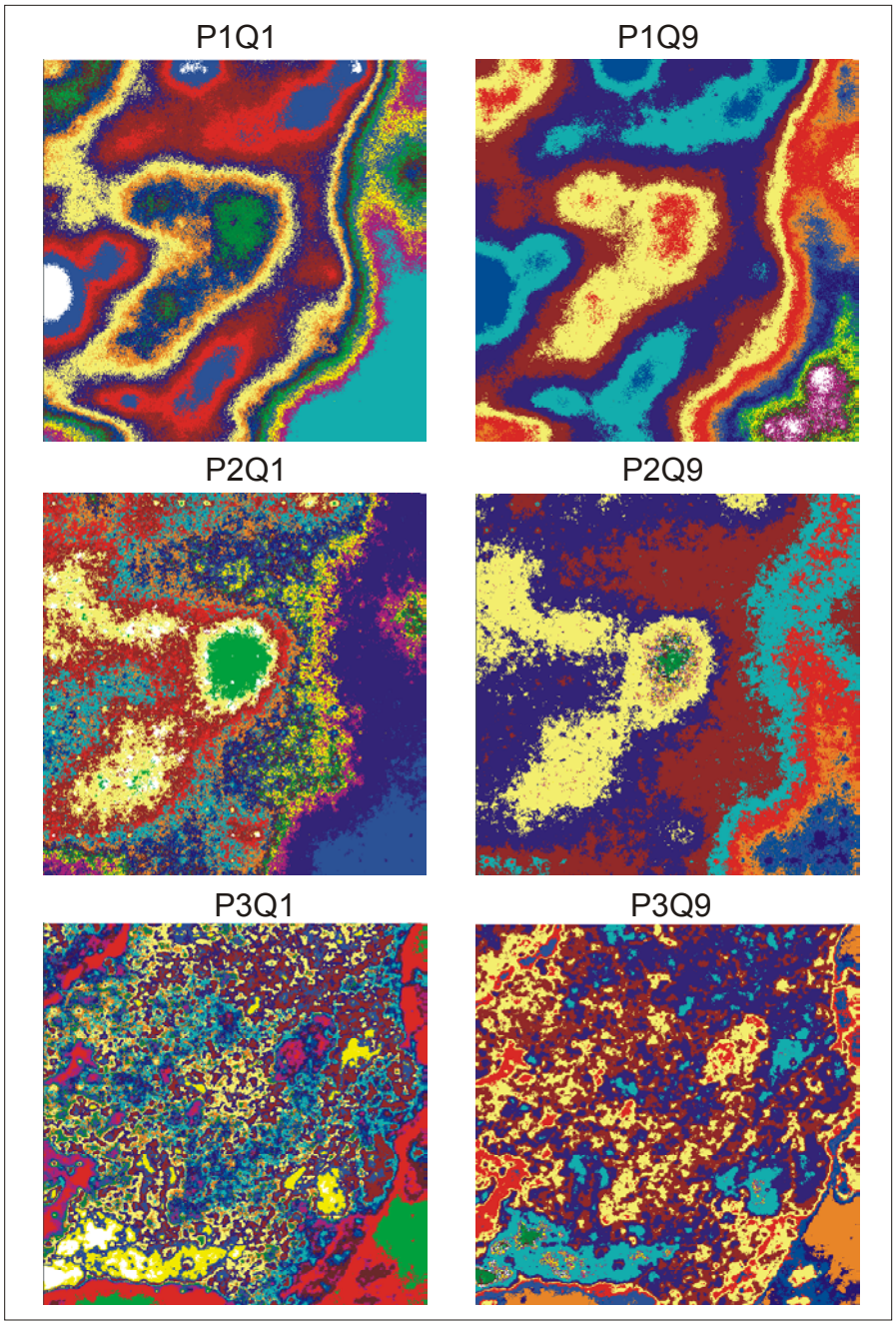

Figure 8.13 – Classified spectral segments based on percent cover of study site A with 16 classes (10^{th} and 90^{th} percentile images).

Figure 8.14 presents the results of segmenting spectrally the study site A images into 10 clusters. The K-means algorithm output based on 10 segments was

different than that based on 16 segments. Greater disparity was observed between the VGT and HRVIR spectral segments. Comparing the other images results to those of the HRVIR percent cover distribution showed that with 10 segments there were fewer similarities between images than when 16 clusters were used.

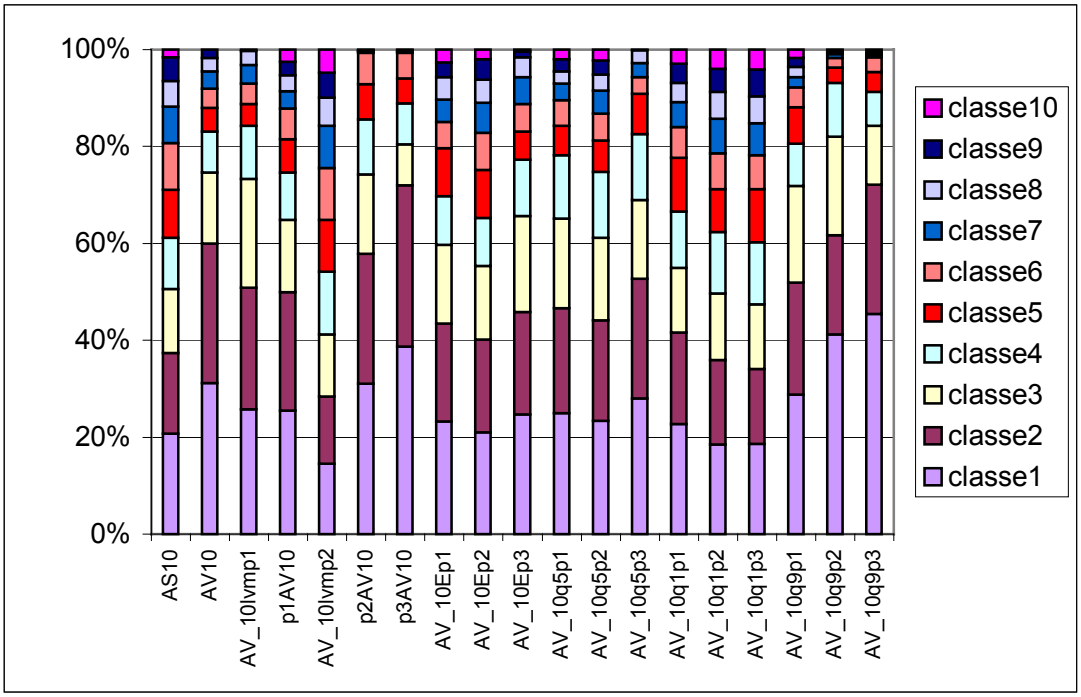

Figure 8.14 – Ranked spectral segments based on the pixel count. The results shown are for study site A and a maximum of 10 groups.

The ranked spectral segments were again used to produce pseudo colour images based on 10 clusters (figure 8.15). In this set, the phase II and III single co-simulation images showed similarities in the spatial position of the ranked clusters. Several images also did not generate the maximum number of spectral segments, such as the VGT and phase I LVM images.

The post-processed images that were produced using only 10 spectral segments and based on the study site A showed similar results (figures 8.16 and 8.17) to their 16 spectral segment counterparts.

The same procedure was applied to the study site B (agricultural scene) images with 16 spectral clusters (figure 8.18). Again, the HRVIR and VGT images produced very different outcomes resulting in segment pixel counts that were difficult to merge. The phase I LVM images cluster percentages on the other hand produced clusters that were quite similar to those derived from the HRVIR imagery. This same result was observed in the study site A with 16 spectral segments. All other single realisation images had quite different cover percentages than the HRVIR image.

Looking at figure 8.18 the phase II and III co-simulated imagery produced some of the worst results compared to HRVIR imagery. The first spectral segments were at least 10% greater than the HRVIR first segment and the others were also much higher. The phase II and III co-simulated image outputs were very similar which was not too surprising because they were based on the same input parameters. No other generated imagery produced a similar pattern.

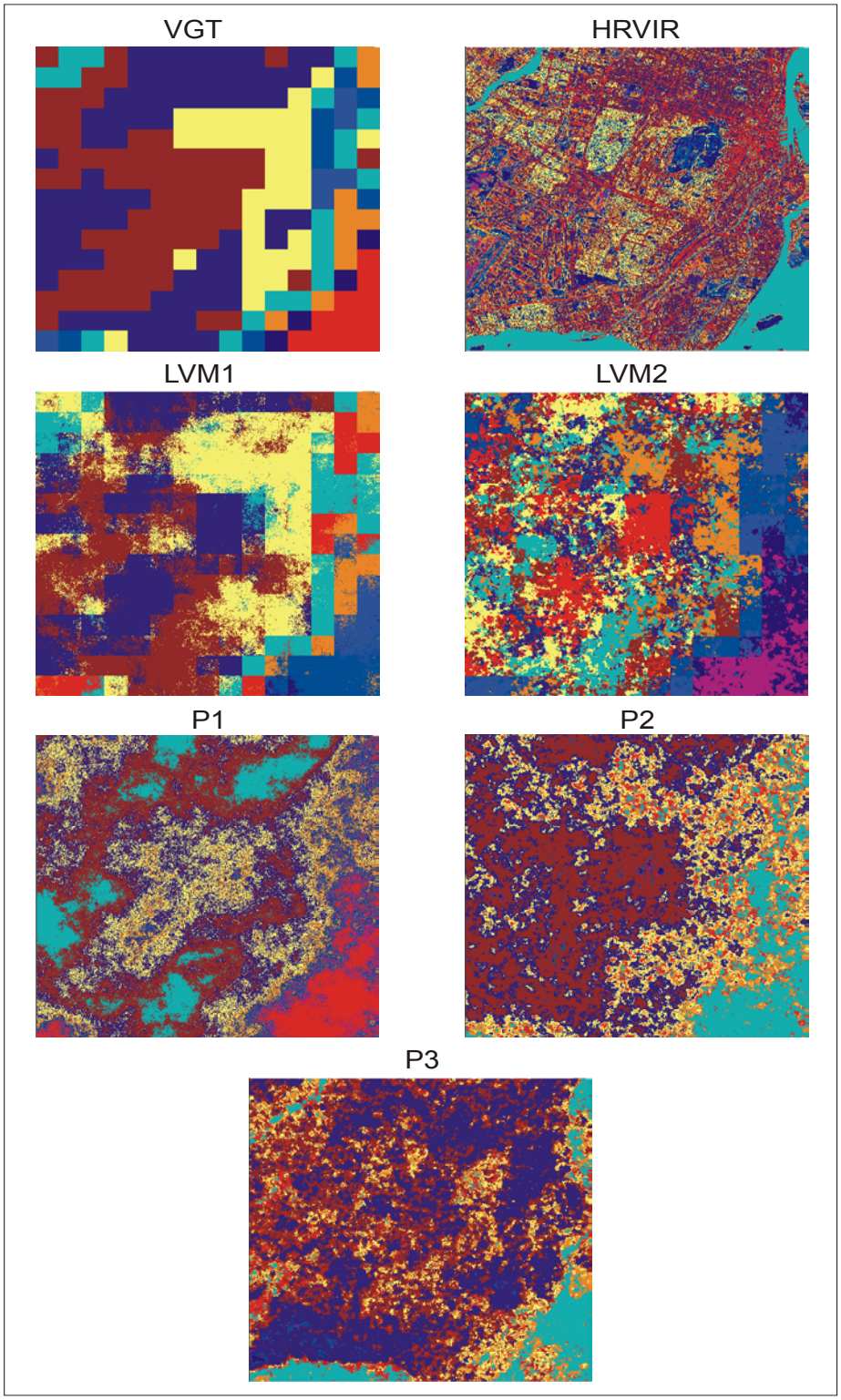

Figure 8.15 – Classified spectral segments based on percent cover of study site A with 10 classes (single realisation images).

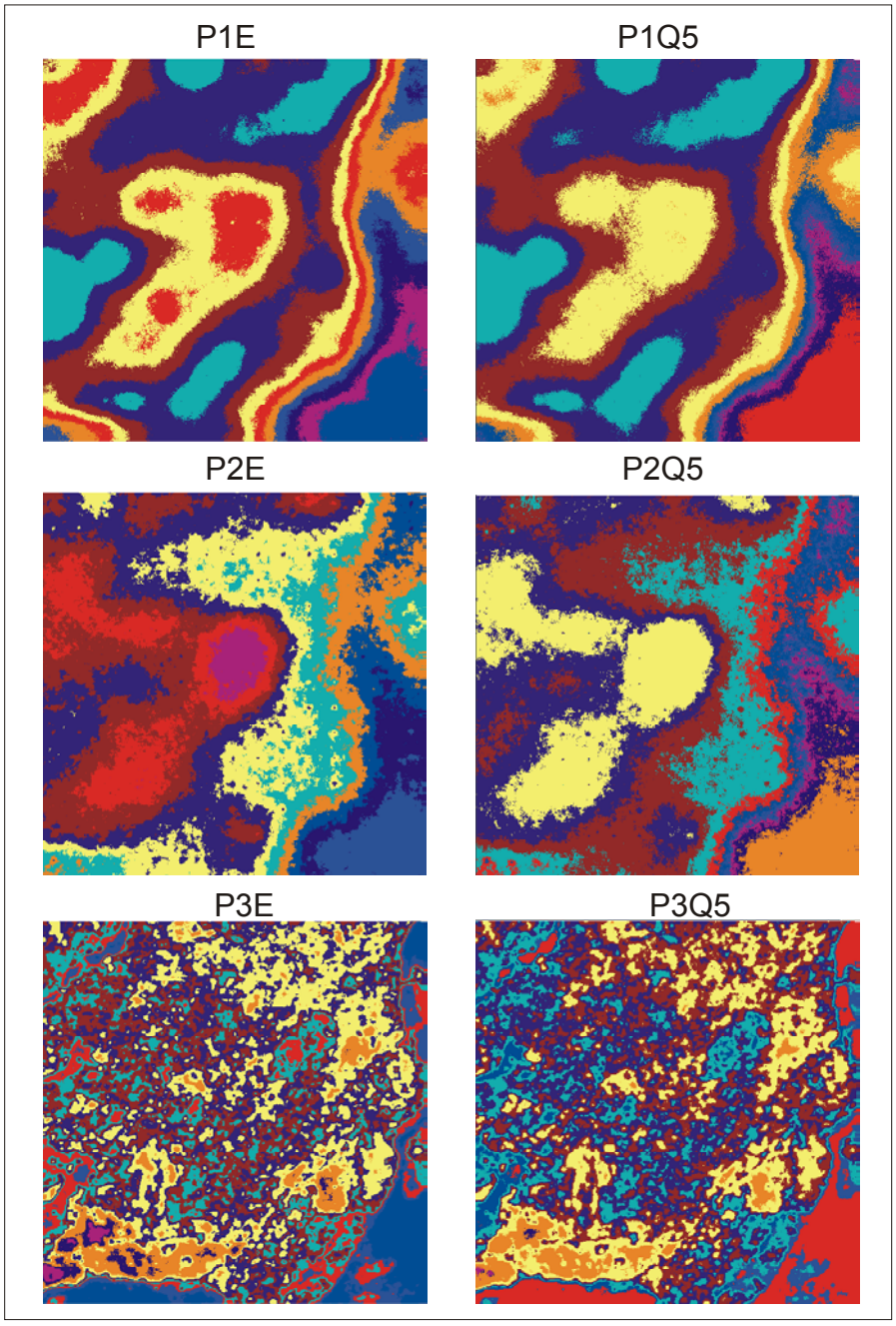

Figure 8.16 – Classified spectral segments based on percent cover of study site A with 10 classes (E-type estimate and median images).

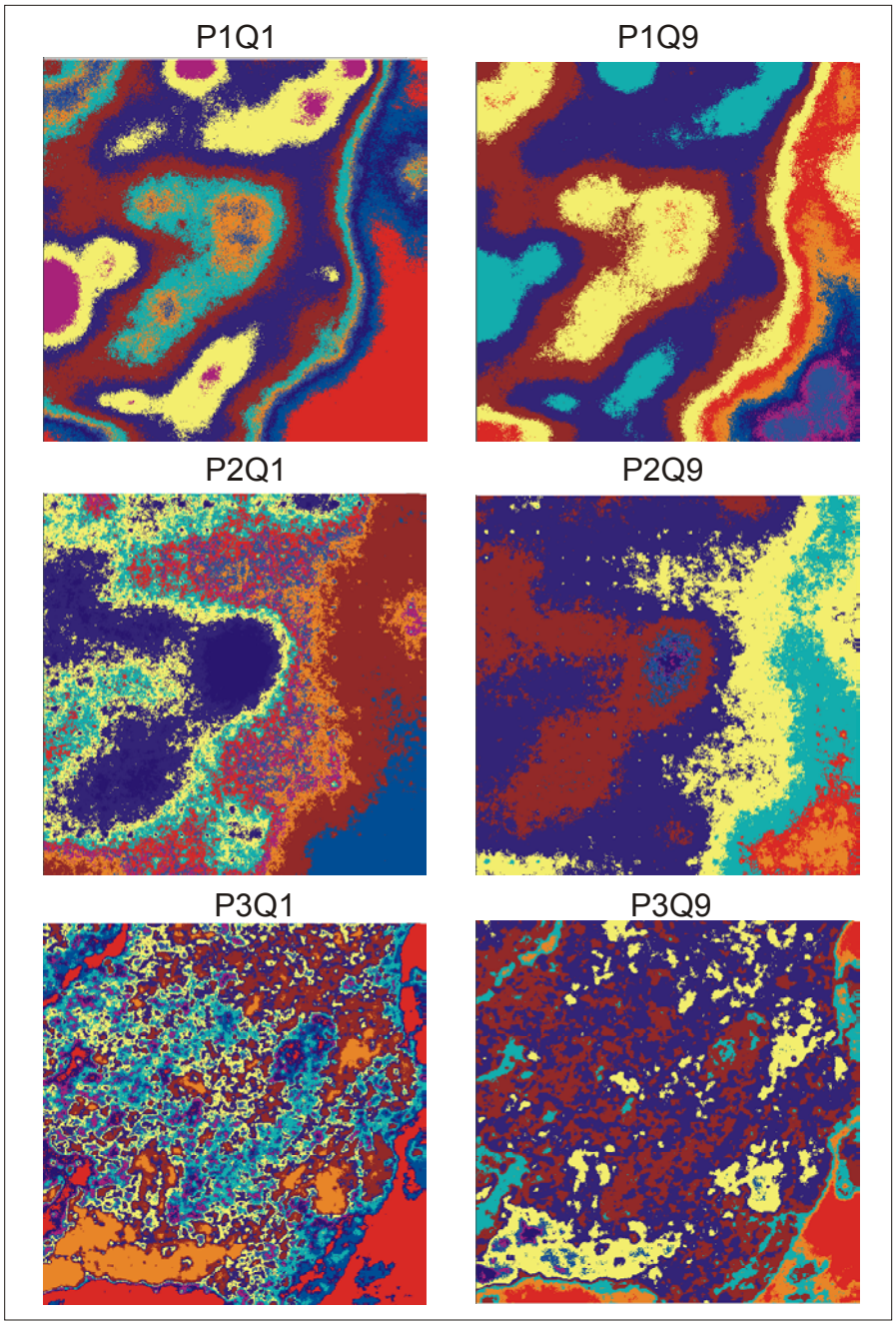

Figure 8.17 – Classified spectral segments based on percent cover of study site A with 10 classes (10^{th} and 90^{th} percentile images).

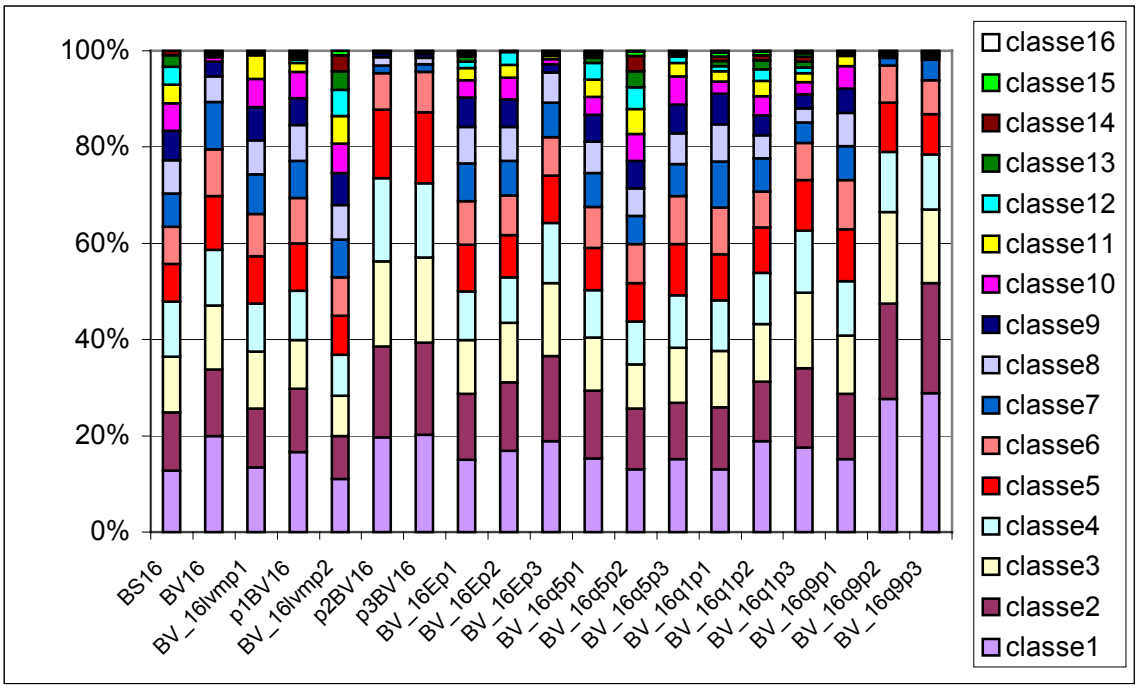

Figure 8.18 – Ranked spectral segments based on the pixel count. The results shown are for study site B and a maximum of 16 groups.

The ranked spectral segments were again used to produce pseudo colour images (figure 8.19). Only the single realisation images are shown. The post-processed images can be found in the appendix because their results were very similar to that of the study site A results.

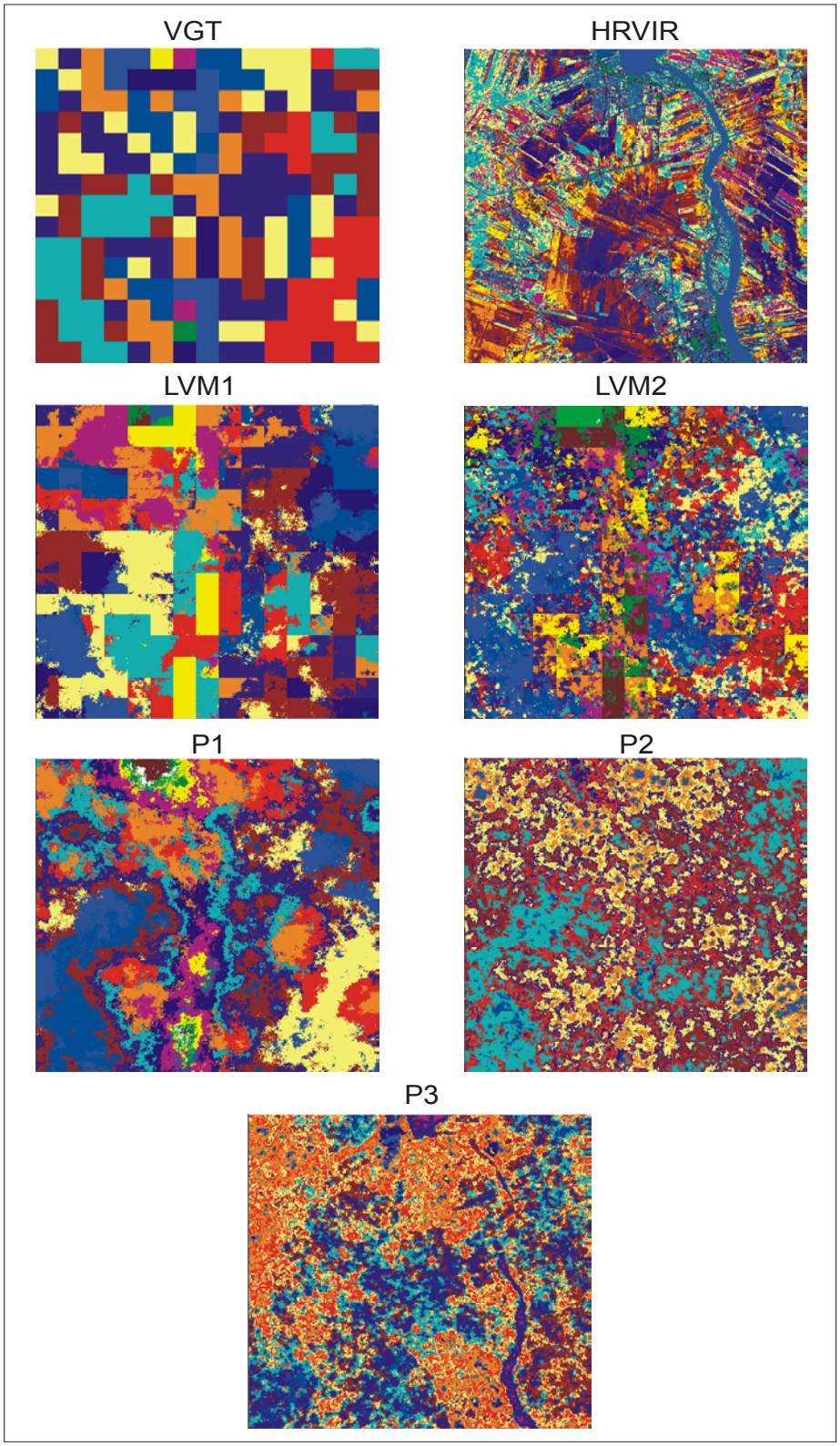

Figure 8.19 – Classified spectral segments based on percent cover of study site B with 16 classes (single realisation images).

The VGT and HRVIR images (figure 8.19) were again visually different both spatially and in terms of the pseudo colouring. The phase I LVM images spectral segment ranking was similar to that of the HRVIR image. The resulting pseudo colour image however was quite different because strong spatial ties to the VGT image were observed. Spatially, the phase III image resembled the HRVIR imagery most (figure 8.19). The dark blue colour of the river was easily recognisable however, the same colour was used within the agricultural region in the phase III image that was more difficult to interpret. The other land-cover objects were not as easily associated because the phase III image did not have the same type of groupings as the HRVIR imagery.

The study site B images were also segmented with a maximum of 10 spectral clusters. The results of this segmentation showed many of the images did not produce the maximum number of segments, e.g. HRVIR, VGT, phase I and II (figure 8.20). The total number of pixels per segment also varied as in the previous attempts. Again the phase II and III co-simulation results differed the most compared to the HRVIR based results.

The ranked segments (maximum of 10) were also used to produce pseudo colour images (figure 8.21). The phase III pseudo colour image accentuated the problem found in chapter 7 with regards to the negative relationship applied between the SAR and channel 2. The water class was quite clearly delineated spatially in the pseudo coloured image however, the segment to which it was associated to did not

conform to the water class. The HRVIR pseudo coloured image had the water segment primarily within the water boundaries. The phase III pseudo colour image on the other hand associated the water with other land-cover types that should not have been a part of the water segment. This association made it difficult to classify the segment as well as provide an accurate estimate of the area taken up by this class.

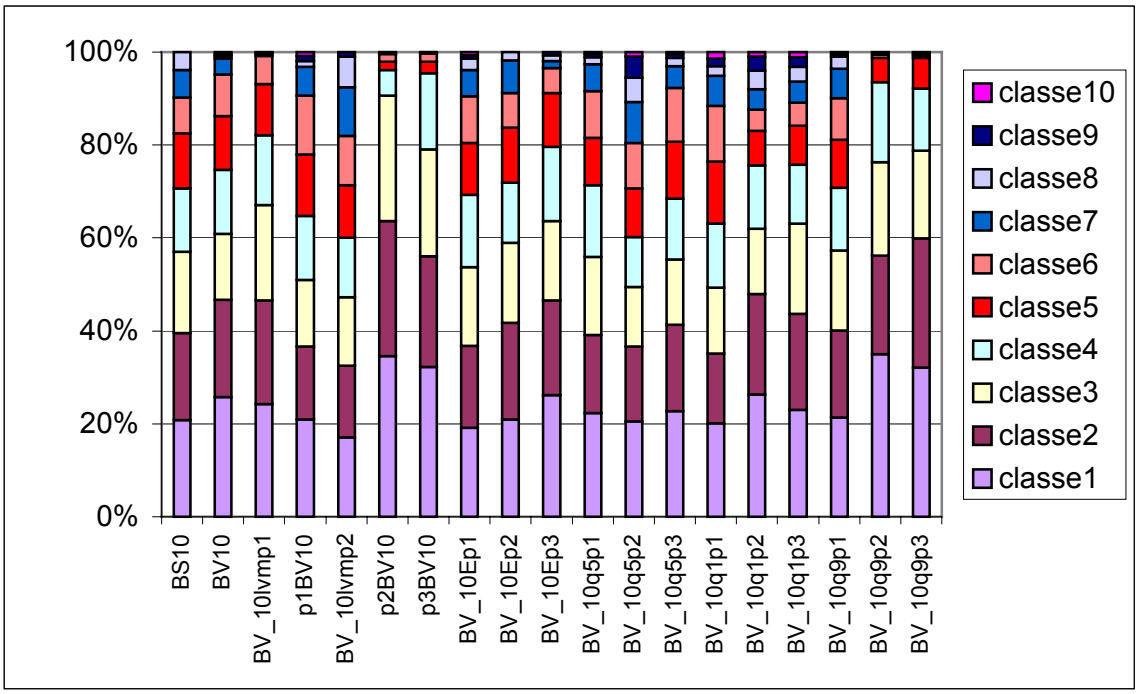

Figure 8.20 – Ranked spectral segments based on the pixel count. The results shown are for study site B and a maximum of 10 groups.

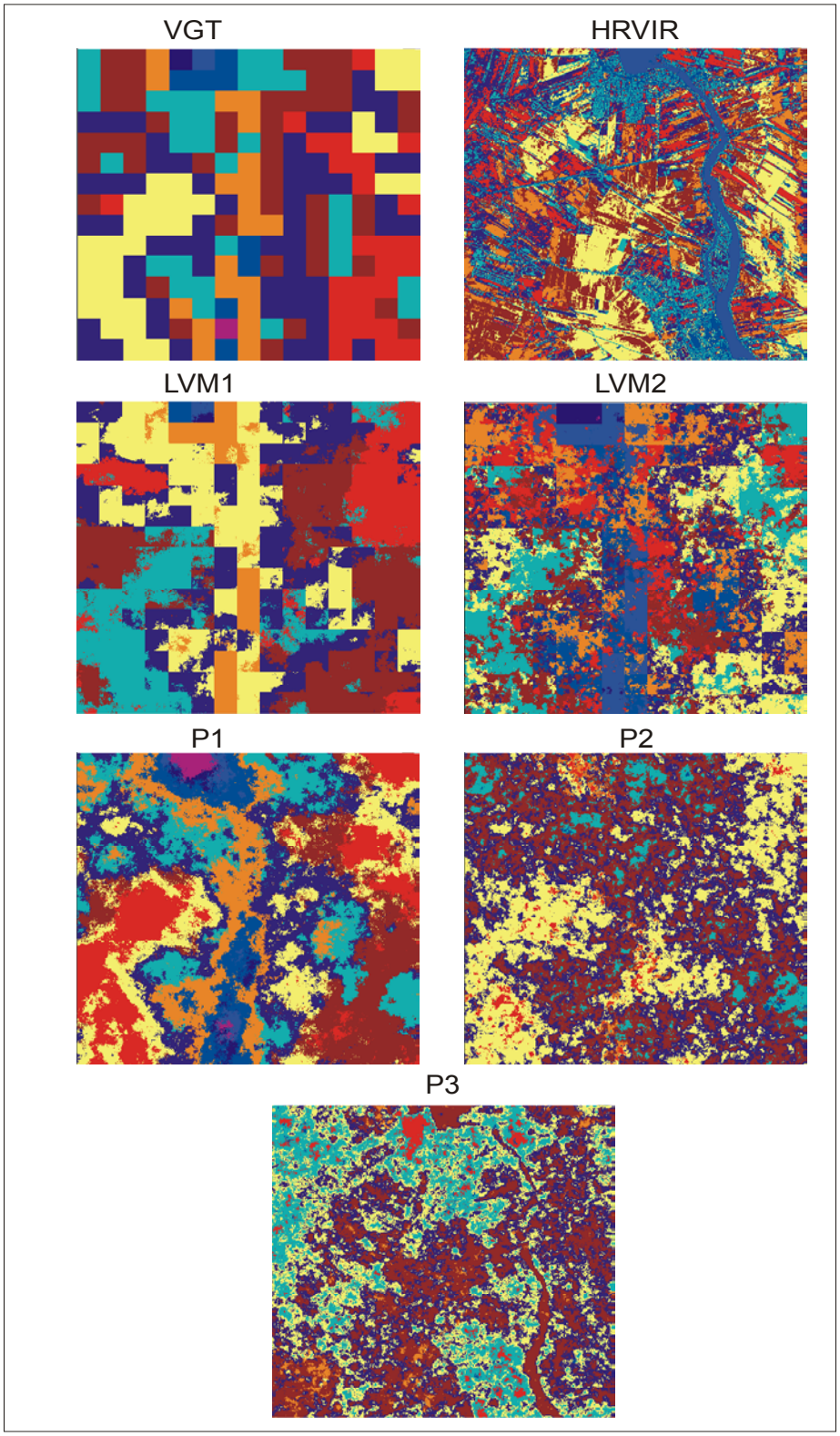

Figure 8.21 – Classified spectral segments based on percent cover of study site B with 10 classes (single realisation images).

The study site C was also an agricultural scene. Generally the results were similar to those seen above. What was interesting to note in some cases was the fact that even though the segment ranking might have been similar, the classes to which the segments referred to on the image were not the same. An example of this was study site C HRVIR and VGT image spectral segments based on 16 clusters (appendix). The output showed that the first three classes had a similar pixel total. However, when this information was compared to the pseudo colour images (appendix), there seemed to be no spatial relationship between the two.

The pseudo colour imagery based on the phase I, II and III co-simulation outputs delineated quite well the forest feature that was visible in the HRVIR imagery (appendix). This was interesting because based on the VGT and LVM phase I and II outputs, this feature was not delineated as strongly. The river features however were not delineated as effectively. The phase III output also suffered from the negative relationship that was imposed on the SAR and channel 2 relationship.

Segmenting the study site C images into 10 clusters resulted in only the HRVIR image producing so many clusters. All the other images were unable to segment the image into so many clusters with the majority of the images having 6 to 8 segments. The phase II and III co-simulated images were again quite similar in terms of the total number of pixels per segment. Unlike previous similarities the pseudo colour image also showed similarities because the forest land-cover was made

up with the same colours. This was not too much of a revelation because the generated images were based on the same finer spatial resolution input parameters.

Again the water class was not properly delineated because of the negative relationship imposed during phase III. However, there was no evidence of the water class in the other generated finer spatial resolution images because it was too small to register properly in the VGT imagery (appendix).

The final study site to be studied was D. Running the K-means algorithm with a maximum of 16 clusters produced results that were inline again with the expectations and results of previous tests. In this case, the two largest clusters of the HRVIR imagery were larger than any of the phase I, LVM1 and LVM2 images. The phase II and III co-simulated images on the other hand produced much larger clusters.

Looking over the pseudo coloured images based on the size of the 16 spectral segments showed that the VGT image was spectrally segmented differently than the output of all the generated finer spatial resolution images. The various pseudo colours that were found in the same location of different images indicated that for the same location, depending on the manner in which the imagery was generated will result in a different estimate of that land-cover. This difference was also seen in the HRVIR image.

The phase III generated image again had difficulty properly segmenting the water class. However, the introduction of the SAR data into the simulation process

resulted in better spatial delineation of the land-cover especially the forest and agriculture classes.

The study site D was also spectrally segmented into 10 clusters (appendix). In this case the VGT image generated a similar first cluster that was very similar in size to that of the HRVIR image. This similarity however did not result in the same land-cover on the ground. The other finer spatial resolution generated images (LVM 1, LVM 2 and phase I co-simulation) produced segments that contained less pixels than the HRVIR image. Again, the phase II and III co-simulation images produced much larger clusters compared to all the other results.

Looking at the pseudo colour images (appendix) the differences in the VGT and HRVIR images were quite clear. Spatially both the HRVIR and VGT images were quite heterogeneous, however the spatial scale of this spatial variability was quite different. The other generated finer spatial resolution images did not resemble either the VGT or HRVIR images because of the pseudo colour ranking based on the total number of pixels per segment. Only the phase III co-simulation image delineated the forest/non-forest land-cover similarly to the HRVIR imagery. Again the water class was wrongly classified due to the imposed negative relationship between the SAR and channel 2.

8.3 Assessment of Accuracy

A final analysis of the accuracy of the generated finer spatial resolution images was done using land-cover data. This vector data came from the Canada Land Inventory Level-II UTM digital data set whose original map scale was 1:250 000 while the second is based on 1:50 000 topographical maps (National Topographic Digital Data Base). The assessment of the accuracy of the segmented images were made by comparing the number of segments and the pixel frequency that falls within specific land-covers.

For each study site certain land-cover classes were chosen and the spectral clusters that were found at those places was extracted. This was done for the VGT, HRVIR and each of the generated finer spatial resolution images.

From section 8.2, the number of clusters into which the image data was spectrally segmented significantly altered the number of pixels associated with any one cluster. In any of the study sites, the number of possible land-cover classes was at least 8. For this reason the assessment was only being tested on the 16 cluster outputs. This was because running the K-means algorithm with only 10 clusters in many cases did not generated even 10 clusters. In order to make sure that enough spectral clusters were available for the accuracy assessment only the results based on 16 clusters was used.

8.3.1 CLI based accuracy

The CLI land-use system has 14 valid codes (table 8.II). Not all land-cover types were assessed during this study because of the location of the study sites. Those land-cover classes that were applied in this section were checked (table 8.II). The land-cover classification for this area is quite old and was produced between 1950 and 1970.

Table 8.II – CLI Valid Land-Use Codes.

Code	Land-Use	
B	Urban built-up area	√
E	Mines, quarries, sand and gravel pits	
O	Outdoor recreation	
H	Horticulture	
G	Orchards and vineyards	
A	Cropland	
P	Improved pasture and forage crops	√
K	Unimproved pasture and range land	
T	Productive woodland	√
U	Non-productive woodland	
M	Swamp, marsh or bog	
S	Unproductive land – sand	
L	Unproductive land – rock	
8	Unmapped areas (subclass Z = Water area)	√

The images in this section are presented in pseudo colours where a single colour was assigned to each spectral segment.

For study site A, only the built-up and water land-cover classes were used. Figure 8.22 shows the area covered by these two classes as well as the outline over the images under investigation. Visually, it was apparent that the VGT imagery would have the greatest error in accuracy because the land-cover border divided the

large pixels and it was difficult to separate them. The vectors that delineated the land-cover classes however were not as accurate as the HRVIR imagery because the vectors sometimes did not properly overlay the imagery. The HRVIR imagery also showed that within the built-up land-cover there was a wider range of spectral segments. However, this was the same for the VGT image as well as all of the generated finer spatial resolution images.

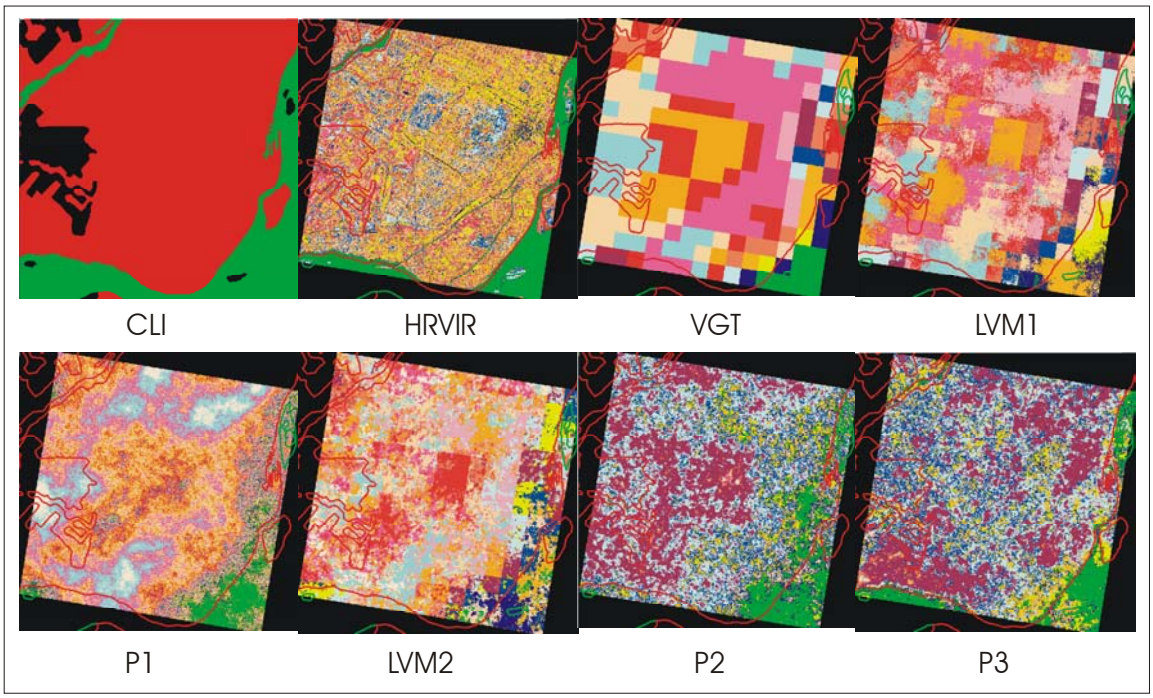

Figure 8.22 – CLI vectors superimposed on the spectrally segmented images of study site A based on 16 clusters.

Even though there was a range of spectral segments within the built-up class, the water class was very homogeneous in the HRVIR image. Only the phase III (figure 8.22, P3) generated image also provided a homogeneous water class that was

well defined. Within the boundaries of the water class, the other images continued to be made up of several different spectral segments.

Figure 8.23 shows the distribution of spectral segments under the built-up land-cover. In a metropolitan region, the built-up land-cover class is made up of many types of objects, which includes both man made and natural.

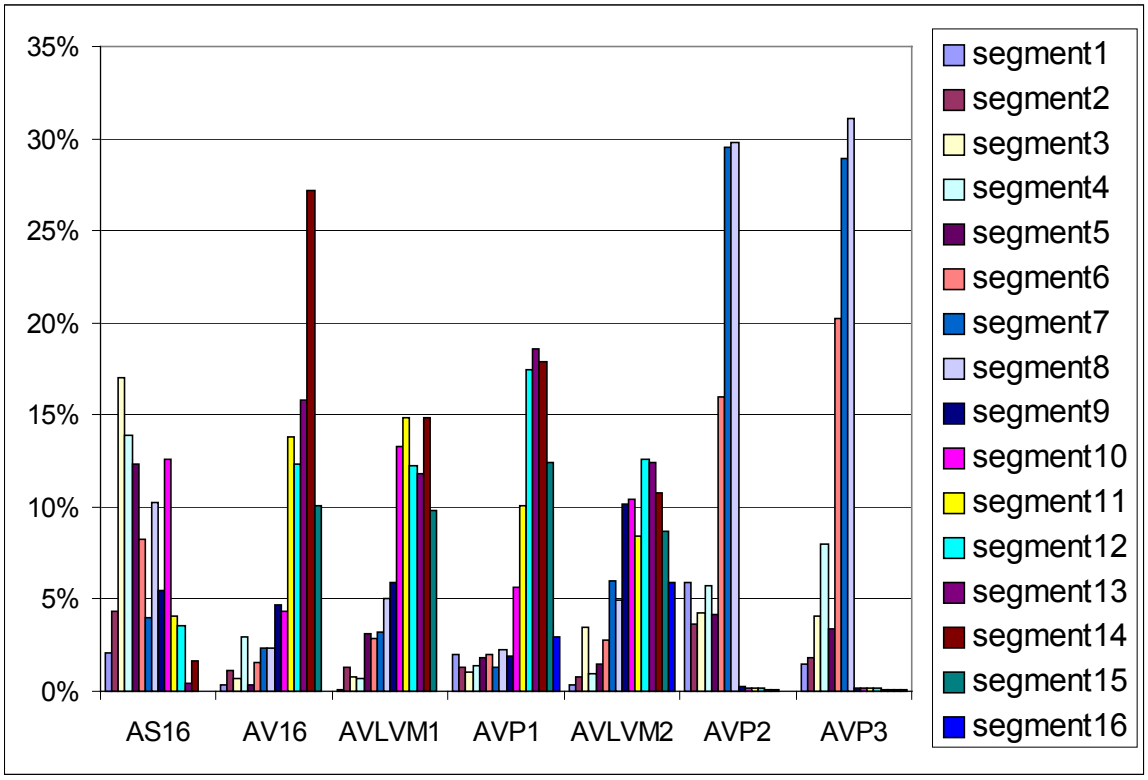

Figure 8.23 – The distribution of spectral segments within the built-up land-cover class for study site A based on 16 clusters.

Based on figure 8.23, the HRVIR image had approximately 5 segments made up of more than 10% of the pixel count. Therefore these 5 segments made up more than 60% of the built-up class for study site A. Therefore, out of a possible 14

spectral segments, five accounted for the majority of the built-up area. The VGT image on the other hand presented a different distribution. One segment rose much higher than the rest attaining over 25%. In association with this segment, four other spectral segments made up 75% of the region. Here there were also five segments that made up most of the region however they account for approximately 75%. One segment took up almost 30%.

The phase I and phase II LVM generated images resembled the HRVIR images spectral segment distribution in that they did not have any one segment that made up most of the built-up land-cover class. All the co-simulated finer spatial resolution images were made up of spectral segments that contained over 25% of the pixels within the urban class. The phase II and III co-simulated images were very distinct having three dominant spectral segments for urban class where over 75% of the pixels came from only three different spectral segments.

The other land-cover of interest at study site A was water (figure 8.24). The HRVIR first segment was made up of just over 80% of the pixels found within the water class. The other spectral segments whose frequencies were very small were most likely due to the inaccuracy of the class vectors. The VGT image also had a spectral segment that rose above the others however it only accounted for 30%. Based on the VGT image output, there seemed to be a trend where the more information was inserted into the generation of the image, a single segment continued to take more and more of the pixels making up the water class. The phase III co-simulation image provided the largest single segment (after the HRVIR image) with the most

number of pixels within the water land-cover class (over 50%). Only the phase I and II LVM images did not produce such a distribution. Their frequencies were fairly equal across all the spectral segments meaning that there was a large mix of different spectral segments within the water land-cover class.

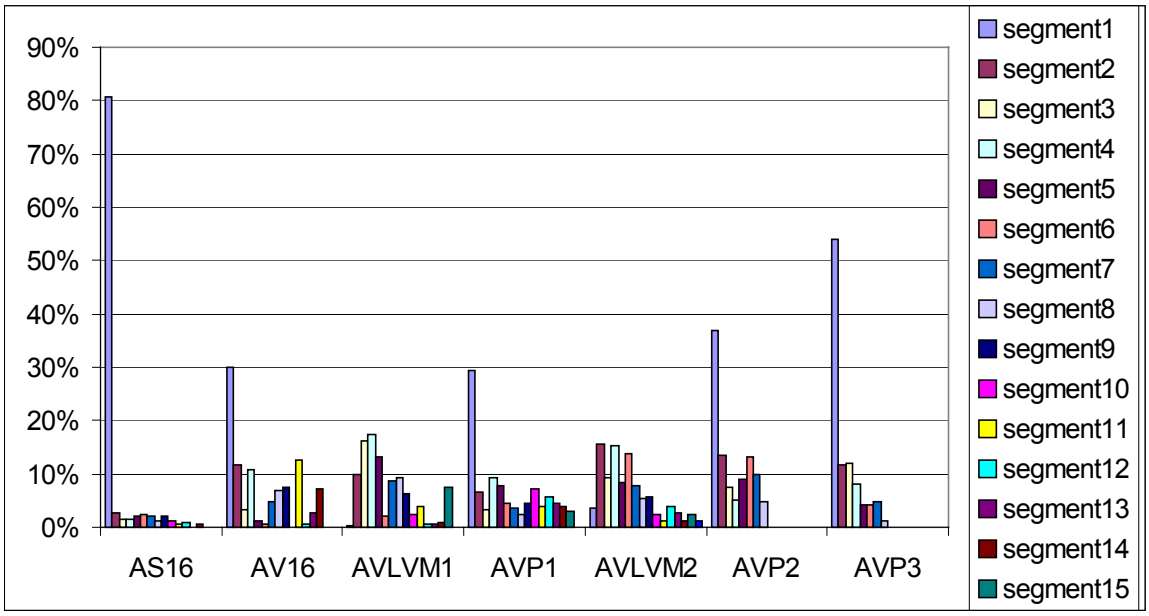

Figure 8.24 – The distribution of spectral segments within the water land-cover class for study site A based on 16 clusters.

The other three study sites were agricultural scenes. For these study sites four main land-cover classes were investigated: built-up, water, improved pasture and productive woodland. The study site B spectrally segmented images with the land-cover class overlay is shown in figure 8.25.

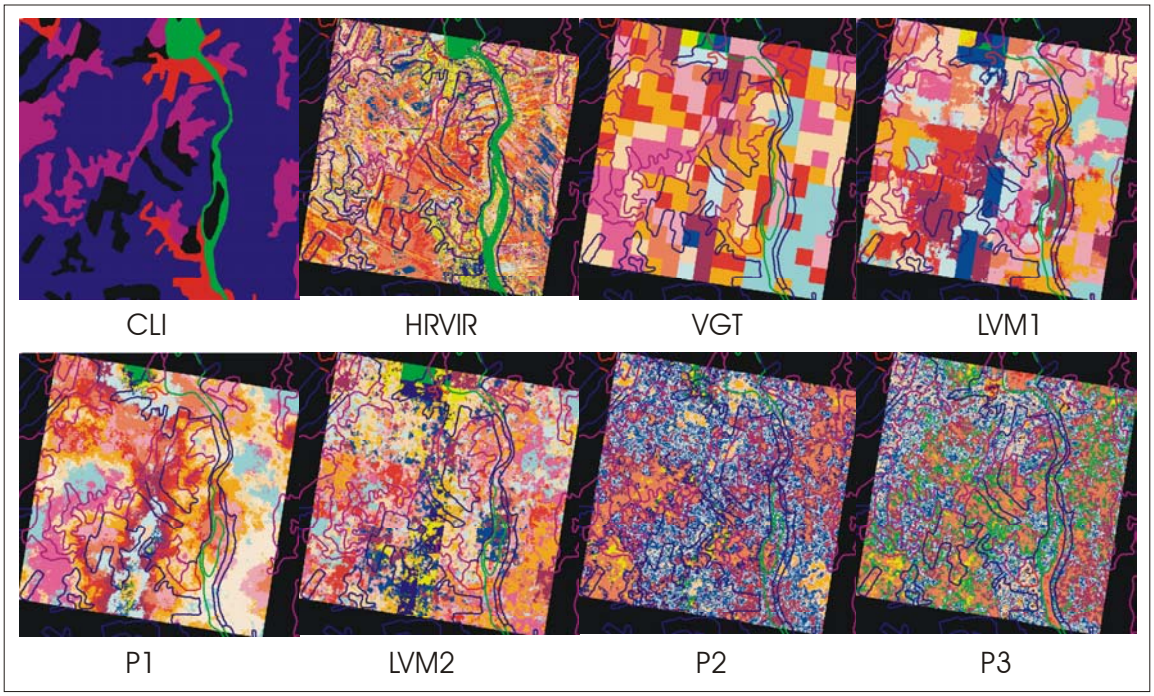

Figure 8.25 – CLI vectors superimposed on the spectrally segmented images of study site B based on 16 clusters.

The study site B image was primarily made up of pasture (figure 8.25 – CLI (blue)). The red sections were built-up areas while the purple was woodland (figure 8.25 – CLI). A river runs through this image and was delineated in green (figure 8.25 – CLI). Based on the HRVIR image (8.25), the vectors appeared to delineate the regions quite loosely because the mapping was based on 1:250 000 map scale. However, it was still possible to see what areas belonged to which land-cover class. The coarse resolution VGT spectrally segmented image pixels however were much larger than some of the land-cover areas themselves delineated by the vectors. This was further observed in the phase I LVM generated imagery. As spatial resolution became more fine, heterogeneity within the land-cover class vectors became more

pronounced but at the same time the boundaries of the spectral segments were also more in line with the land-cover class vectors. The phase II and III co-simulated spectrally segmented images appeared to be the most heterogeneous.

The number of spectral segments found under each of the four land-cover classes was computed for study site B (figures 8.26 through 8.29).

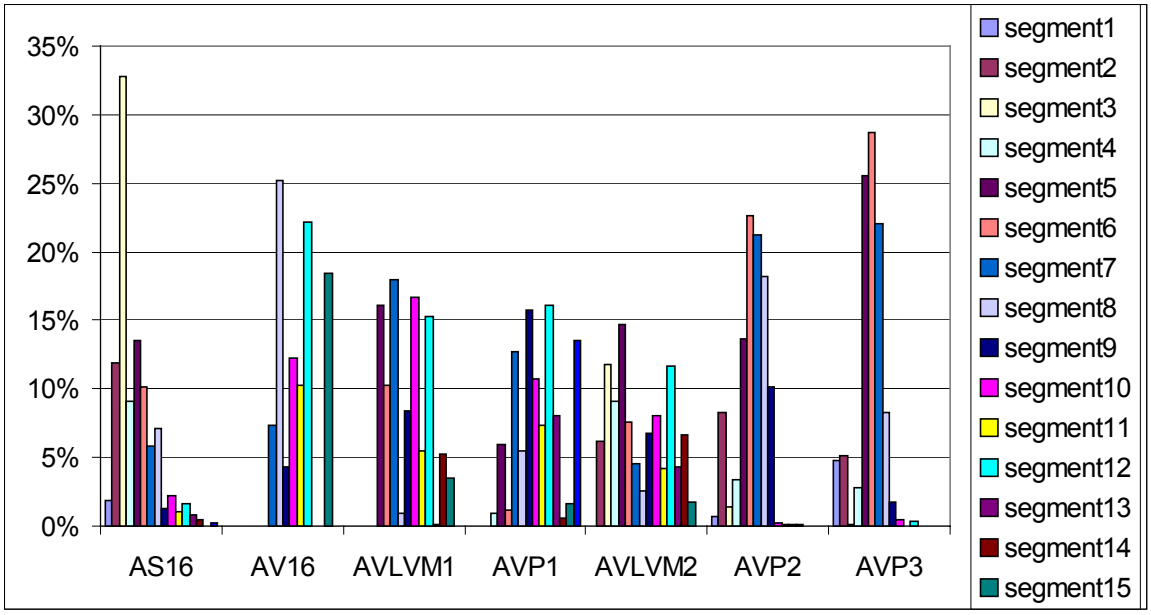

Figure 8.26 – The distribution of spectral segments within the built-up land-cover class for study site B based on 16 clusters.

The built-up areas of study site B were primarily made up of spectral segment three for the HRVIR image because 30% of the pixels came from that segment. However, there were many more spectral segments that were found within the built-up area class for the HRVIR imagery. Another three spectral segments contained over 10% of the total pixels with another three segments making reaching each up over

5%. This variability of the spectral segments that made up a single land-cover class was not exclusive to the HRVIR image. The VGT and generated finer spatial resolution images all had quite a variable number of spectral segments making up the built-up land-cover class. The VGT image had the fewest number of spectral segments that fell into the built-up land cover class because of its coarse spatial resolution. The phase II LVM generated finer spatial resolution image produced the most variable distribution of spectral segments while the phase III co-simulated image produced the highest frequency of pixels for any single spectral segment compared to the HRVIR imagery under the built-up land-cover class.

The distribution of spectral segments under the water land-cover class found at study site B is presented in figure 8.27. The distributions were quite variable for all images other than the HRVIR image. The HRVIR spectrally segmented image had a dominant first segment, which accounted for almost 80% of the pixels within the water class. Although the VGT and phase III co-simulated images also had spectral segments that were quite dominant they did not make up such a large percentage of the total number of pixels under the water land-cover class. This indicated a greater variability of spectral segments thereby introducing more ambiguity with regards to the estimate of the water class. Note however that the segments with the highest frequency in the water land-cover class distributions were very low in the built-up land-cover class figure for both HRVIR and phase III co-simulation based images. This indicated that the spectral segmentation process was able to at least discriminate quite well between the built-up and water classes at study site B.

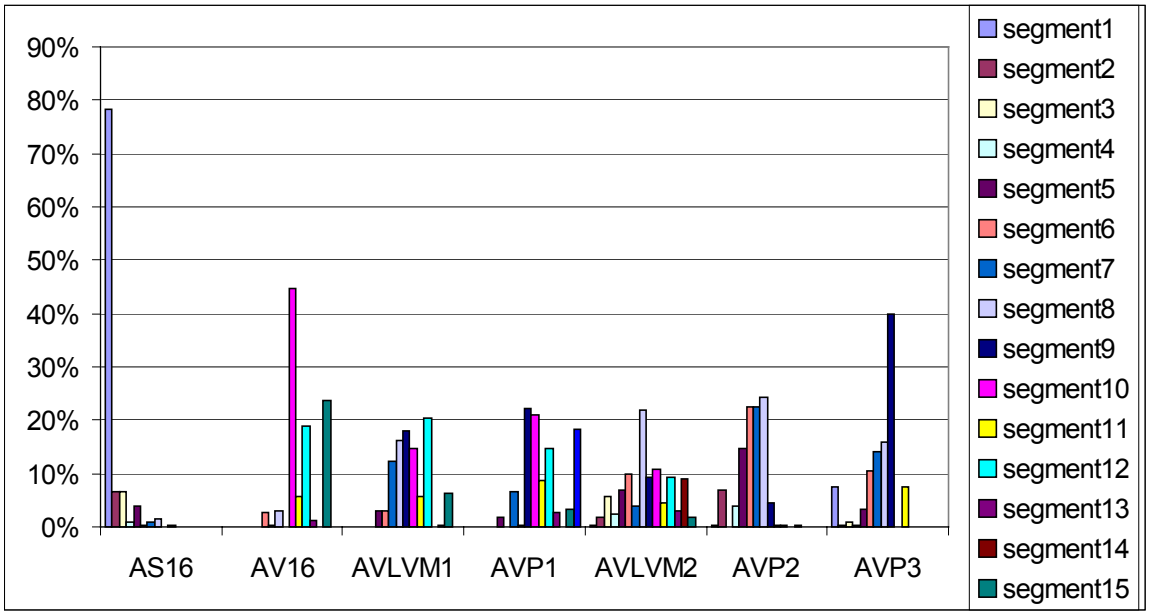

Figure 8.27 – The distribution of spectral segments within the water land-cover class for study site B based on 16 clusters.

The built-up and water land-cover classes were not as prominent at the study site B as in study site A. The figure 8.28 presents the results of the spectral segments found under the improved pasture land-cover class for study site B. The pasture class covered a large percentage of the study site B image and the resulting spectral segment distributions were variable. Such behaviour can be expected because of the wide range vegetation and field that can be found within this land-cover class at the end of May when the image was recorded. The greatest variability in the distribution of spectral segments within the pasture land-cover class was for the phase II LVM based image. This generated imagery always had very variable spectral segment distributions. For this particular land-cover, the HRVIR image spectral segment distribution was much more variable than that found for the phase III co-simulation image. There were four segments from the phase III co-simulation image that were

above 15% and accounted for over 70% of the pasture land-cover. On the other hand, only one segment was greater than 15% for the HRVIR imagery. The VGT image spectral segment distribution in this case was not as variable as that of the HRVIR imagery.

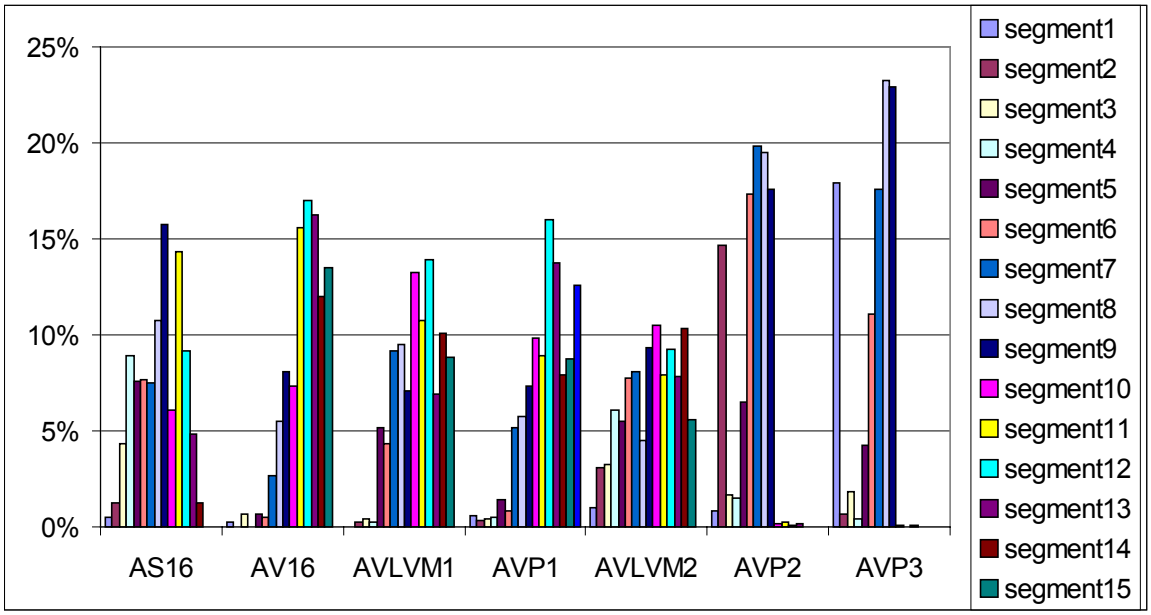

Figure 8.28 – The distribution of spectral segments within the pasture land-cover class for study site B based on 16 clusters.

The phase II co-simulated imagery produced a spectral segment distribution for the pasture class that was similar to the phase III co-simulated results. From the distribution alone it was difficult to tell whether one produced more accurate results than the other in terms of estimating the total area of pasture at study site B.

The final land-cover class investigated for study site B was the productive woodland class (figure 8.29). Two spectral segments based on the HRVIR image

made up over 50% of the woodland class. The phase III co-simulation image had three prominent spectral segments that made up over 70% of the woodland land-cover class however the distribution was much less variable than the HRVIR images. The most variable distribution of spectral segments was again based on the phase II co-simulation image for the woodland land-cover class.

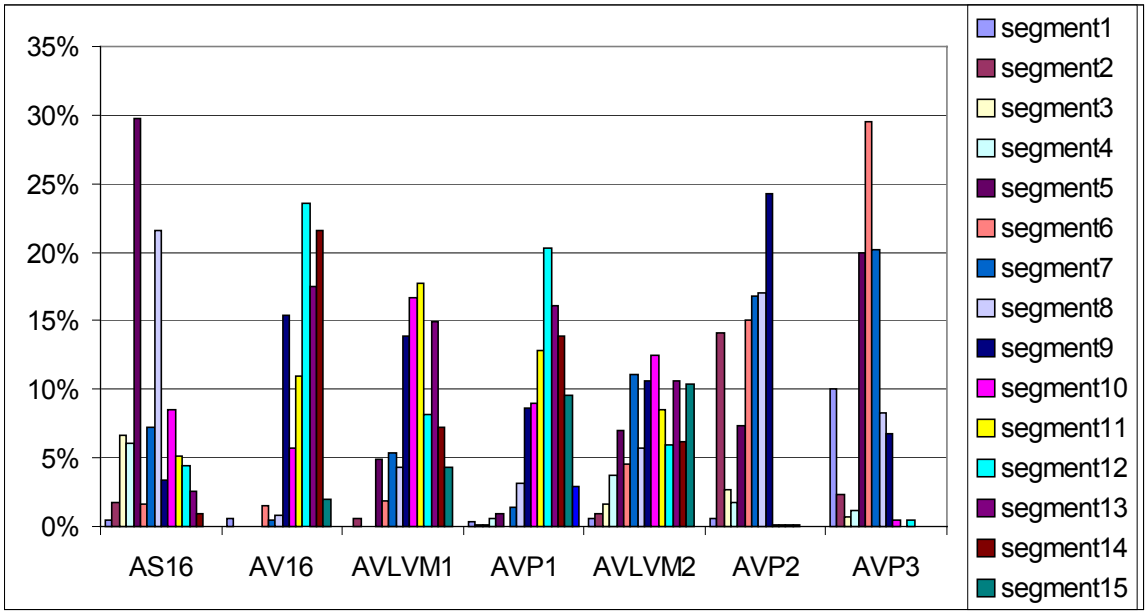

Figure 8.29 – The distribution of spectral segments within the woodland land-cover class for study site B based on 16 clusters.

Classification of the study site B would have been difficult for either the real HRVIR and VGT images as well as the generated finer spatial resolution images because of the variability of spectral segments found within the wanted land-cover classes. Therefore, in order to classify these spectral segments more information was required which was related to location as well as experience.

The study site C was also an agricultural mix region. The same land-cover classes as in study site B dominated in this area (figure 8.30). The horseshoe shaped purple region in the CLI image is the productive woodland land-cover class while the blue areas are pastures. A river running across the image is also classified as well as a few built-up areas in red.

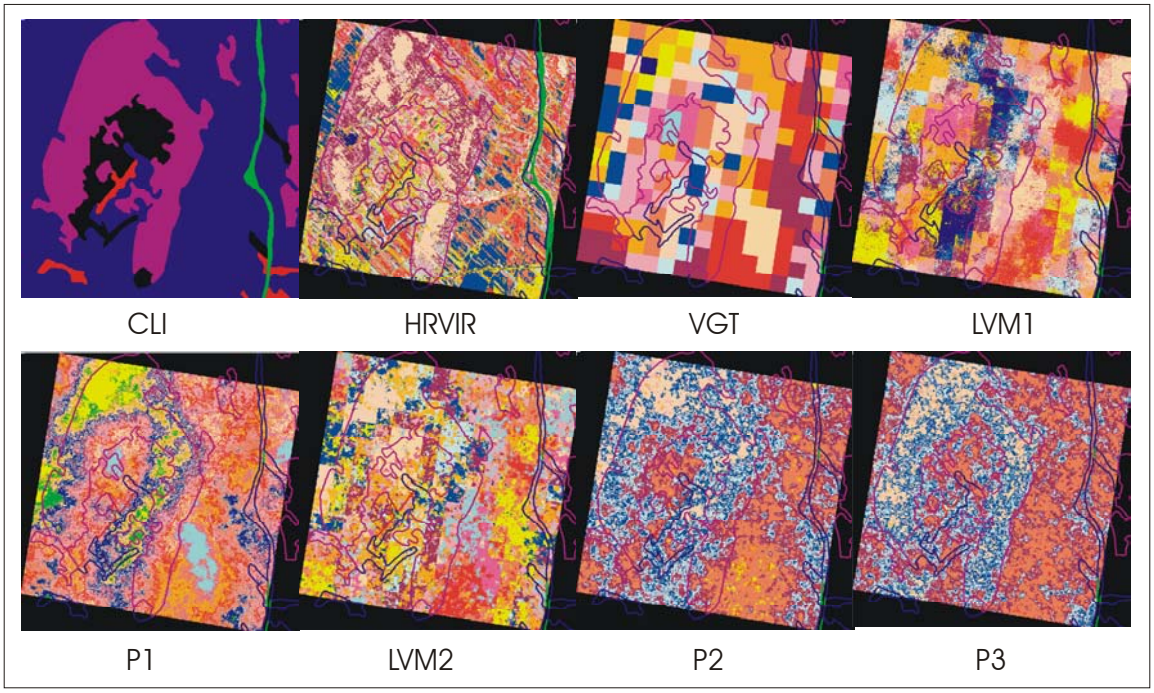

Figure 8.30 – CLI vectors superimposed on the spectrally segmented images of study site C based on 16 clusters.

The study site C results were pretty similar to the results of the previous study sites. Similarities were specifically found between the results of study site B because all the land-cover classes were quite heterogeneous except for the water class in the HRVIR image. As such only the pasture and woodland results were presented (figures 8.31 and 8.32). The results of the built-up and water land-cover class can be

viewed in the appendix. The distribution of the spectral segments for the built-up land-cover class was variable for the HRVIR image as well as the phase I co-simulation and phase I and II LVM generated images. The VGT image as well as the phase II and III co-simulated images had less variable distributions with one or several dominant segments. A single dominant spectral segment for the water class was observed for the HRVIR imagery in study site C. The other images had a much greater distribution of spectral segments associated with this land-cover class.

The pasture land-cover class made up a large percentage of the total area of the study site C. The phase II and III co-simulation images produced spectral segment distributions that were quite similar in shape but differed in frequency (figure 8.31). These same distributions also had dominant spectral segments that made up a large percentage of the pasture land-cover class. The other images produced distributions of spectral segments that were quite variable. This was no surprise because of the heterogeneity seen in the segmented images across the study site C.

The final land-cover class analysed for study site C was the woodland class (figure 8.32). Looking back at the delineated woodland class in the segmented images, the woodland area seemed to be made up of two to four different classes. This fact was supported by the graphs of the distribution of the spectral segments within the woodland land-cover class. The HRVIR image was mostly made up of two spectral segments while the phase II and III co-simulated images had four dominant spectral segments within the woodland class.

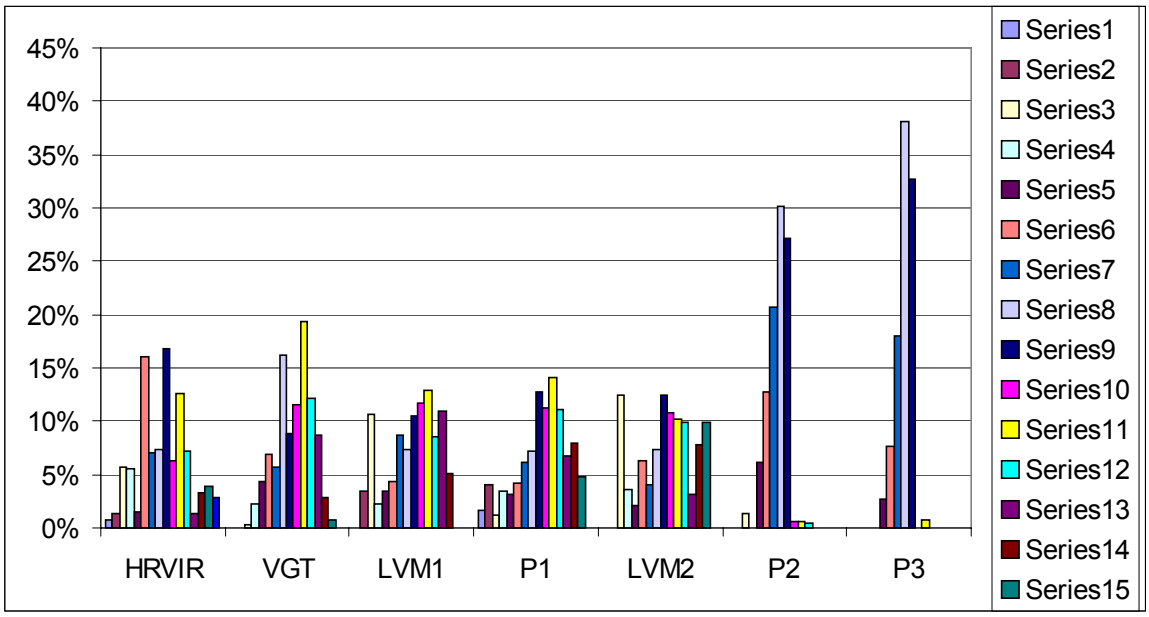

Figure 8.31 –The distribution of spectral segments within the pasture land-cover class for study site C based on 16 clusters.

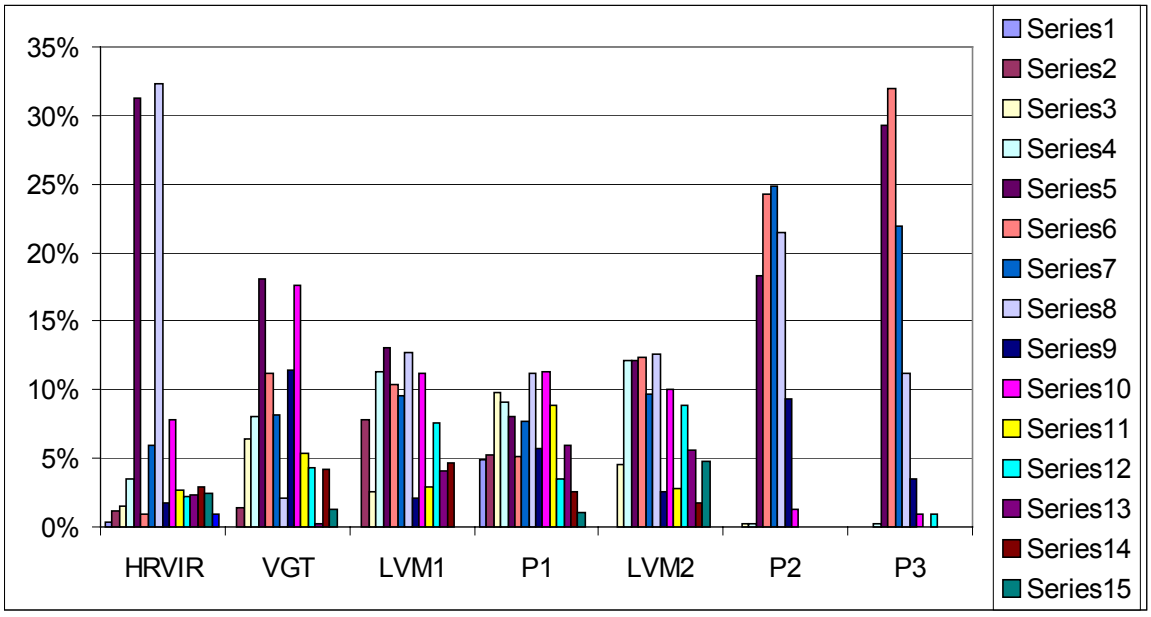

Figure 8.32 – The distribution of spectral segments within the woodland land-cover class for study site C based on 16 clusters.

The other images had more of a variable distribution of spectral segments within the woodland class. The VGT image had two distinct peaks that separated themselves from the rest of the distribution of spectral segments.

The final study site, D, is also based on an agricultural scene with the same four land-cover classes being most significant in the area. In this area the woodland land-cover class was most dominant (figure 8.33 – CLI (purple)). Again, every image provided a different spectral segmentation.

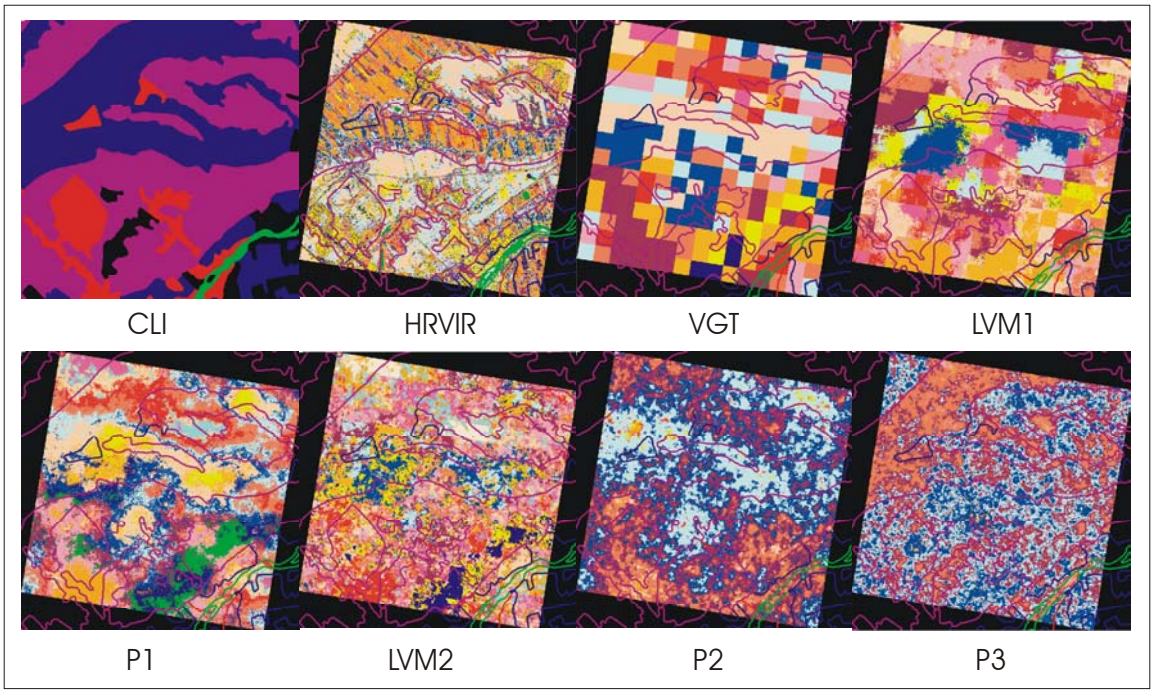

Figure 8.33 – CLI vectors superimposed on the spectrally segmented images of study site D based on 16 clusters.

The graphs of the spectral segments found under the built-up, water and pasture land-cover classes are found in the appendix. The HRVIR imagery had quite

a variable distribution of spectral segments. This result was mirrored loosely by the phase II LVM based generated images spectral segments. The phase II and III co-simulated images spectral segments that were found under the built-up area class were primarily made up of three dominant segments.

The water class again was very well segmented in the HRVIR imagery. The other images had two or three spectral segments that dominated within the boundaries of the water land-cover class. Some of these same dominant segments found within the water class were also found in the pasture class (i.e. phase II and III co-simulated images). For example the eighth segment in the phase II co-simulated image provided just under 25% of the coverage based on the pasture class and just over 45% in the water class. The other images had quite a variable distribution of spectral segments within the pasture land-cover class as was observed in the previous study sites.

The distribution of spectral segments for the study site C woodland land-cover class is presented in figure 8.34. The HRVIR imagery had two spectral segments that dominated this class and accounted for almost 40% of the pixels. Several other spectral segments accounted for the rest making a variable distribution within this class. The VGT, phase I and II LVM based and phase I co-simulation images all had a variable distribution of spectral segments within the woodland land-cover class. The phase II and III co-simulation based images again contained three dominant segments that made up a large part of the class. These images also had a less variable distribution of the spectral segments.

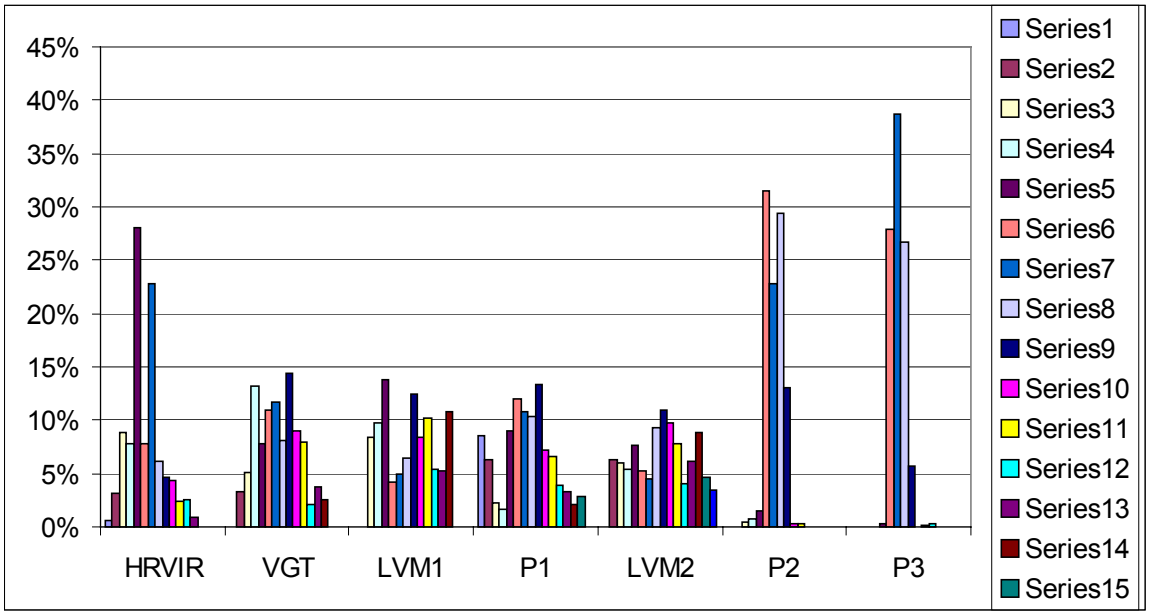

Figure 8.34 – The distribution of spectral segments within the woodland land-cover class for study site D based on 16 clusters.

8.3.2 A more accurate classification

A large area of study site D was made up of the woodland land-cover class based on the CLI. Land-cover information was also available for this sector whose classification was based on a much finer map scale (1:50 000) with a more recent production date (~1990). The woodland class for this area was investigated (figure 8.35). The fineness of this woodland land-cover data set was easily appreciated compared to the CLI image (figure 8.35). The woodland boundaries are much more exact and delineate many smaller areas that were not possible using the CLI land-cover data set. The HRVIR image was finely divided into the woodland land-cover by the vectors. The coarse spatial resolution VGT spectral segments in most cases did not make up an entire polygon making it very difficult to estimate the area taken up

by woodland land-cover. The smooth nature of the phase I LVM and co-simulated imagery also had the same difficulty as the VGT image. The phase II LVM and co-simulated spectrally segmented images were more heterogeneous in nature and therefore had a greater mix of spectral segments within the woodland land-cover class. Finally, the phase III co-simulated image appeared to have certain spectral segments within the woodland land-cover as observed in the HRVIR image.

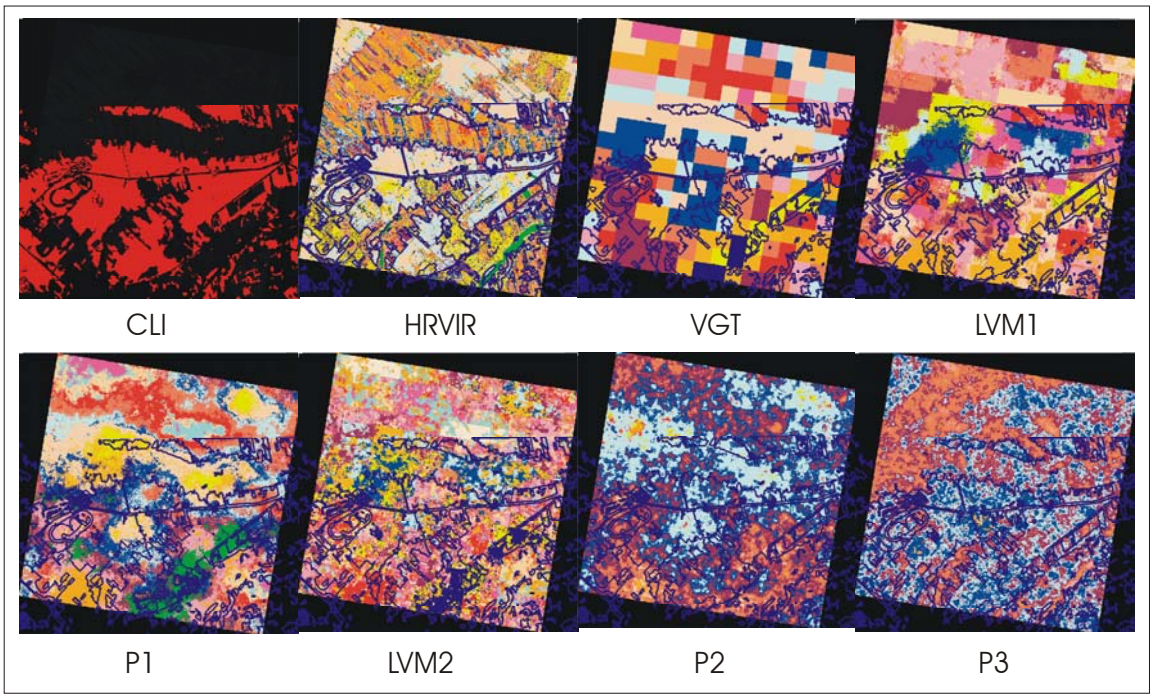

Figure 8.35 – Woodland vectors superimposed on the spectrally segmented images of study site D based on 16 clusters (1:50 000 map scale).

The spectral segments found within the limits of the woodland class boundaries were sampled (figure 8.36). Two spectral segments accounted for over 65% of the pixels found within the boundaries of the woodland land-cover class based on the HRVIR imagery. A little variability was observed with three segments

each taking up just over 5%. The VGT, phase I and II LVM and phase I co-simulation images all resulted in spectral segment distributions that were quite variable with no obvious dominant segment. The phase II and III co-simulated image results showed that between three and four spectral segments dominated within the boundaries of the woodland class. This distribution of spectral segments was similar to that of the HRVIR imagery in the sense that specific segments dominate the woodland class.

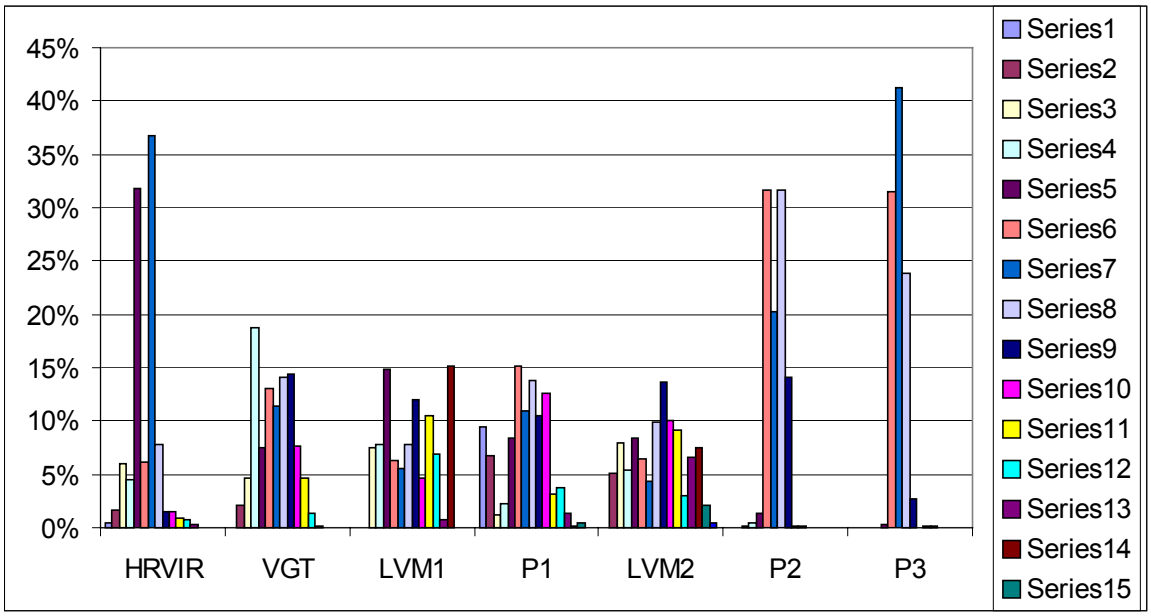

Figure 8.36 – The distribution of spectral segments within the woodland land-cover class for study site D based on 16 clusters (1:50 000 map scale).

8.4 Discussion

There was quite a difference in the type of information that could be extracted from the HRVIR or VGT optical images and the generated finer spatial resolution

images. These differences were shown in the location of the spectral segments in spectral feature space, the total number of pixels that were associated with the spectral segments, and the location of these spectral segments within the image.

The spectral segments in spectral feature space could be generally put into three categories: real fine spatial resolution imagery, real coarse spatial resolution imagery and generated finer spatial resolution imagery. The only spectral segments that fit into the real fine spatial resolution image category were the HRVIR images because their segmentation was very distinct from the others. The second category was made up of the VGT imagery as well as the phase I co-simulated images and phase I and II LVM based images. The spectral segments from these generated finer spatial resolution images closely mimicked the segmentation of the VGT imagery. Although their spatial resolution was not the same, the information that could be extracted from these spectral segments was very similar to that of the original VGT image. The generated image group was made up of the phase II and III co-simulated images. The spectral segments resulting from these images differed from both the real fine and coarse spatial resolution images.

Spectral segments in spectral feature space differed from image to image. The results of section 8.2 provided further evidence of these differences. By ranking each spectral segment based on the number of pixels, comparisons were made between images. It was observed that the ranked segments were not similar geographically overall and therefore the ranked segments could not be matched. For example, the total number of pixels was equal within a spectral segment however in one image the

segment represented water while in the other image the segment represented man made objects. The similarities between ranked segments could not be tested statistically because the number of segments delineated by the K-means algorithm was not constant.

Accuracy is determined by the differences between what is known to be at a specific location and what is considered to be at the same location based on the available data. The smaller the difference, the more accurate the information. In section 8.3, the locations of several known land-cover classes were compared to the spectral segments at those same locations. With the exception of the water land-cover class, there was a variable distribution of spectral segments that made up any single land-cover class. While this in itself was not unusual, the fact that these same spectral segments were found within different land-cover classes does suggest error. The more land-cover classes a spectral segment belongs to, the greater is the error of the classification.

The VGT image results in this chapter could be deceiving because the spatial resolution of the pixels was not 1 km. In order to overlay the VGT image on the other images, the 1 km spatial resolution had to be divided into smaller pixels which were equal in spatial resolution to the HRVIR and generated images. As a consequence of dividing up the large pixels, the resulting distributions of the total percentage found within a given land-cover class was less then what it should have been. For example, if the vector crossed down the middle of a VGT pixel then the entire pixel area would be used to estimate the area. By dividing up the VGT pixel, only half of the pixels

within the area taken up by the original VGT pixel were taken into account thereby decreasing the area taken up by the VGT image data.

Validation requires a high degree of geometric accuracy because geometric error displaces objects from where they should be located or known to be located. The VGT imagery in study site B did not appear to overlay the HRVIR imagery exactly. This has significant implications for validation because errors would then be caused by the error in location and not necessarily spectral segmentation. Geometric accuracy is paramount for this procedure. For validation purposes, both location and class are most important.

In the perfect case, a single spectral segment would be associated with a single land-cover class. However, this idea is the exception rather than the rule because land-cover classes are necessarily made up of a varying number of spectral objects, i.e. the urban land-cover class was made up of vegetation as well as man-made structures. The heterogeneity that was found both in the HRVIR, VGT and generated finer spatial resolution images was normal.

8.4.1 A possible validation procedure

A validation procedure that would be better suited to the type of data available and generated through stochastic imaging techniques is suggested. The primary issues that must be taken into account are the differences in scale between the two data sets as well as the differences in information content, e.g. a topographic

map and a remotely sensed image. Validation would be uncomplicated if the validation data set had the same scale as the data being validated. In such a case there would be no question as to the differences in scale and therefore error could be dealt with directly. However, this is rarely the case requiring users to compare information derived from two different scales and derived in different manners.

There are two aspects to remote sensing image validation: accuracy of classification and accuracy of location. The accuracy of classification is the ability to segment and label pixels within the image with the wanted object classes. The accuracy of location is making sure that the classified pixel is in the correct geographic location. For best results both types of accuracy should have little error.

The validation procedure taken in this dissertation tried to be objective by choosing automatic segmentation procedures. Also, a direct comparison was hoped for between generated finer spatial resolution imagery and HRVIR imagery. From the results that were shown, it is obvious that a direct comparison was not possible. However, further analysis is warranted.

A future study would look at several different scales (figure 8.37). Finer spatial resolution images would be generated in the same manner at four different spatial resolutions, e.g. 500 m, 250 m, 100 m, and 20 m. At the same time, the classified fine spatial resolution image would be generalized to the same spatial resolutions as those generated by stochastic simulation thereby allowing direct comparison of information at different spatial resolutions. Furthermore, the types of

land-cover classes that persist could be observed in the generalization of the finer spatial resolution information.

Once the new data sets are generated, a relationship could be modeled between the spectral segments of the generated finer spatial resolution imagery and those of the generalized land-cover classes to assist in the labeling of the spectral segments of the generated finer spatial resolution imagery.

Finally an accuracy assessment could be made between the classified generated finer spatial resolution imagery and those of the generalized land-cover map. This accuracy assessment could begin based on a single land-cover class such as the forest class. The forest class is a good choice because it is an important object in both global and local scale studies and (depending on size) can be observed at both fine and coarse spatial resolutions.

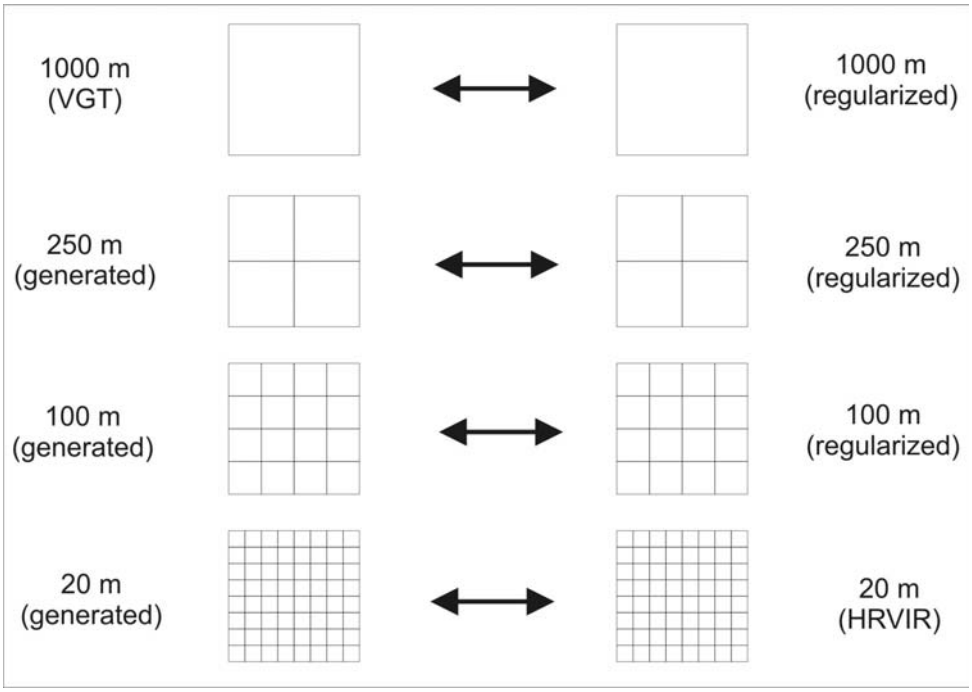

Figure 8.37 – Proposed validation procedure for comparing generated finer spatial resolution images to a validation data set.

Such a study would also help determine whether a break in the range of spatial scales generated is present. The break would be detected with differences found between the generalized and generated images.

The testing of different validation procedures is a necessity in this case in order to better understand what stochastic imaging is capable of in terms of generating finer spatial resolution imagery as well as for quantifying the error that could be expected from using such a technique. It is expected that this procedure could produce valued results when dealing with both large and small changes in spatial resolution.

Chapter 9 – Summary and Conclusions

Two competing procedures are used today for land-cover monitoring at the global scale. The traditional land-cover characterisation and mapping procedure begins with a fine spatial resolution image and then one generalises to the wanted map scale (e.g. 1:100 000). The second procedure is based on a mixed spatial resolution approach that utilises both coarse spatial resolution imagery and fine spatial resolution samples. Both procedures are expensive and have poor temporal cohesion (chapter 1). Here, a less expensive and temporally sound reverse procedure was proposed and tested by generating finer spatial resolution multi-spectral imagery based solely on coarse spatial resolution data.

This research demonstrated that technically it is possible to generate finer spatial resolution images based solely on coarse spatial resolution imagery and stochastic imaging techniques. Between the two sequential gaussian simulation options used, the co-simulation approach produced more realistic results compared to the HRVIR imagery considered as the 'truth'. However, this required the derivation of the fine spatial resolution variogram and object location information.

In phase I, many similarities were observed between the resulting finer spatial resolution imagery and the conditioning VGT imagery. These similarities were observed spatially, statistically and in the spectral segmentation of the imagery. As a result it was necessary to refine the procedure to better match the image

characteristics of the HRVIR imagery. Refining the procedure required determination of the variogram at the finer spatial resolution.

As explained in chapter 6, the derived finer spatial resolution variogram was very different from the variogram computed directly from the HRVIR imagery, even though the imagery was acquired at the same moment in time and with the same spectral bands. The geostatistical theory of regularisation could not be assumed in this case to derive the finer spatial resolution variogram parameters because of differences in the HRVIR and VGT sensor systems. These differences were attributed to the fact that the HRVIR and VGT sensors are separate systems. As a result, it was decided that the computed HRVIR variogram be used instead. The resulting generated finer spatial resolution images had spatial heterogeneity that better resembled the HRVIR imagery. However, spectrally the spatial location of segments did not correspond to either the VGT or HRVIR images.

Geographically improved finer spatial resolution images were generated with the conditioning help of the RADARSAT-1 ScanSAR imagery (phase III – see chapter 7). The co-simulation was able to integrate the location information into the generated finer spatial resolution imagery but was very dependent on the optical and SAR linear relationship. Differences were still observed visually and statistically between the phase III and the HRVIR images. The images showed visual undertones of the conditioning SAR imagery while the statistical results matched the phase II co-simulated images. For mapping purposes, the geographic information provided by the SAR data is essential to better delineate objects when stochastic imaging is applied.

SAR data is also easily acquired because of its active sensor system thereby facilitating the acquisition of images to complement the coarse spatial resolution optical imagery.

The final step in any remote sensing investigation is information extraction. Information extraction began with the automatic spectral segmentation of the original and generated images. Further information extraction was hindered because of the difficulty in matching spectral clusters between images (see chapter 8). As a result, accuracy assessment also proved difficult. Furthermore, the stochastic spatial nature of the generated finer spatial resolution images did not allow for a regular accuracy assessment because the location of simulated pixels varied with each realisation.

Spectral homogeneity within land-cover classes was rare because of the very nature of the land-cover. A class, such as forest or urban, will be quite variable even when spectral segmentation is applied as was demonstrated by the HRVIR imagery (see chapter 8). This same spectral heterogeneity was found in the generated finer spatial resolution images. The difficulty lied in knowing whether a segment was part of a real land-cover class or an artefact of the stochastic imaging process. As a test, known broad land-cover classifications (e.g. urban) were overlaid onto the images and the cluster distributions compared. With the exception of the water class, land-cover classes were made up of several different clusters. The phase II and III results appeared to have dominant clusters but it was difficult to evaluate their significance in terms of land-cover classes. Even the HRVIR imagery behaved in a similar manner.

Overall, this series of experiments served to:

- demonstrate that coarse spatial resolution imagery can be used to generate finer spatial resolution imagery from stochastic imaging techniques. However, before spectral reproducibility can be achieved, the sensing system and scale relationships must be better understood;
- illustrate the appropriateness of the co-simulation technique but also show that the input parameters (variogram and distribution) drive the resulting spatial scale of the generated finer spatial resolution images;
- demonstrate that the use of SAR imagery is beneficial to the process of generating finer spatial resolution imagery because it helps fix the ground scene characteristics, but the relationship to the optical imagery (an important input parameter for co-simulation) varies depending on the scene and must be further investigated;
- show that spectral segmentation of synthetic imagery is possible but validation remains difficult using the standard approach;
- demonstrate that the ground scenes of the study sites were favourable for this methodology. However, this small group of sites does not represent all possible ground scenes and larger areas in different regions must also be tested to see how scene types influence the resulting generated finer spatial resolution imagery.

Several other topics for research emerged from the results of the work presented:

1. The derivation of finer spatial resolution image statistics is paramount to advancing the presented methodology. A better understanding of the relationship between the optical and SAR imagery and the effects of arbitrarily increasing the correlation will provide a better understanding of the potential of this methodology for incorporating different types of image data.

2. The results presented above were based on four distinct regions that were chosen to satisfy the decision of stationarity and other criteria (e.g. different land-covers). Monitoring necessarily covers much larger regions that may not be considered stationary and therefore affect the stochastic imaging procedure. Another consequence of this is the variogram model used for the region under study. A single variogram model that describes the entire region will be very generic and not capable of describing local variability. As a consequence, a better design would be to delineate areas within the study region that are similar before generating finer spatial resolution imagery.

3. Monitoring of a specific region requires imagery to be recorded over time. The behaviour of the resulting generated finer spatial resolution images based on a set of images acquired over time is important because the deviations in the resulting images must be known to be caused by changes on the ground rather than due to the stochastic imaging procedure. Otherwise, real changes could not be separated from artefacts of the simulation process.

4. The statistical images generated from the set of 50 realisations contributed to the understanding of the possible alternatives that each realisation produced. Further study can look into the spectral cluster differences between each of the realisations.

The success of this procedure could lead to the possibility of establishing a procedure that provides image data at the desired scale of observation given the available imagery.

References

Addicott, J.F., Aho, J.M., Antolin, M.F., Padilla, D.K., Richardson, J.S. and Soluk, D.A., 1987. Ecological neighborhoods: scaling environmental patterns, *Oikos* 49: 340-346.

Allen, T.F.H. and Starr, T.B. 1982. Hierarchy: perspectives for ecological complexity, The University of Chicago Press, Chicago.

Almeida, A. and Journel, A., 1994. Joint simulation of multiple variables with a Markov-type coregionalization model, *Mathematical Geology*, 26(5) : 565 – 588.

Atkinson, P.M., and Emery, D.R., 1999. Exploring the relation between spatial structure and wavelength: implications for sampling reflectance in the field, *International Journal of Remote Sensing*, 20(13): 2663 – 2678.

Atkinson, P.M., Cutler, M.E.J. and Lewis, H., 1997. Mapping sub-pixel proportional land cover with AVHRR imagery, *International Journal of Remote Sensing*, 18(4): 917 – 935.

Atkinson, P.M., Curran, P.J., and Webster, R., 1990. Sampling remotely sensed imagery for storage, retrieval, and reconstruction, *Professional Geographer*, 42(3): 345 – 353.

Atkinson, P.M., Webster, R., and Curran, P.J., 1992. Cokriging with Ground-Based Radiometry, *Remote Sensing of Environment*, 41: 45 – 60.

Atkinson, P. M. and Curran P. J., 1995. Defining an Optimal Size of Support for Remote Sensing Investigations, *IEEE Transactions on Geoscience and Remote Sensing*, 33(3) : 768 – 776.

Bellehumeur, C. and Legendre, P., 1998. Multiscale sources of variation in ecological variables: modeling spatial dispersion, elaborating sampling designs, *Landscape Ecology*, 13: 15 – 25.

Benson, B. J. and MacKenzie, M. D., 1995. Effects of sensor spatial resolution on landscape structure parameters, *Landscape Ecology*, 10(2): 113 – 120.

Bielski, C. M., 1997. Spatial structure of dense tropical forest coarse resolution images, Master's thesis, Université Catholique de Louvain.

Bielski, C. M. and Cavayas, F., 1998. A Spatial Estimation Approach to increasing the accuracy of Global tropical Forest Area Estimates. In *First International Conference on Geospatial Information in Agriculture and Forestry*, Lake Buena Vista, Florida, 1-3 June: I 486 – 493.

Bielski, C. M., 1999. Generation of Higher Resolution Land Cover Imagery Derived from Coarse Spatial Resolution Land Cover Classification for the Correction of Land Cover Estimation Error, Report to the Canada Centre for Remote Sensing for Dr. J. Cihlar.

Bhatti, A.U., Mulla, D.J. and Frazier, B.E., 1991. Estimation of Soil Properties and Wheat Yields on Complex Eroded Hills Using Geostatistics and Thematic Mapper Images, *Remote Sensing of Environment*, 37: 181 – 191.

Buttner, G. and Csillag, F., 1989. Comparitive Study of Crop and Soil Mapping Using Multitemporal and Multispectral SPOT and Landsat Thematic Mapper Data, *Remote Sensing of Environment*, 29: 241 – 249.

Carper, W. J., Lillesand, T. M., and Kiefer, R. W., 1990. The use of intensity hue saturation transformations for merging SPOT panchromatic and multispectral image data, *Photogrammetric Engineering & Remote Sensing*, 56(4): 459 – 467.

CCRS 2001 - http://www.ccrs.nrcan.gc.ca/ccrs/eduref/sradar/indexe.html

Chavez, P. S. Jr., Sides, S. C., and Anderson, J. A., 1991. Comparison of three different methods to merge multiresolution and multispectral data: Landsat TM and SPOT panchromatic, *Photogrammetric Engineering & Remote Sensing*, 57(3): 265 – 303.

Christakos, G., 1984. On the problem of permissible covariance and variogram models, *Water Resources Research*, 20(2): 251 – 265.

Cihlar, J., Beaubien, J., Xiao, Q., and Chen, Z. Li, 1997. Land cover of the BOREAS Region from AVHRR and Landsat data, *Canadian Journal of Remote Sensing*, 23(2): 163 – 175.

Cihlar, J., 2000. Land cover mapping of large areas from satellites: status and research priorities, *International Journal of Remote Sensing*, 21(6&7): 1093 – 1114.

Clark, I., 1977. Regularization of a semivariogram, *Computers & Geosciences*, 3:341 – 346.

Cohen, W., Spies, B., Thomas, A., and Bradshaw, G. A., 1990. Semivariograms of Digital Imagery for Analysis of Conifer Canopy Structure, *Remote Sensing of Environment*, 34:167 – 178.

Collins, J.B., and Woodcock, C. E., 1996. Explicit consideration of multiple landscape scales while selecting spatial resolutions. In *Spatial Accuracy Assessment in Natural Resources and Environmental Sciences*, Second International Symposium, 21 –23 May, Fort Collins, Colorado : 121 – 128.

Collins, J. B., and Woodcock, C. E., 1999. Geostatistical Estimation of Resolution Dependent Variance in Remotely Sensed Images, *Photogrammetric Engineering and Remote Sensing*, 65(1): 41 – 50.

Colwell, R. N., 1983. Manual of Remote Sensing, second edition, Volume 1, American Society of Photogrammetry.

Cross, A. M., Settle, J. J., Drake, N. A., and Paivinen, R. T., 1991. Subpixel measurement of tropical forest cover using AVHRR data, *International Journal of Remote Sensing*, 12: 1119 – 1129.

Csillag, F. and Kertesz, M., 1989. Spatial Variability: Error in Natural Resource Maps? *Agrokemia & Talajtan (Agrochemistry and Soil Science)*, 37: 715 – 726.

Csillag, F., Fortin, M-J, and Dungan, J. L., 2000. On the Limits and Extensions of the Definition of Scale, *Bulletin of the Ecological Society of America*, 81(3) : 230 – 232.

Cullinan, V. I. and Thomas, J. M., 1992. A comparison of quantitative methods for examining landscape pattern and scale, *Landscape Ecology*, 7(3): 211 – 227.

Curran, P. J., 1985. Principles of Remote Sensing, Longman Scientific and Technical (John Wiley and Sons), New York.

Curran P. J. and Dungan, J. L., 1988. Zones of information in the AVIRIS spectra, *AVIRIS Airborne Geoscience Workshop Proceedings*, JPL Publication.

Curran, P. J. and Atkinson, P. M., 1998. Geostatistics and remote sensing, *Progress in Physical Geography*, 22(1): 61 – 78.

Cushine, J. L., 1987. The interactive effect of spatial resolution and degree of internal variability within land-cover types on classification accuracies, *International Journal of Remote Sensing*, 81(1): 15 – 29.

Czaplewski, R. L. and Catts, G. P., 1992. Calibration of Remotely Sensed Proportion or Area Estimates for Misclassification Error, *Remote Sensing of Environment*, 39: 29 – 43.

D'Agostino, V., and Zelenka, A., 1992. Supplementing solar radiation network data by co-kriging with satellite images, *International Journal of Climatology*, 12: 749 – 761.

Defries, R.S. and Belward, A.S., 2000. Global and regional land cover characterization from satellite data: an introduction to the Special Issue, *International Journal of Remote Sensing*, 21(6 & 7): 1083 – 1092.

Del Carmen-Valdes, M. and Inamura, M., 2001. Improvement of remotely sensed low spatial resolution images by back-propagated neural networks using data fusion techniques, *International Journal of Remote Sensing*, 22(4): 629 – 642.

Deutsch, C. V. and Journel, A. G., 1998. GSLIB – Geostatistical Software Library and User's Guide, Applied Geostatistics Series, second edition, Oxford Univ. Press, New York.

Dungan, J. L., Peterson, D. L., and Curran, P. J., 1994. Alternative approaches for mapping vegetation quantities using ground and image data. Environmental Information Management and Analysis: Ecosystem to global scales, eds. Michener, William K., Brent, James, W., and Stafford, Susan, G., Taylor and Francis Ltd. Great Britain.

Dungan, J., 1998. Spatial prediction of vegetation quantities using ground and image data, *International Journal of Remote Sensing*, 19(2): 267 – 285.

Eklundh, L. R., 1995. Noise estimation in NOAA AVHRR maximum-value composite NDVI images, *International Journal of Remote Sensing*, 16(15): 2955 – 2962.

Ehrlich, D., Lambin, E. F., and Malingreau, J-P., 1997. Biomass Burning and Broad-Scale Land-Cover Changes in Western Africa, *Remote Sensing of Environment*, 61: 201 – 209.

Fazakas, Z. and Nilsson M., 1996. Volume and forest cover estimation over southern Sweden using AVHRR data calibrated with TM data, *International Journal of Remote Sensing*, 17(9): 1701 – 1709.

Foody, G. M., 1994. Ordinal-Level Classification of Sub-Pixel Tropical Forest Cover, *Photogrammetric Engineering and Remote Sensing*, 60(1): 61 – 65.

Forman, R. T. T. and Godron, M. 1986. Lanscape Ecology, John Wiley and Sons, New York.

Gohin, F., 1989. Analyse structural de la temperature de surface de la mer, Geostatistics, Vol.1 : 433 – 444. M.Armstrong (ed.) Kluwer Academic Publishers.

Gomez-Hernandez, J. and Journel, A., 1993. Joint sequential simulation of multi-Gaussian fields, In A. Soares, editor, Geostatistics Troia '92, volume 1: 85 – 94. Kluwer Academic Publishers, Dordrecht.

Goodchild, M., 1988. The issue of accuracy in global databases, in Mounsey, H. and Tomlinson, R., (Eds.) Building Databases for Global Science, pp. 31-48, London: Taylor and Francis.

Goovaerts, P. 2000. Geostatistical Mapping of Satellite Data using P-field simulation with conditional probability fields, *Proceedings of the Fourth International Symposium on Spatial Accuracy Assessment in Natural Resources and Environmental Sciences* (Amsterdam), pp. 253-260.

Goovaerts, P., 1997. Geostatistics for Natural Resources Evaluation, Oxford Univ. Press, New-York, 483 ~ p.

Goovaerts, P. 1997. Kriging vs. stochastic simulation for risk analysis in soil contamination. In A. Soares, J. Gomez-Hernandez, and R. Froidevaux, editors, geoENV I – Geostatistics for Environmental Applications, pp. 247 – 258. Kluwer Academic Publishers, Dordrecht.

Gosz, J.R. 1986. Biogeochemistry research needs: observations from the ecosystem studies program of The National Science Foundation, *Biogeochemistry*, 2: 101 – 112.

Griffith, D. A., 1993. Advanced spatial statistics for analysing and visualizing geo-referenced data, *International Journal of Geographical Information Systems*, 7(2): 107 – 123.

Gustafson, E. J., 1998. Quantifying Landscape Spatial Pattern: What Is the State of the Art? *Ecosystems*, 1: 143 – 156.

Henderson-Sellers, A., Wilson, M. F. and Thomas, G., 1985. The effect of spatial resolution on archives of land cover type, *Climatic Change*, 7: 391 – 402.

Henry, P. and Meygret, A., 1999. Calibration of VEGETATION Cameras on-board SPOT4, VEGETATION 1999 website.

Isaaks, E. H. and Srivastava, R. M., 1989. An introduction to Applied Geostatistics, Oxford University Press, New York.

Iverson, L. R., Cook, E.A., and Graham, R.L., 1994. Regional forest cover estimation via remote sensing: the calibration center concept, *Landscape Ecology*, 9(3): 159 – 174.

Journel, A. G. and Huijbregts, Ch. J., 1989. Mining Geostatistics, 4th. printing with corrections, London ; Toronto : Academic Press, c1978.

Journel, A. G., 1989. Fundamentals of Geostatistics in Five Lessons, American Geophysical Union.

Journel, A.G., 1996. Modeling uncertainty and spatial dependence: Stochastic imaging, *International Journal of Geographical Information Systems*, 10(5): 517 – 522.

Jupp, D. L.B., Strahler, A. H., and Woodcock, C. E., 1988. Autocorrelation and Regularization in Digital Images I. Basic Theory, *IEEE Transactions on Geoscience and Remote Sensing*, 26(4) : 463 – 473.

Justice, C.O., Markham, B.L., Townshend, J.R.G. and Kennard, R.L., 1989. Spatial degradation of satellite data, *International Journal of Remote Sensing*, 10(9):1539 – 1561.

Kerdiles, H., and Grondona, M.O., 1995. NOAA-AVHRR NDVI decomposition and subpixel classification using linear mixing in the Argentinean Pampa, *International Journal of Remote Sensing*, 16(7): 1303 – 1325.

Kleinn, C., Traub, B., and Dees, M., 1996. Large Area Forest Cover Assessment: Effects of Misregistration in a Double Sampling Approach with Coarse and High Resolution Satellite Images. In *Spatial Accuracy Assessment in Natural Resources and Environmental Sciences: Second International Symposium*, May 21-23, Fort Collins, Colorado, Mowrer, Czaplewski and Hamre Eds. : 391 – 400.

Krige, D., 1951. A Statistical Approach to Some Mine Valuations and Allied Problems at the Witwatersrand. Marster's Thesis, University of Witwatersrand.

Kong, X., N. and Vidal-Madjar, D., 1988. Effet de la resolution spatiale sur des proprietes statistiques des images satellites: une etude de cas, *International Journal of Remote Sensing*, 9(8): 1315 – 1328.

Lacaze, B., Rambal, S., and Winkel, T., 1994. Identifying spatial patterns of Mediterranean landscapes from geostatistical analysis of remotely-sensed data, *International Journal of Remote Sensing*, 15(12): 2437 – 2450.

Lark, R.M., 1996. Geostatistical description of texture on an aerial photograph for discriminating classes of land cover, *International Journal of Remote Sensing*, 17(11): 2115 – 2133.

Ling, B. and Butler, R., 1999. Comparing Effects of Aggregation Methods on Statistical and Spatial Properties of Simulated Spatial Data, *Photogrammetric Engineering & Remote Sensing*, 65(1): 73 – 84.

Liu, J. G., 2000. Smoothing Filter-based Intensity Modulation: a spectral preserve image fusion technique for improving spatial details, *International Journal of Remote Sensing*, 21(18): 3461 – 3472.

Lunetta, R. S., Congalton, R. G., Fenstermaker, L. K., Jensen, J. R., McGwire, K. C., and Tinney, L. R., 1991. Remote Sensing and Geographic Information System Data Integration: Error Sources and Research Issues, *Photogrammetric Engineering and Remote Sensing*, 57(6): 677 – 687.

Markham, B., and Townshend, J. R. G. 1981. Land cover classification accuracy as a function of sensor spatial resolution**,** *Proceedings 15th Int. Symp. on Remote Sensing of Environment*, Ann Arbor, MI : 1075 – 1090.

Marceau, D. J., Howarth, P. J., and Gratton, D. J., 1994a. Remote Sensing and the Measurement of Geographical Entities in a Forested Environment. Part 1: The Scale and Spatial Aggregation Problem, *Remote Sensing of Environment*, 49(2): 93 – 104.

Marceau, D. J., Gratton, P. J., Fournier, R. A., and Fortin, J. P., 1994b. Remote Sensing and the Measurement of Geographical Entities. Part 2: The Optimal Spatial Resolution, *Remote Sensing of Environment*, 49(2): 105 – 117.

Maselli, F., Gilabert, M. A., and Conese, C., 1998. Integration of High and Low Resolution NDVI Data for Monitoring Vegetation in Mediterranean Environments, *Remote Sensing of Environment*, 63: 208 – 218.

Mather, P. M., 1987. Computer Processing of Remotely-Sensed Images: An Introduction, John Wiley and Sons, Chichester.

Mayaux, P. and Lambin E. F., 1995. Estimation of Tropical Forest Area from Coarse Spatial Resolution Data: A Two-Step Correction Function for Proportional Errors Due to Spatial Aggregation, *Remote Sensing of Environment*, 53: 1 – 15.

Mayaux, P. and Lambin E. F., 1997. Tropical Forest Area Measured from Global Land-Cover Classifications : Inverse Calibration Models Based on Spatial Textures, *Remote Sensing of Environment*, 59 : 29-43.

McBratney, A. B. and Webster, R., 1986. Choosing functions for semi-variograms of soil properties and fitting them to sampling estimates, *Journal of Soil Science*, 37: 617 – 639.

Meentemeyer, V. and Box, E.O., 1987. Scale effects in landscape studies, in Landscape Heterogeneity and Disturbance : 15 – 36. Edited by M.G. Turner. Springer -Verlag, New York.

MODIS 2000 - http://ltpwww.gsfc.nasa.gov/MODIS/MODIS.html

Moody, A. and Woodcock, C. E., 1994. Scale-Dependent Errors in the Estimation of Land-Cover Proportions: Implications for Global Land-Cover Datasets, *Photogrammetric Engineering and Remote Sensing*, 60(5): 585 – 594.

Moody, A. and Woodcock, C. E., 1995. The influence of scale and the spatial characteristics of landscapes on land-cover mapping using remote sensing, *Landscape Ecology*, 10(6): 363 – 379.

Moreno, J. F., Melia, J., 1994. An optimum interpolation method applied to the resampling of NOAA AVHHR data, *IEEE Transactions on Geoscience and Remote Sensing*, 32(1): 131 – 151.

Moulin, S., Fischer, A., Dedieu, G., and Delecolle, R., 1995. Temporal Variations in Satellite Reflectances at Field and Regional Scales Compared with Values Simulated by Linking Crop Growth and SAIL Models, *Remote Sensing of Environment*, 54:261 – 272.

NACOG 2000 - North American Council on Geostatistic, August 11, University of Michigan (Ann Arbor).

Nellis, M. D. and Briggs, J. M., 1989. The effect of spatial scale on Konza landscape classification using textural analysis, *Landscape Ecology*, 2(2): 93 – 100.

Narenda, P. M. and Goldberg, M., 1977. A Non-Parametric Clustering Scheme for Landsat, *Pattern Recognition*, 9: 207 – 215.

Olea, R., 1991. Editor, Geostatistical Glossary and Multilingual Dictionary. Oxford University Press, New York.

Oleson, K.W., Sarlin, S., Garrison, J., Smith, S., Privette, J.L., and Emery, W.J., 1995. Unmixing Multiple Land-Cover Type Reflectances from Coarse Spatial Resolution Satellite Data, *Remote Sensing of Environment*, 54: 98 – 112.

Oliver, M. A., 1987. Geostatitics and its application to soil science, *Soil Use and Management*, 3(1): 8 – 20.

O'Neil, R.V., 1973. Error analysis of ecological models : 898 – 908. In D.J. Nelson, ed. Radionuclides in ecosystems. CONF-710501. National Technical Information Service, Springfield, Virginia, USA.

O'Neil, R.V., DeAngelis, D. L., Waide, J. B. and Alle, T. F. H., 1986. A hiearchical concept of ecosystems. Princeton University Press, Princeton, New Jersey.

Openshaw, S., 1981. Le probleme de l'agregation spatiale en geographie, *L'Espace geographique*, 1:15 – 24.

Ouaidrari, H., Begue, A., Imbernon, J., and D'Herbes, J.M., 1996. Extraction of the pure spectral response of the landscape components in NOAA-AVHRR mixed pixels-application to the HAPEX-Sahel degree square.

PCI ,2000. Geomatica version 8.0, PCI Geomatics remote sensing software, Richmond Hill, Canada.

Pardo-Iguzquiza, E., 1999. VARFIT: a fortran-77 program for fitting variogram models by weighted least squares, *Computers & Geosciences*, 25: 251 – 261.

Pohl, C., and J. L. van Genderen, 1998. Multisensor image fusion in remote sensing: Concepts, methods and applications, *International Journal of Remote Sensing*, 19(5): 823 – 854.

Ranchin, T. and Wald, L., 2000. Fusion of High Spatial and Spectral Resolution Images: The ARSIS Concept and Its Implementation, *Photogrammetric Engineering & Remote Sensing*, 66(1): 49 – 61.

Raney, R. K., A. P. Luscombe, and E. J. Langham, 1991. RADARSAT, *Proceedings of the IEEE*, 79(6): 839 – 849.

Rastetter, E. B., King, A. W., Cosby, B. J., Hornberger, G. M., O'Neil, R. V., and Hobbie, J. E., 1992. Aggregating fine-scale Ecological Knowldge to model coarser-scale attributes of ecosystems, *Ecological Applications*, 2(1):55 – 70.

Richards, J. A. and Jia, X., 1999. Remote Sensing Digital Image Analysis; an Introduction, Springer.

Risser, P.G., Forman, R. T. T. and Karr, J. R. 1984. Landscape ecology: directions and approaches, Special Publications No. 2. Illinois Natural History Survey, Champaign.

Robinson, A. H., Sale, R. D., Morrison, J. L., and Phillip C. M., 1984. Elements of Cartography fifth edition, John Wiley & Sons, New York.

Rossi, R. E., Dungan, J. L. and Beck, L. R., 1994. Kriging in the Shadows: Geostatistical Interpolation for Remote Sensing, *Remote Sensing of Environment*, 49: 32 – 40.

Rosswall, T., Woodmansee, R. G. and Risser, P.G. (Eds) 1988. Scales and global change. John Wiley and Sons, New York.

RSI, 1995. Radarsat International, RADARSAR Illuminated – user guide, RSI client services, Richmond, B.C., Canada.

Rubin, Y. and Gomez-Hernandez, J., 1990. A stochastic approach to the problem of upscaling of conductivity in disordered media - theory and unconditional numerical simulations, *Water Resources Research*, 26: 691 – 701.

Sellers, P., F. Hall, H. Margolis, B., Kelly, D. Baldocchi, G. den Hartog, J. Cihlar, M.G. Ryan, B. Goodison, P. Crill, K.J. Ranson, D. Lettenmaier, and D.E. Wickland. 1995. The boreal ecosystem-atmosphere study (BOREAS): an overview and early results from the 1994 field year, *Bulletin of the American Meteorological Society*, 76(9): 1549 – 1577.

SPOT 2000 - http://www.spot.com/home/support/faq/welcome.htm

Srivastava, R., 1987. Minimum variance or maximum profitability? *CIM Bulletin*, 80(901): 63 – 68.

St-Onge, B.A., and Cavayas, F., 1995. Estimating forest stand structure from high resolution imagery using the directional variogram, *International Journal of Remote Sensing*, 16(11): 1999 – 2021.

Townshend, J. R. G., Justice, C. O., Gurney, C. McManus, J., 1992. The Impact of misregistration on change detection, *IEEE Transactions on Geosciences and Remote Sensing*, 30(5): 1054 – 1060.

Townshend, J.R.G., Justice, C.O., Li, W., Gurney, C., and McManus, J., 1991. Global land cover classification by remote sensing: present capabilities and future possibilities, *Remote Sensing of Environment*, 35: 243 – 255.

Townshend, J.R.G, Justice, C. O., Skole, D., Malingreau, J.-P., Cihlar, J., Teillet, P., Sadowski, F., and Ruttenberg, S., 1994. The 1-km AVHRR global data set: needs of the International Geosphere Biosphere Program, *International Journal of Remote Sensing*, 15(17): 3417 – 3441.

TREES 1999 - http://www.gvm.sai.jrc.it/Forest/defaultForest.htm

Turner, M.G. (Ed) 1987. Landscape Heterogeneity and Disturbance. Springer-Verlag, New York.

Turner, M.G. 1989. Landscape ecology: the effect of pattern on process. *Annu. Rev. Ecol. Syst.*, 20: 171 – 197.

Turner, M. Dale, G., Virginia, H., and Gardner, R. H., 1989a. Predicting across scales: Theory development and testing, *Landscape Ecology*, 3(3/4): 245 – 252.

Turner, M. G., O'Neil, R. V., Gardner, R. H., and Milne, B. T., 1989b. Effects of changing spatial scale on the analysis of landscape pattern, *Landscape Ecology*, 3(3/4): 153-162.

UMD, 1998, http://www.geog.umd.edu/tropical/

UNFCCC 2001 - http://www.unfccc.de/resource/convkp.html

Van der Meer, F. 1996. Classification of remotely sensed imagery using an indicator kriging approach: application to the problem of calcite-dolomite mineral mapping, *International Journal of Remote Sensing*, 17(6): 1233 – 1249.

VEGETATION 1999 – http://vegetation.cnes.fr

VITO 2000 - http://www.vgt.vito.be/faq/faq.html

Webster, R., Curran P.J., and Munden J. W., 1989. Spatial Correlation in Reflected Radiation from the Ground and Its Implications for Sampling and Mapping by Ground-Based Radiometry, *Remote Sensing of Environment*, 29: 67 – 78.

Wiens, J. A. 1989. Spatial scaling in ecology, *Functional Ecology*, 3:385 – 397.

Woodcock, C. E. and Strahler, A. H., 1987. The Factor of Scale in Remote Sensing, *Remote Sensing of Environment*, 21: 311 – 332.

Woodcock, C. E., Strahler, A. H., and Jupp, D. L.B., 1988a. The Use of Variograms in Remote Sensing : I. Scene Models and Simulated Images, *Remote Sensing of the Environment*, 25 : 323 – 348.

Woodcock, C., Strahler, A., and Jupp, D., 1988b. The use of variograms in Remote Sensing II: Real digital images, *Remote Sensing of Environment*, 25: 349 – 379.

Wulder, M. A., LeDrew, E. F., Franklin, S. E., and Lavigne, M. B., 1998. Aerial Image Texture Information in the Estimation of Northern Deciduous and Mixed Wood Forest Leaf Area Index (LAI), *Remote Sensing of Environment*, 64: 64 – 76.

Zhang, R., Warrick, A., and Myers, D., 1990. Variance as a function of sample support size, *Mathematical Geology*, 22: 107 – 121.

Zhang, W. and Montgomery, D. R., 1994. Digital elevation model grid size, landscape representation, and hydrologic simulations, *Water Resources Research*, 30(4): 1019 – 1028.

Zhu, Z. and Evans, D. L., 1994. U.S. forest types and predicted percent forest cover from AVHRR data, *Photogrammetric Engineering and Remote Sensing* 60(5): 525 – 531.